17459

NATIONAL LIBRARY
OTTAWA

CANADA

BIBLIOTHÈQUE NATIONALE
OTTAWA

NAME OF AUTHOR....PETER....C.....BOETZKES..

TITLE OF THESIS....A....SPINNER...MAGNETOMETER

FOR....SUSCEPTIBILITY........

ANISOTROPY.....IN.....ROCKS

UNIVERSITY........ALBERTA..............................

DEGREE FOR WHICH THESIS WAS PRESENTED........Ph.D...............

YEAR THIS DEGREE GRANTED......1973.......................

Permission is hereby granted to THE NATIONAL LIBRARY OF CANADA to microfilm this thesis and to lend or sell copies of the film.

The author reserves other publication rights, and neither the thesis nor extensive extracts from it may be printed or otherwise reproduced without the author's written permission.

(Signed)...Peter C. Boetzkes...

PERMANENT ADDRESS:

...12920 - 124 Ave...
...Edmonton, Alberta...
T5L 2Z6

DATED.....Oct. 24.....1973

NL-91 (10-68)

THE UNIVERSITY OF ALBERTA

A SPINNER MAGNETOMETER FOR SUSCEPTIBILITY ANISOTROPY IN ROCKS

by

© PETER C. BOETZKES

A THESIS
SUBMITTED TO THE FACULTY OF GRADUATE STUDIES AND RESEARCH
IN PARTIAL FULFILMENT OF THE REQUIREMENTS FOR THE DEGREE
OF DOCTOR OF PHILOSOPHY

DEPARTMENT OF PHYSICS

EDMONTON, ALBERTA

FALL, 1973

THE UNIVERSITY OF ALBERTA

FACULTY OF GRADUATE STUDIES AND RESEARCH

The undersigned certify that they have read, and recommend to the Faculty of Graduate Studies and Research, for acceptance, a thesis entitled "A SPINNER MAGNETOMETER FOR SUSCEPTIBILITY ANISOTROPY IN ROCKS" submitted by PETER CHRISTIAN BOETZKES in partial fulfillment of the requirements for the degree of Doctor of Philosophy in Geophysics.

D. I. Gough
Supervisor

J. A. Jacobs

J. S. Rogers

D. Routledge

External Examiner

Date August 7th 1973

ABSTRACT

The thesis surveys the principles of measurement of magnetic susceptibility anisotropy in rocks and its application to petrofabric analysis. A new spinner instrument of very high sensitivity is described and sample measurements on sandstone specimens are presented. In addition a differential transformer for measuring bulk susceptibility is described.

Chapter 1 summarizes physical fundamentals of susceptibility anisotropy and discusses its applications in geology. Several ways in which rocks acquire anisotropy in magnetic susceptibility are discussed. Case histories are described.

Chapter 2 turns specifically to instrumental methods developed by previous workers. Sensitivity limits are derived for torque-meters and for A.C. bridge type instruments. Maximum sensitivity and other limiting parameters for a new instrument are defined in terms of magnetic properties and grain statistics in rocks.

Chapter 3 develops the design of a magnetic circuit in which an anisotropic rotating specimen produces variation of magnetic reluctance. Several types of transducer are considered which could be used to produce electric output from the flux variations. Theoretical sensitivity limits are calculated for each type of transducer.

In Chapter 4 a full description is given of the instrument which has been constructed. Provision is made for the use of various transducers. A set of coils near the specimen gives adequate sensitivity in terms of drift of the signal generated by the shaft assembly, which in practice limits the sensitivity. The rms noise level of the instrument with its shaft spinning outside the specimen gap is about 4 x 10^{-11} mks units. Fluctuations from the shaft and specimen holder increase the noise level to about 1.5 x 10^{-9} mks units. Reliable measurement is possible at a level of 10^{-8} mks units.

Chapter 5 gives an account of the assembly of the stator of the instrument, which includes the magnetic circuit and magnetizing and sensing coils.

Chapter 6 describes the differential transformer used for measurement of bulk susceptibility. It allows measurement of diamagnetic substances in a one-inch cylindrical specimen.

In Chapter 7 some results are presented for two sets of rock specimens, as a demonstration that the new instrument produces meaningful results at a very high sensitivity.

ACKNOWLEDGEMENTS

I wish to express my sincere gratitude to Dr. D. I. Gough for supervising the research project. I am thankful for his advice and continuous encouragement during the course of this study.

Dr. H. A. K. Charlesworth provided supervision during the early stages of the project, and for this I am grateful.

I would like to thank Messrs. N. Riebeek, A. Mannes, J. Cuthiell, K. Preston, M. Rancourt, and W. Volk for the excellent machine work which they did on various components of the magnetometer, and also for doing the annealing of all the permalloy laminations used in the instrument.

I am particularly thankful to my brother, Willie, for his assistance in the actual construction of the instrument and for his help in various other stages of the project.

I wish to thank my parents for bringing me to Canada, and for their many years of support and encouragement.

Lastly, I wish to thank my wife, Cheryl, for her valuable assistance in the preparation of this thesis.

TABLE OF CONTENTS

Page

ABSTRACT iv

ACKNOWLEDGEMENTS vi

TABLE OF CONTENTS vii

LIST OF TABLES xii

LIST OF ILLUSTRATIONS xiii

LIST OF PLATES xviii

CHAPTER 1 FUNDAMENTAL PRINCIPLES AND GEOLOGICAL APPLICATIONS OF MAGNETIC SUSCEPTIBILITY ANISOTROPY IN ROCKS 1

1.1 Fundamentals of the Magnetic Properties of Rocks 1

1.2 Magnetic Susceptibility Anisotropy in Rocks 3

1.3 Geological Applications of Magnetic Susceptibility Anisotropy 13

1.4 Previous Studies of Susceptibility Anisotropy 14

1.5 Statistical Significance of Measured Susceptibility Anisotropy 20

1.6 Ambiguities in Magnetic Data 25

CHAPTER 2 PREVIOUS INSTRUMENTS USED FOR MAGNETIC SUSCEPTIBILITY ANISOTROPY STUDIES 33

2.1 The Torque Method 33

2.2 Spinner Magnetometers for Susceptibility Anisotropy 47

2.3 D. C. Spinner Instruments 60

Page

2.4 Requirements for the New Magnetometer 62

CHAPTER 3 DESIGN OF FLUX SENSORS FOR A SPINNER MAGNETOMETER 70

3.1 The Basic Susceptibility-Anisotropy Instrument 71

3.2 Noise Generated by the Signal Coil 80

3.3 Noise Due to the Magnetic Core 83

3.3.1 Types of Noise 83

3.3.2 Nyquist Noise in the Magnetic Core 85

3.3.3 Laminations Much Thinner than Skin Depth 90

3.3.4 Laminations Much Thicker than Skin Depth 95

3.3.5 Noise in Ferrite Cores 99

3.3.6 Excess Noise Due to Magnetic Viscosity in Cores 103

3.4 Sensitivity of the Basic Instrument 104

3.5 Design of Magnetic Bridge 107

3.6 Design of a Magnetic Helix 117

3.6.1 Optimization of Johnson and Magnetic Noise 120

3.6.2 Inter-Turn Flux Leakage 125

3.7 Magnetic Modulators 126

3.7.1 Nonlinear Magnetization Modulator 127

3.7.2 Villari-Effect Modulators 135

3.7.3 Mechanical Variable Air Gap Modulator 140

Page

3.8 Signal Coils in the Specimen Gap 153

CHAPTER 4 DESIGN OF A NEW MAGNETOMETER 163

4.1 The Magnetic Circuit 163

4.1.1 Field Uniformity 163

4.1.2 Materials and Dimensions of Components Requiring High Permeability 171

4.1.3 Eddy Current Noise 174

4.2 Establishing the Bias Field 182

4.2.1 Design of the Magnet Structure 182

4.2.2 Magnetizing Requirements and Magnetizing Coils 198

4.2.3 The Magnetizing Power Supply 204

4.2.4 Power Supply Circuit Description 212

4.3 Electrical Interference and Shielding 221

4.3.1 Types of Interference and Methods of Shielding 221

4.3.2 Effects of a Hole in the Shield 226

4.4 Encapsulation of the Transducer 235

4.4.1 Encapsulation Requirements 235

4.4.2 Encapsulant Limitations 241

4.5 Electronics 256

4.5.1 Preamplifier 259

4.5.2 Main Amplifier 268

4.5.3 Phase Sensitive Detectors 271

Page

4.5.4 Integrator 274

4.6 Design of Spinner Shaft and Motor Drive 277

4.6.1 Shaft Bearings 277

4.6.2 Spinner Shaft 288

4.6.3 Spinner Motor 292

4.6.4 Motor Drive Electronics 298

CHAPTER 5 CONSTRUCTION OF THE MAIN TRANSDUCER BLOCK 304

5.1 Preparation of the Permalloy Strips 304

5.2 Annealing of the Moly-Permalloy 305

5.3 Assembly of the Polepieces 306

5.4 Assembly of the Magnetizing and Sensing Coils 306

5.5 Magnetic Bridge Subassembly 312

5.6 Assembly of the Main Magnetic Transducer 315

5.7 The Vacuum Impregnation Procedure 334

CHAPTER 6 INSTRUMENT FOR BULK SUSCEPTIBILITY 348

CHAPTER 7 OBSERVATIONS WITH THE NEW INSTRUMENT 354

7.1 Noise Levels in the Spinner Instrument 354

7.2 Operating Sensitivity of the Spinner 358

7.3 Instrument Output for a General Susceptibility Matrix 367

7.4 Geometrical Representation of a Tensor 375

7.5 Calibration 376

Page

7.6 Correction for Orientation of the Specimens in the Outcrop 382

7.7 Comparison with Torque-Meter Measurements 388

7.8 Measurements on Cardium Specimens 394

BIBLIOGRAPHY 409

APPENDIX 1 OWENS SPECIMENS A1

APPENDIX 2 CARDIUM SPECIMENS (ANGLES) A3

APPENDIX 3 CARDIUM SPECIMENS (AMPLITUDES) A5

APPENDIX 4 A LISTING OF IMPORTANT SYMBOLS WITH THE PHYSICAL QUANTITY REPRESENTED AND THE UNITS EMPLOYED A7

LIST OF TABLES

Table Page

7.1 Results of a series of 20 sets of measurements taken on the spinner shaft with an empty specimen cube

(A) Spin Axis 1 364

(B) Spin Axis 2 365

(C) Spin Axis 3 366

LIST OF ILLUSTRATIONS

Figure Page

1.1 Minimum statistically-significant susceptibility anisotropy 27

1.2 Qualitative effects of saturation of elongated grains 31

2.1 General layout of the torsional magnetometer 36

2.2 Relationship of applied field, specimen susceptibility, and resultant torque in a torsional magnetometer 38

2.3 Theoretical sensitivity of torsional magnetometer as a function of suspension time constant 46

2.4 Bridge configurations used in magnetometers 49

2.5 Block diagram of Graham's A.C. Bridge spinner 54

2.6 Shape anisotropy effects with specimens of nonspherical shape 66

3.1 The basic magnetic circuit 73

3.2 Electrical equivalent of the basic magnetic circuit 75

3.3 Model for calculating noise flux of a laminated core 89

3.4 Noise current in a lamination much thinner than skin depth 92

3.5 Assumed flux and current penetration in a lamination thicker than twice skin depth 97

3.6 Noise flux of laminated moly-permalloy and ferrite cores 102

3.7 Plan view of magnetic bridge 109

3.8 Electrical equivalent of the magnetic bridge 111

Figure Page

3.9 A generalized magnetic helix 119

3.10 Principles of second-harmonic-type magnetic modulator 130

3.11 Initial permeability of moly-permalloy as a function of applied tensile stress 137

3.12 Variable-air-gap magnetic modulator 142

3.13 Electrical equivalent of the variable-air-gap magnetic modulator 145

3.14 Acoustic drive for variable-air-gap magnetic modulator 152

3.15 Cross-field specimen gap signal coils 155

3.16 Specimen gap signal coils as viewed along spinner shaft 157

3.17 Field-parallel specimen gap signal coils 160

4.1 Magnetic circuit dimensions for gap-field calculations 167

4.2 Computed magnetic field contours for specimen gap 170

4.3 Plan view of the main magnetic circuit 176

4.4 Perspective view of the main magnetic circuit 178

4.5 Division of the magnetic circuit for magnetic core noise calculation 181

4.6 Magnetic core noise from the main magnetic circuit as a function of lamination thickness 184

4.7 Direct-flux leakage paths within main magnetic circuit 188

4.8 Generalized polepiece dimensions for estimating flux leakage 190

4.9 Flux leakage factor of a pair of cylindrical polepieces 192

Figure Page

4.10 Demagnetizing curve for Arnox 5 197

4.11 Magnetizing curve for Arnox 5 200

4.12 Magnetizing force requirements of the main magnetic circuit elements 203

4.13 Equivalent circuit of solenoid and capacitor bank just before magnetizing pulse 210

4.14 Block diagram of pulse-discharge magnetizing power supply 214

4.15 Schematic of primary power supply for the capacitor bank 216

4.16 Schematic of voltage regulator for magnetizing power supply 218

4.17 Diode decoupling network for the capacitor bank 220

4.18 Magnetic equipotentials in a magnetic shield wall containing a hole 230

4.19 Change in magnetic equipotentials due to a collared hole 234

4.20 Effective mass and spring for estimating lowest mechanical resonance within the transducer block 240

4.21 Pressure exerted by a "flexibilized" epoxy resin as it cools from its curing temperature 246

4.22 Pressure due to cure-induced strain for Scotchcast No. 237 resin 251

4.23 Viscosity as a function of time for Scotchcast No. 237 resin while curing 253

4.24 Block diagram of the signal electronics 258

4.25 Noise characteristics of 2N3906 transistor 264

4.26 Schematic of preamplifier 266

Figure Page

4.27 Schematic of main amplifier 270

4.28 Schematic of phase-sensitive detector 273

4.29 Schematic of integrator 276

4.30 Aerostatic journal bearings for the spinner shaft 281

4.31 General performance of aerostatic journal bearings 284

4.32 Load coefficient versus gauge pressure ratio for aerostatic journal bearings 287

4.33 Relation between jet diameter and clearance for annular orifices 290

4.34 Overall arrangement of the spinner shaft and drive motor 294

4.35 Three views of the specimen cube 296

4.36 Block diagram of motor speed regulator 300

4.37 Schematic of motor speed regulator 302

5.1 Magnetic bridge subassembly 314

5.2 Schematic of the hydraulic circuit used for encapsulation 338

6.1 Schematic of bulk susceptibility 350

6.2 Cross-section of the bulk susceptibility instrument 353

7.1 Noise level in the spinner instrument 356

7.2 Operating sensitivity of the spinner 361

7.3 Comparison of theoretical and observed noise effects 369

7.4 Generalized magnetization and applied field vectors 372

Figure Page

7.5 Comparison of flux, voltage, and current waveforms for the standard solenoid 380

7.6 Generalized orientation of rock specimen 384

7.7 Generalized orientation of susceptibility vector 386

7.8 Directional plot of specimens supplied by Dr. Owens
(A) SI specimens 390
(B) SF specimens 391
(C) NIB specimens 392
(D) KA13 specimens 393

7.9 Map showing locations from which the Cardium Sandstone specimens were taken 396

7.10 Directional plot of Limb 1 susceptibility maxima 399

7.11 Directional plot of Limb 2 susceptibility maxima 401

7.12 Directional plot of Limb 3 susceptibility maxima 403

7.13 Directional plot of Cardium susceptibility intermediate values 405

7.14 Directional plot of Cardium susceptibility minima 407

LIST OF PLATES

Plate		Page
1	Magnetizing coils	309
2	Specimen gap sensing coils	309
3	Direct sensing coils	311
4	Polepiece subassembly	311
5	Magnetic bridge subassembly	317
6	Magnetic bridge subassembly	317
7	Polepiece block and specimen gap	319
8	Location of direct specimen-gap signal coil	319
9	Cross-field sensing coils are added	322
10	Direct nulling coils are inserted	322
11	Outer polepiece subassembly is added	324
12	The cross-field nulling coils are added	324
13	Completed inner magnetic circuit	327
14	Outer permalloy yoke	327
15	Routing of electrical wires	329
16	Permeability-monitoring winding	329
17	Completed internal transducer assembly	331
18	Completed internal transducer assembly	331
19	Completed internal transducer assembly	333
20	Filling of voids with glass beads	333
21	Shield top with ceramic bars	336

Plate		Page
22	Sealed transducer assembly in vacuum chamber, ready for vacuum impregnation	336
23	Overall view of the spinner instrument and its associated electronics	343
24	Transducer block and spinner shaft assembly	345
25	Spinner shaft assembly	345
26	Standard solenoid, standard-size specimens, and the specimen cube	347
27	The instrument for bulk susceptibility	347

STATEMENT CONCERNING CONVENTIONS EMPLOYED IN THIS THESIS

1 Units

The units employed in this thesis are SI units, defined by the Eleventh General Conference on Weights and Measures in Paris in 1960. Electromagnetic units are included in parentheses where it is thought that this will help readers more familiar with these units.

Although in the International System of Units magnetic susceptibility is a dimensionless ratio, the term "mksu" is used in order to avoid confusion with similar quantities expressed in electromagnetic units.

A list of symbols with their definitions and units employed is included in Appendix 4.

2 Projections

All diagrams employing a projection are drawn using the azimuthal equal area or Schmidt projection.

CHAPTER 1

FUNDAMENTAL PRINCIPLES AND GEOLOGICAL APPLICATIONS OF MAGNETIC SUSCEPTIBILITY ANISOTROPY IN ROCKS

1.1 Fundamentals of the Magnetic Properties of Rocks

All materials are magnetic to some extent. They may be classified as being diamagnetic, paramagnetic, or ferromagnetic, depending upon the principal mechanism causing the magnetization induced within the material. In predominantly diamagnetic materials, in terms of simple Bohr theory, the electron orbits, together with their associated magnetic moments, precess about the field direction in such a direction as to produce a net magnetic field opposite to the imposed field. Therefore the magnetic susceptibility

$$\chi = \frac{J}{H} \tag{1.1}$$

where J is the induced magnetization and H is the applied field, is always negative. In addition to the orbital motion, electrons in orbit also spin on their own axes. The associated permanent magnetic moments tend to align themselves with an applied magnetic field. Electron spins tend to orient themselves in opposition, so that in atoms with even numbers of electrons there is no net reaction to a magnetic field. If there is an odd number, however, the unpaired electron can react to an applied magnetic field and contribute to paramagnetism. The transition elements may have several unpaired electron spins, as many as five in the iron series. These materials are all paramagnetic. Since magnetization tends to be in the same direction as the applied field, the magnetic susceptibility is positive, and of the same order of magnitude as diamagnetic susceptibility.

It is the ferromagnetic properties of minerals that are of most importance in studies involving rock susceptibility. When ions are brought together to form crystalline solids, the electron spins in adjacent atoms orient themselves in such a way as to minimize the exchange energy. In most substances this energy is minimized when adjacent electron spins are oppositely oriented. With some substances, however, a parallel configuration of spins is energetically preferable. As a result such materials are highly magnetic. The magnetic moment resulting from an array of these parallel spins does not depend on an externally applied field, and the array therefore constitutes a permanent magnet. The magnetostatic energy in and around a crystal with parallel electron spins rises rapidly as the crystal dimensions increase. In order to minimize this energy, zones of oppositely, or at least unequally, oriented magnetization are formed adjacent to each other. Groups of these zones then form small closed magnetic circuits which minimize the magnetostatic energy while increasing the exchange energy at their boundaries. The dimensions of these zones, or domains, tend to be those which minimize the sum of magnetostatic and exchange energy.

If the magnetic moments of all the ions in the lattice tend to point in the same direction, the material is said to be truly ferromagnetic. Examples are metallic iron, nickel, and cobalt. If some of the moments are antiparallel to others, the material is said to be ferrimagnetic. Magnetite (Fe_3O_4) is one important example. In the special case in which the ions of the lattice are divided into two equal antiparallel sublattices, so that there is no residual moment, the material is termed anti-ferromagnetic. Hematite (αFe_2O_3) is such a material. Hematite also has a weak ferromagnetism superimposed on its anti-ferromagnetic structure. This is thought to be due to imperfect antiparallel alignment or to a small parasitic component of ferromagnetism (Irving, 1964).

1.2 Magnetic Susceptibility Anisotropy in Rocks

Most rocks contain a small proportion of ferrimagnetic or ferromagnetic minerals in particulate form. This fact makes it possible to use magnetic methods in petrofabric analysis. When a specimen of such a rock is placed in a weak magnetic field a magnetization is induced in it. In general the magnetization is a function of orientation of the specimen with respect to the applied field. For many rocks the relationship between applied field and induced magnetization may be usefully approximated by the relation

$$J_i = \kappa_{ij} H_j \qquad (1.2)$$

where: κ_{ij} = apparent magnetic susceptibility, a symmetric tensor of rank two

J_i = intensity of magnetization

H_j = applied field.

The subscripts (i, j) denote any two of three orthogonal specimen axes, and are used in the Einstein convention. Note that the symbol χ is used for intrinsic susceptibility of a material, while the symbol κ is used for apparent susceptibility of a grain or array of grains in a rock specimen.

Anisotropy of susceptibility arises in rocks by two main mechanisms. One depends on the effect of shape of the magnetic grains on the susceptibility. Elongated grains of intrinsically isotropic materials produce anisotropic susceptibility in this way. Cubic minerals in magnetic fields of low intensity are in this category. The other mechanism depends on magnetocrystalline anisotropy in materials like hematite, coupled with an anisotropic crystal habit. Most studies have involved the shape anisotropy, although the magnetocrystalline anisotropy has been studied (Hargraves, 1959; Fuller, 1960, 1963; Porath, 1966;

Hrouda and Janak, 1971). Even a weak alignment of magnetite grains of average elongation produces a much stronger anisotropy than a near-perfect alignment of hematite basal planes, unless the volume fraction of hematite in the rock specimen is several times that of the magnetite (King, 1966).

Shape anisotropy arises because of the inequality of the demagnetizing factors in different directions across non-equidimensional magnetic grains. The intensity of magnetization J in one direction can be expressed as

$$\begin{aligned} J &= \kappa H \\ &= \chi H_{eff} \\ &= \chi (H - NJ) \end{aligned} \qquad (1.3)$$

This can be rearranged to give

$$J = \frac{\chi H}{1 + N\chi} \qquad (1.4)$$

where: κ = apparent susceptibility

H = external field

χ = intrinsic susceptibility of the ferromagnetic material

H_{eff} = effective magnetizing field

N = demagnetizing factor.

In general, the demagnetizing factors of irregular grains are difficult to calculate. However, real grain shapes may be realistically approximated by ellipsoids of revolution whose demagnetizing factors are known (Bozorth, 1951). Although the ellipsoid of revolution may not closely approximate the shape of a single grain, the resultant susceptibility of the rock specimen containing many grains often very nearly approaches that of an ellipsoid. The closeness of fit probably results from cancellation of random components of susceptibility due to grain irregularity. The susceptibility tensor may then be represented by an ellipsoid, with the maximum, intermediate, and minimum values of susceptibility κ_a, κ_b, and κ_c, respectively, corresponding to the principal axes.

Consider a single spheroidal grain having minimum and maximum demagnetizing factors N_a and N_b, respectively. It is placed in a uniform field H with the long axis at an angle θ from the field direction. One can resolve the induced magnetization into components along the two principal axes. From Eq. 1.4,

$$J_a = \frac{\chi H \sin\theta}{1 + \chi N_a}$$

$$J_b = \frac{\chi H \cos\theta}{1 + \chi N_b} \qquad (1.5)$$

In order to find the apparent susceptibility, one needs to find the component of magnetization in the direction of the applied field. The susceptibility $\kappa_{\parallel}$ parallel to H is

$$\kappa_{\parallel} = \frac{J_{\parallel}}{H}$$

$$= \frac{J_a \sin\theta + J_b \cos\theta}{H}$$

$$= \frac{\chi \sin^2\theta}{1 + \chi N_a} + \frac{\chi \cos^2\theta}{1 + \chi N_b}$$

$$= \chi \left[\frac{\left(\frac{1 + \chi N_a}{1 + \chi N_b} \right) \sin^2\theta + \cos^2\theta}{1 + \chi N_b} \right] \qquad (1.6)$$

Now the term in the inner brackets is

$$\frac{1 + \chi N_b}{1 + \chi N_a} = \frac{1 + \chi N_a + \chi(N_b - N_a)}{1 + \chi N_a}$$

$$= 1 + \frac{\chi(N_b - N_a)}{1 + \chi N_a} \qquad (1.7)$$

Therefore

$$\kappa_{\parallel} = \frac{\chi}{1 + \chi N_b} \left[\frac{\chi(N_b - N_a)}{1 + \chi N_a} \sin^2\theta + 1 \right]$$

$$= \frac{\chi}{1 + \chi N_b} \left[\frac{\chi(N_b - N_a)}{2 + 2\chi N_a} (1 - \cos 2\theta) + 1 \right] \qquad (1.8)$$

The component of κ which varies with θ is

$$\kappa_{\parallel}(\theta) = - \frac{\chi^2(N_b - N_a)}{2(1 + \chi N_b)(1 + \chi N_a)} \cos 2\theta \qquad (1.9)$$

For small values of anisotropy the demagnetizing factors in the denominator may be replaced with a mean demagnetizing factor, namely that for a sphere, which is 0.33.

$$\kappa_{\parallel}(\theta) = -\frac{\chi^2 (N_b - N_a)}{2(1 + \frac{\chi}{3})^2} \cos 2\theta \qquad (1.10)$$

Also, for small values of anisotropy, the term $(N_b - N_a)$ can be expressed (Stacey, 1960-a) in terms of $\left[1 - (\frac{b}{a})^2\right]$ where a is the major semiaxis and b is the minor semiaxis of the grain.

$$N_b - N_a \cong 0.2\left[1 - (\frac{b}{a})^2\right]$$

$$\sim 0.4\left[1 - \frac{b}{a}\right] \qquad (1.11)$$

Therefore Eq. 1.10 becomes

$$\kappa_{\parallel}(\theta) = -\frac{0.2\,\chi^2}{(1 + \frac{\chi}{3})^2} (1 - \frac{b}{a}) \cos 2\theta \qquad (1.12)$$

For a single magnetically isotropic grain of spheroidal shape, the anisotropy factor ζ is defined as

$$\zeta = \frac{\kappa_a}{\kappa_b}$$

$$= \frac{1 + \chi N_b}{1 + \chi N_a} \qquad (1.13)$$

Stoner (1945) described the method of calculating the demagnetizing factor, and tabulated the numerical values of N_a and N_b for prolate and oblate ellipsoids of revolution. He shows that the anisotropy due to shape is very small when bulk susceptibility is small. This can be shown by rearranging Eq. 1.13

$$\zeta = \frac{1 + \chi N_b}{1 + \chi N_a}$$

$$= \frac{1 + \frac{1}{2}\chi (N_b + N_c)}{1 + \chi N_a}$$

(since for spheroidal grains $N_b = N_c$)

$$= \frac{1 + \frac{1}{2}\chi(1 - N_a)}{1 + \chi N_a} \qquad (1.14)$$

(since $N_a + N_b + N_c = 1$)

Therefore if intrinsic susceptibility is, say, 10^{-2}, the maximum anisotropy factor is $\zeta = 1.005$ at $N_a = 0$. N_a being zero implies an infinite dimension ratio of a prolate ellipsoid of revolution. It is for this reason that minerals of the ferrimagnetic magnetite-ulvospinel series are by far the most important contributor to the susceptibility anisotropy of rocks. Khan (1962) showed that the magnitude of susceptibility anisotropy in rocks can be accounted for by the shape anisotropy of a very small proportion of magnetite or titanomagnetite in them. The intrinsic susceptibility of natural multicrystalline magnetites varies considerably depending on impurities which block domain wall movement and thereby decrease susceptibility. A value determined by

Uyeda et al (1963) was 9.4 mksu. Werner (quoted by Strangway, 1967) has measured susceptibility values ranging from 5.0 mksu to 35.1 mksu. Hematite, with an intrinsic susceptibility of about 10^{-2} mksu, can generate very little susceptibility anisotropy through shape effects. Similarly, diamagnetic materials seem quite isotropic, no matter what the grain elongation and alignment may be. For a fixed ratio of dimensions of the principal elongation axes, the ζ factor approaches a limiting value asymptotically as κ is increased. Uyeda et al. (1963) tested the ellipsoidal approximation by measuring the demagnetizing factors of cylindrical specimens of various dimensional ratios from polycrystalline magnetite ore. They found quite good agreement with the approximation.

Stacey (1960) has investigated anisotropy of saturation magnetization. It, also, is due to differences in demagnetizing factor and, in favorable circumstances, calculations based on its measurement yield the same fabric as those based on anisotropy of susceptibility. In this case the anisotropy is expressed as directional differences in the energy of saturation magnetization, rather than directional differences in the intensity of magnetization for a given applied field.

The susceptibility ellipsoid may be completely specified by the magnitudes of its principal axes κ_a, κ_b, and κ_c, and their directions. For convenience, the directional information is expressed in terms of maximum and minimum susceptibility, often displayed stereographically. The magnitude information is expressed in suitable combinations of the three principal values (Hamilton and Rees, 1971). The main combinations are magnetic lineation

$$\mathbf{l} = \kappa_a - \kappa_b \qquad (1.15)$$

and magnetic foliation

$$\mathbf{f} = \frac{\kappa_a + \kappa_b}{2} - \kappa_c \qquad (1.16)$$

The extent to which the susceptibility ellipsoid approaches a prolate, rather than an oblate, shape can be represented by the factor $\mathbf{P}$ (Khan, 1962) where

$$\mathbf{P} = \frac{\kappa_a - \kappa_b}{\kappa_b - \kappa_c} \qquad (1.17)$$

When $\mathbf{P} > 1$ prolateness predominates. When $\mathbf{P} < 1$ oblateness predominates. The quantity

$$\mathbf{h} = \frac{\kappa_a - \kappa_c}{\kappa_b} \qquad (1.18)$$

may be used to compare the degree of alignment, in a general sense, of one sample with that of another containing the same minerals. For most rocks, $\mathbf{h}$ is substantially independent of the volume fraction of magnetic mineral. Closely related to $\mathbf{P}$ is the factor $\mathbf{q}$, where

$$q = \frac{1}{f}$$

$$= \frac{\kappa_a - \kappa_b}{\frac{1}{2}(\kappa_a + \kappa_b) - \kappa_c} \qquad (1.19)$$

It indicates the relative importance of the fabric elements of lineation and foliation, and hence can be used for comparing the fabrics of different rocks. q is essentially independent of the volume fraction of magnetic mineral, and varies only slowly with bulk susceptibility.

When the intrinsic susceptibility of a magnetic particle is less than unity, the shape effect is not as easily observed and, if the crystal is not cubic, the crystalline anisotropy predominates over any shape effect there may be. Examples of this are pyrrhotite, hematite, and the rhombohedral ilmenite-hematite series. In rocks where some mechanism has preferentially aligned crystal axes, the crystalline anisotropy may be used to advantage in determining the rock fabric (Hrouda, 1971). Because of the very large ratio of maximum to minimum susceptibility, often greater than 100, of hematite in weak fields, magnetization remains essentially in the most susceptible planes regardless of the direction of the applied field. When the field is sufficiently large to saturate the rock in certain directions, the nonlinear effects become clear (Porath, 1966). This extremely strong crystalline anisotropy makes it possible, in principle, to distinguish two or more lineations within a single structure, provided sufficiently high fields are used. This is further discussed in Section 1.6.

1.3 Geological Applications of Magnetic Susceptibility Anisotropy

Measurements of anisotropic susceptibility of rocks have been used successfully to estimate the direction and degree of preferred orientation of elongated magnetic particles which are constituents of the rock material. This orientation, as well as many other rock fabric elements, may be a result of forces acting during rock formation or alteration. A study of fabric elements which result from these forces may be used to provide information about the nature of the forces.

Conventionally, grain orientation studies have been done by specifying orientation of individual particles in oriented thin sections, using a microscope or enlarged photographs. This method is both tedious and potentially misleading. The orientation of detrital quartz grains depends on grain shape rather than crystallography, and shape orientation is usually more difficult to determine. Specification of the longest apparent axis requires considerable care, since quartz grains are considerably irregular in shape. Although most such work is done in two dimensions, a few investigators have used binocular microscopes and multi-axis stages to determine the three-dimensional orientation of long axes (e.g. Rusnak, 1957). Grain counts of between 100 and 200 are commonly used.

Aggregate methods depend on the anisotropy of a bulk parameter which correlates in some way with the grain fabric. These methods are appealing because of their relative ease of determination and the fact that they effectively integrate the directional information from a much larger number of grains than would be examined individually. Magnetic susceptibility is one such bulk parameter whose anisotropy correlates well with grain alignment. The grains whose alignment is correlated with susceptibility are, of course, grains of magnetic accessory minerals, not the major rock minerals. Other parameters which have been investigated include dielectric coefficient, monochromatic light transmissibility (for thin sections), and sonic transmissibility.

1.4 Previous Studies of Susceptibility Anisotropy

Ising (1942) was the first to make extensive use of magnetic susceptibility anisotropy in petrofabric studies. He worked on a series of clay varves in southern Sweden. Ising's measurements were done mostly with a torsional magnetometer. They established that the two principal axes lying in the horizontal bedding plane possessed about 10 to 20% higher susceptibility in the bedding plane than the axis normal to the plane. The high susceptibility in the bedding plane was ascribed to purely mechanical actions on the elongated and plate-shaped grains during and after their deposition. Ising suggested that magnetic lineation direction would be controlled by the earth's magnetic field.

Graham (1954) suggested that susceptibility anisotropy measurements could be used to solve many other problems in petrofabrics and structure. As an example, he noted a correlation between the orientation of the susceptibility ellipsoid orientation with that of a fold axis, throughout the fold, of a ferruginous sandstone. He also found some diabase dykes showing 0.1 to 10% anisotropy.

Granar (1958) followed up Ising's measurements on the Swedish varves. He showed that there was a noticeable magnetic foliation approximately parallel to bedding. Granar's work did not confirm Ising's hypothesis concerning the relation between the geomagnetic field and any magnetic lineation. Rather, he tried to relate magnetic lineation with palaeocurrent directions, but with mixed results.

Six major factors have been identified as affecting magnetic fabrics in sediments (Rees et al., 1968).

1. Gravity tends to align all elongated sediment

grains, including magnetic ones, with the horizontal plane. Its orienting effect is a function of the product of particle weight and linear dimensions, and hence is proportional to the fourth power of particle dimension. A planar structure results which has been called magnetic foliation (Rees, 1966). In the absence of another orienting force, the longest axes are randomly distributed in the horizontal plane, allowing only a statistical lineation. Values of **q**, therefore, are very low.

2. Water currents create hydrodynamic couples on all elongated grains. Their aligning effect is a function of the product of cross-sectional area of the particle, the velocity difference between its extremities, and the linear dimension (Hamilton and Rees, 1971). The force is therefore proportional to the fourth power of particle dimension, as it is for gravity. Water currents produce a magnetic lineation by alignment of long axes of grains with the current direction (Rees, 1961, 1965; Hamilton, 1963, 1967; Galehouse, 1968). Rees (1965) noted a case of lineation normal to the current direction. Either type of lineation will be superimposed on a gravity-produced magnetic foliation. Observed values of **q** range up to 0.5. Very similar susceptibility patterns are noted in glacial tills (Fuller, 1962).

3. The geomagnetic field produces an orienting effect which is a function of the magnetic moment induced in the particle being oriented. Since this moment is proportional to particle volume, the orienting force is proportional to the cube of particle dimension. It is therefore much weaker than the forces due to gravity and current flow, except for very fine sediments. This has been demonstrated experimentally in flume deposits (Rees, 1961; Hamilton, 1967).

4. When sediments are deposited on slopes whose angle is less than the angle of repose of the sediment, the component of gravity tangential to the slope produces a magnetic lineation which is superimposed on the normal gravity-produced magnetic foliation. Rees (1966) demonstrated this effect in the laboratory for still-water deposition. The intensity of the lineation increases with the angle of the slope and approaches the intensities caused by running water. For slopes just greater than the angle of repose, material avalanches downslope. Gravitational foliation ceases to be dominant and the minimum susceptibility is normal to the slope (Rees, 1968; Hamilton et al., 1968).

5. Post-depositional deformation was studied by Graham (1966) in his work on the Paleozoic rocks of the Valley and Ridge province of the Appalachian Mountains.

Three phases of deformation were distinguished. Strain resulting from stresses in the original magnetic foliation plane caused the magnetic lineations of individual specimens to rotate into a close group normal to its line of action. Secondly, shortening of the line of action of the stress caused interchanging of the minimum and intermediate principal susceptibility axes. Finally, the maximum susceptibility axis became oriented normal to bedding and minimum susceptibility paralleled the compression axis. Crimes and Oldershaw (1967) point out that magnetic fabrics are quite sensitive to deformation, and often reveal deformation not otherwise visible.

6. Non-systematic post-depositional deformation is exemplified by the action of plants and burrowing animals on a primary fabric. Their randomizing effect will degrade, if not destroy, the primary fabric. If the primary fabric has been completely randomized, only statistical alignment remains and $q = 0.67$. Rees et al (1968) show an association between scattered principal axes of susceptibility, highly variable q-values, and visible traces of organic activity in certain fine-grained sediments.

There are indications in the paleomagnetic literature that magnetic grains, under the influence of the geomagnetic field, often rotate in sediment after its deposition but while a large water content remains in it (Irving and Major, 1964). This fact could complicate all effects on bulk anisotropy produced during deposition of sediments. However, it does not necessarily follow that the depositional fabric of susceptibility would be seriously degraded. This is because the susceptibility anisotropy is generated mainly by the larger particles, those which are oriented by hydrodynamic and gravitational forces. These particles have high specific susceptibility and low coercive force. On the other hand, it seems reasonable that the post-depositional detrital remanent magnetization reported by Irving and Major (1964) was due to alignment of extremely small particles exhibiting single-domain behaviour, and therefore having low susceptibility and high remanence per unit volume. It was shown by Morrish and Yu (1955) that elongated magnetite particles of axial ratio 10:1 or more could be single-domained for lengths up to several microns. For very small multi-domain grains the Barkhausen discreteness of the positions of the grain boundaries generally prevents them from being positioned in such a way that the grain retains zero magnetic moment. Such grains therefore behave in a manner similar to those having single domains. Stacey (1963) terms these pseudo-single-domain grains. He estimates the critical size for four-domain grains to be about 17 microns. Stacey (1967) has concluded that most rocks contain enough particles smaller than about 20 microns, in the case of magnetite, for these grains to dominate their remanence.

Khan (1962) examined the magnetic susceptibility anisotropy of igneous and metamorphic rocks. A number of Tertiary lava flows were examined and, although most showed widely dispersed principal susceptibility directions, some had the minima grouped tightly around the pole of the flow plane, with the intermediate axes parallel to the flow direction and the maxima normal to it, in the flow plane. Basic gneisses were seen to have their maxima concentrated in the direction of visible lineations and minima normal to the visible foliation.

1.5 Statistical Significance of Measured Susceptibility Anisotropy

It is necessary to determine whether or not the susceptibilities which are measured or are measurable are statistically significant. In any random collection of elongated particles there is a statistically predictable alignment, resulting in a corresponding susceptibility anisotropy. Stacey (1960-a) showed a similar result for random alignment of crystal axes for which no aligning mechanism was thought to exist.

Consider n randomly distributed grains with volume V_0 each. The long axes of the grains may be treated as n randomly directed unit vectors. Rayleigh (1919) derived an expression for the probability that the vector sum would have any particular value. The 50% probability occurs at a vector sum of approximately $n^{1/2}$. Therefore in a collection of rock specimens one would expect to see a randomly directed grain alignment corresponding to an alignment of approximately $n^{1/2}$ aligned grains in each specimen. Thus the total effective aligned volume is $V_0 n^{1/2}$.

In nonsaturating fields, an assemblage of elongated grains with long axes aligned will show a directional apparent susceptibility κ:

$$\kappa = \frac{\epsilon \chi}{1 + \chi N} \tag{1.20}$$

where: ϵ = volume fraction of specimen occupied by the magnetic material

χ = intrinsic susceptibility of magnetic material

N = demagnetizing factor of grains in the direction of susceptibility measurement.

Given that the grains have, on average, minimum demagnetizing factor N_a and maximum demagnetizing factor N_b, the apparent susceptibility anisotropy observed will be

$$\begin{aligned} \Delta\kappa &= \kappa_a - \kappa_b \\ &= \frac{\epsilon\chi}{1 + \chi N_a} - \frac{\epsilon\chi}{1 + \chi N_b} \end{aligned}$$

$$= \frac{\epsilon \chi^2 (N_b - N_a)}{1 + \chi(N_b + N_a) + \chi^2 N_b N_a} \qquad (1.21)$$

For small anisotropies resulting from relatively small elongation of grains, N_b and N_a are both approximately 0.33, the demagnetizing factor of a sphere. The intrinsic susceptibility of magnetite is about 10 mksu. Therefore

$$\Delta\kappa \sim \frac{100\,\epsilon\,(N_b - N_a)}{1 + 6.7 + 10}$$

$$= 5.65\,\epsilon\,(N_b - N_a) \qquad (1.22)$$

Stoner (1945) derived expressions for $(N_b - N_a)$ in terms of elongation ratio $\frac{b}{a}$. For small anisotropy ($\frac{b}{a}$ near unity) terms higher than the first power of $\left[1 - (\frac{b}{a})^2\right]$ may be neglected. The relation then becomes

$$N_b - N_a = 0.2 \left\{ 1 - \left[\frac{b}{a}\right]^2 \right\}$$

$$\cong 0.4 \left\{ 1 - \frac{b}{a} \right\} \qquad (1.23)$$

Substituting this into Eq. 1.22, one obtains

$$\Delta\kappa \cong 2.3\,\epsilon \left\{ 1 - \frac{b}{a} \right\} \qquad (1.24)$$

These relations may now be used to determine the minimum susceptibility anisotropy which may be considered statistically significant. From data gathered by Mooney and Bleifuss (1953) the apparent susceptibility of magnetite-bearing rocks follows approximately the relation

$$\kappa = 3.63\ \epsilon^{1.01} \text{ mksu}$$
$$= 0.289\ \epsilon^{1.01} \text{ emu/cm}^3 \qquad (1.25)$$

where ϵ is the volume fraction of magnetite. Balsley and Buddington (1958) determined a similar relation which differed mainly in the exponent of ϵ, which they determined to be 1.33. If we can assume that the majority volume of magnetite consists of multi-domain grains, and that these are non-interacting, an exponent of unity may be taken for ϵ. Therefore, in a rock specimen of volume V_r containing a volume of magnetite V_m, the apparent susceptibility will be:

$$\bar{\kappa} = 3.63\ \frac{V_m}{V_r} \qquad (1.26)$$

If the magnetite grains have an average diameter d, and hence average volume $V_0 = \frac{\pi}{6} d^3$, the number of grains is

$$n = \frac{V_m}{V_0}$$
$$= \frac{6V_m}{\pi d^3} \qquad (1.27)$$

Furthermore, since statistically we can expect an effective aligned volume $V_0 n^{1/2}$ if no grain-alignment mechanism exists, the effective aligned volume V_A is

$$V_A = V_0 n^{1/2}$$

$$= \frac{\pi}{6} d^3 \left\{ \frac{6\,V_m}{\pi d^3} \right\}^{1/2}$$

$$= \left\{ \frac{\pi V_m d^3}{6} \right\}^{1/2} \qquad (1.28)$$

Thus, from Eq. 1.22, susceptibility anisotropy will have a statistical minimum:

$$\Delta\kappa \cong 2.3\,\epsilon \left\{ 1 - \frac{b}{a} \right\}$$

$$= 2.3\,\frac{V_A}{V_r} \left\{ 1 - \frac{b}{a} \right\}$$

$$= \frac{2.3}{V_r} \left\{ \frac{\pi\,V_m d^3}{6} \right\}^{1/2} \left\{ 1 - \frac{b}{a} \right\}$$

Substituting Eq. 1.26, this becomes:

$$\Delta\kappa = \frac{\bar{\kappa}^{-1/2} V_r^{1/2}}{1.90\,V_m^{1/2}} \left\{ \frac{2.3}{V_r} \right\} \left\{ \frac{\pi V_m d^3}{6} \right\}^{1/2} \left\{ 1 - \frac{b}{a} \right\}$$

$$= 0.874\,\bar{\kappa}^{-1/2}\,\frac{d^{3/2}}{V_r^{1/2}} \left\{ 1 - \frac{b}{a} \right\} \quad \text{mksu} \qquad (1.30)$$

And for a standard specimen with diameter 2.5 cm and length 2.5 cm $V_r = 1.23 \times 10^{-5}\ m^3$. Therefore

$$\Delta\kappa = 249\,\bar{\kappa}^{-1/2}\,d^{3/2} \left\{ 1 - \frac{b}{a} \right\} \quad \text{mksu} \qquad (1.31)$$

If we take minimum average grain elongation as being 5%, minimum average grain diameter as 10^{-5} m, and minimum bulk susceptibility (due to the ferromagnetic fraction as distinct from the diamagnetic rock materials) as 10^{-7} mksu, the minimum statistically significant anisotropy is

$$\Delta\kappa = 1.25 \times 10^{-10} \quad \text{mksu} \tag{1.32}$$

It is possible, in principle, for the ferromagnetic component of the bulk susceptibility of a rock to be even less than 10^{-7} mksu. In that case, even though the specimen might contain a geologically significant grain alignment, which it might if the grains were small enough, it would be very difficult to identify it as being significant since the bulk ferromagnetic susceptibility would be swamped by the much larger diamagnetic susceptibility of most of the other rock materials.

The graph in Figure 1.1 shows the minimum statistically significant anisotropy as a function of the bulk anisotropy and mean grain diameter.

1.6 Ambiguities in Magnetic Data

For a specimen showing only a foliation, or plane of preferred orientation, the equivalent magnetic ellipsoid is oblate, with its short axis perpendicular to the plane of foliation. If the specimen shows only a lineation, the equivalent magnetic ellipsoid is prolate, with its long axis parallel to the lineation. In general, however, the

Figure 1.1 The lower limit to geologically-significant anisotropy set by statistical anisotropy for rocks containing pure magnetite of the grain sizes indicated. Grain elongation is 5%.

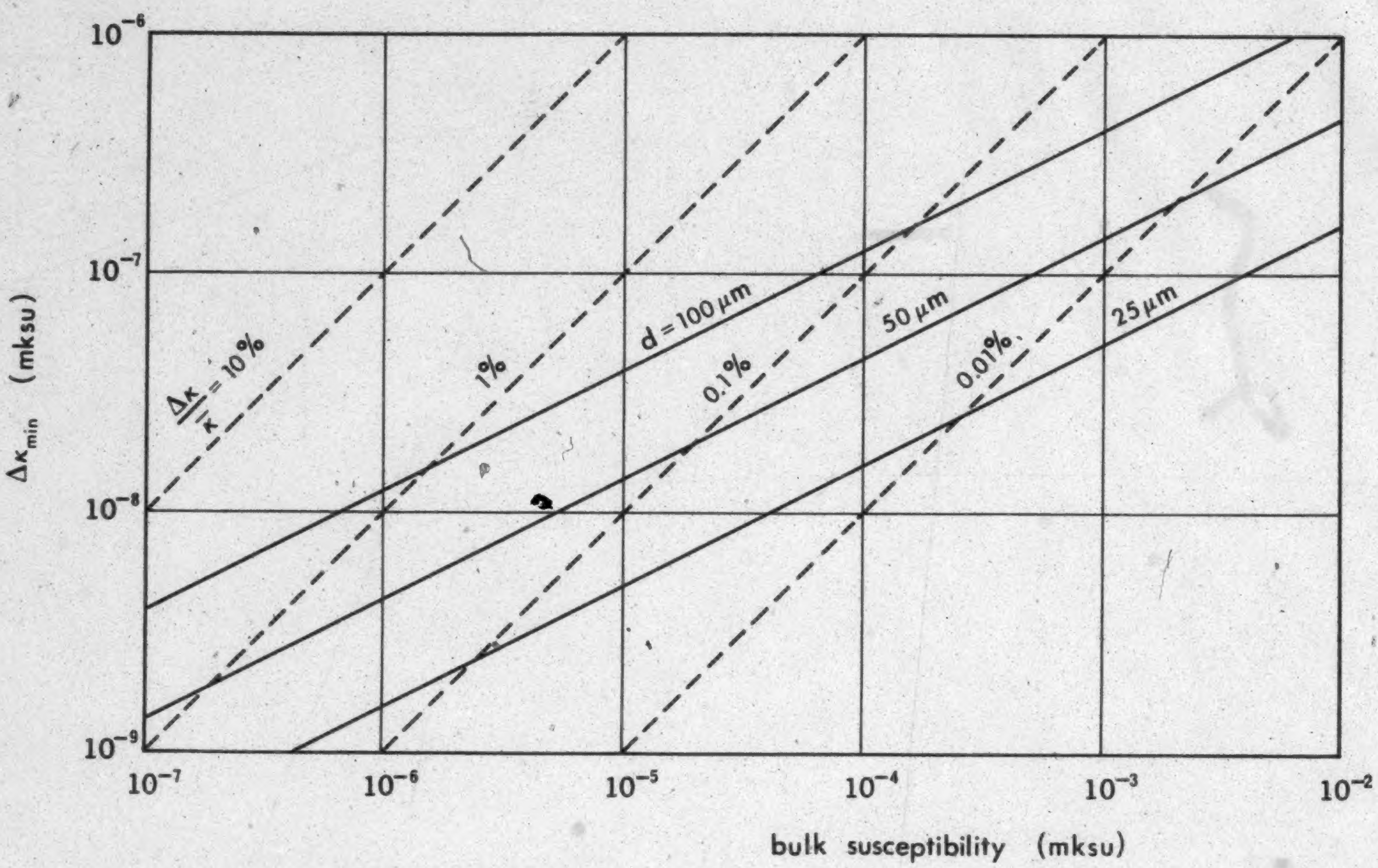
10^-6
10^-7
10^-8
10^-9
Δκmin (mksu)
10^-7
10^-6
10^-5
10^-4
10^-3
10^-2
bulk susceptibility (mksu)
Δκ/κ = 10%
1%
0.1%
0.01%
d = 100 µm
50 µm
25 µm

observed magnetic ellipsoids have three unequal axes. Stacey et al. (1960) point out that there are several combinations of two foliations, two lineations, or one foliation plus one lineation which can be found to fit the same magnetic ellipsoid. Whatever the combination present in a specimen, the magnetic ellipsoid merely averages the effects. In particular, they note, two foliations in different planes are equivalent to a single foliation between the two plus a lineation along their line of intersection. Also, a foliation plus a lineation in another plane appears magnetically as a foliation plus a lineation in a plane between the two.

If two magnetic features are to be distinguished and both delineated, it is necessary to extract more information than is available from the second-rank tensor normally obtained. This can be done, in special circumstances at least, by using the nonlinear magnetization characteristics of the magnetic materials involved. From Eq. 1.9 it can be seen that if χ is either very large ($\chi \gg 3$) or if it is constant, the apparent susceptibility variation is sinusoidal. However, when a material such as magnetite saturates for part of the cycle, neither of these conditions holds. Any particular grain, or aligned array of grains, will have lower intrinsic susceptibility, and therefore lower apparent susceptibility, when the semimajor axis or axes align with the applied field. The sinusoidal variation obtained in lower fields will be distorted in a manner like to that illustrated in Figure 1.2. If the signal is passed through a filter which removes only the fundamental frequency, the components remaining can hold sufficient information to define at least two separate fabric features. The applied field would, for optimum response, have to be adjusted for optimum nonlinearity with the magnetic materials and average grain elongation present in the specimen. If the specimen susceptibility is low or the aspect ratio of the average grains is small, it would be necessary, with a spinner-type instrument, to electronically cross-correlate the higher harmonic content of the signal with that from a shaft-synchronous gating device. A torque-meter with its discrete readings probably would not suffice.

The effects of harmonics due to crystalline susceptibility anisotropy should be separated from grain alignment if meaningful results are to be obtained. Effects from different minerals (e.g. hematite) can be distinguished by their different coercive force and saturation flux density, and hence the different behaviour when the bulk applied field is changed. Statistical crystalline alignment of the magnetite particles being observed cannot be as readily distinguished. However, if the magnetite grains are sufficiently small and the bulk susceptibility is sufficiently

Figure 1.2 Qualitative effects of saturation of elongated grains. In the upper diagram the solid line indicates signal flux using low, nonsaturating field intensity. The dashed line indicates signal flux for a field intensity which produces an appreciable variation in intrinsic susceptibility as the specimen rotates. The lower diagram shows the difference between the two signal fluxes shown in the upper diagram.

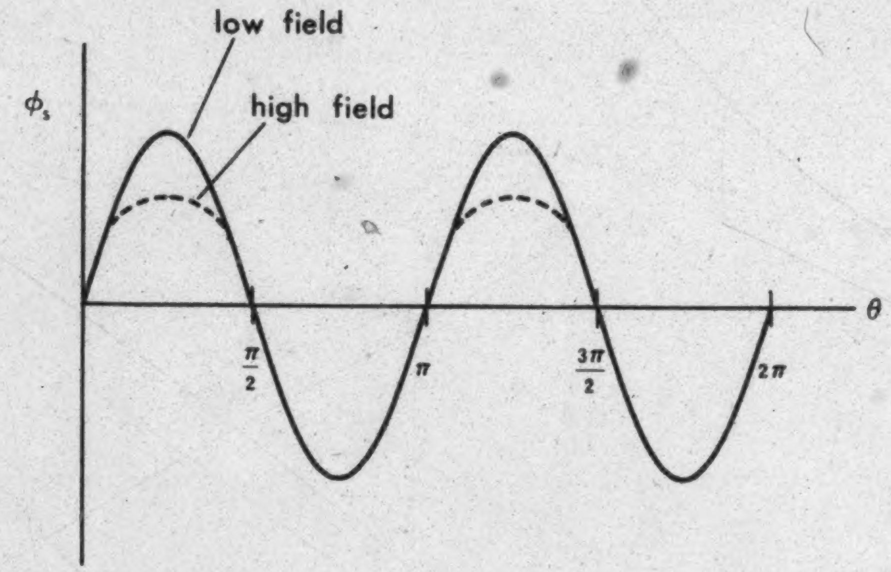
low field
high field
ϕ_s
θ
$\frac{\pi}{2}$
π
$\frac{3\pi}{2}$
2π

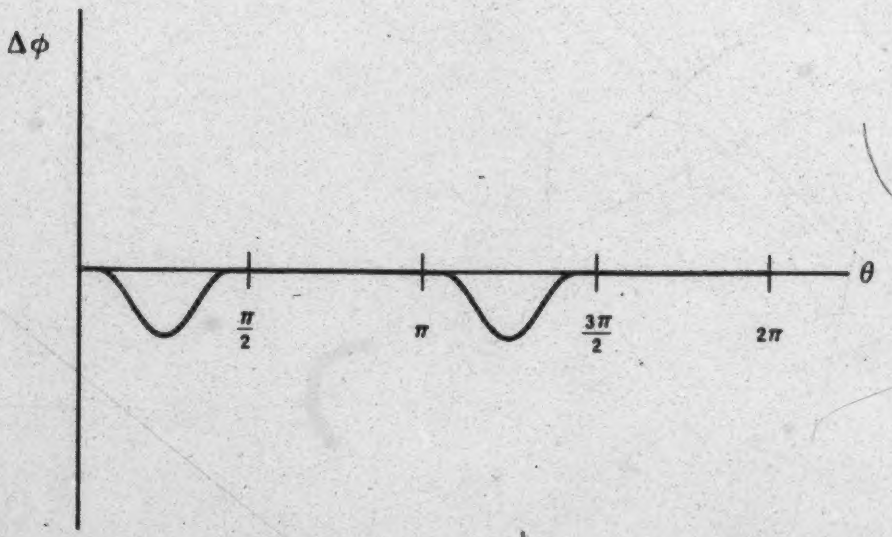
$\Delta\phi$
θ
$\frac{\pi}{2}$
π
$\frac{3\pi}{2}$
2π

high (that is, magnetite grains are sufficiently numerous) the effects of statistical crystalline alignment (Stacey, 1960-a) may be negligible compared to the effects observed.

CHAPTER 2

PREVIOUS INSTRUMENTS USED FOR MAGNETIC SUSCEPTIBILITY ANISOTROPY STUDIES

2.1 The Torque Method

Ising (1942) describes a torsional magnetometer which measures magnetic anisotropy in terms of the couple acting on a sample suspended in a magnetic field. More recently Granar (1958) used an instrument of this type in rock fabric studies. King and Rees (1962) describe two variations of Granar's magnetometer, one of which has a theoretically-predicted sensitivity of 10^{-9} mksu at fields of about 1600 amp/meter.

In torsional magnetometers of the suspended specimen type, the specimen is suspended from a fine fiber in a region where a uniform horizontal magnetic field is established. This is usually done with a Helmholtz coil pair, but for large applied fields it can be done with iron-cored coils. When a current is passed through the coils, a torque is produced on the specimen which tends to rotate it so as to align the direction of maximum susceptibility with the direction of the applied field. The magnetostatic energy within the specimen and its surroundings is minimized when such alignment exists. Furthermore, if there is any remanent magnetization within the specimen, a further torque will tend to align it with the applied field.

It is necessary for the measuring instrument to distinguish between torque produced by susceptibility anisotropy and that due to remanence. If possible, the latter should be eliminated. This may be done by making the applied field alternate at a frequency well above the torsional resonant frequency of the specimen with suspension system. The torque due to remanence will then alternate in direction and because of the high frequency of the direction reversals the specimen will not deflect appreciably in response. The susceptibility anisotropy torque will remain in the same direction, however. This is because the induced moment changes in direction as the applied field changes, and the resultant couple will remain in the same direction. Its magnitude varies with the absolute magnitude of the applied field. The direct component of the couple is then measured by observing the resultant steady angular deflection of the specimen.

Consider a specimen of volume V meter^3 having two principal apparent susceptibilities κ_a and κ_b mksu at right angles to each other in the plane of measurement. The specimen is suspended in a field H_0 amp/meter at an angle θ radians to κ_a, as shown in Figures 2.1 and 2.2. The induced magnetic moment in the direction of κ_a will be

Figure 2.1 General layout of torsional magnetometer.

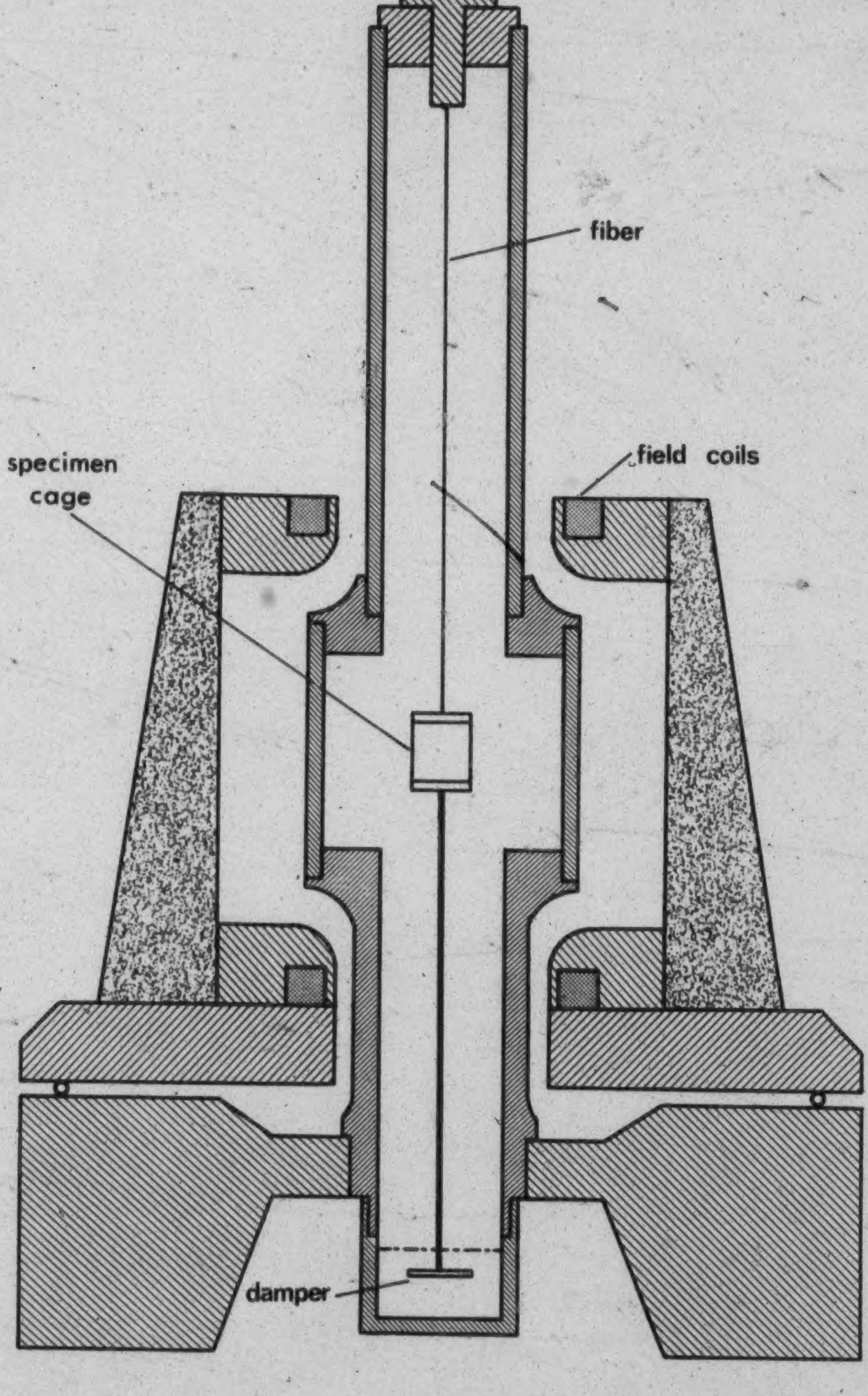
fiber
specimen
cage
field coils
damper

Figure 2.2 Principal susceptibilities of the specimen in the plane of observation, shown with the applied field and resultant torque components as viewed along the suspension fiber.

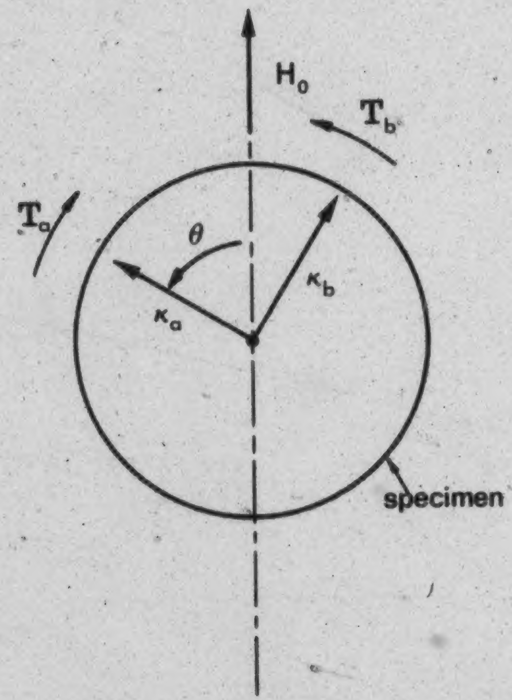
H_0
T_b
T_a
θ
κ_a
κ_b
specimen

$$m_a = \kappa_a H_0 V \cos\theta \qquad (2.1)$$

Similarly, for the direction of κ_b

$$m_b = \kappa_b H_0 V \sin\theta \qquad (2.2)$$

The torques $\mathbf{T}_a$ and $\mathbf{T}_b$ due to moments m_a and m_b, respectively, are given by

$$\begin{aligned}
\mathbf{T}_a &= m_a B_0 \sin\theta \\
&\cong m_a \mu_0 H_0 \sin\theta \\
&= \kappa_a \mu_0 H_0^2 V \sin\theta\cos\theta && \text{(from Eq. 2.1)} \\
&= \tfrac{1}{2}\kappa_a \mu_0 H_0^2 V \sin 2\theta && (2.3) \\
\mathbf{T}_b &= -m_b B_0 \cos\theta \\
&\cong -m_b \mu_0 H_0 \cos\theta \\
&= -\kappa_b \mu_0 H_0^2 V \cos\theta \sin\theta && \text{(from Eq. 2.2)} \\
&= -\tfrac{1}{2}\kappa_b \mu_0 H_0^2 V \sin 2\theta && (2.4)
\end{aligned}$$

The net torque on the specimen is the sum of $\mathbf{T}_a$ and $\mathbf{T}_b$.

$$\mathbf{T} = \tfrac{1}{2}(\kappa_a - \kappa_b)\,\mu_0 H_0^2 V \sin 2\theta \qquad (2.5)$$

This has a root-mean-square value

$$\mathbf{T}_{rms} = \tfrac{1}{4}\sqrt{2}\,(\kappa_a - \kappa_b)\,\mu_0 H_0^2 V \qquad (2.6)$$

The deflection $\Delta\theta_{rms}$ resulting from this torque is

$$\begin{aligned}
\Delta\theta_{rms} &= \frac{1}{\tau}\mathbf{T}_{rms} \\
&= \frac{\sqrt{2}\,(\kappa_a - \kappa_b)\,\mu_0 H_0^2 V}{4\tau} && (2.7)
\end{aligned}$$

where τ is the torsional rigidity of the suspension fiber.

There are two principal theoretical limitations to the sensitivity of the instrument. One is the thermal deflection, or Brownian motion, of the suspended system. The other is the minimum detectable angular deflection of the suspended system. The latter depends on the mechanism used to measure the deflection.

The rms value of the thermal deflection $\Delta\theta_{B\,rms}$ is given by the relation

$$\Delta\theta_{B\,rms} = \left(\frac{kT}{\tau}\right)^{1/2} \text{ radians} \tag{2.8}$$

where: k = Boltzmann's constant

= 1.38 x 10^{-23} joules/°K

T = absolute temperature (°K).

From Eqs. 2.7 and 2.8, the signal-to-noise ratio is

$$\frac{\Delta\theta_{rms}}{\Delta\theta_{B\,rms}} = \left(\frac{2}{kT}\right)^{1/2} \frac{(\kappa_a - \kappa_b)\,\mu_0 H_0^2 V}{4\,\tau^{1/2}} \tag{2.9}$$

There is a lower limit to the torsional rigidity τ of the fiber set by observation time required, even if the fiber's physical dimensions are not a limiting factor. With nearly-critical damping the approximate settling time of the suspended system is

$$t_0 = 2\pi\left(\frac{I}{\tau}\right)^{1/2} \tag{2.10}$$

where I is the moment of inertia of the specimen plus cage.

If we take the ideal limit of negligible moment of inertia for the specimen cage and suspension, then we have for an axially-suspended cylindrical specimen of equal length and diameter that

$$t_0 = 2\pi \left\{ \frac{\frac{1}{2} M r_s^2}{\tau} \right\}^{1/2}$$

$$= 2\pi \left\{ \frac{\frac{1}{2} V \sigma r_s^2}{\tau} \right\}^{1/2} \qquad (2.11)$$

where: M = mass of specimen (kg)

r_s = radius of specimen (m)

σ = density of specimen (kg/m^3)

Therefore we obtain by rearranging Eq 2.11

$$\frac{V}{\tau} = \frac{t_0^2}{2\pi^2 \sigma r_s^2} \qquad (2.12)$$

Substituting this into Eq 2.9,

$$\frac{\Delta\theta_{rms}}{\Delta\theta_{B\,rms}} = \left(\frac{2}{kT}\right)^{1/2} \frac{(\kappa_a - \kappa_b)\,\mu_0 H_0^2}{4} \left\{\frac{1}{2\pi^2\sigma}\right\}^{1/2} \frac{t_0}{r_s} V^{1/2} \qquad (2.13)$$

Since an alternating field is required, Helmholtz coil pairs are normally used to provide the necessary field uniformity. As dimensional and power-dissipation difficulties increase rapidly in so generating fields larger than about 10^4 amp/meter, it is appropriate to calculate a sensitivity based on $H_0 = 10^4$. We set reasonable values on T of 293°K and on σ of 3.0 gm/cm^3. Thus we obtain for a standard specimen of radius 1.27 cm and volume 12.9 cm^3

$$\frac{\Delta\theta_{\mathrm{rms}}}{\Delta\theta_{B\,\mathrm{rms}}} = \left\{\frac{2}{(1.38 \times 10^{-23})(293)}\right\}^{1/2} \frac{(\kappa_a-\kappa_b)(4\pi \times 10^{-7})(10^{8})}{4} \cdot$$

$$\cdot \left(\frac{12.9 \times 10^{-6}}{6.0 \times 10^{3}\pi^{2}}\right)^{1/2} \frac{t_0}{1.27 \times 10^{-2}}$$

$$= 0.81 \times 10^{9} \; (\kappa_o-\kappa_b)t_0 \qquad (2.14)$$

Thus one is just able to detect an anisotropy

$$\Delta\kappa_{\min} = \frac{1.23 \times 10^{-9}}{t_0} \;\text{mksu} \qquad (2.15)$$

The lower limit to detectable anisotropy due to minimum detectable angular deviation can be similarly calculated. The sensitive detectors with the smallest inherent moment of inertia employ a mirror connected to the specimen cage deflecting a light beam. Using long optical "levers" and magnifiers, the small angular deviations become readily observable linear deviations of a light spot. The limitation arises from the scattering of the light beam by diffraction from the mirror's periphery. Even if an ideal point source of light is used, and there are no appreciable diffraction effects from elsewhere in the optical train, the focused image after reflection from an optically perfect mirror is an Airy pattern of which the first dark circle subtends at the mirror an angle β given by

$$\beta = \frac{2.44\,\lambda}{a} \;\text{radians} \qquad (2.16)$$

where: λ = wavelength of light used (m)

a = diameter of mirror (m).

To avoid substantial increase in the moment of inertia, the mirror cannot be much larger in diameter than 2 cm. With this and light of wavelength 5000 Å

$$\beta = \frac{(2.44)(5 \times 10^{-7})}{2 \times 10^{-2}}$$

$$= 6.1 \times 10^{-5} \text{ radians} \tag{2.17}$$

When the mirror deviates 3×10^{-6} radians, the Airy disc deviates 6×10^{-6} radians, which is about 10% of the inner circle's diameter. It is unlikely that much smaller deviation could be reliably detected. Thus, the rms value of diffraction "noise" is

$$\Delta\theta_{D\,rms} = 3 \times 10^{-6} \text{ radians} \tag{2.18}$$

From Eqs. 2.7 and 2.18, signal-to-noise ratio is

$$\frac{\Delta\theta_{rms}}{\Delta\theta_{D\,rms}} = \frac{\sqrt{2}\,(\kappa_a-\kappa_b)\,\mu_0 H_0^{\,2} V}{12\,\tau} \times 10^6 \tag{2.19}$$

Substituting Eq. 2.12, the above result becomes

$$\frac{\Delta\theta_{rms}}{\Delta\theta_{D\,rms}} = \frac{\sqrt{2}\,(\kappa_a-\kappa_b)\,\mu_0 H_0^{\,2} t_0^{\,2}}{24\pi^2 \sigma r_s^{\,2}} \times 10^6 \tag{2.20}$$

Using the same magnetic field (10^4 amp/meter) and specimen dimensions as used in deriving Eq. 2.14, this becomes

$$\frac{\Delta\theta_{rms}}{\Delta\theta_{D\,rms}} = \frac{\sqrt{2}\,(\kappa_a-\kappa_b)(4\pi \times 10^{-7})(10^8)(t_0^{\,2})(10^6)}{24\pi^2(3 \times 10^3)(1.61 \times 10^{-4})}$$

$$= 3.09 \times 10^6 \ (\kappa_a - \kappa_b)\ t_0^{\ 2} \qquad (2.21)$$

Thus we can just detect an anisotropy $(\kappa_a - \kappa_b)_{min}$ of

$$\Delta\kappa_{min} = \frac{3.24 \times 10^{-7}}{t_0^{\ 2}} \ \text{mksu} \qquad (2.22)$$

The two theoretical limits on sensitivity are shown graphically in Figure 2.3, plotted against minimum observation time t_0.

Using Granar's method, five torque readings are required for each of three orthogonal specimen axes. Thus the total settling time required per specimen is at least $15\,t_0$. Allowing for the intermediate operations, a settling time of 60 seconds would mean a total observation time per specimen of about 20 minutes. Thus a sensitive torsional anisotropy meter is of necessity a long-period device. A direct-field spinner, on the other hand, does not have its sensitivity as strongly dependent on time constant. High sensitivities are theoretically possible with short total observation times. This is fully discussed in the next chapter.

Figure 2.3 Theoretical minimum on magnetic susceptibility anisotropy detectable by a torsional magnetometer having a suspension time constant t_0.

Conditions:

H_0 = rms field intensity = 10^4 amp/meter

r_s = radius of specimen = 1.27 cm

h = axial length of specimen = 2.54 cm

σ = density of specimen = 3.0 gm/cm^3

a = mirror diameter = 2.0 cm

λ = wavelength of light used = 5000 Å.

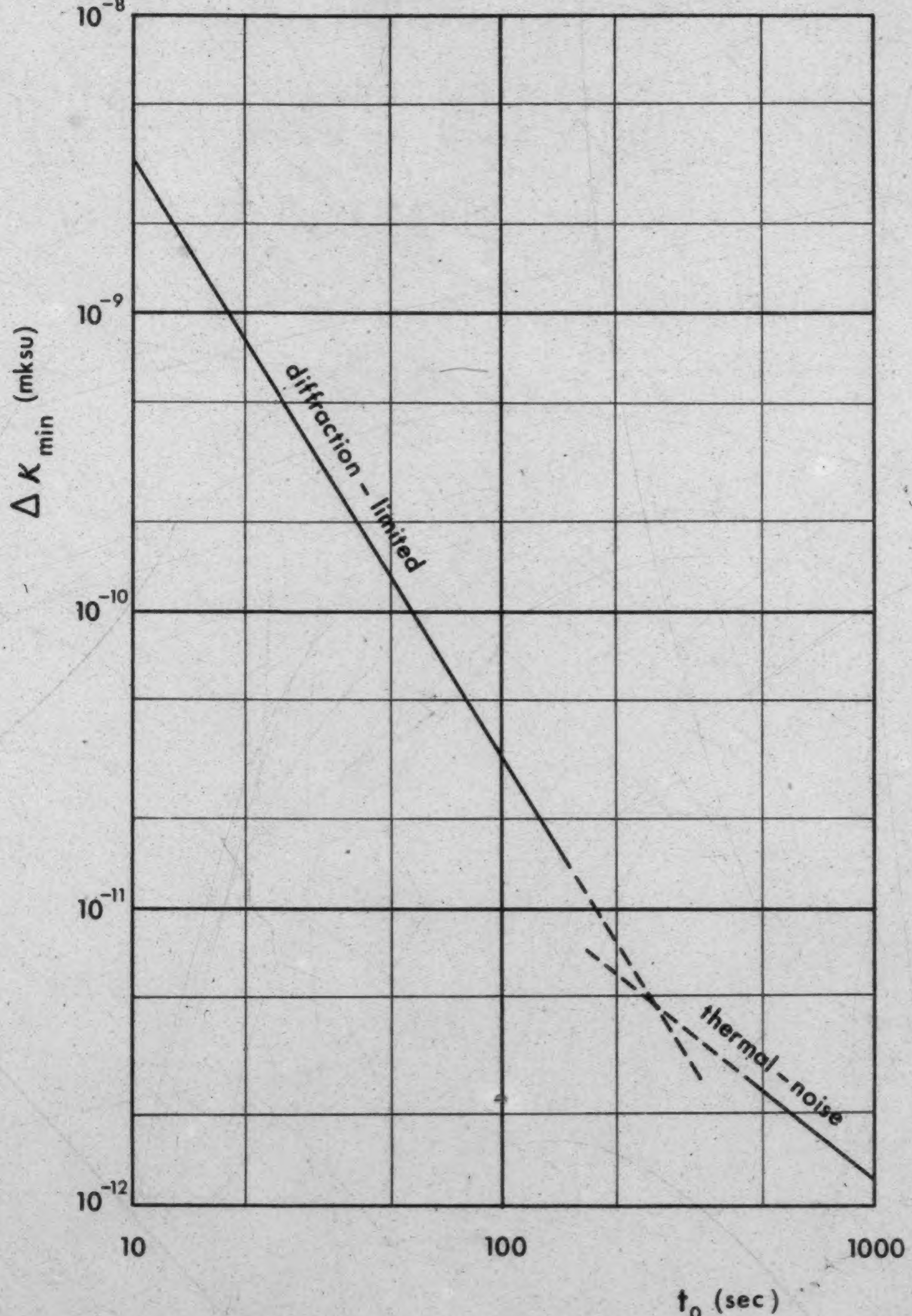
10^{-8}
10^{-9}
10^{-10}
10^{-11}
10^{-12}
ΔK_{min} (mksu)
diffraction - limited
thermal - noise
10
100
1000
t_0 (sec)

2.2 Spinner Magnetometers for Susceptibility Anisotropy

In theory, any instrument capable of measuring bulk magnetic susceptibility may be made to measure the anisotropy of magnetic susceptibility by causing the specimen to rotate at a suitable speed and measuring the time-varying apparent susceptibility. One susceptibility meter which has been successfully converted to a spinner-type instrument is the A.C. bridge.

Three types of A.C. bridge networks have been used to make susceptibility measurements. The single-inductor bridge (Bhattacharya, 1950) shown in Figure 2.4 (A) is balanced resistively with three resistors and reactively with a single capacitor diametrically opposite the inductor. Its main drawback is its asymmetry. This causes the individual legs of the bridge to react differently to temperature changes and causes thermal offset. In this aspect, the bridge may be improved by using two identical air-core coils balanced by two resistors, as in Figure 2.4 (B) (Michelson, 1952). Both of these bridges are susceptible to drift caused by movement of conductive objects in the vicinity of the bridge elements. Such movements are virtually unavoidable, and by providing different stray capacitance to earth for each of the bridge elements, they cause the bridge to be offset from balance. The problem can be lessened by extensive electrostatic shielding, although this solution can actually aggravate the thermal drift problem (Fuller, 1967).

Figure 2.4 Bridge configurations used in susceptibility anisotropy studies

(A) Bhattacharya

(B) Michelson

(C) Girdler

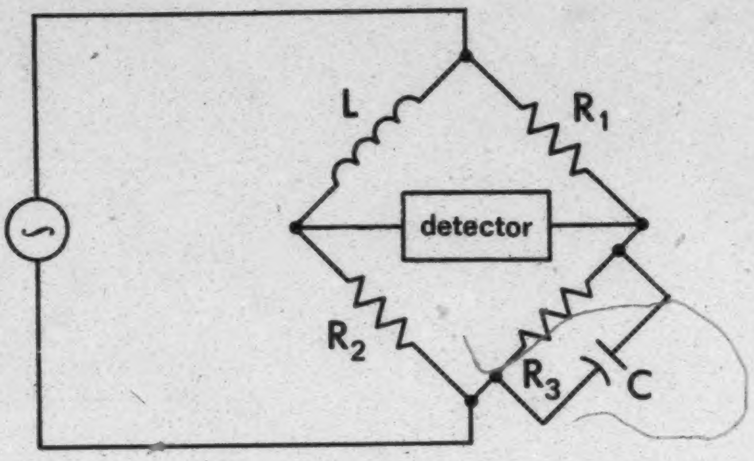
L
R$_1$
detector
R$_2$
R$_3$
C

A

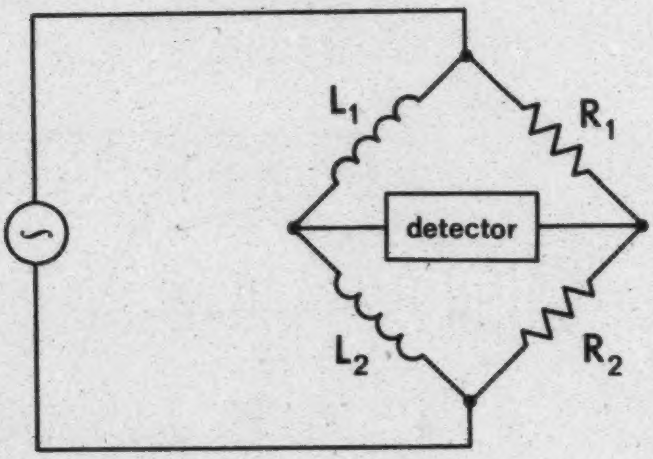
L$_1$
R$_1$
detector
L$_2$
R$_2$

B

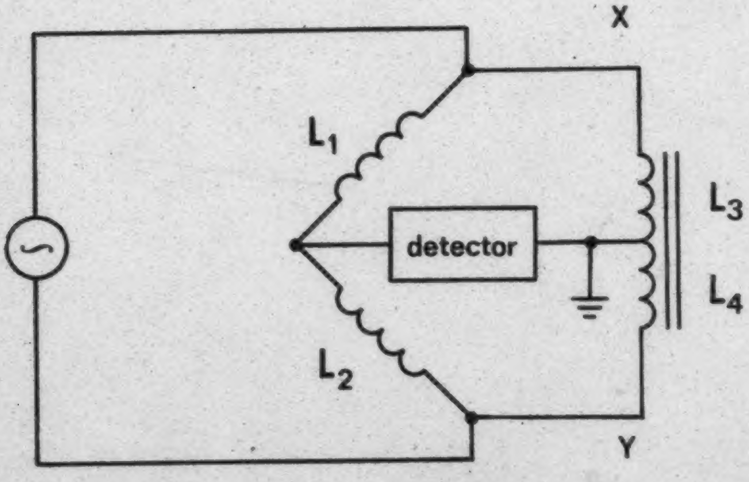
X
L$_1$
L$_3$
detector
L$_4$
L$_2$
Y

C

Drift due to stray capacitance may be very neatly dealt with by using the transformer bridge network of Figure 2.4 (C). It was described by Kirke (1945) and discussed by Clark and Vanderlyn (1949) and Watton and Pemberton (1949). In this version (Girdler, 1961) two air core inductors are balanced with tightly coupled ratio arms, which are the two windings of a 1:1 transformer. The two windings are assumed to be perfectly coupled. In that case, mutual inductance M is given by

$$M = \sqrt{L_3 L_4} \tag{2.23}$$

Therefore the ratio of impedance of the two bridge legs made up by the transformer is

$$\frac{Z_3}{Z_4} = \frac{L_3 + M}{L_4 + M}$$

$$= \frac{L_3 + \sqrt{L_3 L_4}}{L_4 + \sqrt{L_3 L_4}}$$

$$= \sqrt{\frac{L_3}{L_4}}$$

$$= \frac{n_3}{n_4} \tag{2.24}$$

where n_3 and n_4 are the number of turns on the two windings of the transformer. If the numbers are equal, we have

$$\frac{Z_3}{Z_4} = 1$$

and

$$L_3 = L_4 = M$$

Now assuming perfect coupling between the equal transformer windings and zero winding resistance and transformer core losses, we can find expressions for the potentials with respect to ground of points X and Y, given a current $i_0 \cos \omega t$ through the windings.

$$\begin{aligned} V_x &= j\omega L_3 i_0 - j\omega M i_0 \\ &= 0 \end{aligned} \tag{2.27}$$

$$\begin{aligned} V_Y &= j\omega L_4 i_0 - j\omega M i_0 \\ &= 0 \end{aligned} \tag{2.28}$$

Therefore points X and Y are effectively held at ground potential by grounding the center-tap of the transformer. This greatly reduces the effects of stray capacitance to ground.

The A.C. bridge used by Fuller (1967) employs split air-core coils of 13 cm diameter and 4 cm total axial length. They provide a field uniformity of about 1% over the volume of a standard 2.5 cm cylindrical specimen. The bridge is excited at 1000 Hz with a total power of about 1 watt. The limits of operation were shown to be thermal drift. After smoothing the output of a continuously recorded trace of apparent susceptibility, a susceptibility anisotropy noise of about 2×10^{-6} mksu (1.6×10^{-7} gauss/oe) remains.

Thermal drift, like most random and quasi-random noise effects, has a fairly wideband spectrum. Thus, it is possible to minimize the effects of thermal drift by looking at as small a spectral "window" as possible. This may be done by rotating the specimen at a fixed frequency, and analyzing the signal within a fairly narrow passband about that frequency. This procedure is most effectively accomplished by phase-sensitive detection of the signal, using a shaft-actuated generator to supply a reference signal. Furthermore, most thermal "drift" and other excess noise forms which depend on external energy sources and sinks, tend to have a characteristic $\frac{1}{f}$ spectral density, unlike equipartition noise at thermal equilibrium. Therefore it is advantageous to employ a high rotational speed for the specimen, at least to the point where other noise effects become dominant. This general approach was followed by Graham (1967) in developing his A.C. bridge for susceptibility anisotropy.

A simplified block diagram of the essential parts of Graham's A.C. bridge spinner are shown in Figure 2.5. The bridge itself uses two nearly identical modified Helmholtz coils connected in a bridge arrangement with a tape-wound-core transformer with two equal bifilar windings. The susceptibility variation of the spinning specimen changes the inductance of one coil and upsets the balance of the bridge. The off-balance signal is processed and recorded.

Figure 2.5 Block diagram of Graham's A.C. bridge spinner for susceptibility anisotropy.

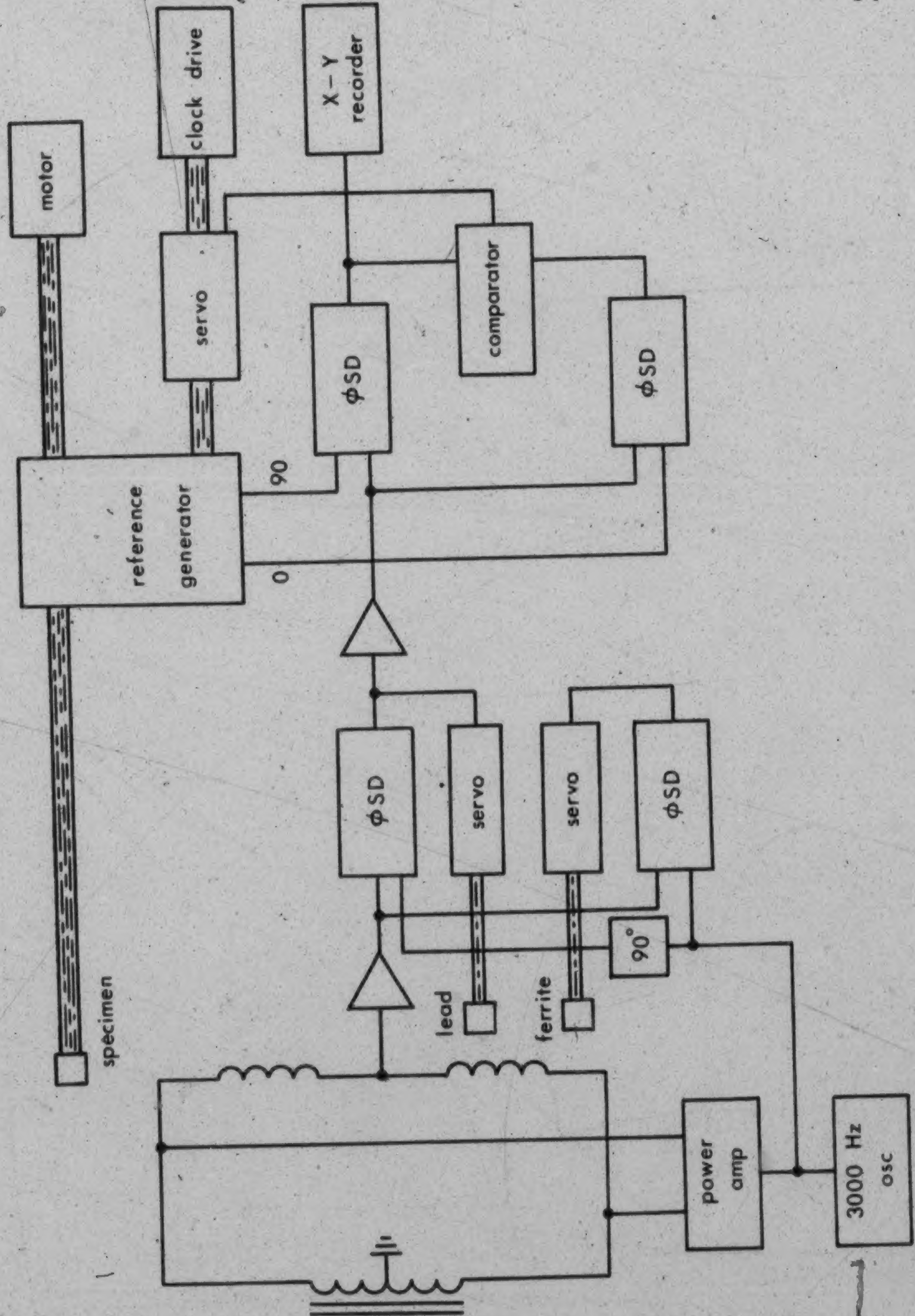
motor
clock drive
X – Y recorder
servo
comparator
φSD
φSD
reference generator
90
0
φSD
servo
servo
φSD
90°
lead
ferrite
specimen
power amp
3000 Hz osc

The processing consists of two stages of phase-sensitive detection - one at the bridge energizing frequency and one at twice the specimen rotational frequency. The demodulated signal is fed to a modified X-Y recorder with a suitably slow clock drive. This constitutes in effect a long time-constant integrator which determines the bandwidth of the observed signal. Graham also employed servo-mechanisms carrying pieces of lead and ferrite near one of the Helmholtz coils to keep the bridge in long-term equilibrium. He provided for a servo-mechanism which automatically "locked-on" to either maximum or minimum susceptibility in a given rotational plane. This latter feature is useable only if signal-to-noise ratio is considerably larger than unity.

The thermal-noise-limited sensitivity of a bridge susceptibility meter such as Graham's is now derived. The spinner is limited fundamentally by thermal (Johnson) noise generated within its bridge inductor windings. This limit is now determined for instruments of reasonable dimensions and operating conditions.

Graham's inductors were Helmholtz pairs of coils of inside diameter 7.0 cm, outside diameter 12.0 cm, and length 2.5 cm. They produce a magnetic field which is uniform to about 1% over a volume of 10 cm^3 and whose intensity is 6620 amp/meter for a 1 ampere energizing current. Their inductance is 53 mh and their resistance is 5 ohms.

Since Johnson noise is proportional to coil resistance$^{1/2}$, it is desirable to minimize resistance for a given number of turns. However, any change in dimensions to decrease resistance (i.e. either increasing current cross-sectional area or decreasing coil diameter) will increase relative field nonuniformity. In fact Graham's Helmholtz coils had close to optimum dimensions for maximum sensitivity on rocks having percentage anisotropies of greater than about 1%.

We calculate the signal induced by an anisotropic susceptibility κ. Given an energizing current i amperes, the magnetic field intensity in the region of the rotating specimen is

$$H_0 = 6.62 \times 10^3\, i \quad \text{amp/meter} \tag{2.29}$$

Given a specimen of volume V and susceptibility κ immersed in a uniform field of this magnitude, the presence of the specimen accounts for a relative increase in magnetic energy equal to

$$\frac{\Delta E_m}{E_m} = \frac{\text{change in energy due to specimen}}{\text{total energy in coil's field}}$$

$$\cong \frac{\frac{1}{2}(\mu H_0^2 V - \mu_0 H_0^2 V)}{\frac{1}{2} L i^2} \tag{2.30}$$

where: μ = apparent permeability of rock specimen

H_0 = magnetic field intensity with no specimen

L = coil inductance.

Therefore

$$\frac{\Delta E_m}{E_m} = \frac{\mu_0(\mu_r - 1)H_0^{\,2}V}{Li^2}$$

$$= \frac{\mu_0 \kappa H_0^{\,2} V}{Li^2}$$

Substituting $4\pi \times 10^{-7}$ henry/m for μ_0, 5.3×10^{-2} henry for L, and Eq. 2.29 for H_0, Eq 2.31 becomes

$$\frac{\Delta E_m}{E_m} = \frac{(4\pi \times 10^{-7})\,\kappa\,(4.37 \times 10^{7}\ i^2)V}{0.053\,i^2}$$

$$= 1.03 \times 10^3\ \kappa V \qquad (2.32)$$

It follows that the inductance of the coil changes by this same ratio. That is,

$$\Delta L = 1.03 \times 10^3\ \kappa V L$$

$$= 55\,\kappa V \qquad (2.33)$$

If, now, we have an rms current $i_0 \cos \omega t$ energizing the coil, the rms signal output will be

$$e_s = i_0\,\omega\,\Delta L$$

$$= 55\,\kappa V i_0 \omega \qquad (2.34)$$

Since the coils are tuned to resonance, they appear to the amplifier to be essentially resistive. Thus, noise voltage from the coil is given by

$$e_n = (4kTR\Delta f)^{1/2} \qquad (2.35)$$

where: k = Boltzmann's constant

T = absolute temperature

R = coil resistance

Δf = frequency bandwidth observed.

Since R is 5 ohms, and temperature is about 293°K, we obtain

$$e_n = 4.1 \times 10^{-10}\ \Delta f^{1/2} \tag{2.36}$$

Both signal and noise are equally increased by virtue of the Q-factor of the resonant circuit. Thus, Q need not be calculated for determining signal-to-noise ratio.

$$\frac{e_s}{e_n} = \frac{55\, i_0 \omega \kappa V}{4.1 \times 10^{-10} \Delta f^{1/2}}$$

$$= 1.34 \times 10^{11}\ \frac{i_0 \omega \kappa V}{\Delta f^{1/2}} \tag{2.37}$$

Current i_0 is limited by thermal drift caused by high power dissipation in the main coils, as well as by vibration of coils carrying large alternating currents. Frequency f is limited by self-resonance of the Helmholtz coils and, in some rocks, by eddy current losses in the specimen. Any anisotropy in the eddy-current response produces a spurious susceptibility anisotropy signal. Bandwidth Δf is limited by observation time permissible. Consider Graham's values for i_0 and ω:

i_0 = 25 mA rms (H_0 = 165 amp/meter ~ 2 oe)

$\omega = 1.88 \times 10^4$ radians/sec.

Take as reasonable limits:

$$V = 12\ \text{cm}^3$$

$$\Delta f = 10^{-3}\ \text{Hz}.$$

Then signal-to-noise ratio becomes

$$\frac{e_s}{e_n} = 2.39 \times 10^{10}\ \kappa \qquad (2.38)$$

In order that a change in susceptibility κ may be detected, it is necessary that it produce a change in signal voltage e_s greater than or equal to the noise voltage e_n. Thus the minimum detectable change in κ is just equal to the value of κ which, in Eq. 2.38, would make signal-to-noise ratio equal unity. Therefore minimum detectable susceptibility anisotropy is

$$\Delta\kappa_{min} = 4.18 \times 10^{-11}\ \text{mksu} \quad (3.32 \times 10^{-12}\ \text{emu/cm}^3) \qquad (2.39)$$

Graham's observed noise levels were about 1.3×10^{-8} mksu (1.0×10^{-9} emu/cm^3) under good conditions. Noise was attributable in part to residual drift and vibration of the bridge inductors.

One possible source of noise was fluctuation in the frequency of the oscillator driving the bridge. This frequency modulation would have introduced spurious signals because the bridge balance was quite sensitive to frequency. This can be attributed to the fact that the resistive effect caused by conductors near the coils, including that of the lead slugs used for bridge-balancing, is frequency-dependent.

If the balance is to be substantially frequency-independent it is necessary to ensure that all bridge elements are frequency-independent, unless, of course, the frequency dependence itself is balanced.

At the time when, by Dr. Graham's kind cooperation, the author made use of the bridge, it was noted that normal floor-transmitted vibrations produced noticeable spurious signals. It was not clear, however, whether these were due to internal vibrations changing the dimensions of the main coils, or bulk vibrations changing the coils' position and making them interact with external fields. The latter form of noise could, in principle, have been alleviated with an externally-closed magnetic circuit for the main exciting field.

2.3 D.C. Spinner Instruments

D.C. spinner-type instruments have been described by de Sa and Molyneux (1963). A rock specimen spins in a uniform magnetic field generated by a pair of Helmholtz coils. The spinning specimen sets up a secondary field alternating at twice the rotational frequency. Noltimier (1967) describes such an instrument which uses coils separate from the field coils as sensors. One set of sensing coils is placed parallel to the field coils while another set is placed perpendicular. Noltimier notes that the normal set, although it presents the same signal phase-shifted 90°, produces less noise since it is at null with the field coils.

Noltimier cites four main sources of noise:

1. Electromagnetic noise from A.C. mains at 50 Hz and at 150 Hz. It is reduced by fixed and variable compensating coils. Both sets of field coils are bypassed for A.C. with large capacitors.

2. Vibrations in a magnetic gradient. Those induced in the pickup coil by direct coupling with the spinning top gave a noise of 1.2×10^{-10} A·m^2 (1.5×10^{-6} gauss cm^3). This value has more pertinence to remanence than to anisotropy because of the stronger fundamental component of vibration, and hence is not the dominant noise contribution for anisotropy.

3. Electrostatic noise due to accumulating charge on the nonconductive rotor surface. This noise was about 1.2×10^{-10} A·m^2 (1.5×10^{-6} gauss cm^3). After coating with graphite the noise falls to less than 2.4×10^{-11} A·m^2 (3×10^{-7} gauss cm^3). In a field of about 5500 amp/meter this meant, for the specimen size used, a noise anisotropy of 1.1×10^{-8} mksu (0.85×10^{-9} gauss/oe). The coating must not be too conductive because eddy currents would produce a magnetic moment to simulate susceptibility anisotropy.

4. Feedthrough of remanence signal. A maximum remanence of 2.4×10^{-9} A·m^2 (3×10^{-5} gauss cm^3) was found to permit measurement of anisotropies greater than 2.5×10^{-6} mksu (2×10^{-7} gauss/oe), in low fields at least.

Noltimier quotes an overall low achievable anisotropy noise level of 1.1×10^{-8} mksu (0.85×10^{-9} gauss/oe) and a practical measuring sensitivity limit of ten times this value, or 1.1×10^{-7} mksu.

2.4 Requirements for the New Magnetometer

Three main criteria were used to determine the type and configuration of the magnetometer described in this thesis:

1. Ease of operation
2. Speed of operation
3. Sensitivity.

In order that the instrument be easy to use and rapid in operation, it is of great advantage that components which are handled or otherwise disturbed be robust and not cause serious offset of the signal output. Therefore instruments with robust mechanical parts and sensitive electronics, such as spinners, are to be preferred to instruments with robust electronics and sensitive mechanical parts, such as torque-meters.

A very important factor in the speed of operation is the integrating time required to attain the required level of signal sensitivity. In torque-meters this is the settling time of the suspended mass, whereas in spinner instruments it is normally the charging time of an integrating capacitor in a phase-sensitive detector. Even for equal integrating times, spinners are preferable to torquemeters because they require only three observations (one for each of three orthogonal specimen axes) whereas torquemeters normally require at least 15 observations (five for each axis).

If high sensitivity is to be attained in a spinner instrument, the measurable parameters which are altered by specimen susceptibility must be very constant, or at least contain no strong time-varying components at twice the spinner shaft frequency. A.C. bridge spinners, for which the inductance of a bridge element is the salient parameter, are normally limited by inductance variations or movements of ferromagnetic materials in the vicinity of the bridge inductors. In order to minimize these external effects, it was decided that the bulk field should be generated by an externally-closed magnetic circuit situated within an effective magnetic shield. To keep vibration problems under control, the entire field-generating and sensing structure was cast into a single block using thermosetting epoxy resins. To minimize variations in the field due to power supply fluctuations at the signal frequency, it was decided that a direct, rather than an alternating field would be used. Variations are more readily filtered from a direct current supply. Alternatively, permanent magnets may be used.

There is a practical lower limit to the susceptibility anisotropy which may be detected, set by diamagnetic effects within the spinner shaft and specimen cup, and indeed within the specimen itself. A typical susceptibility for diamagnetic rock-forming materials is -10^{-5} mksu. For crystalline quartz the value is about -1.63×10^{-5} mksu. The Permali impregnated laminated beechwood, of which the shaft and specimen cups are constructed, has a measured susceptibility of about -7×10^{-6} mksu, a value which is typical of organic materials. If the shaft and rock specimen had complete circular symmetry about their rotational axes, or if they rotated in an absolutely uniform magnetic field, no problems would arise. This is because diamagnetism is intrinsically isotropic, and, because of its very small value, the effects of demagnetizing factor on elongated diamagnetic grains is negligible.

Consider a diamagnetic body with single axis symmetry, shown in Figure 2.6 (A), rotating in a field with a symmetric component of deviation from uniformity. That is, for a point on the periphery of the rotating body, the dominant terms in the expression for flux density are

Figure 2.6 "Dumbbell" equivalent of the shape anisotropy of nonspherical shapes with:

(A) single-axis symmetry

(B) double-axis symmetry

about the axis of rotation.

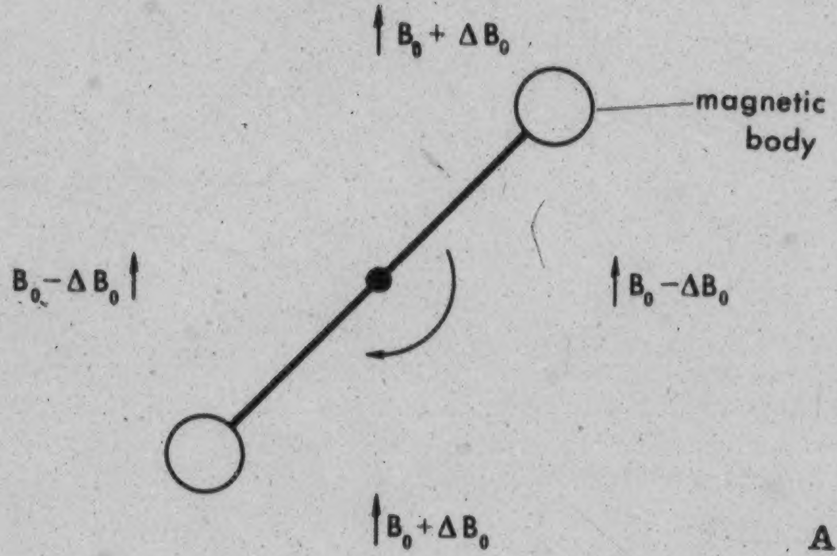
$B_0 + \Delta B_0$
magnetic body
$B_0 - \Delta B_0$
$B_0 - \Delta B_0$
$B_0 + \Delta B_0$

A

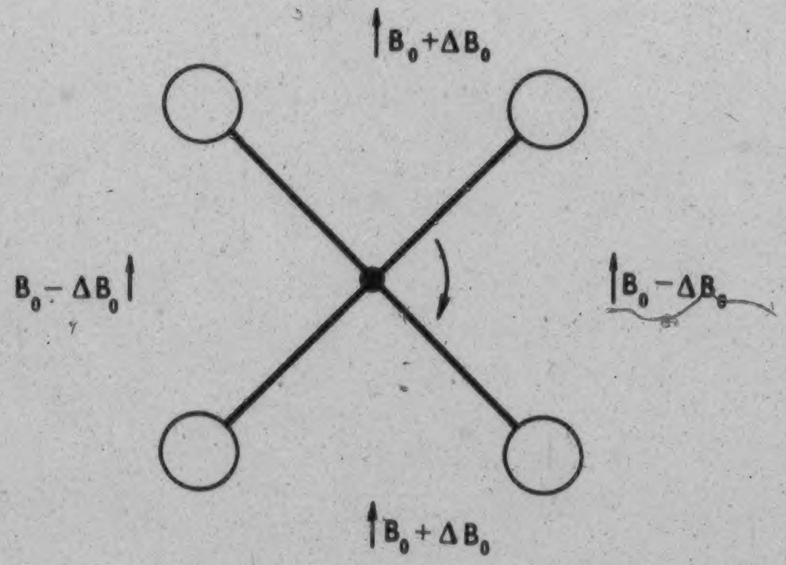
$B_0 + \Delta B_0$
$B_0 - \Delta B_0$
$B_0 - \Delta B_0$
$B_0 + \Delta B_0$

B

$$B[\theta] = B_o + \Delta B_o \sin 2\theta \tag{2.40}$$

where θ is the angle of rotation from the initial position. Then each sphere on the "dumbbell" in Figure 2.6 (A) will generate a dominantly sin 2θ flux variation as it rotates. This has the same frequency as the susceptibility anisotropy signal. Further, since the two spheres are separated by an angle $\theta = \pi$, the two flux variations are in phase. Therefore the combination of single-axis symmetry on the rotating shaft and symmetric deviation in field intensity must be minimized.

Note that if another "dumbbell" is added at right angles to the first, as in Figure 2.6 (B), the two spurious flux variations are equal in magnitude and 180 out of phase. Hence a rotating member with a double axis of symmetry is not nearly as objectionable as one with but a single axis.

It should also be noted that a constant field gradient across the rotating specimen volume is not as objectionable as a symmetric gradient with a maximum or minimum field near the center of the specimen. This is because, even with single axis symmetry of the specimen and specimen cup, one half of the equivalent "dumbbell" is, at any particular instant, passing into a higher-field region while the other half passes into a lower-field region. Their effects therefore cancel to a considerable extent.

The shaft proper has a double-axis rotational symmetry, as does the specimen cup when spinning on its cylindrical axis. When spinning normal to this axis, however, the specimen cup, like the specimen itself, has effectively single-axis symmetry.

Consider a specimen cup for cylindrical specimens of 2.5 cm length and 2.5 cm diameter spinning in a field having a deviation of ±0.1% over the volume of the cup. When it spins about an axis other than the cylindrical axis, the effective asymmetrical volume is approximately that of the cup bottom. The cups used on this instrument have a bottom thickness of 0.25 cm and volume of 1.25 cm^3. Then the spurious susceptibility anisotropy signal is

$$\Delta\kappa \simeq \frac{\text{asymmetrical volume}}{\text{specimen volume}}\left[\kappa\right]\left[\frac{\text{field deviation}}{\text{mean field}}\right]$$

where κ = diamagnetic susceptibility of cup.

Therefore

$$\begin{aligned}\Delta\kappa &= (0.1)(7 \times 10^{-6})(2 \times 10^{-3}) \\ &= 1.4 \times 10^{-9} \text{ mksu} \qquad (2.41)\end{aligned}$$

Since this signal is stable and readily measured, it may be deducted from the observed signal. Therefore its effects can readily be made smaller than the levels of statistical anisotropy expected.

The specimens themselves, when spinning about an axis other than the cylindrical axis, have about 10% shape anisotropy. The apparent diamagnetic susceptibility anisotropy is the product of bulk diamagnetic susceptibility, peak-to-peak fractional field nonuniformity, and fractional shape anisotropy. For field deviations of ±0.1% the apparent susceptibility anisotropy will be about 2×10^{-9} mksu. Unlike diamagnetic effects from the shaft, those from the specimen are not readily measured and deducted from observations. The problem can be somewhat alleviated by cutting three orthogonal cores from each specimen and spinning only about cylindrical axes. The sample holder may then be similarly symmetric. This expedient can add at most one or two orders of magnitude of sensitivity, as rock nonuniformity and statistical anisotropy become noticeable. It is therefore conceivable that a sensitivity of about 10^{-11} mksu (8×10^{-13} emu/cm^3) could be used. It would be desirable to have full sensitivity with observation time constants of about 15 seconds or less and rotational speeds of 50 Hz, at least with maximum bulk field intensity.

CHAPTER 3

DESIGN OF FLUX SENSORS FOR A SPINNER MAGNETOMETER

This chapter discusses principles of design of flux sensors for a spinner magnetometer employing a direct main field and a closed magnetic circuit, and providing high sensitivity. Only one of the sensing systems described has been fully implemented in the existing instrument, because signal induced by the spinner shaft limits sensitivity to a level accessible with that system (the specimen-gap coils). It is necessary to understand, however, that the instrument has been built to provide optional use of the low-direct-flux coils, the magnetic helix, and the magnetic modulator sensing systems, all of which are intrinsically more sensitive than the specimen-gap coils system. Much of the design of the magnetic circuit including its bridge configuration, is determined by the more sensitive sensing systems. It is therefore necessary to discuss designs of these systems even though they have not been fully implemented. The next chapter discusses the instrument as it has been implemented.

3.1 The Basic Susceptibility-Anisotropy Instrument

The type of susceptibility-anisotropy measuring instrument chosen for development operates by measuring the small flux variations due to the time-varying magnetic moment induced into the rock specimen when it rotates in a direct, uniform magnetic field. Such an instrument is shown schematically, in its most basic form, in Figure 3.1. The magnetic circuit resembles that of a shell-type transformer, and retains the magnetic shielding characteristics of that construction. The inner leg of the magnetic circuit contains an air gap and a pair of permanent magnets to establish a direct magnetic field in the air gap. The reluctance of the gap varies with time when an anisotropic rock specimen is made to rotate in the gap. The resulting variation in gap flux is measured as a voltage across a solenoid wound around the inner leg of the magnetic circuit. The sensitivity of such an arrangement, excluding limitations of the electronic amplifiers, is now derived.

The rock specimen behaves very nearly like, and indeed usually consists of, a large array of particles of high magnetic permeability suspended within an essentially nonmagnetic matrix. These particles are so dispersed that they do not appreciably affect the magnetic environment of each other. That is, magnetically, they are linearly

Figure 3.1 Plan and end views of the basic magnetic circuit.

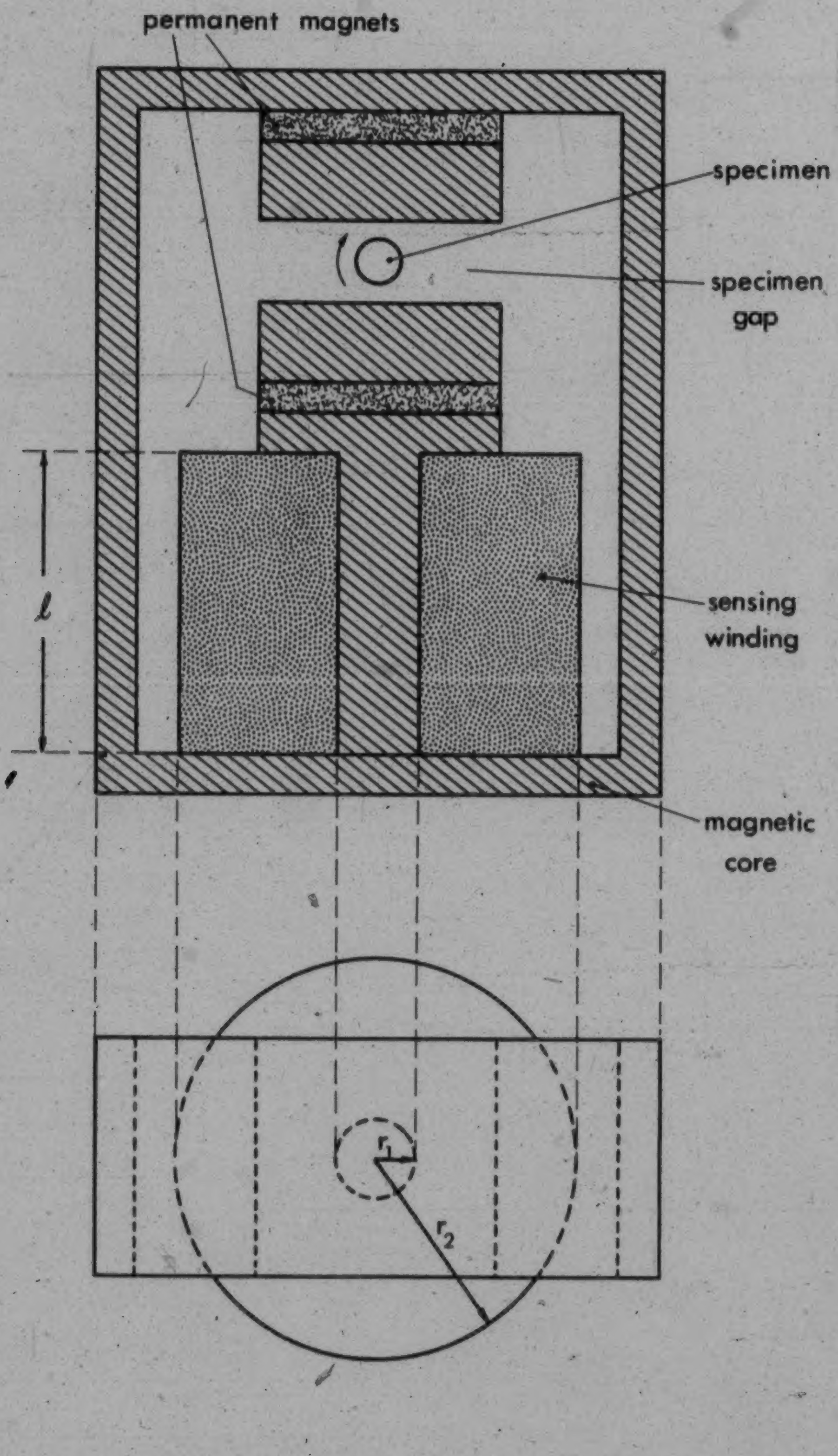
permanent magnets
specimen
specimen gap
sensing winding
magnetic core
l
r1
r2

Figure 3.2 Electrical equivalent of the basic magnetic circuit.

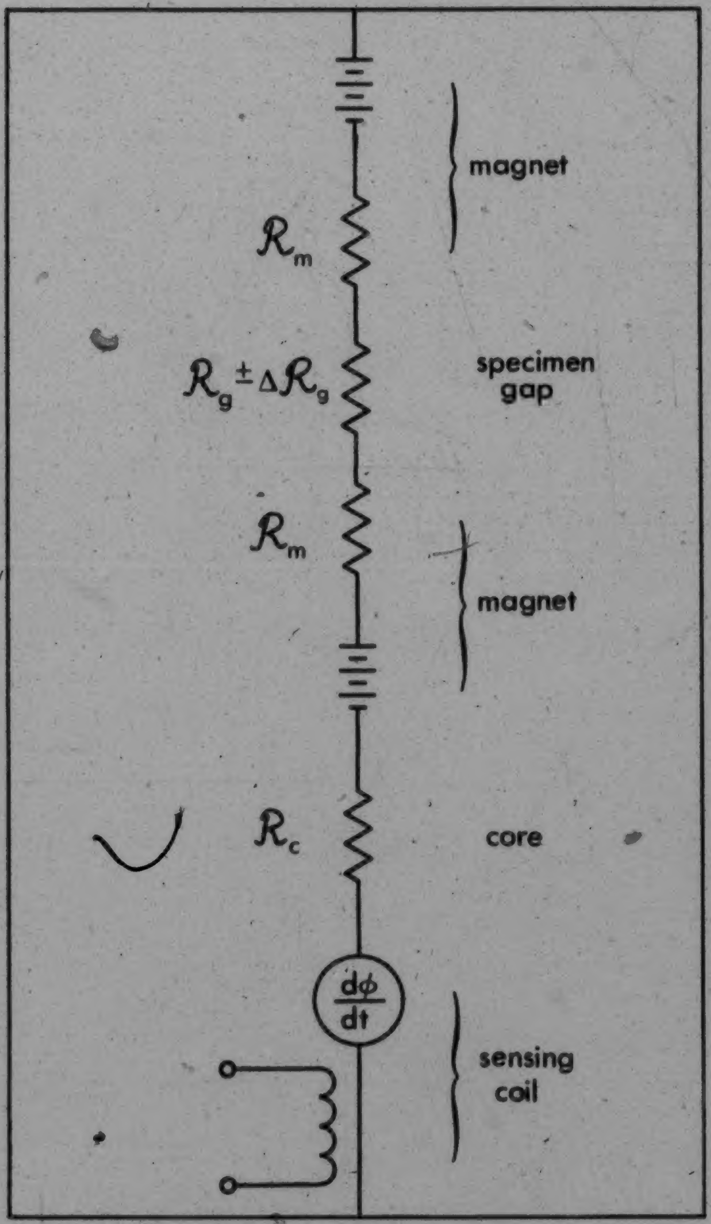
magnet
$\mathcal{R}_m$
$\mathcal{R}_g \pm \Delta\mathcal{R}_g$
specimen gap
$\mathcal{R}_m$
magnet
$\mathcal{R}_c$
core
$\frac{d\phi}{dt}$
sensing coil

independent. Thus, if the magnetic flux density could be made uniform throughout the specimen gap, the position of a particle within the gap would not matter at all, in terms of signal output. For purposes of calculating signal flux, therefore, we may consider the magnetic particles within the rock specimen to be uniformly dispersed over the gap volume, assuming the gap to have a uniform flux density equal to the mean flux density at the position of the specimen. The specimen gap then becomes a reluctance whose variation is easily obtained from its apparent variation of susceptibility. The product of the time-variation of apparent susceptibility of the gap and the gap volume equals the product of the orientation-variation of apparent susceptibility of the specimen and the specimen volume. If we take the volume of the specimen gap to be that extrapolated from the polepiece area, the assumption of uniform flux density is invalidated by the fringing field. However, it is possible to calculate a leakage factor ξ such that a hypothetical gap with area $(1 + \xi)$ times the real polepiece area, width identical to that of the real gap, and a completely uniform flux density with no fringing, would "look" to the specimen exactly as the real gap does. Thus, if the flux passing through the projected polepiece area A_0 is

$$\phi_0 = B_0 A_0 \tag{3.1}$$

where B_0 is the flux density at the center of the gap, then the flux contained in the fringing field is $\xi\phi_0$ and the total magnetic flux leaving the polepiece is $\phi_0(1 + \xi)$. The apparent volume of the gap, then, is $(1 + \xi)$ times its polepiece-extrapolated volume.

The leakage factor is discussed further in Section 4.2 in connection with establishing the direct biasing field. It is there shown that the leakage factor for the specimen gap of the dimensions chosen is about 0.45. That for each magnet block is 0.25. This latter is calculated using the normal relative permeability of the permanent magnets. Strictly speaking, when alternating signal flux is considered, the leakage factor should be determined from the reversible relative permeability, which is 1.05 for the material chosen. This gives the magnet blocks an AC leakage factor of 0.26.

Let the apparent susceptibility of a rock specimen range, in a particular plane, between a minimum of κ_1 and a maximum of κ_2. Then the peak-to-peak anisotropy-of-susceptibility of the specimen in this plane is

$$\Delta\kappa = \kappa_2 - \kappa_1 \quad . \qquad (3.2)$$

When the rock is spun about an axis normal to this plane, the apparent peak-to-peak time variation of susceptibility of the specimen gap $\Delta\kappa_g$ is given by

$$\Delta\kappa_g = \frac{(\Delta\kappa)(\text{rock specimen volume})}{(\text{gap volume})(1 + \text{gap leakage})} \qquad (3.3)$$

Consider a cylindrical specimen of diameter 2.5 cm. and length 2.5 cm. The gap volume is dictated by the need to accommodate the rotating specimen and provide the necessary field uniformity. The choice of gap dimensions is discussed in Section 4.1 and indicates a projected gap volume of 1.18×10^{-3} meter^3. Then

$$\Delta\kappa_g = \frac{(\Delta\kappa)(1.23 \times 10^{-5}\ \text{meter}^3)}{(1.18 \times 10^{-3}\ \text{meter}^3)(1.45)}$$

$$= 7.19 \times 10^{-3}\ \Delta\kappa \qquad (3.4)$$

If $\Delta\kappa \ll 1$, then the resultant peak-to-peak change in reluctance of the specimen gap may be very closely approximated by

$$\Delta\mathcal{R}_g = \mathcal{R}_g \Delta\kappa_g \qquad (3.5)$$

where $\mathcal{R}_g$ is the mean reluctance of the specimen gap.

The parameters indicated in Figure 3.2 can now be quantified. The relative reversible permeability of the permanent magnet material used is 1.05. Therefore

$$\mathcal{R}_m = \frac{(\text{magnet length})}{(\text{magnet area})(1 + \text{leakage factor})(\mu_0 \mu_r)}$$

$$= \frac{(1.90 \times 10^{-2}\ \text{meter})}{(2.32 \times 10^{-2}\ \text{m}^2)(1.26)(4\pi \times 10^{-7}\ \text{Wb/A}\cdot\text{m})(1.05)}$$

$$= 0.49 \times 10^{6}\ \text{amperes/weber} \qquad (3.6)$$

$$\mathcal{R}_g = \frac{\text{(gap length)}}{\text{(gap area)(1 + leakage factor)}(\mu_0\mu_r)}$$

$$= \frac{(5.08 \times 10^{-2}\ \text{meter})}{(2.32 \times 10^{-2}\ \text{m}^2)(1.45)(4\pi \times 10^{-7}\ \text{Wb/A}\cdot\text{m})}$$

$$= 1.20 \times 10^6\ \text{amperes/weber} \qquad (3.7)$$

Therefore, Eq. 3.5 becomes

$$\Delta\mathcal{R}_g = (\mathcal{R}_g)(\Delta\kappa_g)$$

$$= (1.20 \times 10^6\ \text{A/Wb})(7.19 \times 10^{-3}\Delta\kappa)$$

$$= 8.63 \times 10^3\Delta\kappa\ \ \text{amperes/weber} \qquad (3.8)$$

Because the sensing coil's core must carry the direct flux ϕ_0 without saturating, the core reluctance is negligible for reasonable dimensions and permeability. Since $\Delta\kappa \ll 1$, it follows that $\Delta\mathcal{R}_g \ll \mathcal{R}_g$. Thus the peak-to-peak flux variation can be very closely approximated by the relation

$$\Delta\phi = \phi_0 \frac{\Delta\mathcal{R}_g}{2\mathcal{R}_m + \mathcal{R}_g + \mathcal{R}_c}$$

$$= (B_0)\text{(gap area)}(1+\xi_g)\left(\frac{\Delta\mathcal{R}_g}{2\mathcal{R}_m + \mathcal{R}_g + \mathcal{R}_c}\right) \qquad (3.9)$$

where B_0 is the flux density in the specimen gap at the position of the specimen. It is shown in Section 4.2 that the maximum direct flux density is 0.115 teslas. Therefore if $\mathcal{R}_c$ is small relative to $\mathcal{R}_g$ and $\mathcal{R}_m$

$$\Delta\phi = (0.115\ \mathrm{T})(2.32 \times 10^{-2}\mathrm{m}^2)(1.45)\cdot \cdot \frac{(8.63 \times 10^3 \Delta\kappa\ \mathrm{A/Wb})}{(2.18 \times 10^6\ \mathrm{A/Wb})}$$

$$= 1.53 \times 10^{-5}\ \Delta\kappa\ \text{webers} \qquad (3.10)$$

Thus the rms flux variation ϕ_s is

$$\phi_s = \frac{\Delta\phi}{2\sqrt{2}}$$

$$= 5.41 \times 10^{-6}\ \Delta\kappa\ \text{webers} \qquad (3.11)$$

If the specimen rotates at frequency f_r , the induced signal voltage is at frequency $f = 2f_r$. Thus, assuming no signal flux leakage around the core reluctance $\mathcal{R}_c$, the rms induced voltage in a signal coil of n turns is

$$e_s = 2\pi f n\,\phi_s$$

$$= (2\pi f n\ \ \mathrm{s}^{-1})(5.41 \times 10^{-6}\ \Delta\kappa\ \mathrm{Wb})$$

$$= 3.40 \times 10^{-5}\ f n\,\Delta\kappa\ \text{volts} \qquad (3.12)$$

3.2 Noise Generated by the Signal Coil

A fundamental lower limit to detectable signal voltage is set by thermal noise generated by various component parts of the instrument. One noise mechanism is the random motion of electrons in the signal coil windings. The Fermi gas of electrons interacts with the atoms in the crystal lattices of the conductor. If the winding is open-circuited, the current pulses resulting from all the moving electrons sum to produce a voltage across the winding resistance (Johnson noise). From thermodynamic considerations, the rms value of this open-circuit voltage can be shown to be

$$e_n = (4kT R_c \Delta f)^{1/2} \tag{3.13}$$

where: k = Boltzmann's constant

$= 1.38 \times 10^{-23}$ joules/°K

T = absolute temperature in °K

R_c = resistance of sense winding in ohms

Δf = frequency bandwidth observed (Hz).

Thus, at an absolute temperature of 293°K (20°C), the Johnson noise voltage is

$$e_n = 1.27 \times 10^{-10} \ (R_c \Delta f)^{1/2} \quad \text{volts} \tag{3.14}$$

The resistance of a cylindrical solenoid with current density inversely proportional to radius is

$$R_c = \frac{2\pi\rho n^2}{q\ell \ \ln \frac{r_2}{r_1}} \tag{3.15}$$

where: ρ = resistivity of wire (ohm meters)

n = number of turns

q = filling factor of winding

ℓ = axial length of coil (meters)

r_1 = inner radius (meters)

r_2 = outer radius (meters)

Substituting this expression for R_c, Eq. 3.14 becomes

$$e_n = 1.27 \times 10^{-10} \left(\frac{2\pi\rho n^2 \Delta f}{q\ell \ \ln \frac{r_2}{r_1}} \right)^{1/2} \quad \text{volts}$$

$$= 3.19 \times 10^{-10} n \left(\frac{\rho \Delta f}{q\ell \ \ln \frac{r_2}{r_1}} \right)^{1/2} \quad \text{volts} \qquad (3.16)$$

If one uses copper wire with a resistivity of 1.724×10^{-8} ohm meters at 20°C., and one obtains a filling factor of 75% (i.e. $q = 0.75$), then

$$e_n = 4.83 \times 10^{-14} n \left(\frac{\Delta f}{\ell \ \ln \frac{r_2}{r_1}} \right)^{1/2} \quad \text{volts} \qquad (3.17)$$

It is convenient, for purposes of comparison with other noise sources, to express this noise voltage in terms of the equivalent noise flux ϕ_n passing through a noiseless coil having the same number of turns. Thus

$$\phi_n = \frac{e_n}{2\pi f n}$$

$$= 7.69 \times 10^{-15} \ \frac{1}{f} \left(\frac{\Delta f}{\ell \ \ln \frac{r_2}{r_1}} \right)^{1/2} \quad \text{webers} \qquad (3.18)$$

The noise voltage given by Eq. 3.17 gives a good indication of thermal noise generated within the sensing winding itself, provided the impedance of the winding is dominantly resistive. If its inductive reactance becomes considerably larger than its resistance, the reactive component must be cancelled with a suitable capacitive reactance either in parallel or in series with the coil.

If this is not done, noise contribution from the electronic amplifier will increase. This may or may not be important, depending on the design of the amplifier and the ratio of reactance to resistance.

3.3 Noise Due to the Magnetic Core

3.3.1 Types of Noise

The flux in any ferromagnetic core will show fluctuations with time. These fluctuations can be observed as an open-circuit noise voltage $e_n(t)$ at the terminals of a solenoid wound around the core. Bittel (1969) distinguishes three different types of noise:

1. External exciting field intensity H_0 is constant or zero and temperature T is constant. In this case one observes thermal, or Nyquist, noise. It is caused mainly by the thermal energy of the spin system and, in metallic cores, also by the thermal energy of the conduction electrons.
2. H_0 is constant while temperature T is not constant. In this case excess noise is observed with both ferromagnetic metals and ferrites, caused by changes in the domain configuration due to thermal strain.

3. H_0 is not constant. Wideband fluctuations result from the discontinuous magnetization of the core by the changing field excitation. This is called Barkhausen noise.

Of these three categories of noise, the Nyquist noise is relatively weak. Excess noise due to thermal strain, or indeed to any changing mechanical strain, can be considerably stronger. Barkhausen noise can be strongest by far. This can be ascribed to a pronounced tendency to form clusters of Barkhausen jumps. The frequency spectra of the Nyquist and excess noise are quite different. The spectral density $W(f)$ of the mean square noise voltage $\overline{e_n^2(t)}$ due to thermal energy within the core is typically directly proportional to frequency. That due to Barkhausen jumps, on the other hand, typically shows a $f^{-1.6}$ dependence down to a frequency of about 10 Hz. Thus the relative importance of Barkhausen noise is greater at lower frequencies.

In the instrument here described, great care has been taken to avoid excess noise in the magnetic circuit. During normal operation there is no significant thermal dissipation within the main transducer block and hence thermal drift and consequent strains are avoided. The core and associated coils and shields were cast into a single unit and mounted in such a way that changing mechanical strains would be minimized. Barkhausen noise is avoided by ensuring that the direct exciting field is as nearly as possible constant. This is done by using permanent magnets whose temperature fluctuations are kept to a minimum. The design of the magnetic circuit therefore assumes that Nyquist noise will be dominant.

3.3.2 Nyquist Noise in the Magnetic Core

Callen and Welton (1951) related generalized noise and loss mechanisms. By extension of their arguments to the case of nonlinear ferromagnetic materials, one can predict that each component of magnetic loss has associated with it a fluctuation of magnetic induction. Eddy currents are one such loss component. Hysteresis losses, because of their strong dependence on peak-to-peak flux variation, cease to be important for vanishingly small flux amplitudes. There are several types of so-called residual losses (Latimer, 1953) which can be distinguished by their direct dependence on f (as distinct from the f^2 dependence of eddy current losses) and their independence of the dimensions of the ferromagnetic specimen. These losses become important at very low frequencies and for very thinly laminated metallic magnetic materials. Direct measurements (Brophy, 1958) of magnetic fluctuations from a toroidal core wound with molypermalloy tape of 25 micron thickness, indicated that the main noise component, at least down to about 1000 Hz., was that associated with eddy-current loss.

It should be noted that eddy-current loss may be considerably larger than that calculated by assuming homogeneous permeability for the magnetic material (Polder, 1953). The reason lies in the fact that initial permeability of soft ferromagnetics is mainly due to reversible wall displacements. When a field is applied, there is a large flux change in the region of the domain wall, but little elsewhere. This effect causes micro-eddy currents to be set up. As a result, power dissipation is larger than it would have been for uniform eddy currents. The loss ratio is minimized by ensuring that lamination thickness is not appreciably smaller than domain wall spacing. Enoch and Winterborn (1967) showed that high-permeability Ni-Fe-Cu-Mo alloys in sheet thicknesses greater than 25 microns have reasonably small loss ratios. They observed minimum loss ratio when specimens were annealed with a cooling rate of about 65°C./hour.

One can therefore get a reasonably close estimate of core noise by calculating fluctuations associated with eddy currents which are assumed to be uniformly distributed. The noise, then, is due to thermal motion of the conduction electrons. Their stochastic circular movements generate local magnetic fields in all directions and cause movements of domain walls.

Consider a section of magnetic core with reluctance $\mathcal{R}_1$ and dimensions as indicated in Figure 3.3, connected magnetically in series with a lossless and noiseless section of core with reluctance $\mathcal{R}_2$. The circuit is closed to form a continuous magnetic loop of reluctance $\mathcal{R} = \mathcal{R}_1 + \mathcal{R}_2$. The section of core under test is divided into N laminations of length ℓ, width w, and thickness t. It has a cross-sectional area $A_m = Nwt$ normal to the direction of signal flux. Two distinct limiting cases are possible for the calculation of magnetic noise: the laminations are much thinner than the skin depth (depth of penetration) of the material used, or they are much thicker. The alternating magnetic flux may be assumed to be distributed uniformly throughout the cross-section of the very thin laminations, whereas it is concentrated near the surface of the thick ones. The effects of electric noise currents have the same distribution.

Within the skin depth, noise paths may be assumed to be essentially resistive. Permeability is assumed to be completely uniform. Only magnetic noise flux in the axial direction around the entire circuit is here considered. Therefore noise currents in planes normal to this axis are examined.

Figure 3.3 General model for calculating noise flux due to a laminated core.

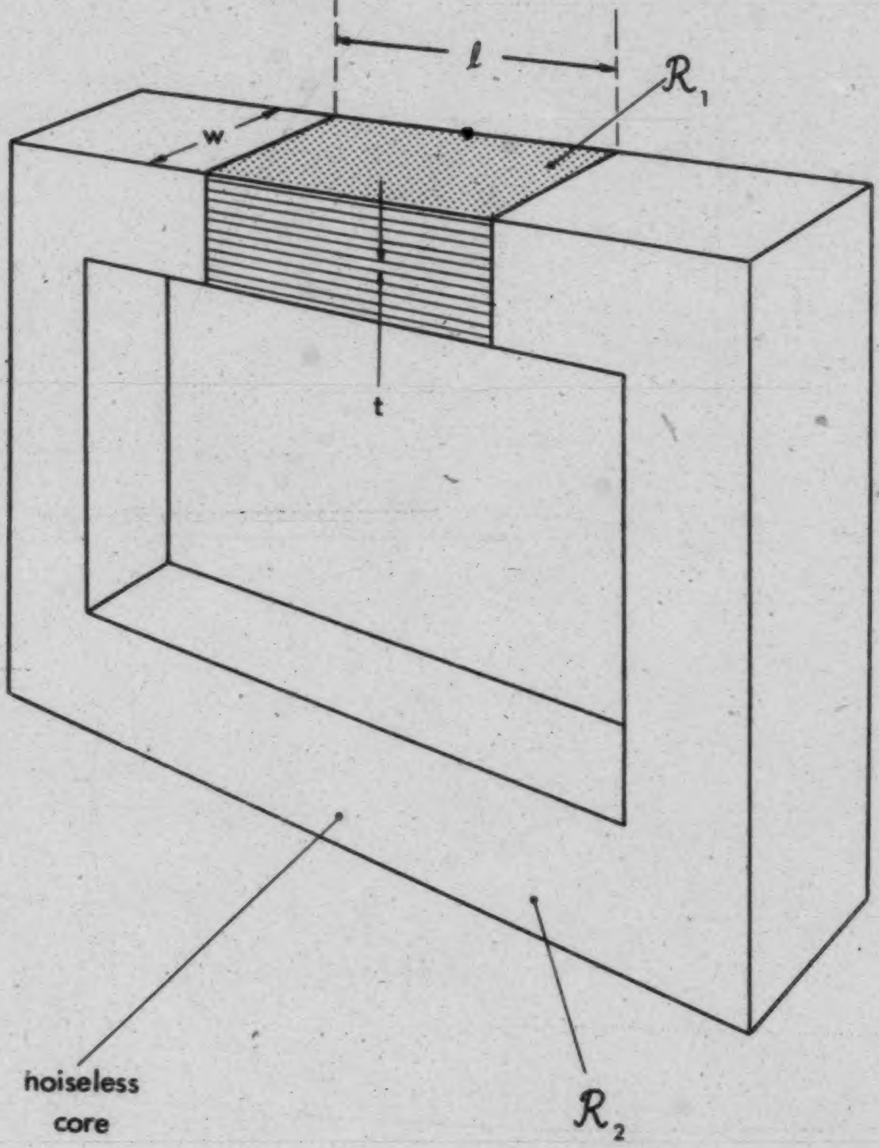
l
$\mathcal{R}_1$
w
t
noiseless core
$\mathcal{R}_2$

3.3.3 Laminations Much Thinner Than Skin Depth

In any closed circuit of resistance R, there exists a circulating noise power which, from thermodynamic considerations, has a value

$$P_n = 4kT\Delta f \tag{3.19}$$

where: k = Boltzmann's constant

$= 1.38 \times 10^{-23}$ joules/°K

T = absolute temperature (°K)

Δf = frequency bandwidth considered (Hz).

Each lamination can be thought of as being divided into a series of nested current loops of incremental width dx and extending the whole length ℓ of the lamination, as is shown in Figure 3.4. Assuming $t \ll w$, the resistance of such a loop of resistivity ρ is

$$dR = \frac{(\rho)\,(\text{length of conductor})}{(\text{cross-sectional area of conductor})}$$

$$= \frac{(\rho)\,(2w)}{\ell\, dx} \tag{3.20}$$

Since each such loop has a circulating noise power $4kT\Delta f$, it follows that the incremental noise current in the loop has a value

$$di_n = \left(\frac{4kT\Delta f}{dR}\right)^{1/2}$$

$$= \left(\frac{4kT\Delta f\ell dx}{2\rho w}\right)^{1/2}. \tag{3.21}$$

Figure 3.4 Noise current within a single lamination of thickness much less than skin depth.

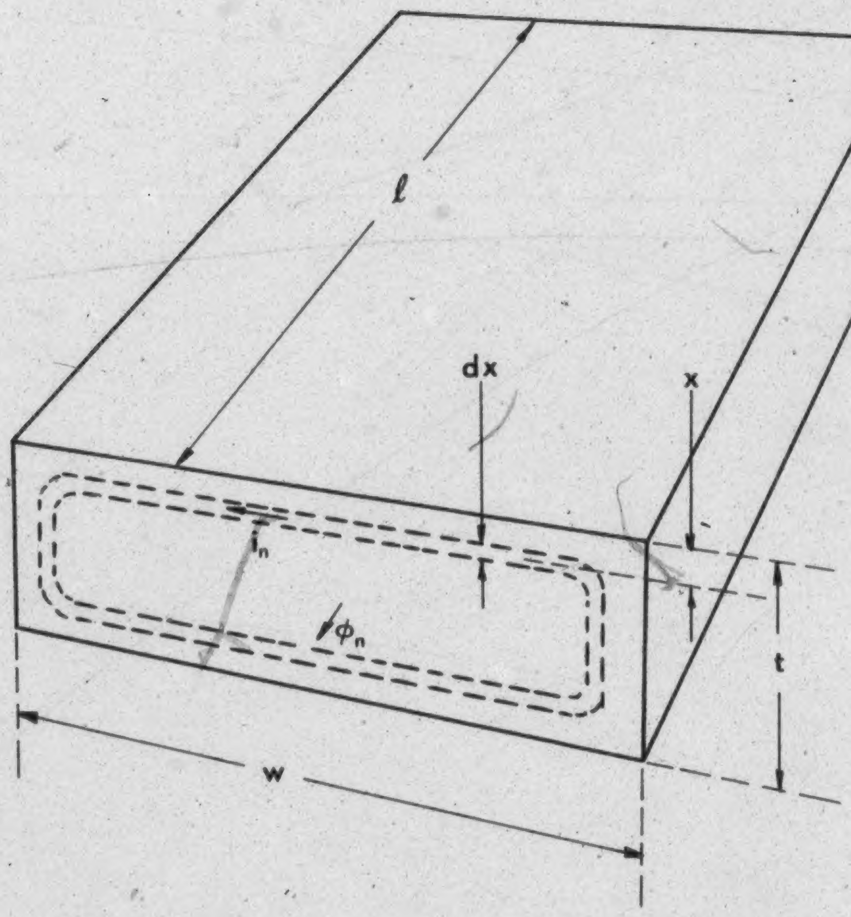
ℓ
dx
x
i_n
ϕ_n
t
w

This current loop produces an incremental magnetic moment given by

$$dm_n = \text{(magnetic potential)(area of loop)}$$

$$= (d\,i_n)\,(2wx)$$

$$= \left(\frac{2kT\Delta f\,\ell\,dx}{\rho w}\right)^{1/2} (2wx) \qquad (3.22)$$

Because the thermally generated currents are uncorrelated, the mean squares of the magnetic moments sum, rather than their root mean squares.

$$dm_n^{\,2} = \left(\frac{2kT\Delta f\,\ell\,dx}{\rho w}\right)(4\,w^2 x^2)$$

$$= \frac{8kT\;\Delta f\;\;\ell\,w\;\;x^2}{\rho}\,dx \qquad (3.23)$$

For the effective magnetic moment for the whole lamination, one integrates $dm_n^{\,2}$.

$$m_n^{\,2} = \int_{x=0}^{t/2} dm_n^{\,2}$$

$$= \int_{x=0}^{t/2} \frac{8kT\,\Delta f\;\;\ell\,w}{\rho}\;x^2\,dx$$

$$= \left(\frac{8kT\Delta f\,\ell w}{\rho}\right)\frac{x^3}{3}\Bigg]_{x=0}^{t/2}$$

$$= \frac{kT\Delta f\;\ell\,w\,t^3}{3\rho} \qquad (3.24)$$

Again, since the magnetic moments are uncorrelated from one lamination to another, their squares are summed to yield a total squared magnetic moment

$$m_{N_n}{}^2 = N m_n{}^2$$

$$= \frac{N k T \Delta f \ell w t^3}{3\rho} \qquad (3.25)$$

Noting that the total cross-sectional area A_m of the core under test is

$$A_m = N w t \qquad (3.26)$$

one obtains

$$m_{N_n}{}^2 = \frac{k T \Delta f \ell t^2 A_m}{3\rho} \qquad (3.27)$$

Therefore the total magnetic moment is

$$m_{N_n} = t \left(\frac{k T \Delta f \ell A_m}{3\rho} \right)^{1/2} \qquad (3.28)$$

It then follows that with total magnetic circuit reluctance $\mathcal{R}$ the magnetic noise flux is

$$\phi_n = \frac{m_{N_n}}{A_m' \mathcal{R}} \qquad (3.29)$$

where A_m' is the effective cross-sectional area for magnetic flux variation. Since it is assumed that flux distribution is uniform, $A_m' = A_m$. Therefore

$$\phi_n = \frac{t}{A_m \mathcal{R}} \left(\frac{kT \Delta f \, \ell A_m}{3\rho} \right)^{1/2}$$

$$= \frac{t}{\mathcal{R}} \left(\frac{kT \Delta f \, \ell}{3\rho \, A_m} \right)^{1/2} \qquad (3.30)$$

Substitute into Eq. 3.30 the values:

$T = 293$ °K (20°C)

$k = 1.38 \times 10^{-23}$ joules/°K

$\rho = 6.0 \times 10^{-7}$ ohm meter (for moly-permalloy).

Then one obtains from Eq. 3.30

$$\phi_n = 4.74 \times 10^{-8} \frac{t}{\mathcal{R}} \left(\frac{\ell \Delta f}{A_m} \right)^{1/2} \text{ webers} \qquad (3.31)$$

For a small value of magnetic Nyquist noise, therefore, it is desirable to have a thinly laminated, short core with a large effective cross-sectional area.

3.3.4 Laminations Much Thicker Than Skin Depth

Consider now the case of laminations thicker than twice the skin depth δ. As a first approximation, assume a uniform mean distribution of magnetic flux and electric noise current to a depth δ and no penetration of either flux or current below that level.

Consider a single lamination, as in Figure 3.5. Assume its thickness t to be much less than either its width w or its length ℓ. Then the situation is equivalent to that for a single lamination of the same length and

Figure 3.5 Assumed flux and current penetration within a lamination whose thickness exceeds twice skin depth.

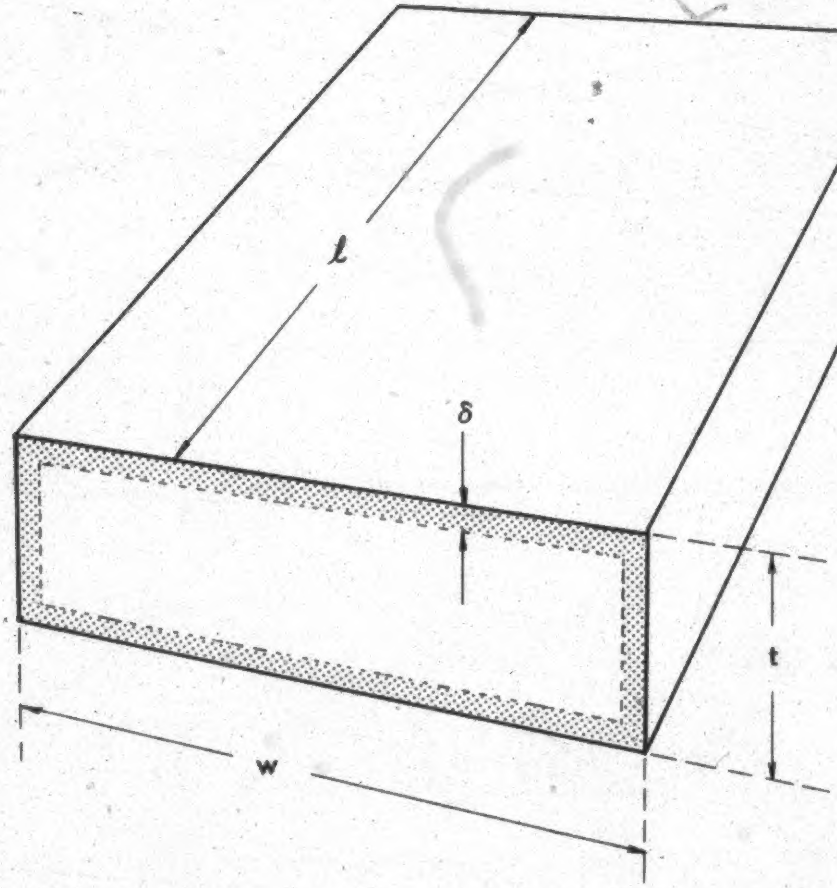

ℓ
δ
t
w

width, but with thickness $t = 2\delta$. Substitution of this value for t into equation 3.25 yields an expression for the total squared magnetic moment of a circuit element with N such laminations

$$m_{Nn}^2 = \frac{8NkT\Delta f \ell w \delta^3}{3\rho} \tag{3.32}$$

Since flux is assumed to penetrate only to a depth δ, the effective total cross-section for magnetic flux is

$$A_m' = 2N\delta w \tag{3.33}$$

Therefore the noise flux, given a total reluctance $\mathcal{R}$ is

$$\begin{aligned} \phi_n' &= \frac{m_{Nn}}{A_m'\mathcal{R}} \\ &= \left(\frac{8NkT\Delta f \ell w\delta^3}{3\rho}\right)^{1/2}\left(\frac{1}{2N\delta w\mathcal{R}}\right) \\ &= \frac{1}{\mathcal{R}}\left(\frac{kT\Delta f \ell}{3\rho A_m}\right)^{1/2}\left(\frac{2\delta A_m}{Nw}\right)^{1/2} \end{aligned} \tag{3.34}$$

Since the total cross-sectional area of the core is $A = Ntw$

$$\phi_n' = \frac{1}{\mathcal{R}}\left(2\delta t\right)^{1/2}\left(\frac{kT\Delta f \ell}{3\rho A_m}\right)^{1/2} \tag{3.35}$$

When $t = 2\delta$, this equation reduces to Eq. 3.30 as expected. Substitute the same numerical values for k, T, and ρ.

$$\phi_n' = 6.70 \times 10^{-8}\,\frac{\sqrt{\delta t}}{\mathcal{R}}\left(\frac{\ell}{A_m}\Delta f\right)^{1/2} \text{webers} \tag{3.36}$$

3.3.5 Noise in Ferrite Cores

In ferrites, eddy currents are only of secondary importance because of the low conductivity, especially at low frequencies. Hysteresis losses, like those of metallic ferromagnetics, cease to be important at vanishingly small alternating magnetic fields.

Consider a section of ferrite core of length ℓ and cross-sectional area A_m connected magnetically in series with a lossless and noiseless section of core, similar to the arrangement in Figure 3.2. Let total magnetic circuit reluctance be $\mathcal{R}$. The residual loss resistance R_r, referred to a signal coil wound on the core, can then be found from the effective residual loss angle δ_{re}. For a coil of inductance L the residual loss resistance is

$$\begin{aligned} R_r &= \omega L \tan \delta_{re} \\ &= \omega L \frac{\tan \delta_r}{\mu_i} \left(\frac{\ell}{\mathcal{R} A_m \mu_0} \right) \qquad (3.37) \end{aligned}$$

where: $\omega = 2\pi f$

δ_r = intrinsic residual loss angle of the ferrite material

μ_i = initial permeability of the ferrite.

The inductance of a coil of n turns wound about a magnetic circuit with total reluctance $\mathcal{R}$ is

$$L = \frac{n^2}{\mathcal{R}} \qquad (3.38)$$

Substituting this expression into Eq. 3.37 one obtains

$$R_r = \frac{\omega n^2 \ell \tan\delta_r}{\mathcal{R}^2 A_m \mu_0 \mu_i} \qquad (3.39)$$

From Eq. 3.14, the Johnson noise voltage generated across this resistance would be

$$e_n = 1.27 \times 10^{-10} \left(R_r \Delta f\right)^{1/2} \text{ volts} \qquad (3.40)$$

and this is equivalent to a noise flux

$$\phi_n = \frac{e_n}{\omega n}$$

$$= \left(\frac{1.27 \times 10^{-10}}{\omega n}\right) \left(\frac{\omega n^2 \ell \Delta f \tan\delta_r}{\mathcal{R}^2 A_m \mu_0 \mu_i}\right)^{1/2} \text{ webers}$$

$$= 4.52 \times 10^{-8} \, \mathcal{R}^{-1} \left\{\left(\frac{\tan\delta_r}{\mu_i}\right) \frac{\ell \Delta f}{A_m f}\right\}^{1/2} \qquad (3.41)$$

Ferrite materials with $\tan\delta_r = 1.4 \times 10^{-3}$ and $\mu_i = 2200$ are available (Siemens specifications for their type N28 material at frequencies below 1000 Hz). Therefore noise flux becomes

$$\phi_n = \frac{3.61 \times 10^{-11}}{\mathcal{R}} \left(\frac{\ell}{A_m} \frac{\Delta f}{f}\right)^{1/2} \text{webers} \qquad (3.42)$$

The graph in Figure 3.6 shows the spectral density of conduction electron noise for moly-permalloy cores of the indicated lamination thicknesses, and residual noise for ferrite cores, as given by Eqs. 3.31, 3.36 and 3.42. Typical values are taken for operating

Figure 3.6 Noise flux as a function of ratio of length to cross-sectional area of magnetic circuit for laminated moly-permalloy and ferrite cores.

$f = 100$ Hz

$\Delta f = 0.1$ Hz

$\mathcal{R} = 10^6$ A/Wb

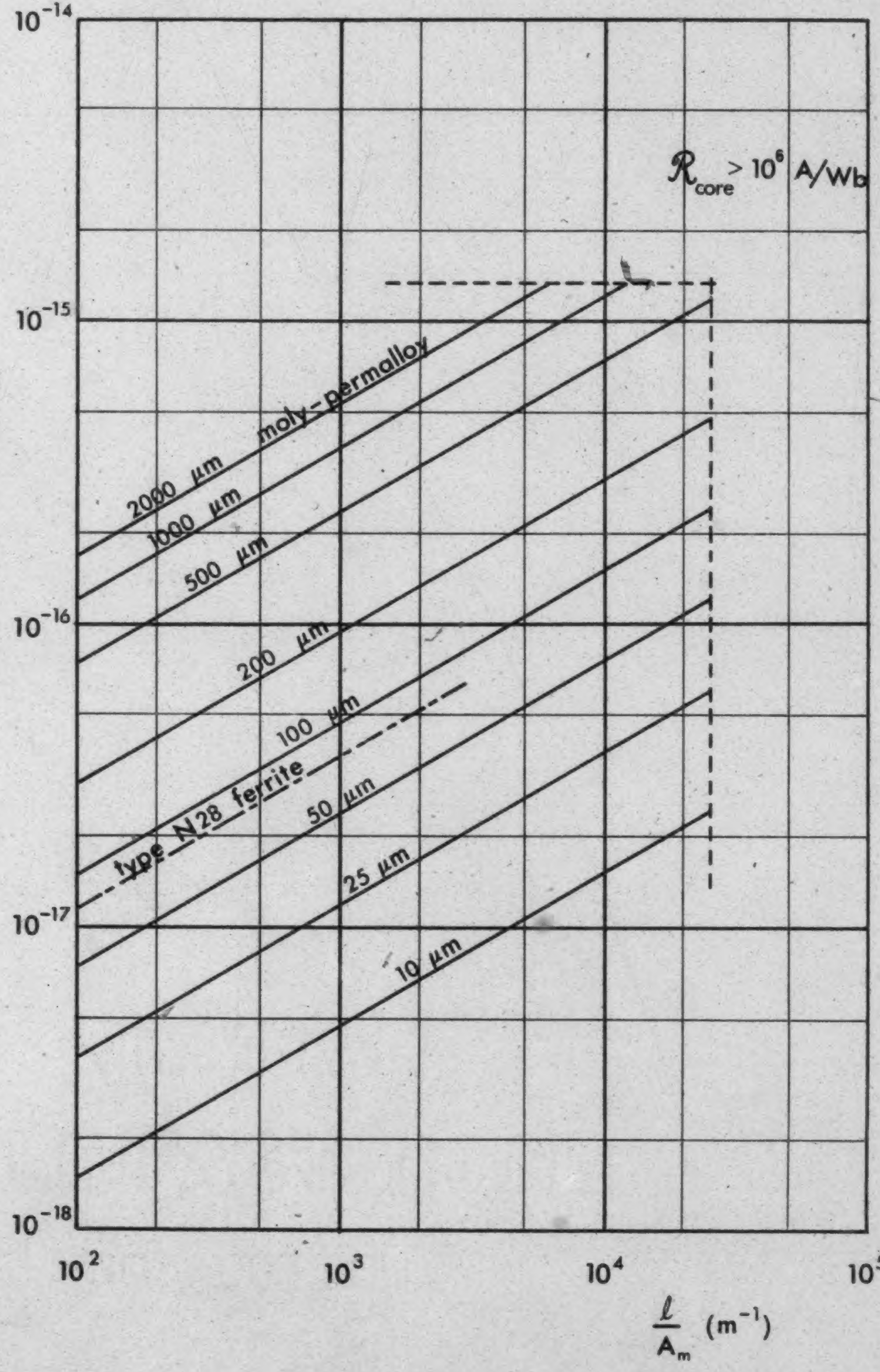

$\mathcal{R}_{core} > 10^6$ A/Wb
Noise flux (Wb)
10^{-14}
10^{-15}
10^{-16}
10^{-17}
10^{-18}
10^2
10^3
10^4
10^5
$\frac{l}{A_m}$ (m^{-1})
moly-permalloy
2000 μm
1000 μm
500 μm
200 μm
100 μm
type N28 ferrite
50 μm
25 μm
10 μm

frequency and total reluctance. The curves are drawn up to that value of ℓ/A_m which would make the total reluctance of the core-under-test equal to the assumed total reluctance of 10^6 amperes/weber.

Note the closer spacing of the moly-permalloy curves where lamination thickness exceeds twice the skin depth. The skin depth is given by

$$\delta = \left(\frac{\rho}{\pi f \mu_o \mu_r}\right)^{1/2} \qquad (3.43)$$

For moly-permalloy with $\mu_r = 2 \times 10^4$ and $\rho = 6 \times 10^{-7}$ ohm meters, the skin depth at $f = 100$ Hz is

$$\delta = \frac{6 \times 10^{-7}}{(\pi)(100)(4\pi \times 10^{-7})(2 \times 10^4)} \text{ meters}$$

$$= 2.8 \times 10^{-4} \text{ meters} \qquad (3.44)$$

3.3.6 Excess Noise Due to Magnetic Viscosity in Cores

This section has considered thermally-generated magnetic fluctuations for cores assumed to be in thermodynamic equilibrium. In general, however, after a macroscopic change of magnetic state, a ferromagnetic material takes a finite period of time to return to thermodynamic equilibrium. This effect manifests itself as a lag, or magnetic viscosity (Bozorth, 1951) which is not due to eddy currents. While the magnetization is decaying to its stable value, excess noise is evident. This may continue for a period of hours after a large change in magnetization. To minimize this form of excess noise, it is necessary to avoid large changes in magnetization, especially in the high-reluctance portions of the magnetic circuit, if maximum sensitivity will be required soon after.

3.4 Sensitivity of the Basic Instrument

Sensitivity of the basic instrument is now calculated, based on the assumption that thermal noise from the copper signal coil is the dominant noise component. From Eq. 3.11 for rms signal flux and Eq. 3.18 for rms noise-flux-equivalent of the Johnson noise of the coil, one can derive an expression for signal-to-noise ratio.

$$\frac{\phi_s}{\phi_n} = \frac{5.41 \times 10^{-6}}{7.69 \times 10^{-15}} \; \frac{f \ell^{1/2} \left(\ln \frac{r_2}{r_1}\right)^{1/2} \Delta\kappa}{\Delta f^{1/2}}$$

$$= 7.03 \times 10^{8} \; f \Delta\kappa \left\{ \frac{\ell \ln \frac{r_2}{r_1}}{\Delta f} \right\}^{1/2} \qquad (3.45)$$

Of the parameters in Eq. 3.45, dimensions ℓ and r_2 are limited by the necessity to keep the instrument down to a reasonable size and cost, while r_1 is limited by the saturation of the magnetic core material. Frequency f is fundamentally limited by the structural integrity of the rock specimen and shaft materials. A rotational speed of 200 rps, hence a signal frequency of 400 Hz, is possible.

However, to avoid the more careful balancing required at higher speeds, a rotational speed of around 50 Hz is desirable for routine observations. Bandwidth Δf is limited by the time required to complete a single observation. Signal integrating times up to about 15 minutes can be useful since they restrict effective bandwidth to about 10^{-3} Hz. For reasonably fast observations, however, an integrating time of about 10 seconds is preferable. All sensitivities are therefore calculated for a signal frequency of 100 Hz and a bandwidth of 0.1 Hz. The capability for high rotational speeds and long integrating times is nevertheless built into the instrument for use with extremely weak or small specimens, or for measurements at low field intensities. If one limits the dimensions to:

$$\ell = 0.2 \text{ meters}$$
$$r_2 = 0.12 \text{ meters} \qquad (3.46)$$
$$r_1 = 0.05 \text{ meters}$$

then the corresponding signal-to-noise ratio is

$$\frac{\phi_s}{\phi_n} = (7.03 \times 10^8)(100)\left(\frac{0.2 \ \ln 2.4}{10^{-1}}\right)^{1/2} \Delta\kappa$$

$$= 9.30 \times 10^{10}\ \Delta\kappa \qquad (3.47)$$

Signal amplitude must at least equal noise amplitude to be detectable. Thus one can detect a susceptibility anisotropy

$$\Delta\kappa_{min} = 1.08 \times 10^{-11} \text{ mksu} \quad (0.86 \times 10^{-12} \text{ emu/cc}) \qquad (3.48)$$

One can now determine how thinly the sensor's magnetic core needs to be laminated in order that noise due to thermally excited conduction electrons within the core material not become a dominant source of noise. Taking the thin-lamination worst case,

$$\begin{aligned} A_m &= \pi r_1^2 = 7.85 \times 10^{-3} \text{ meter}^2 \\ \ell &= 0.2 \text{ meters} \qquad\qquad (3.49) \\ \mathcal{R} &= 2.18 \times 10^6 \text{ A/Wb} \quad \text{(from Eqs. 3.6 and 3.7)} \\ \Delta f &= 10^{-1} \text{ Hz} \\ \phi_n &= 5.82 \times 10^{-17} \text{ Wb} \quad \text{(from Eqs. 3.11 and 3.48)} \end{aligned}$$

Define critical lamination thickness t_c as that thickness which would make the noise from thermally-excited conduction electrons in the magnetic material equal to Johnson noise from the signal coil. Then

$$\begin{aligned} t_c &= \frac{\phi_n \mathcal{R}}{4.74 \times 10^{-8}} \left(\frac{A_m}{\ell \Delta f}\right)^{1/2} \\ &= \frac{(5.82 \times 10^{-17})(2.18 \times 10^6)}{4.74 \times 10^{-8}} \left(\frac{7.85 \times 10^{-3}}{0.2 \times 10^{-1}}\right)^{1/2} \\ &= 1.67 \times 10^{-3} \text{ meters} \qquad\qquad (3.50) \end{aligned}$$

Therefore using laminations of thickness less than about 0.5 mm would keep noise from the magnetic circuit negligible.

One drawback of the configuration in Figure 3.1 is that it is unbalanced with respect to external interfering magnetic fields. Although the high-permeability shell type of magnetic circuit affords considerable shielding, the shielding factor is not sufficient for the magnitude of magnetic fields expected, especially of those synchronous with the signal. Considerable advantage is gained by using balanced sensors which can be adjusted to null out response to interfering fields. Such arrangements are discussed in the following sections.

3.5 Design of Magnetic Bridge

It can be seen from Eq. 3.45 that if the inner and outer radii r_1 and r_2 of the sensing coil are reduced in the same proportion, sensitivity is not impaired. The reduced coil dimensions would allow a pair of coils to be arranged in a balanced configuration to null out effects of external fields. It is, however, necessary to ensure that a reduction in r_1 does not cause saturation of the magnetic cores of the signal coils. This latter requirement can be met by arranging the main magnetic circuit in a bridge configuration as illustrated in Figure 3.7. Thus only a slight off-balance direct magnetic flux passes through the magnetic cores about which the signal coils are wound. This configuration also makes the signal coils balanced with respect to external fields normal to the axis of the specimen gap.

To calculate the peak-to-peak flux variation $\Delta_1\phi$

Figure 3.7 Plan view of a bridge configuration of the magnetic circuit.

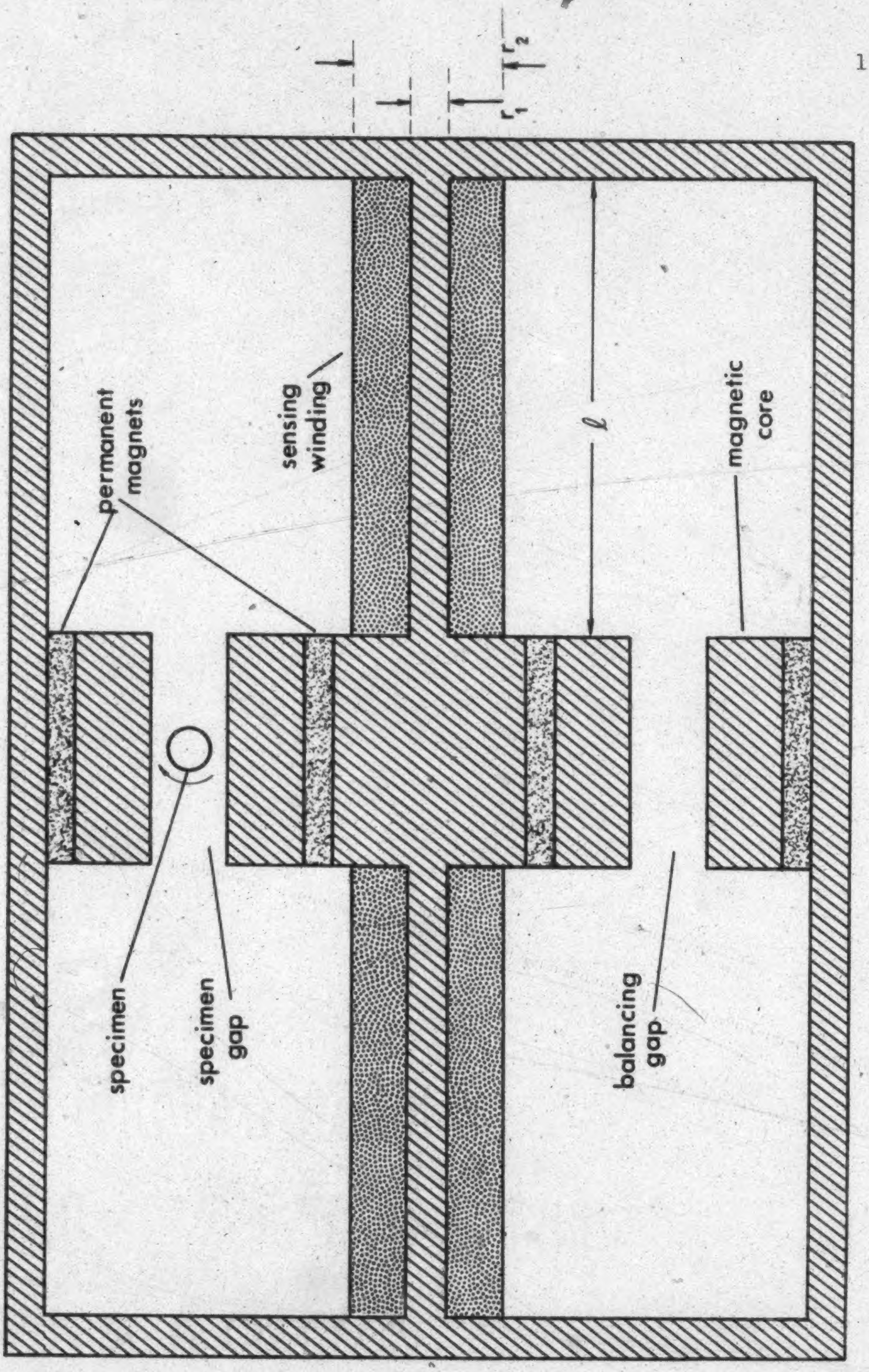
r_2
r_1
permanent magnets
sensing winding
ℓ
magnetic core
specimen
specimen gap
balancing gap

Figure 3.8 Electrical equivalent of the bridge configuration of the magnetic circuit.

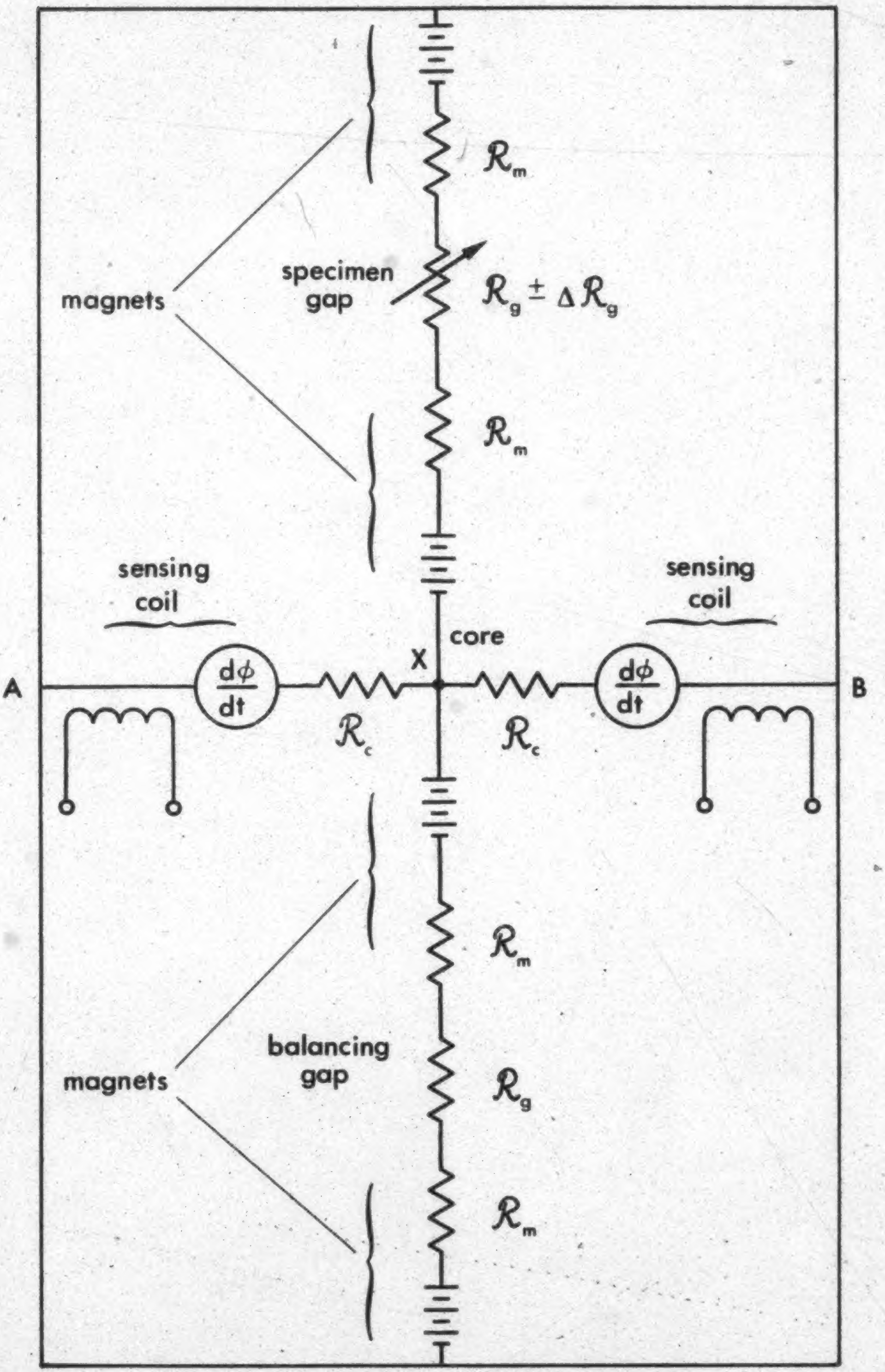

$\mathcal{R}_m$
magnets
specimen gap
$\mathcal{R}_g \pm \Delta\mathcal{R}_g$
$\mathcal{R}_m$
sensing coil
sensing coil
core
X
A
$\frac{d\phi}{dt}$
$\frac{d\phi}{dt}$
B
$\mathcal{R}_c$
$\mathcal{R}_c$
$\mathcal{R}_m$
magnets
balancing gap
$\mathcal{R}_g$
$\mathcal{R}_m$

analogous to $\Delta\phi$ in Eq. 3.10, one must consider the reluctance of the balancing gap and the now-finite reluctances of the signal coil cores in parallel. The combined reluctance is in series with the reluctance of the specimen gap. Therefore

$$\Delta_1\phi = \phi_0 \frac{\Delta\mathcal{R}_g}{2\mathcal{R}_m + \mathcal{R}_g + \left[(2\mathcal{R}_m + \mathcal{R}_g) \parallel \frac{1}{2}\mathcal{R}_c\right]} \tag{3.51}$$

Furthermore only part of $\Delta_1\phi$ passes through the signal sensing coil. Call this part $\Delta_2\phi$. The remainder $(\Delta_1\phi - \Delta_2\phi)$ passes through the balancing gap. Therefore

$$\begin{aligned} \Delta_2\phi &= \Delta_1\phi \left\{ \frac{\frac{1}{2}\mathcal{R}_c \parallel (2\mathcal{R}_m + \mathcal{R}_g)}{\frac{1}{2}\mathcal{R}_c} \right\} \\ &= \Delta_1\phi \left\{ \frac{2\mathcal{R}_m + \mathcal{R}_g}{2\mathcal{R}_m + \mathcal{R}_g + \frac{1}{2}\mathcal{R}_c} \right\} \end{aligned} \tag{3.52}$$

Combining Eqs. 3.51 and 3.52 one obtains

$$\begin{aligned} \Delta_2\phi &= \phi_0 \left\{ \frac{\Delta\mathcal{R}_g}{2\mathcal{R}_m + \mathcal{R}_g + \left[(2\mathcal{R}_m + \mathcal{R}_g) \parallel (\frac{1}{2}\mathcal{R}_c)\right]} \right\} \left\{ \frac{2\mathcal{R}_m + \mathcal{R}_g}{2\mathcal{R}_m + \mathcal{R}_g + \frac{1}{2}\mathcal{R}_c} \right\} \\ &= \phi_0 \left\{ \frac{\Delta\mathcal{R}_g}{2\mathcal{R}_m + \mathcal{R}_g + \dfrac{(2\mathcal{R}_m + \mathcal{R}_g)(\frac{1}{2}\mathcal{R}_c)}{2\mathcal{R}_m + \mathcal{R}_g + \frac{1}{2}\mathcal{R}_c}} \right\} \left\{ \frac{2\mathcal{R}_m + \mathcal{R}_g}{2\mathcal{R}_m + \mathcal{R}_g + \frac{1}{2}\mathcal{R}_c} \right\} \\ &= \phi_0 \left\{ \frac{\Delta\mathcal{R}_g}{2\mathcal{R}_m + \mathcal{R}_g + \mathcal{R}_c} \right\} \end{aligned} \tag{3.53}$$

The direct flux is given by

$$\phi_0 = B_0 A_0 (1 + \xi_g)$$

$$= (0.115 \text{ tesla})(2.32 \times 10^{-2} \text{ meter}^2)(1.45)$$

$$= 3.87 \times 10^{-3} \text{ webers} \qquad (3.54)$$

The values of $\mathcal{R}_m$, $\mathcal{R}_g$, and $\Delta\mathcal{R}_g$ are substituted from Eqs. 3.6, 3.7 and 3.8, respectively. Then

$$\Delta_2\phi = (3.87 \times 10^{-3} \text{ Wb}) \frac{(8.63 \times 10^3 \ \Delta\kappa \text{ A/Wb})}{(2.18 \times 10^6 + \mathcal{R}_c \text{ A/Wb})}$$

$$= \frac{33.4 \ \Delta\kappa}{2.18 \times 10^6 + \mathcal{R}_c} \text{ webers} \qquad (3.55)$$

If $\mathcal{R}_c$ is small relative to $\mathcal{R}_m$ and $\mathcal{R}_g$, the signal flux variation is

$$\phi_s = \frac{\Delta_2\phi}{2\sqrt{2}}$$

$$= 5.41 \times 10^{-6} \ \Delta\kappa \text{ webers} \qquad (3.56)$$

From Eqs. 3.15 and 3.17 it can be seen that signal coil resistance, and hence noise voltage, is decreased by decreasing core cross section πr_1^2 or by increasing its length ℓ, both of which increase its reluctance $\mathcal{R}_c$. One can determine an optimum value for $\mathcal{R}_c$, given that the core cross-section is kept constant and only its length is varied. This optimum is nevertheless close to optimum values obtained by varying other parameters. From Eq. 3.55 signal flux shows a proportionality

$$\phi_s \propto (2.18 \times 10^6 + \mathcal{R}_c)^{-1} \qquad (3.57)$$

Similarly, from Eq. 3.18 for noise flux

$$\phi_n \propto \ell^{-\frac{1}{2}} \propto \mathcal{R}_c^{-\frac{1}{2}} \tag{3.58}$$

Combining Eqs. 3.57 and 3.58 yields

$$\frac{\phi_s}{\phi_n} \propto \frac{\mathcal{R}_c^{\frac{1}{2}}}{2.18 \times 10^6 + \mathcal{R}_c} \tag{3.59}$$

Therefore

$$\frac{d}{d\mathcal{R}_c}\left(\frac{\phi_s}{\phi_n}\right) = \frac{(2.18 \times 10^6 + \mathcal{R}_c)(\frac{1}{2}\mathcal{R}_c^{-\frac{1}{2}}) - \mathcal{R}_c^{\frac{1}{2}}}{(2.18 \times 10^6 + \mathcal{R}_c)^2}$$

$$= 0 \quad \text{(for maximum sensitivity)}$$

Hence

$$\mathcal{R}_c' = 2.18 \times 10^6 \quad \text{A/Wb} \tag{3.60}$$

Then from Eq. 3.55, signal flux is

$$\phi_s = \frac{\Delta_2 \phi}{2\sqrt{2}}$$

$$= 2.71 \times 10^{-6}\, \Delta\kappa \quad \text{webers} \tag{3.61}$$

If the signal coil's core is cylindrical as before, its reluctance is given by

$$\mathcal{R}_c = \frac{\text{(length of core)}}{\text{(cross-sectional area of core)}(\mu_0 \mu_r)} \tag{3.62}$$

where μ_r is the relative reversible permeability of the core material. It is about 2×10^4 for moly-permalloy, given a direct flux density ≤ 0.1 tesla. Thus if the cross-sectional area of the core is restricted to, say, 1.0 cm^2, the reluctance is

$$\mathcal{R}_c = \frac{\ell}{(10^{-4} m^2)(4\pi \times 10^{-7} \text{ Wb/A}\cdot\text{m})(2 \times 10^4)}$$

$$= 3.98 \times 10^5 \ \ell \ \text{A/Wb} \tag{3.63}$$

Taking $\mathcal{R}_c$ to the limit determined in Eq. 3.60,

$$3.98 \times 10^5 \ell = 2.18 \times 10^6$$

$$\ell = 5.48 \text{ meters} \tag{3.64}$$

This core length is too large to be practical for a cylindrical sensing coil. Since a considerably shorter length must be used, core reluctance $\mathcal{R}_c$ becomes negligible with respect to $(2\mathcal{R}_m + \mathcal{R}_g)$. Therefore signal flux is found from Eq. 3.56.

$$\phi_s = 5.41 \times 10^{-6} \Delta\kappa \text{ webers} \tag{3.65}$$

By inspection of Eq. 3.18 for the flux-equivalent of the thermal noise of a cylindrical solenoid, it can be seen that there is little point in making r_2 larger than about 10 r_1. Therefore substitute into Eq. 3.18 the values:

$$\begin{aligned} f &= 100 \text{ Hz} \\ \ell &= 0.2 \text{ m} \\ r_2 &= 5 \times 10^{-2} \text{ m} \\ r_1 &= 5 \times 10^{-3} \text{ m} \end{aligned} \tag{3.66}$$

A factor of $\sqrt{2}$ is included for summing noise due to both coils.

$$\phi_n = (\sqrt{2})(7.69 \times 10^{-15})(10^{-2}) \left(\frac{10^{-1}}{(0.2)(\ln 10)}\right)^{\frac{1}{2}} \text{ webers}$$

$$= 5.06 \times 10^{-17} \text{ webers} \qquad (3.67)$$

From Eqs. 3.65 and 3.67, signal-to-noise ratio is

$$\frac{\phi_s}{\phi_n} = \frac{5.41 \times 10^{-6}\Delta\kappa}{5.06 \times 10^{-17}}$$

$$= 1.07 \times 10^{11}\Delta\kappa \qquad (3.68)$$

Thus the minimum detectable susceptibility anisotropy, as limited by Johnson noise, is

$$\Delta\kappa_{min} = 0.94 \times 10^{-11} \text{ mksu} \quad (0.75 \times 10^{-12} \text{ emu/cc}) \qquad (3.69)$$

The critical lamination thickness is now calculated assuming a signal coil inner radius of 0.5 cm and length of 20 cm. The reluctance of the magnetic circuit as "seen" by the signal cores is just that of the specimen gap assembly and the balancing gap assembly in parallel.

$$\mathcal{R} = \mathcal{R}_m + \frac{1}{2}\mathcal{R}_g$$

$$= 1.09 \times 10^{6} \text{ A/Wb} \qquad (3.70)$$

Then from Eqs. 3.31 and 3.67 one obtains

$$t_c = \frac{\phi_n \mathcal{R}_o}{4.74 \times 10^{-8}}\left(\frac{A_m}{\ell\Delta f}\right)^{\frac{1}{2}}$$

$$= \frac{(5.06 \times 10^{-17})(1.09 \times 10^{6})}{4.74 \times 10^{-8}} \left\{\frac{2\pi(5 \times 10^{-3})^2}{0.2 \times 10^{-1}}\right\}^{\frac{1}{2}}$$

$$= 1.03 \times 10^{-4} \text{ meters} \tag{3.71}$$

Thus a lamination thickness of about 100 microns or less would be required. It can be seen from the graph in Figure 3.6 that Siemens' type N28 ferrite material would also suffice.

3.6 Design of a Magnetic Helix

It was noted in the previous section that the sensitivity of the bridge configuration was limited by the maximum practicable sensing coil length. A value of 0.2 meters was used. If this length were increased without changing the ratio of coil radii $\frac{r_2}{r_1}$, the decreased coil resistance would result in a decrease in Johnson noise. By a sufficient increase in magnetic core radius and decrease in lamination thickness, the core noise could be reduced in the same proportion. The limitation of maximum coil length could be avoided if the magnetic core for the signal coil were wrapped into a helical shape. This geometry would also permit more efficient use of the copper wire since, instead of winding a coil around each helix element, a toroidal winding would be put around the entire magnetic helix.

The geometry described above is shown with generalized dimensions in Figure 3.9. The helical core would be divided into two halves. The adjacent core ends would be

Figure 3.9 Generalized configuration of a magnetic helix.

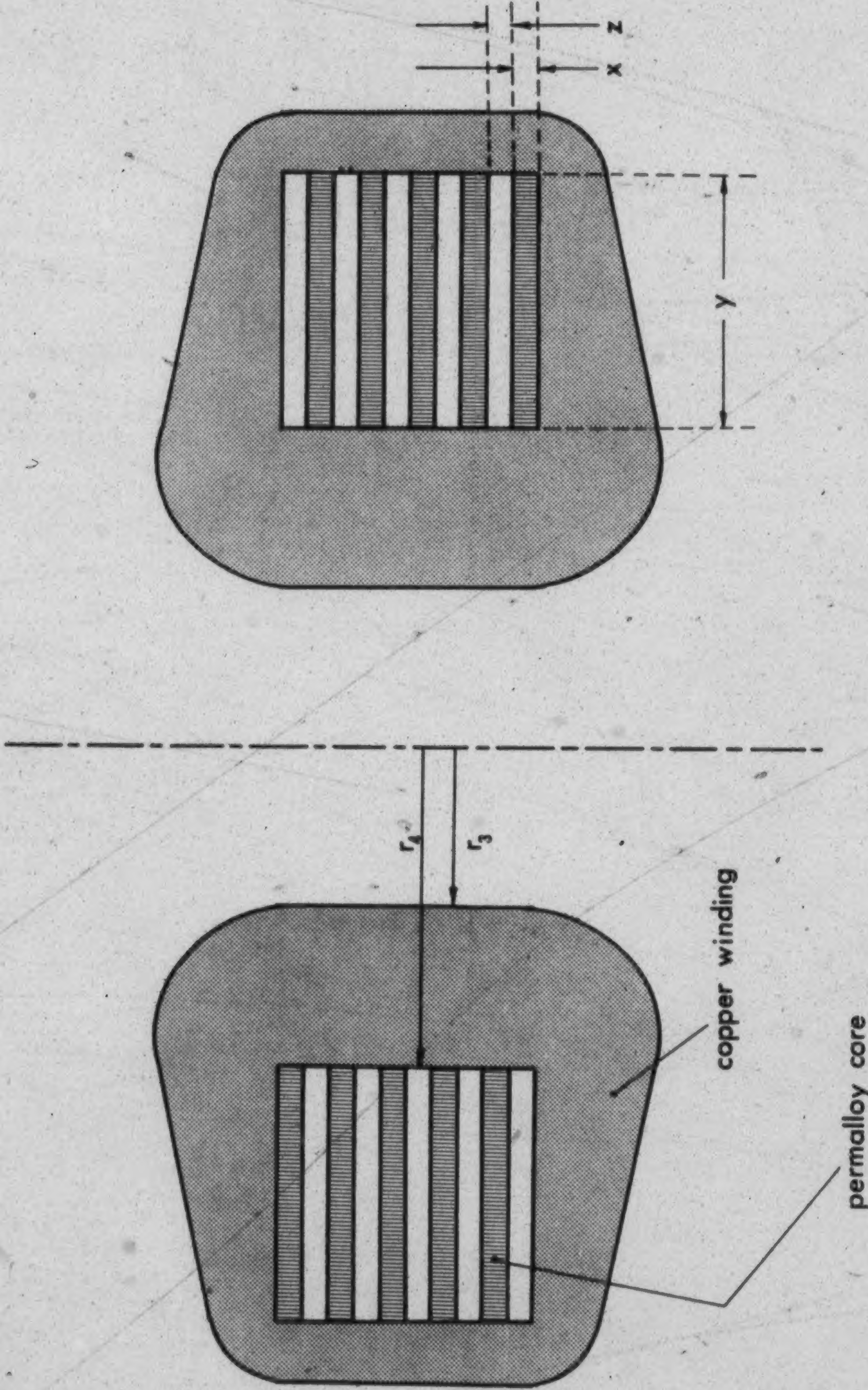
z
x
y
r_4
r_3
copper winding
permalloy core

joined together and connected to point X in the bridge circuit shown in Figure 3.8. The opposite core ends would be joined to points A and B shown in the same diagram. The two halves of the helix, each with N turns, should be wound in opposite directions - one clockwise and one counterclockwise. This is because, due to the bridge configuration, the two halves of the signal flux $\Delta_2\phi$ would pass through the helix in opposite directions.

3.6.1 Optimization of Johnson and Magnetic Noise

It can be seen from Eq. 3.17 that Johnson noise is made smaller by increasing core length ℓ and by decreasing core radius r_1, and hence its cross-sectional area A_m. However, it can be seen from the graph in Figure 3.6 that the resultant increase in $\frac{\ell}{A_m}$ will increase magnetic noise for any given lamination thickness. Therefore the helix dimensions are a compromise between Johnson noise and magnetic core noise. The critical lamination thickness for the bridge solenoids discussed in Section 3.5 was shown to be about 100 microns (Eq. 3.71). Inspection of Figure 3.6 shows that an improvement of 4:1 in sensitivity, as limited by magnetic core noise, might be obtained by using 25-micron laminations and the same ratio $\frac{\ell}{A_m}$. For thinner laminations micro-eddy currents and other noise-producing mechanisms become dominant and prevent further improvement in sensitivity. To gain an equivalent decrease in Johnson noise, it would be necessary to decrease coil resistance by a factor of about 16. The more efficient use of copper around a helical core would also contribute. However, the increase in core length would require a proportionate increase in cross-sectional area if the ratio $\frac{\ell}{A_m}$ were to be kept constant. Therefore the core volume ℓA_m would increase rapidly. This increased volume would set a practical limit to increased sensitivity.

The factor $\frac{\ell}{A_m}$ for the bridge solenoids discussed in Section 3.5 is

$$\frac{\ell}{A_m} = \frac{0.2 \text{ m}}{2\pi(5 \times 10^{-3})^2 \text{ m}^2}$$

$$= 1.27 \times 10^{3} \text{ m}^{-1} \qquad (3.72)$$

Since noise flux due to the magnetic core is proportional to lamination thickness and to $\left(\frac{\ell}{A_m}\right)^{\frac{1}{2}}$ as shown in Eq. 3.31, it follows from Eqs. 3.67, 3.71 and 3.72 that a reduction in lamination thickness to 25 microns would make noise flux due to the core equal to

$$\phi_{nM} = (5.06 \times 10^{-17} \text{ Wb})\left(\frac{0.25 \times 10^{-4} \text{ m}}{1.03 \times 10^{-4} \text{ m}}\right)\left(\frac{\ell}{1.27 \times 10^{3} A_m}\right)^{\frac{1}{2}}$$

$$= 3.45 \times 10^{-19} \left(\frac{\ell}{A_m}\right)^{\frac{1}{2}} \text{ Wb} \qquad (3.73)$$

To a first approximation, the core length ℓ of each half of the helix is

$$\ell \sim 2\pi r_4 N \tag{3.74}$$

For the most efficient use of the copper wire on the toroidal coil, the helix cross-section should be made nearly square. That is,

$$y = 2N(x + z) \tag{3.75}$$

For low coil resistance, helix turn-separation z should be minimized. It cannot be made very small because inter-turn flux leakage would become considerable. We arbitrarily set $z = x$ in order to minimize its effect on coil resistance. The resulting leakage will be determined in Section 3.6.2. Thus Eq. 3.75 becomes

$$y = 4Nx \tag{3.76}$$

Substituting Eqs. 3.74 and 3.76 into Eq. 3.73,

$$\begin{aligned} \phi_{nM} &= 3.45 \times 10^{-19} \left(\frac{\ell}{2xy} \right)^{\frac{1}{2}} \\ &= 3.45 \times 10^{-19} \left(\frac{2\pi r_4 N}{y^2/2N} \right)^{\frac{1}{2}} \\ &= 1.22 \times 10^{-18} \frac{(r_4)^{\frac{1}{2}} N}{y} \end{aligned} \tag{3.77}$$

We now determine the helix dimensions required to reduce the noise-flux-equivalent of Johnson noise to this same level. The electrical resistance of the copper toroid is

$$R_c = \frac{\rho}{q} \left(\frac{\text{length of a single turn}}{\text{coil cross-section}} \right) n^2 \tag{3.78}$$

where: ρ = resistivity of copper

= 1.724×10^{-8} ohm m @ 20°C

q = filling factor = 0.75, say.

Since we have assumed a square cross-section, the coil resistance is approximately

$$R_c = \frac{1.724 \times 10^{-8}}{0.75}\left(\frac{4y}{\pi(r_4^2 - r_3^2)}\right)n^2$$

$$= 2.93 \times 10^{-8} \frac{n^2 y}{r_4^2 - r_3^2} \text{ ohms} \tag{3.79}$$

A lower limit on coil inner radius r_3 would be set by difficulty in applying the toroidal winding. If we arbitrarily set $r_3 = r_4/2$, coil resistance would be

$$R_c = 3.91 \times 10^{-8} \frac{n^2 y}{r_4^2} \text{ ohms} \tag{3.80}$$

Therefore the noise-flux-equivalent of Johnson noise is

$$\phi_{nJ} = \frac{e_n}{\omega N n}$$

$$= \frac{\sqrt{4kTR_c\Delta f}}{\omega N n}$$

$$= \frac{\left[4(1.38 \times 10^{-23})(3.91 \times 10^{-8})(y \times 10^{-1})(293)\right]^{\frac{1}{2}} \frac{n}{r_4}}{(2\pi \times 10^2)Nn}$$

$$= 1.26 \times 10^{-17} \frac{y^{1/2}}{r_4 N} \text{ webers} \tag{3.81}$$

If we arbitrarily set maximum helix radius r_4 to be 10 cm then Eqs. 3.77 and 3.81 become:

$$\phi_{nM} = 3.86 \times 10^{-19} \frac{N}{y} \text{ webers} \qquad (3.82)$$

$$\phi_{nJ} = 1.26 \times 10^{-16} \frac{y^{1/2}}{N} \text{ webers} \qquad (3.83)$$

If these two noise contributions are to be equal in magnitude, we obtain

$$\frac{N^2}{y^{3/2}} = \frac{1.26 \times 10^{-16}}{3.86 \times 10^{-19}}$$

$$= 326$$

$$= 18.0 \; y^{3/4} \text{ turns} \qquad (3.84)$$

Therefore total noise flux due to each of Johnson noise and magnetic core noise is

$$\phi_n = 3.86 \times 10^{-19} \left(\frac{18.0 \, y^{3/4}}{y} \right)$$

$$= 6.95 \times 10^{-18} \; y^{-1/4} \text{ webers} \qquad (3.85)$$

If we arbitrarily set maximum helix core width y, and hence helix height $4Nx$, to be 8 cm then

$$\phi_n = 1.31 \times 10^{-17} \text{ webers} \qquad (3.86)$$

This is about one quarter of the noise level given by Eq. 3.67 for the dual-solenoid bridge.

3.6.2 Inter-turn Flux Leakage

Setting $y = 8 \times 10^{-2}$ m in Eq. 3.84 gives for the number of turns on each half of the helix:

$$N = 2.71 \tag{3.87}$$

Therefore the total number of turns on the helix would be 5.42. The relative flux leakage which would result from the relatively low-reluctance leakage path between the turns can be estimated by comparing the leakage reluctance between two adjacent turns of core with the reluctance of one turn of the core. The leakage reluctance is

$$\begin{aligned} \mathcal{R}_l' &= \frac{\text{length of leakage path}}{\text{area of leakage path}} \left(\frac{1}{\mu_o} \right) \\ &= \frac{z}{(y)(2\pi r_4)(4\pi \times 10^{-7})} \\ &= \frac{x}{(10.84x)(2\pi \times 10^{-1})(4\pi \times 10^{-7})} \\ &= 1.17 \times 10^5 \quad \text{A/Wb} \end{aligned} \tag{3.88}$$

Similarly, core reluctance per turn is

$$\begin{aligned} \mathcal{R}_c' &= \frac{2\pi r_4}{(xy)(\mu_o \mu_r)} \\ &= \frac{(2\pi)\,10^{-1}}{(y^2/10.84)(4\pi \times 10^{-7})(2 \times 10^4)} \\ &= 4.23 \times 10^4 \quad \text{A/Wb} \end{aligned} \tag{3.89}$$

Therefore the leakage factor is

$$\xi_h = \frac{\mathcal{R}_c'}{\mathcal{R}_l' + \mathcal{R}_c'}$$

$$= 0.27 \qquad (3.90)$$

This is an acceptable figure. The actual leakage would be somewhat lower since there is no leakage from the end turns.

3.7 Magnetic Modulators

It can be seen from Eq. 3.45 that the sensitivity of the instrument is directly proportional to the signal frequency, and hence the shaft rotation frequency. The latter is limited by the structural integrity of the rock specimens and by microphonic signals due to the slight imbalance of the specimen on the shaft. It is, however, possible to raise the signal frequency without raising the shaft speed. This is done by modulating the magnetic signal flux at high frequency. This modulation process must be accomplished without transforming the magnetic signal into an electronic one because such transformation would "lock in" the thermal noise due to reasonably-sized signal coils. The process should therefore use a variable reluctance in the magnetic circuit. This may be accomplished electromagnetically, taking advantage of the nonlinear magnetization of ferromagnetic materials, or mechanically, either by changing the dimensions of an air gap by moving a ferromagnetic polepiece, or by elastically straining a ferromagnetic circuit element, changing its permeability through the Villari effect.

A magnetic modulator would allow one to take measurements of bulk susceptibility by taking readings before and after a specimen is introduced into the specimen gap.

3.7.1 Nonlinear Magnetization Modulator

The most sensitive method yet devised for modulating by virtue of nonlinear magnetization of ferromagnetic materials is the second-harmonic type of magnetic modulation. The ferromagnetic core of an inductor is subjected to a symmetrical alternating magnetizing force, and the signal polarizes this core at low frequency (twice the shaft frequency) and distorts the flux wave asymmetrically (see Figure 3.10). In the absence of polarization the flux wave is symmetrical, and in particular contains no second-harmonic component. Polarization upsets the symmetry of the B/H loop (from the point of view of the alternating flux drive) and introduces a second-harmonic term into the flux waveform. This term is proportional to the polarization and reverses in phase when the polarization is reversed (Williams and Noble, 1950).

It can be shown that if triangular-wave modulation is used, and if one assumes the idealized magnetization curve of Figure 3.10 with the effects of eddy currents and hysteresis completely negligible, then the rms second-harmonic output for rms signal flux ϕ_s is

$$e_2 = -8n\phi_s f \sin(\pi \frac{H_{sat}}{\hat{H}}) \sin 4\pi ft \qquad (3.91)$$

where: f = modulator driving frequency

H_{sat} = saturation field intensity of the core material

$\hat{H}$ = peak modulating field intensity

n = number of turns on sensing coil.

Substituting from Eq. 3.56, rms signal becomes

$$e_2 = -8n\ (5.41 \times 10^{-6} \Delta\kappa)\ f \sin(\pi \frac{H_{sat}}{\hat{H}}) \sin 4\pi ft$$

$$= -\ 4.32 \times 10^{-5}\ nAf \sin(\pi \frac{H_{sat}}{\hat{H}}) \sin 4\pi ft \qquad (3.92)$$

Three main sources of noise are present:

1. Modulated thermal noise
2. Direct thermal noise
3. Barkhausen effect.

The modulated thermal noise is that generated by the flow of low-signal-frequency currents in the polepiece laminations. These currents generate signal flux indis-

Figure 3.10 Basic Principles of an idealized second-harmonic-type magnetic modulator.

(A) Assumed reversible magnetization curve.

(B) Drive field intensity, with and without signal polarization.

(C) Core flux density, with and without signal polarization.

(D) Signal coil voltage, with and without signal polarization.

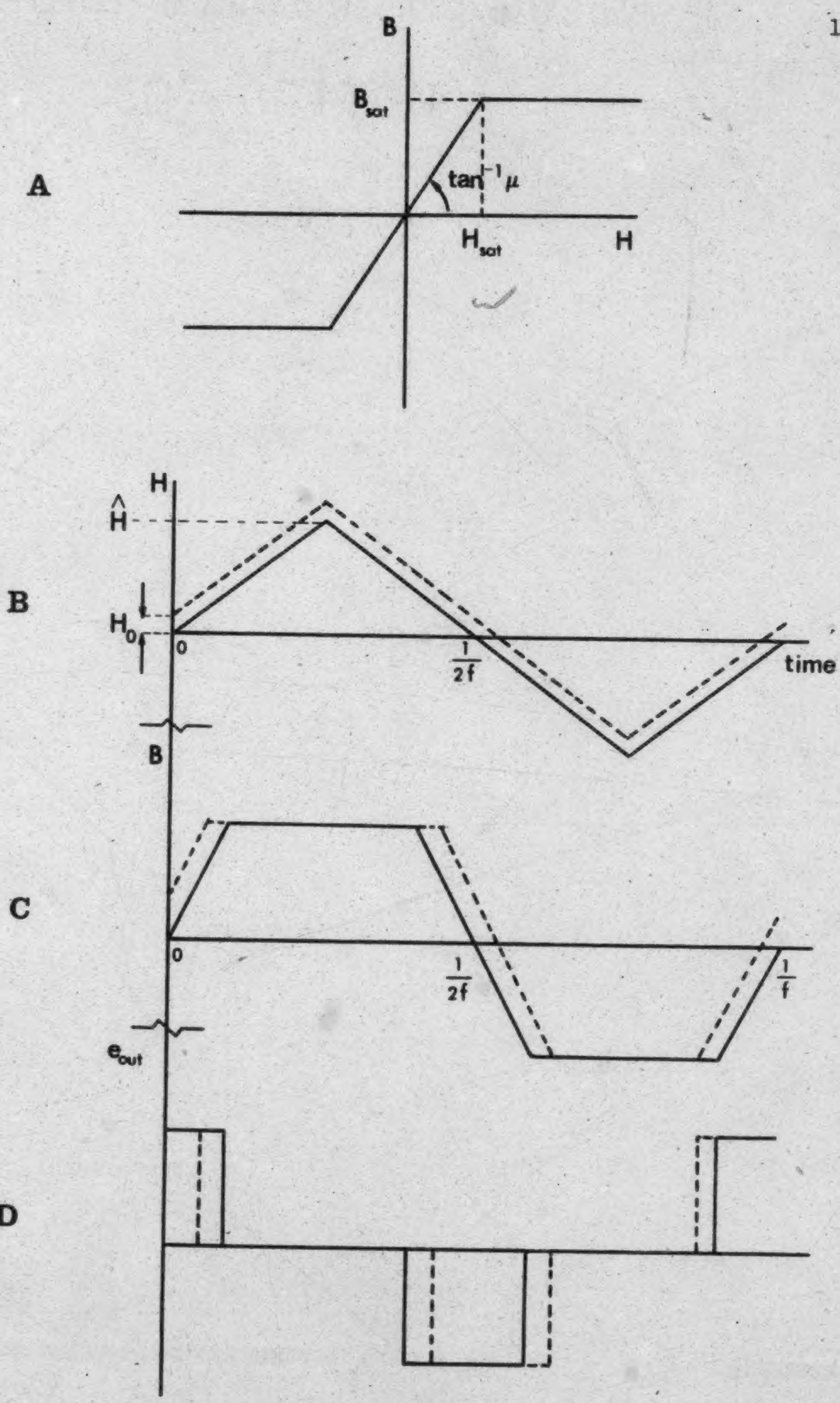
A
B
B_{sat}
$\tan^{-1}\mu$
H_{sat}
H
B
H
$\hat{H}$
H_0
0
$\frac{1}{2f}$
time
B
C
0
$\frac{1}{2f}$
$\frac{1}{f}$
e_{out}
D

tinguishable from that due to the rotating specimen. The effect can be made negligible by suitable lamination of the magnetic circuit, as was discussed in Section 3.3.

The direct thermal noise is that generated by thermal agitation in the resistance and losses of the signal winding at the high signal frequency. It is of the same order of magnitude as that for the direct-sensing coils considered in Section 3.5 but its effects are less because of the high sensitivity of this coil by virtue of the high signal frequency.

Barkhausen noise is that arising from the randomly timed impulses which comprise the essentially discontinuous process of magnetization. The spectral density of Barkhausen noise near the output frequency of a magnetic modulator has been analyzed (Macfarlane, 1950), making several simplifying assumptions. Although no absolute quantity could be predicted, the spectral power density of noise was predicted to be

$$W_n \propto \frac{A_o^2 f^3 s^2}{M} \Theta \qquad (3.93)$$

where: A_o = cross-sectional area of modulator core

M = number of Barkhausen transitions between zero magnetization and saturation s = standard deviation of the instant of occurrence of a particular pulse

$$\Theta = 1 + \frac{\sin(2\pi \frac{H_{sat}}{\hat{H}})}{2\pi \frac{H_{sat}}{\hat{H}}} \tag{3.94}$$

It is assumed that s is inversely proportional to the speed of transition, i.e.

$$s \propto \left|\frac{dH}{dt}\right|^{-1}$$

$$\propto \frac{1}{f\hat{H}} \tag{3.95}$$

It is further assumed that the number of transitions M is proportional to the core volume $A_0 \ell$, where ℓ is modulator core length. Thus Eq. 3.93 becomes

$$W_n \propto \frac{A_0 f}{\ell \hat{H}^2} \Theta \tag{3.96}$$

Since noise voltage is proportional to the square root of noise power,

$$e_n \propto \left(\frac{A_0 f}{\ell} \Theta\right)^{1/2} \frac{1}{\hat{H}} \tag{3.97}$$

and from Eq. 3.92 signal voltage is proportional to

$$e_2 \propto f \Delta \kappa \sin (\pi \frac{H_{sat}}{\hat{H}}) \tag{3.98}$$

Therefore we obtain for signal-to-noise ratio

$$\frac{e_2}{e_n} \propto \Delta\kappa \left(\frac{f\ell}{A_o}\right)^{\frac{1}{2}} \left\{\hat{H} \sin\left(\pi \frac{H_{sat}}{\hat{H}}\right) \Theta^{-\frac{1}{2}}\right\} \tag{3.99}$$

The term in $\{\ \}$ is a constant depending on $\hat{H}$ and H_{sat} and comes within 10% of its maximum possible value when $\hat{H} = 2H_{sat}$. Therefore:

$$\frac{e_2}{e_n} \propto \Delta\kappa \left\{\frac{f\ell}{A_o}\right\}^{\frac{1}{2}}$$

$$\propto \Delta\kappa \left\{f\mathcal{R}_m\right\}^{\frac{1}{2}} \tag{3.100}$$

where $\mathcal{R}_m$ is the reluctance of the modulator core.

An experimental determination of the proportionality constant has been made for Permalloy C (Williams and Noble, 1950). Their test specimen had a cross-sectional area of 0.7 cm^2 and a length of 10 cm, and hence its reluctance was about 10^5 amp/weber. The observed signal-to-noise ratio was unity, at 1500 Hz modulating frequency and 1.0 Hz observed bandwidth, with an input magnetomotive force of 7.2×10^{-8} amperes, hence an input flux of 7.2×10^{-13} Wb. Substituting this value of input flux into Eq. 3.56 relating flux and susceptibility anisotropy for a magnetic bridge, we find that the input anisotropy would have been

$$\Delta\kappa_{min} = \frac{\phi_s}{5.41 \times 10^{-6}}$$

$$= 1.33 \times 10^{-7} \text{ mksu} \tag{3.101}$$

Similar modulator noise characteristics were reported by Higuchi (1970). Eq. 3.100 now becomes

$$\frac{e_2}{e_n} = k\Delta\kappa(f\mathcal{R}_m)^{1/2} \tag{3.102}$$

where

$$k = \frac{1}{\Delta\kappa_{min}(f'\mathcal{R}'_m)^{1/2}}$$

$$= \frac{1}{(1.33 \times 10^{-7})(1500 \times 10^5)^{1/2}}$$

$$= 614 \tag{3.103}$$

Therefore Eq. 3.102 becomes

$$\frac{e_2}{e_n} = 614\Delta\kappa(f\mathcal{R}_m)^{1/2} \tag{3.104}$$

It was shown in Eq. 3.60 that $\mathcal{R}_m$ must not exceed 2.18×10^6 amp/weber. With that value, and $f = 10^4$ Hz, the signal-to-noise ratio becomes

$$\frac{e_2}{e_n} = 9.06 \times 10^7\ \Delta\kappa \tag{3.105}$$

Thus one should be able to detect $\Delta\kappa = 1.1 \times 10^{-8}$ mksu in a bandwidth of 1 Hz, or 3.5×10^{-9} mksu in a bandwidth of 10^{-1} Hz.

Scouten (1972) suggested the use of an improved modulating waveform to effect higher sensitivity. Kawanishi

(1972) reports a gain in sensitivity of about an order of magnitude with dual-frequency excitation of the modulator core. Even allowing for such improvements, however, the sensitivity of this type of modulator is much inferior to that attainable with other signal coil arrangements previously discussed. It could be useful for measurement of bulk susceptibility, however.

3.7.2 Villari-effect Modulators

In a mechanically driven modulator Barkhausen noise can be made arbitrarily small by minimizing the direct flux passing through the modulator. The total input direct flux can be made vanishingly small by means of a feedback winding carrying a current proportional to the peak intensity of the modulated signal flux, and of such polarity as to reduce the modulated flux intensity.

A mechanically driven modulator making use of the Villari effect would require that a permalloy circuit element be strained so as to reduce its reversible permeability by an appreciable amount. The sensitivity of the modulator is directly proportional to the fractional change in permeability. This is limited by the amount of tension which can be applied before the elastic limit of the core material is reached, as shown in Figure 3.11. The applied tension must be carefully controlled to avoid degrading the element irreversibly. A stretching mechanism which produces

Figure 3.11 Variation of relative initial permeability with applied uniform tensile stress for 4 - 79 Moly-permalloy. (After Bozorth, 1951).

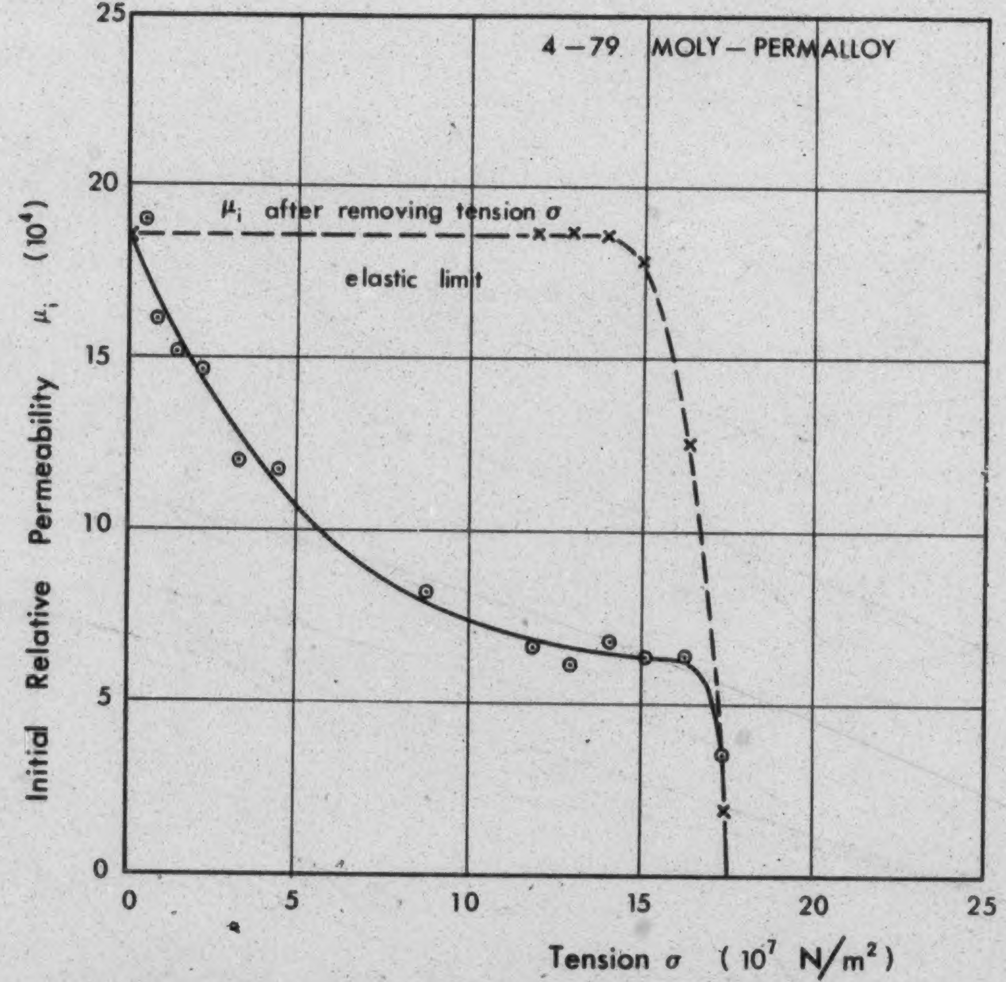
4 – 79 MOLY – PERMALLOY
μ_i after removing tension σ
elastic limit
Initial Relative Permeability μ_i (10^4)
Tension σ (10^7 N/m^2)
0
5
10
15
20
25

non-uniform tension (e.g. simple beam bending) makes this limit even more critical, since the peak stress is higher than the mean stress. It appears, then, that a mean applied stress of $1.4 \times 10^7\ \mathrm{N \cdot m^{-2}}$, or about 10% of the elastic limit, is reasonable. From Figure 3.11 it can be seen that this would result in a reluctance variation of about 14%. Therefore the modulated flux waveform has an amplitude of about 0.14 times that of the unmodulated signal flux. To regain the loss in sensitivity incurred by this amplitude reduction, and to allow a possible improvement in sensitivity of an order of magnitude over simple solenoid sensors, a modulating frequency of about 100 times the original signal frequency would be required. For a signal frequency of 100 Hz, which has been assumed thus far, the modulating frequency would have to be about 10 kHz.

In order to minimize the mechanical drive power required, one would normally employ a tuned mechanical circuit. The dissipated power is a function of the mechanical Q-factor:

$$P = \frac{\omega_m \hat{E}}{Q} \tag{3.106}$$

where: $\hat{E}$ = peak stored energy

ω_m = modulating angular frequency

The approximate drive power required can then be found by assuming uniform stress and strain. Peak stored energy, for a given applied pressure, is directly proportional to the volume of the modulating element, which is therefore made small. The volume is primarily dictated by the magnetic reluctance needed and the ease of obtaining the required dimensions. It can be seen from Eqs. 3.67 and 3.73 that if one is to achieve a sensitivity gain of, say, 4 over the bridged solenoid pair, it is necessary that the ratio $\frac{\ell}{A_m}$ for the modulator core be less than 10^3 m^{-1}, even with 25-micron laminations. Arbitrarily setting the minimum usable length at 1 cm, we thus find that the minimum cross-sectional area is 0.1 cm^2. This can be realized by a thickness of 0.1 cm and a width of 1 cm. The peak energy stored is

$$\hat{E} = \frac{1}{2}\text{(peak pressure)(cross-section)(linear strain)}$$

$$= \frac{\frac{1}{2}\text{(peak pressure)}^2\text{(cross-section)(length)}}{\text{Young's modulus}}$$

$$= \frac{\frac{1}{2}(1.4 \times 10^7\ N \cdot m^{-2})^2 (10^{-5}\ m^2)(10^{-2}\ m)}{2 \times 10^{11}\ N \cdot m^{-2}}$$

$$= 4.9 \times 10^{-5}\ N \cdot m \qquad (3.107)$$

Say that a mechanical Q of 20 can be obtained. Then substituting Eq. 3.107 back into Eq. 3.106 gives

$$P = 2.5 \times 10^{-6}\omega \qquad (3.108)$$

Thus for $\omega = 6.28 \times 10^4$ (10 kHz) drive power is 0.15 watts. This is not difficult to generate and dissipate.

3.7.3 Mechanically Variable Air Gap Modulator

A possible design for a modulator utilizing the changing reluctance of variable-width air gaps is shown in Figure 3.12. Signal flux enters the modulator via the permalloy rings, passes through an air gap to the permalloy film, and by axial vibration of the film is shuttled alternately to polepieces A and B. The outer frame returns the flux to the main transducer to complete the circuit. The signal coils shown produce an electrical output proportional to the magnitude of the modulated flux and its frequency.

Assume that the reluctances of polepieces A and B, the permalloy rings, and the air gaps between the rings and the permalloy diaphragm are negligible. All reluctance is assumed to be in the air gaps between polepieces A and B and the diaphragm. In the diaphragm signal flux is essentially radial through an annulus with outside radius r_2 and inside radius $0.707\, r_1$. The latter represents the radius of central portions of polepieces A and B through which 50% of signal flux passes.

The increment of the factor $\frac{\ell}{A_m}$ of an annular element of radius r and radial width dr is

$$d\left\{\frac{\ell}{A_m}\right\} = \frac{dr}{2\pi rh} \tag{3.109}$$

Thus the total effective ratio is

Figure 3.12 Possible configuration for a variable-air-gap magnetic modulator.

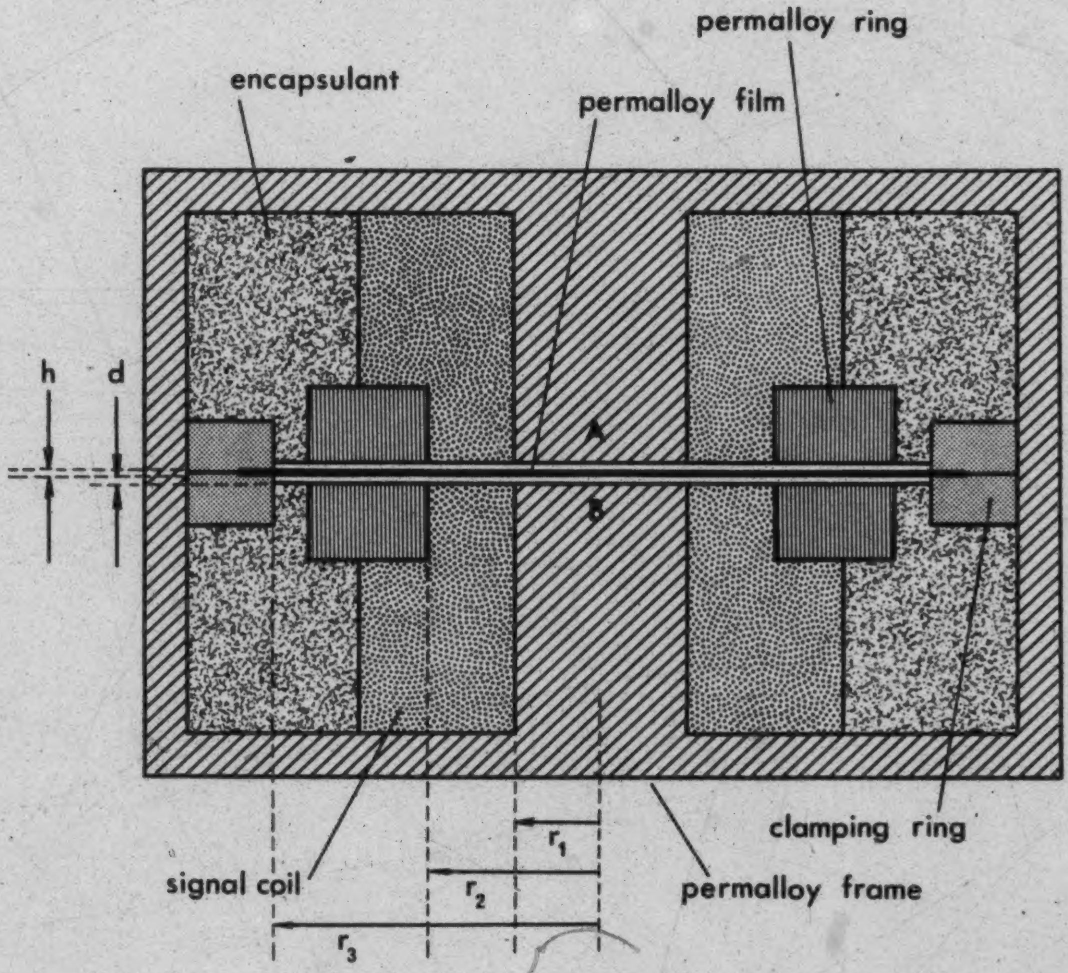
permalloy ring
encapsulant
permalloy film
h
d
A
B
clamping ring
signal coil
permalloy frame
r_1
r_2
r_3

$$\frac{\ell}{A_m} = \int_{.707 r_1}^{r_2} \frac{dr}{2\pi r h}$$

$$= \left.\frac{\ln r}{2\pi h}\right]_{.707\, r_1}^{r_2}$$

$$= \frac{\ln(0.707\ \ r_2/r_1)}{2\pi h} \qquad (3.110)$$

The numerator equals unity for $r_2 = 1.92 r_1$. This is a reasonable ratio. Then since, as in the Villari-effect modulator, the ratio $\frac{\ell}{A_m}$ must be less than $10^3\ m^{-1}$,

$$h \geq 1.6 \times 10^{-4}\ m \qquad (3.111)$$

The equivalent circuit of the modulator is shown in Figure 3.13. Note that the sensing coils are connected in series opposition to common-mode magnetic flux input. This makes the modulator insensitive to signal-frequency noise from the main transducer. This is important for avoiding modulating-frequency interference during bulk susceptibility measurements. As the diaphragm moves, $\mathcal{R}_A$ increases when $\mathcal{R}_B$ decreases, and vice versa. From Eq. 3.60 the average value of the parallel combination of $\mathcal{R}_A$ and $\mathcal{R}_B$ must be $\lesssim 2.18 \times 10^6$ amp/weber. That is, at the median position of the permalloy diaphragm,

$$\mathcal{R}_A = \mathcal{R}_B \lesssim 4.36 \times 10^6 \quad A/Wb$$

For the air gap indicated,

Figure 3.13 Electrical equivalent circuit of the variable-air-gap magnetic modulator.

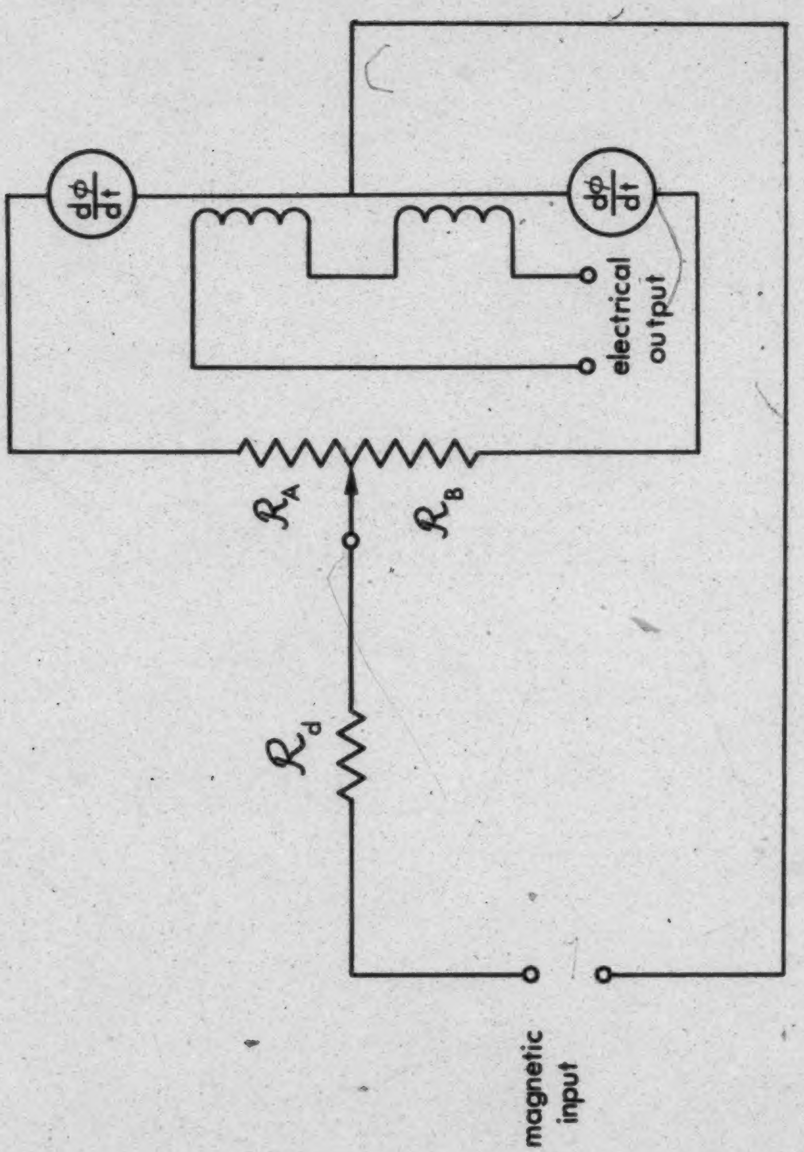
dφ/dt
dφ/dt
electrical output
$\mathcal{R}_A$
$\mathcal{R}_B$
$\mathcal{R}_d$
magnetic input

$$\mathcal{R}_A = \left\{\frac{\text{length}}{\text{area}}\right\}\left\{\frac{1}{\mu_o}\right\}$$

$$= \frac{d}{\pi r_1^2 \mu_o} \qquad (3.112)$$

A reasonable minimum value for d is 2.5×10^{-4} meters. This is limited by deviations from flatness of the diaphragm. Therefore

$$r_1 = \left\{\frac{d}{\pi \mu_o \mathcal{R}_A}\right\}^{1/2}$$

$$\geq \left\{\frac{2.5 \times 10^{-4}}{\pi (4\pi \times 10^{-7})(4.36 \times 10^{6})}\right\}^{1/2}$$

$$= 3.81 \times 10^{-3} \text{ m} \qquad (3.113)$$

Therefore, since we set $r_2 = 1.92\, r_1$,

$$r_2 \geq 7.32 \times 10^{-3} \text{ m} \qquad (3.114)$$

In order to minimize stresses incurred in the diaphragm as its central portion is made to oscillate axially, the suspension radius r_3 should be maximized. We arbitrarily set $r_3 = 3$ cm.

If we treat the diaphragm as a flat plate suspended with negligible tension, and made to vibrate by applying a uniform pressure to its free surfaces, then maximum deviation is (Spotts, 1964)

$$\Delta d = \frac{3 p r_3^4 \ (1 - \sigma_p^2\ )}{16\, Y h^3} \qquad (3.115)$$

where: σ_p = Poisson's ratio
Y = Young's modulus
p = applied uniform pressure
r_3 = radius of plate
h = thickness of plate

For permalloy with $Y \sim 2 \times 10^{11}$ $N \cdot m^{-2}$ and $\sigma_p \sim 0.3$:

$$\Delta d \sim \frac{(3)(0.91)}{(16)(2 \times 10^{11})} \frac{pr_3^4}{h^3}$$

$$= 8.53 \times 10^{-13} \frac{pr_3^4}{h^3} \tag{3.116}$$

Since $h = 1.6 \times 10^{-4}$ m and $r_3 = 3 \times 10^{-2}$ m,

$$\Delta d \sim 1.69 \times 10^{-7} p \tag{3.117}$$

Thus for maximum deviation of 1.25×10^{-4} meters, applied pressure is

$$p = \frac{\Delta d}{1.69 \times 10^{-7}}$$

$$= \frac{1.25 \times 10^{-4}}{1.69 \times 10^{-7}}$$

$$= 7.40 \times 10^{2} \ N \cdot m^{-2} \tag{3.118}$$

The maximum stress in the diaphragm is at the edge and has a value (Spotts, 1964)

$$S = \frac{3pr_3^2}{4h^2}$$

$$= \frac{(0.75)(7.40 \times 10^2)(3 \times 10^{-2})^2}{(1.6 \times 10^{-4})^2}$$

$$= 1.95 \times 10^7 \quad \mathrm{N \cdot m^{-2}} \qquad (3.119)$$

This is a factor of eight below the inelastic-strain limit for permalloy. Unforeseen effects apart, this fact makes the air-gap modulator superior to the Villari-effect modulator which could attain only about 14% conversion efficiency with comparable stresses.

In order to minimize mechanical driving power, it would be desirable to drive the diaphragm at its fundamental resonant frequency. The fundamental resonance of the edge-clamped diaphragm, assuming negligible spring constant from adjacent enclosed air spaces, is (Morse and Ingard, 1968)

$$f_0 = 0.47 \frac{h}{r_3^2} \left\{ \frac{Y}{\rho(1 - \sigma_p^2} \right\}^{1/2} \qquad (3.120)$$

where: ρ = density of the diaphragm material

= 8.72×10^3 kg/m^3 for moly-permalloy.

Substituting previously stated values for h, r_3, Y and σ_p, we obtain

$$f_0 = 0.47 \left\{ \frac{1.6 \times 10^{-4}}{9.0 \times 10^{-4}} \right\} \left[\frac{2 \times 10^{11}}{8.72 \times 10^3 \quad (1 - 0.09)} \right]^{1/2}$$

$$= 419 \text{ Hz} \qquad (3.121)$$

This frequency is too low to be useful for some purposes.

If a higher resonant frequency is desired, it may be obtained by sealing one of the cavities adjacent to the diaphragm. This cavity would have the same area as the diaphragm and a mean depth d. If the axial movement of the diaphragm is assumed to be uniform over its surface area, the mechanical compliance C of the air cavity would be (Beranek, 1954)

$$C = \frac{\text{volume of cavity}}{\rho_0 c^2 \text{ (area of diaphragm)}^2}$$

$$= \frac{d}{(\rho_0 c^2)(\pi r_3^2)} \tag{3.122}$$

where: ρ_0 = density of air

c = velocity of sound in air.

At an atmospheric pressure of 10^5 N/m^2 and an ambient temperature of 22°C,

$$C = \frac{2.5 \times 10^{-4}}{(407)(344.2)(\pi)(3 \times 10^{-2})^2}$$

$$= 6.31 \times 10^{-7} \text{ m/N}$$

Thus the resonant frequency of the diaphragm would be

$$f_0 = \frac{1}{2\pi}\left[(\rho)(\pi r^2 h)(C)\right]^{-1/2}$$

$$= 3190 \text{ Hz.} \tag{3.123}$$

The actual resonant frequency would be somewhat lower than this because the diaphragm is restrained at its edges and therefore does not move uniformly.

The required diaphragm pressure of 740 $N \cdot m^{-2}$ could be conveniently applied as air pressure since it represents about 0.7% of atmospheric pressure. There are no problems with phase variations across the diaphragm if frequency is kept sufficiently low that the polepiece radius r_1 is much smaller than the wavelength of the corresponding sound wave in air. This is true for any operating frequency below about 10 kHz.

The pressure level of 740 $N \cdot m^{-2}$ represents a sound pressure level of 151 dB (0 dB = 2×10^{-5} $N \cdot m^{-2}$). This level should be readily obtainable in a small cavity by using a small (approximately 10 cm) loudspeaker. The sound wave can be ducted through fairly rigid tubing, such as copper, with approximately 5 mm inside diameter. This effects separation of the loudspeaker coil from the signal coil, thus minimizing coupling between them. The main driving frequency of the voice coil is not critically important, unless it causes overload, since it differs from the signal frequency by twice the shaft rotational frequency. However, the band of noise about the driving frequency and the finite bandwidth of the synchronous detector demand that coupling be minimized. A schematic diagram of the acoustical driver is shown in Figure 3.14.

Figure 3.14 Possible acoustic drive arrangement for the variable-air-gap magnetic modulator.

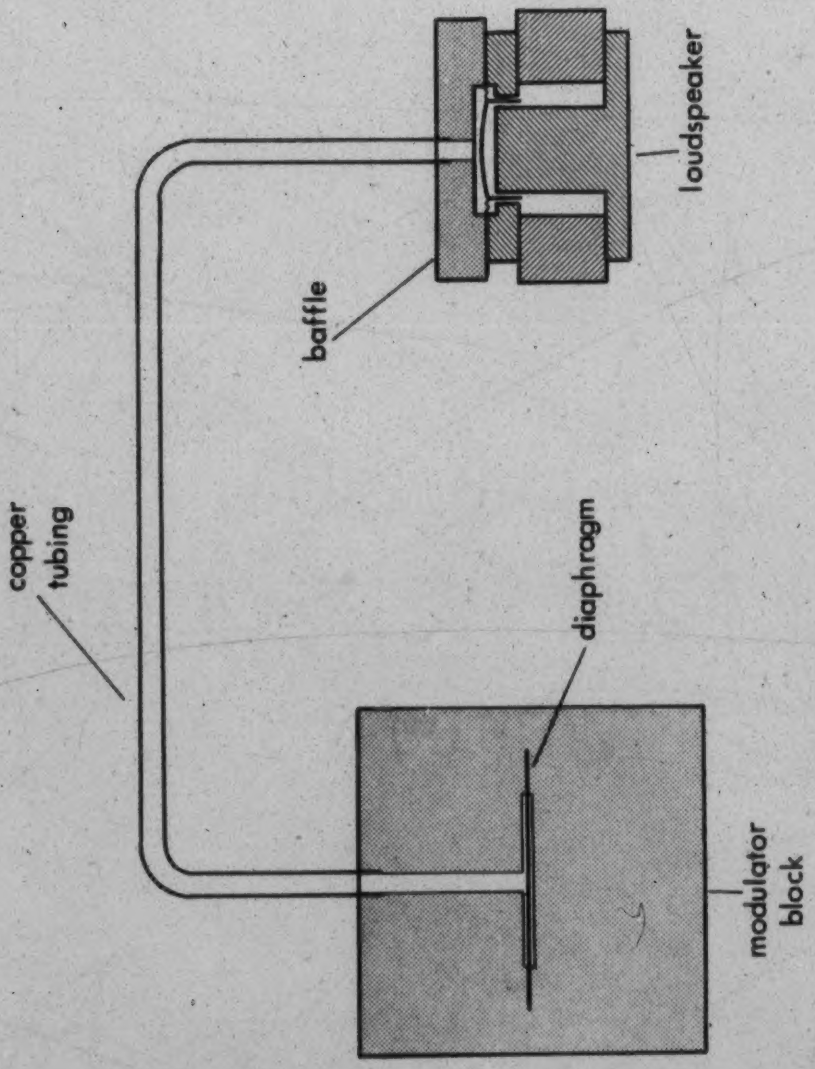
copper tubing
baffle
loudspeaker
diaphragm
modulator block

3.8 Signal Coils in the Specimen Gap

As the direct field applied to the specimen is increased certain magnetic components of the rock begin to behave nonlinearly or even saturate, especially if they appear as acicular particles of high aspect ratio. Even stronger nonlinearities can occur with basal-plane alignment of hematite crystals. This was discussed in Section 1.6. To examine this behaviour and its possible usefulness in conveying geological information, it is desirable to be able to detect the specimen's magnetization perpendicular to the applied field as the specimen rotates. This can be done by placing sensing coils near the specimen and in the plane parallel to that containing the bulk field direction and the axis of rotation of the spinner shaft. These coils would require a fairly wide phase-linear bandwidth so that most of the harmonic content of the nonlinearities could be retrieved. The dimensions of the coils are limited by the specimen gap dimensions and those of the cylindrical opening for the spinner shaft. The coils are shaped to partially wrap around this cylindrical opening and thus optimize coupling to the specimen. See Figures 3.15 and 3.16. A large number of turns, which implies high impedance, would minimize amplifier noise effects while a smaller number of turns with lower impedance would avoid the effects of interturn capacitance in producing resonances in the band of

Figure 3.15 Specimen gap signal coils for measuring magnetization perpendicular to the applied field.

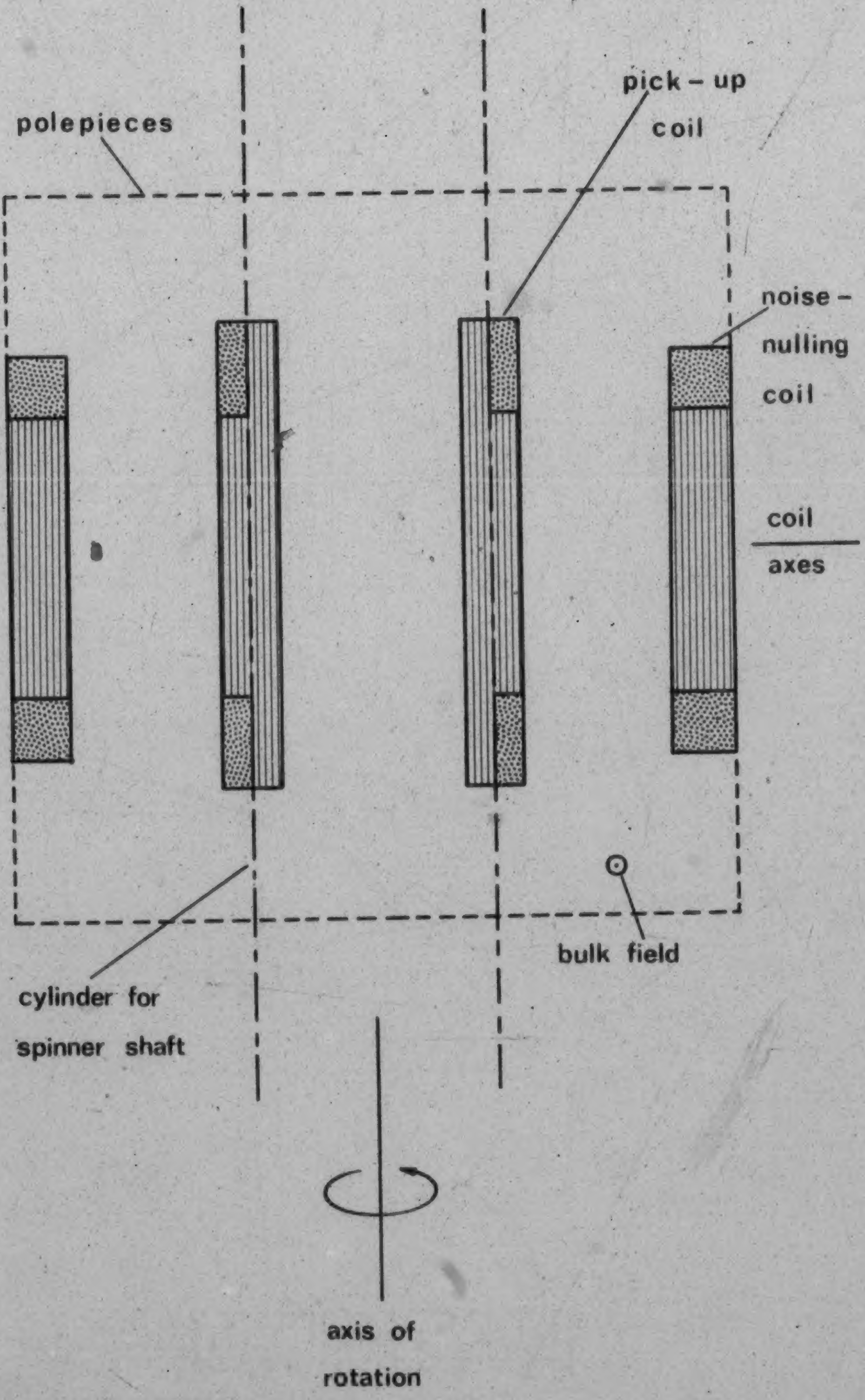
pick - up
coil
polepieces
noise -
nulling
coil
coil
axes
bulk field
cylinder for
spinner shaft
axis of
rotation

Figure 3.16 Cross-section of the specimen gap signal coils as they would appear when viewing along the spinner shaft.

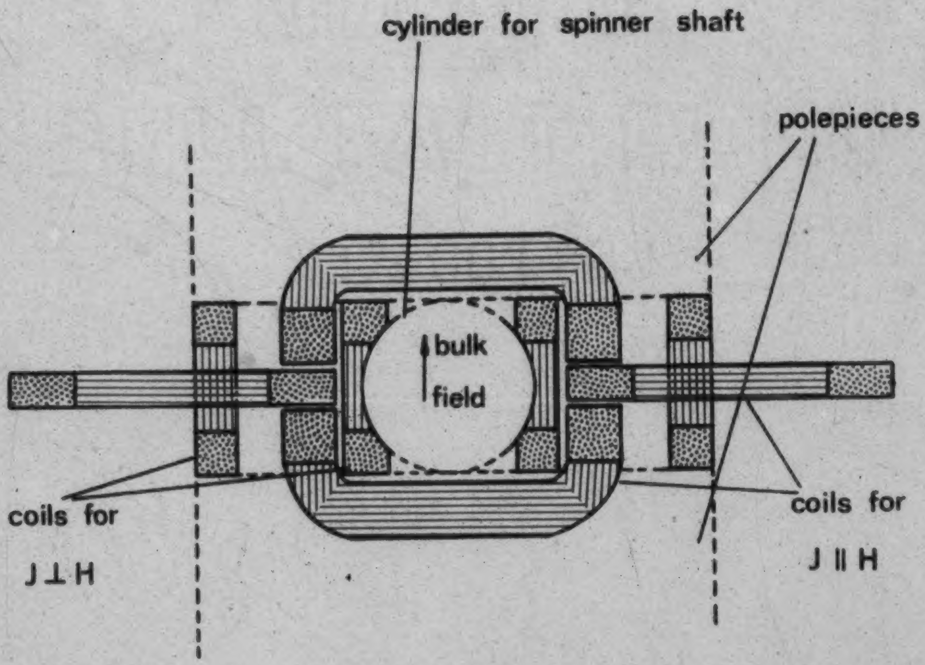
cylinder for spinner shaft
polepieces
bulk
field
coils for
J ⊥ H
coils for
J ∥ H

frequencies useful for signal. As a compromise between these requirements the coils are wound with 2500 turns each of #35 AWG enameled wire. Coil resistance is 700 ohms. A second pair of coils of comparable size but square cross-section is placed on the same axis as the above-described coils, but 4 cm farther from the specimen. They have the same number of turns and 600 ohms resistance. They are connected to a separate preamplifier and by appropriate gain adjustment their output is used to cancel noise pickup of the coil pair nearer the specimen. The combination constitutes essentially a field gradient sensing arrangement.

Another set of four coils is placed in the specimen gap to sense magnetization parallel to the applied field. Again, one pair of coils is wrapped around the cylindrical shaft opening, as well as around the polepiece, while the other pair of coils is placed on either side of the shaft opening for noise pick-up cancellation. See Figures 3.16 and 3.17. These coils have 1750 turns of #30 AWG enameled copper wire each. The coils nearer the specimen have 350 ohms resistance, while the far coils have 300 ohms.

Figure 3.17 Specimen gap signal coils for measuring magnetization parallel to the applied field.

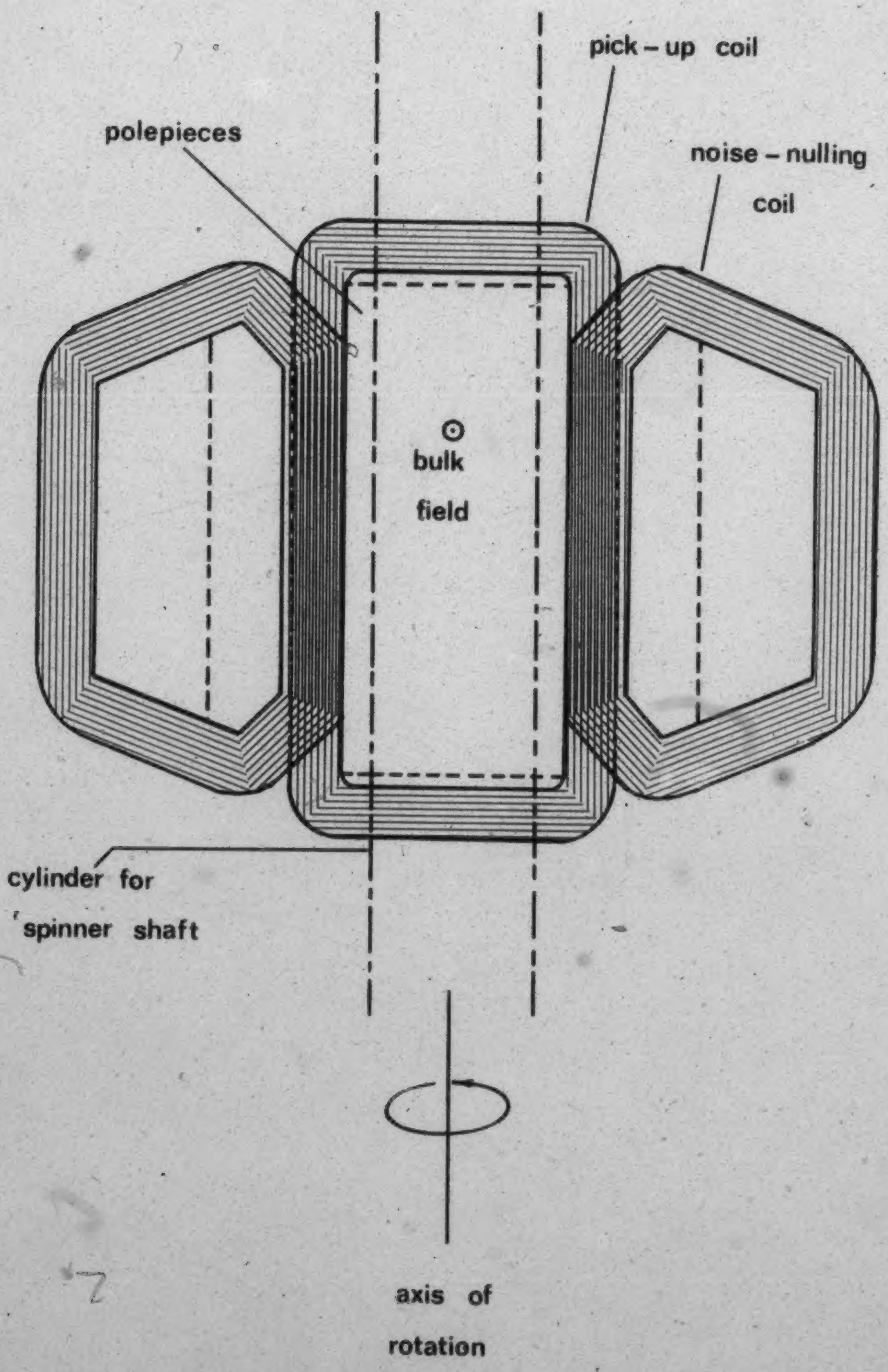
pick - up coil
polepieces
noise - nulling coil
bulk field
cylinder for spinner shaft
axis of rotation

The sensitivity of the coil pair for measuring magnetization parallel to the applied field is calculated for comparison with previously calculated sensitivities. For peak-to-peak susceptibility anisotropy $\Delta\kappa$ the rms signal output can be found from Eq. 3.12

$$e_s = 3.40 \times 10^{-5} f n \Delta\kappa \quad \text{volts} \tag{3.124}$$

In this case $n = 3500$ turns for the series connected pair, while their resistance is 700 ohms. The actual sensitivity is rather larger than this because the coil is more closely coupled to the specimen than coils which are wound around the magnetic circuit elements. In effect, the gap volume is decreased by approximately the ratio of coil-to-polepiece area. This increases signal output by the same ratio, as shown in Eq. 3.3. For the dimensions used, this ratio is approximately 2.0. Thus signal output is

$$e_s = 6.8 \times 10^{-5}\ (3500) f \Delta\kappa$$

$$= 0.24\ f\Delta\kappa \tag{3.125}$$

The rms thermal noise voltage (Johnson noise) produced by the coil pair is, from Eq. 3.13,

$$e_n = (4kTR_c\Delta f)^{1/2} \tag{3.126}$$

For $T = 293°K$ and $R_c = 700$ ohms, noise voltage is

$$e_n = 3.36 \times 10^{-9} (\Delta f)^{1/2} \text{ volts} \tag{3.127}$$

Thus from Eqs. 3.125 and 3.127 the signal-to-noise ratio is

$$\frac{e_s}{e_n} = \frac{2.4 \times 10^{-1} f \Delta\kappa}{3.36 \times 10^{-9} \Delta f^{\frac{1}{2}}}$$

$$= 0.71 \times 10^{8} \frac{f\Delta\kappa}{\Delta f^{\frac{1}{2}}} \qquad (3.128)$$

Substitute the same reasonable limits on f and Δf as before:

f = 100 Hz

Δf = 0.1 Hz

Thus a reasonable limit on signal-to-noise ratio is

$$\frac{e_s}{e_n} = 2.25 \times 10^{10} \Delta\kappa \qquad (3.129)$$

Thus the thermal-noise-limited sensitivity, based on signal being equal to noise, is

$$\begin{aligned} \Delta\kappa_{min} &= 4.4 \times 10^{-11} \text{ mksu} \\ &= 3.5 \times 10^{-12} \text{ emu/cm}^3 \end{aligned} \qquad (3.130)$$

if the coils' thermal noise is the limiting factor.

CHAPTER 4

DESIGN OF A NEW MAGNETOMETER

4.1 The Magnetic Circuit

4.1.1 Field Uniformity

The dimension which was arbitrarily established at the beginning was a specimen size of 2.5 cm diameter and 2.5 cm length. To allow for the specimen to be rotated about three perpendicular axes, and to allow space for a specimen holder and shaft, with suitable clearance for the latter, it was decided that the specimen gap should be 5.0 cm wide. This dimension sets a lower limit on the pole-piece dimensions by virtue of the field uniformity necessary.

It was shown in Section 2.4 that symmetric deviations from field uniformity over the space occupied by the rotating specimen should have a peak-to-peak value of less 0.1% for acceptably small effects of bulk susceptibility nonuniformity within the specimen, as well as effects from the specimen shape factor. Deviation components which increase monotonically and linearly over this critical volume are not as objectionable, at least from the point of view of the shape factor of symmetrical specimens, and about 0.25% could be tolerated. Assuming that individual pole-piece laminations have straight edges, and that the plane of the laminations of the outer polepieces coincides with the plane of rotation of the specimen, a taper of as much as 1% over a 15 cm polepiece can be tolerated. For a 5.0 cm gap this necessitates spacing accuracy of about 0.5 mm. This is not very difficult. Had the plane of the laminations been placed so that a normal to the laminations was perpendicular to the shaft axis, then the taper problem would have been aggravated by the difficulty in producing a flat surface in the specimen's rotational plane. For perfectly straight-edged laminations having a very high normal permeability, the principal cause of symmetric deviation from uniformity is the fringing field. To calculate field uniformity, a computer program was drawn up by R. Teshima of the Physics Department at the University of Alberta to solve numerically Laplace's equation in cylindrical coordinates:

$$r \frac{\partial^2 \Psi}{\partial r^2} + \frac{\partial \Psi}{\partial r} + r \frac{\partial^2 \Psi}{\partial z^2} = 0 \qquad (4.1)$$

where: Ψ = magnetic potential

r = radial dimension

z = axial dimension

Not only the polepiece frontal surfaces, but the polepiece edges, the magnet edges, and the entire outer magnetic circuit are accounted for. It is assumed that the polepieces and outer magnetic circuit have infinitely high normal permeability and therefore represent equipotential surfaces. The magnet blocks are assumed to have a linear increase in potential with distance along their magnetic axes. The generalized configuration and dimensions are shown in Figure 4.1.

The relaxation method is used to calculate the field within the gap (Della Torre and Longo, 1969). The magnetic potential $\Psi(r,z)$ is repeatedly evaluated for all points on a cylindrical coordinate grid with points separated both radially and axially by distances of 0.5 cm. At each reevaluation the results of the most recent computation are used at the neighbouring points. This process is continued until the incremental change at each iteration becomes satisfactorily small. The incremental change worked toward in these evaluations is 0.001%. Typically, some 200 iterations are required to accomplish this. Briefly stated, the results indicate a symmetric peak-to-peak deviation as indicated below:

diameter of main polepiece	deviation
12.0 cm	0.25%
13.0 cm	0.10%
15.0 cm	0.05%
17.0 cm	0.025%

The other magnetic circuit dimensions used in this

Figure 4.1 Magnetic circuit dimensions for gap-field calculations.

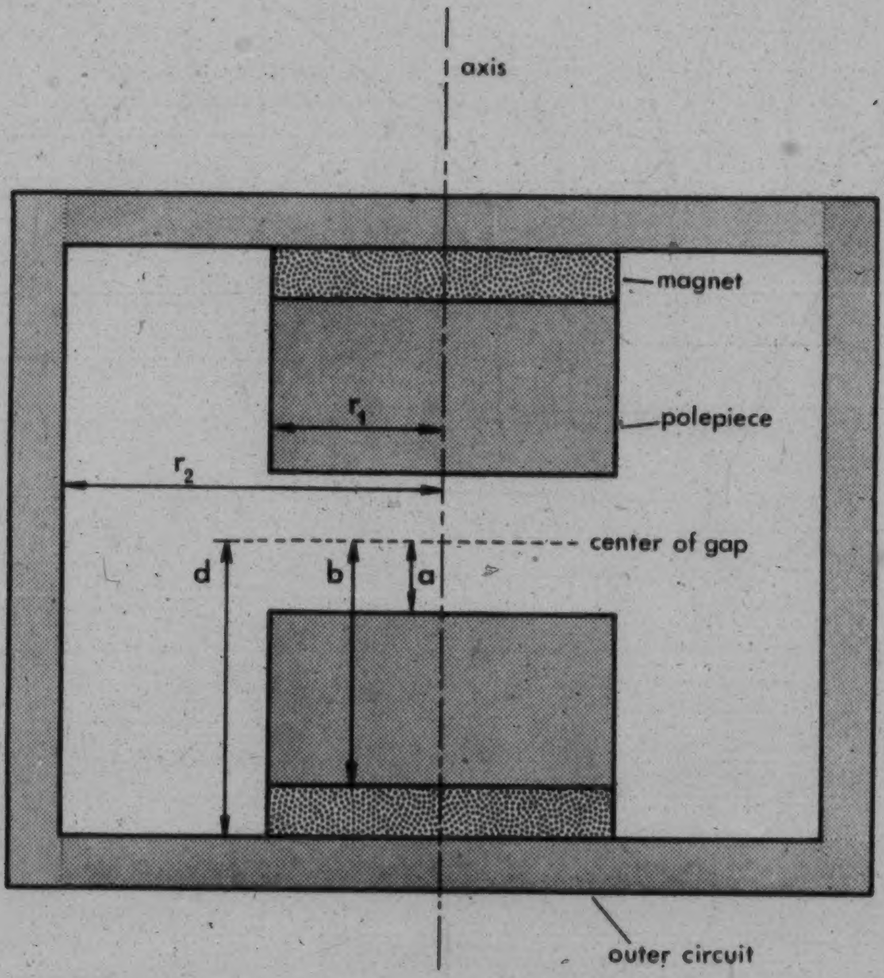
axis
magnet
polepiece
r_1
r_2
center of gap
d
b
a
outer circuit

computation were:

$r_2 = 17$ cm

$a = 2.5$ cm

$b = 7.5$ cm

$d = 9.5$ cm

The largest polepiece diameter (17 cm) was chosen in order that residual nonlinearities were due to unavoidable dimensional and permeability effects in the polepieces.

Figure 4.2 shows the field contours which were computed for the 17 cm polepiece diameter. The contours show the percentage deviation from the field intensity at the center of the gap.

Because of the necessity to use a laminated structure, it was decided that cylindrical symmetry could not be maintained in the polepieces and outer magnetic circuit. Accordingly, square polepieces of side 15 cm, thus having the same area as the 17 cm circular ones, are used. The outer magnetic circuit does not cylindrically envelope the inner magnetic circuit. It was found from the uniformity program that this does not have an important deteriorating effect.

In practice it is expected that potential gradients along the polepiece surfaces, due to transverse flux components, set the limit to field uniformity for the dimensions chosen. The air gaps between the polepiece

Figure 4.2 Magnetic field contours computed for cylindrical polepieces of 17 cm diameter. Other polepiece dimensions are:

r_2 = 17 cm

a = 2.5 cm

b = 7.5 cm

d = 9.5 cm

The diagram shows deviations in the axial flux density from its mean value on the central axis. Deviations are plotted on a 0.5 cm grid. Values are in parts per million. Curves of equal deviation are plotted for 0, 100 ppm, and 200 ppm. Since the field contours are symmetrical, only one quadrant is plotted.

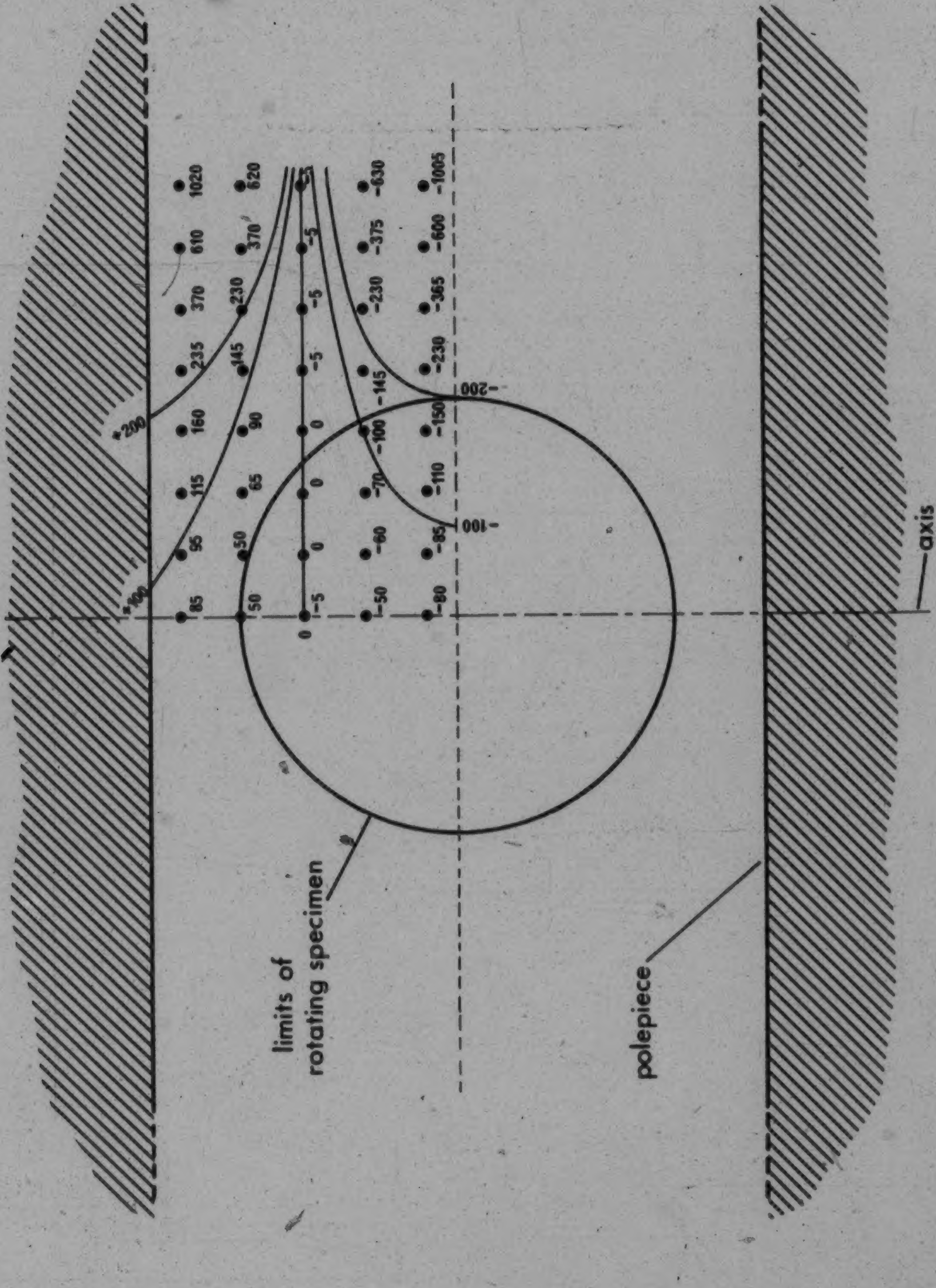
+200
+100
85
95
115
160
235
370
610
1020
50
50
65
90
145
230
370
620
0
-5
0
0
0
0
-5
-5
-5
-5
-50
-60
-70
-100
-145
-230
-375
-630
-80
-85
-110
-150
-230
-365
-600
-1005
-100
-200
limits of
rotating specimen
polepiece
axis

sections on either side of the specimen gap serve to ensure that the main transverse fields are within the polepiece halves farthest from the specimen gap. Even so, fringing field flux demands transverse components of about 10% of the bulk axial component. This amounts to about 0.01 T, and with a normal permeability of 10^4 causes a magnetic potential gradient of about 1.0 A/m along the poleface. The gradient is somewhat higher in the direction normal to the plane of the laminations because of the higher reluctance due to the minute air gaps crossed between laminations. Therefore this direction is kept out of the plane of rotation of the specimen.

4.1.2 Materials and Dimensions of Components Requiring High Permeability

The magnetic circuit shown in Figure 3.7 uses a high-permeability shell rather than placing the magnets in the outer legs because this configuration shields the specimen gap from externally-produced magnetic variations, at least in the direction of the signal flux. For this reason the outer shell should have a very high reversible permeability, even while carrying the direct magnetic flux.

A molybdenum permalloy alloy, Permalloy 80, manufactured by Magnetics, Inc. in the form of cold rolled strip, was chosen as the material for the polepieces and outer shell. Its composition includes 80.4% nickel, 4.4% molybdenum, and 0.6% manganese. It was chosen because:

1. It has very high initial and reversible permeabilities, with an acceptably high saturation flux density of 0.8 tesla.
2. At the composition of Permalloy 80, and with suitable heat treatment, the magnetostrictive coefficients are minimized (Weiner, 1969). This is very important in eliminating spurious magnetic effects due to vibration and strain.

In order that the outer shell retain a high reversible permeability, even at high signal frequencies, it is necessary to laminate it. The skin depth of permalloy at 400 Hz, assuming a reversible permeability reduced to 5000 due to direct flux, is about 2.7×10^{-4} m. This suggests the use of laminations about 6×10^{-4} m thick. As will be shown later in this section, the requirement of thermally generated noise is even more restrictive. Thus laminations of thickness 3.56×10^{-4} m (the standard 14 mil gauge) were chosen. The same laminations are used for the polepieces.

The initial design was based on a maximum direct flux density of about 0.1 tesla in the gap. For the size of polepieces used and the leakage factor associated with them, this implies a total flux of 3.37×10^{-3} webers. If this flux is to be carried by an external shell consisting of two 15 cm stacks of 2.5 cm wide laminations, the flux density in the shell is 0.449 tesla. This is sufficiently far below saturation to be acceptable. Two stacks of laminations of this width make up the 5 cm thick polepieces. The laminations in each stack are at right angles to those in the other to afford the best field uniformity across the entire poleface. A small air gap of depth 0.18 cm between the polepiece stacks allows the polepiece to behave as a filter for inhomogeneities in the magnet blocks (Evans, 1960).

It remains to consider the balancing gap necessary for the magnetic bridge configuration, and the small polepieces to carry the signal flux from the balanced bridge to the flux sensor (solenoid, magnetic helix, or magnetic modulator). The field need not be uniform in the balancing gap and so polepieces are dispensed with. The magnet blocks for the balancing gap are similar to those for the specimen gap, since equal magnetic potential and flux are required to balance the bridge. The magnetic potential due to the signal is developed between the outer shell and a 15 cm by 15 cm stack of 2.5 cm wide laminations between the central magnet blocks. Signal flux is carried to the sensor through 2.5 cm stacks of 1.25 cm wide, 100 micron thick permalloy laminations. These do not carry the magnet flux and so operate with initial permeability. A diagram of the magnetic circuit is shown in Figure 4.3. It is shown in perspective in Figure 4.4.

4.1.3 Eddy Current Noise

Assume a uniform permeability throughout the permalloy laminations. Therefore thickness must be less than skin depth. For the material used, a reversible permeability of 8000 implies a skin depth of 427 microns. Since the main magnetic circuit carries a direct flux as well as a signal flux, the reversible permeability is smaller than the normally assumed value of 20,000.

As shown in Eq. 3.31, the magnetic noise flux associated with eddy currents in a circuit of length ℓ, cross-sectional area A, and having total reluctance $\mathcal{R}$ is

$$\phi_n = \frac{4.74 \times 10^{-8} t}{\mathcal{R}} \sqrt{\frac{\ell \Delta f}{A}} \text{ webers} \qquad (4.2)$$

where: t = lamination thickness

Δf = observed bandwidth

Therefore for a bandwidth of 0.1 Hz:

$$\phi_n = \frac{1.50 \times 10^{-8} t}{\mathcal{R}} \sqrt{\frac{\ell}{A}} \text{ webers} \qquad (4.3)$$

Since the reluctances of the specimen gap and the balancing gap are equal, the square magnetic noise flux is simply the

Figure 4.3 Plan view of the magnetic circuit.

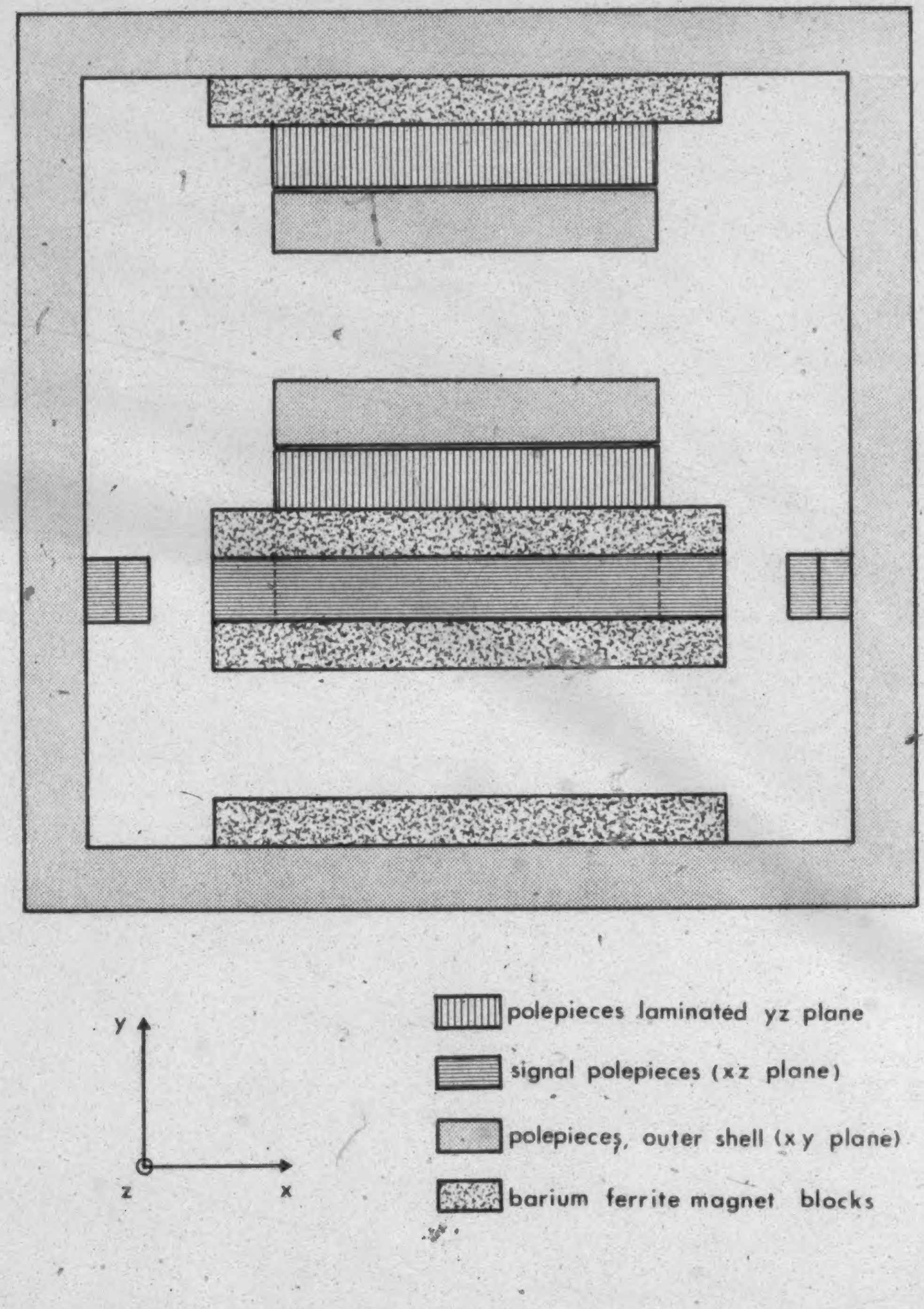
y
z
x
polepieces laminated yz plane
signal polepieces (xz plane)
polepieces, outer shell (xy plane)
barium ferrite magnet blocks

Figure 4.4   Perspective view of the magnetic circuit.

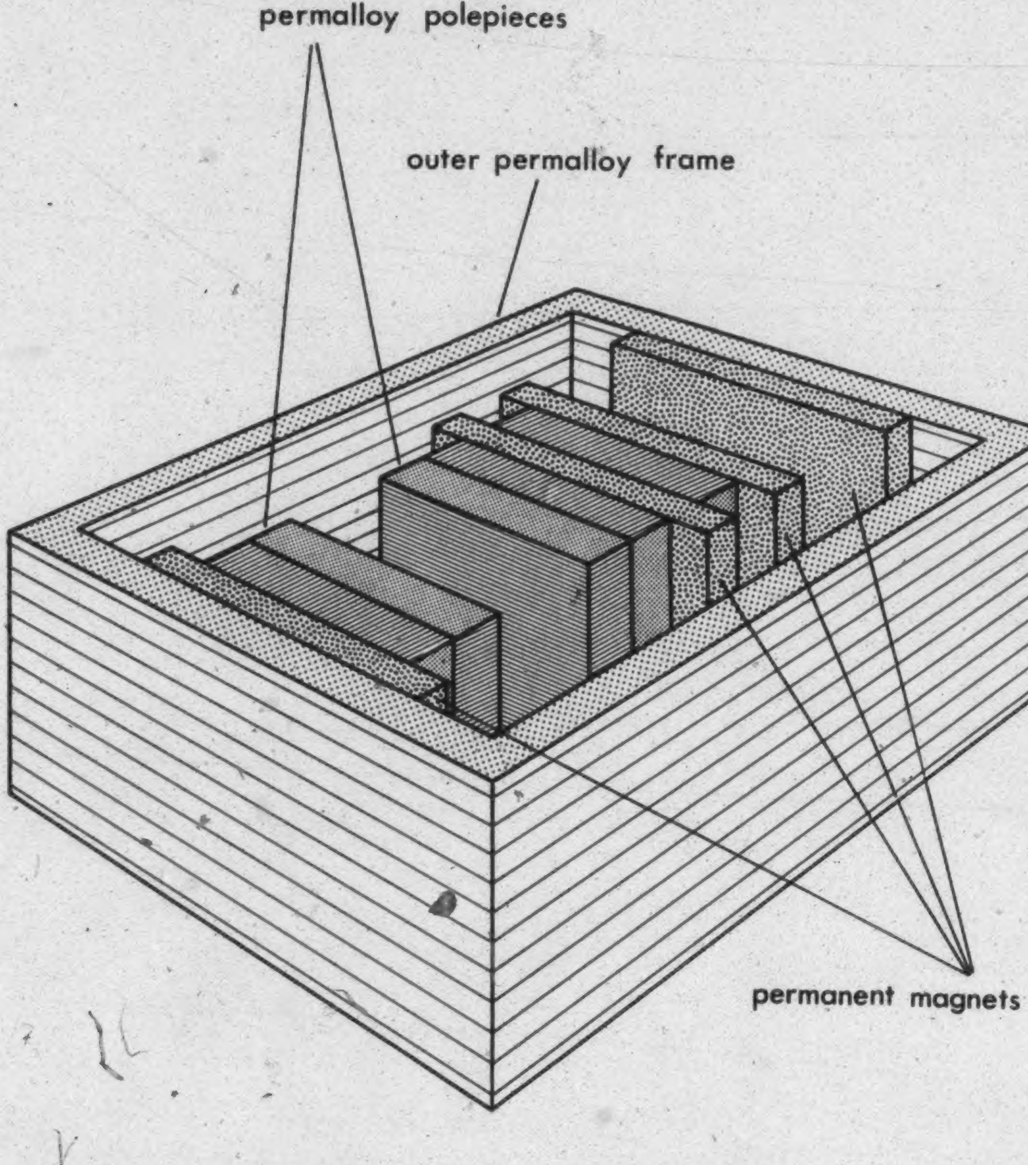
permalloy polepieces
outer permalloy frame
permanent magnets

sum of the squares of the magnetic noise fluxes of the magnetic circuit elements in series with either gap.

$$\phi = \phi_A + \phi_B + \phi_C + \phi_D \qquad (4.4)$$

where the subscripts refer to the four sections of the magnetic circuit similarly labeled in Figure 4.5. The ratios of length to area for the circuit elements are:

$$\begin{aligned}
&\text{A:} \quad \frac{\ell}{A} = \frac{0.33 \text{ m}}{0.77 \times 10^{-2} \text{ m}^2} = 43 \text{ m}^{-1} \\
&\text{B:} \quad \frac{\ell}{A} = \frac{1.02 \times 10^{-1} \text{ m}}{2.32 \times 10^{-2} \text{ m}^2} = 4.4 \text{ m}^{-1} \\
&\text{C:} \quad \frac{\ell}{A} = \frac{7.5 \times 10^{-2} \text{ m}}{3.85 \times 10^{-3} \text{ m}^2} = 19.5 \text{ m}^{-1} \\
&\text{D:} \quad \frac{\ell}{A} = \frac{0.23 \text{ m}}{0.77 \times 10^{-2} \text{ m}^2} = 29.9 \text{ m}^{-1}
\end{aligned} \qquad (4.5)$$

One can now substitute these values into Eqs. 4.3 and 4.4. If the reluctance of the permalloy circuit elements and the flux sensor are assumed to be negligible, the reluctance may be taken to be 2.18×10^6 A/Wb. Thus the total noise flux is

$$\begin{aligned}
\phi_{nt} &= \frac{1.50 \times 10^{-8} t}{2.18 \times 10^6} \left\{43 + 4.4 + 19.5 + 29.9\right\}^{1/2} \\
&= 6.77 \times 10^{-14} \, t
\end{aligned} \qquad (4.6)$$

Figure 4.5 Divisions of the magnetic circuit to facilitate estimation of magnetic core noise produced.

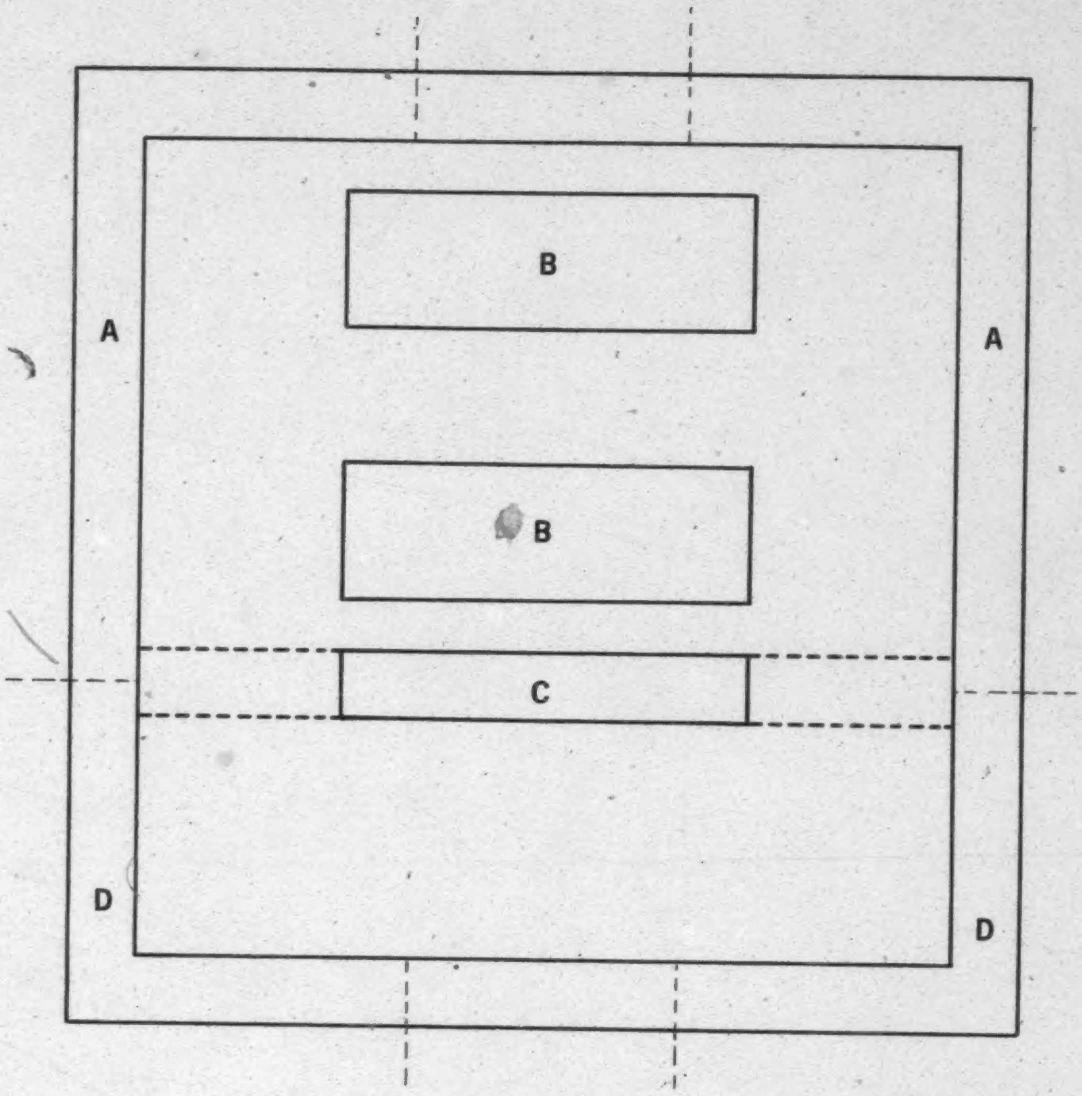
B
A
A
B
C
D
D

To convert this noise flux into an apparent susceptibility anisotropy, consider Eq. 3.56 for signal flux given negligible bridge sensor core reluctance.

$$\phi_s = 5.41 \times 10^{-6}\,\Delta\kappa \quad \text{webers} \tag{4.7}$$

Then if noise flux equals signal flux, the limiting susceptibility anisotropy which can be detected is

$$\Delta\kappa_{min} = \frac{6.77 \times 10^{-14} t}{5.41 \times 10^{-6}}$$

$$= 1.25 \times 10^{-8} t \tag{4.8}$$

The above result is shown graphically for a series of lamination thicknesses in Figure 4.6. It can be seen that if the limiting sensitivity is to be that of the magnetic helix sensor (i.e. about 4×10^{-12} mksu) the lamination thickness should be about 300 microns. For this reason the 356 micron thickness (standard 14 mil gauge) was used.

4.2 Establishing the Bias Field

4.2.1 Design of the Magnet Structure

For reasons mentioned in Section 2.4, it was decided to use a direct field rather than an alternating one to magnetize the specimen. It is difficult to get sufficient amplitude stability in an alternating field. Also, magnetic hysteresis and eddy current losses involved

Figure 4.6 Magnetic core noise produced by the main magnetic circuit, as a function of lamination thickness t.

Bandwidth $\Delta f = 0.1$ Hz

Reversible permeability $\mu_r = 8000$

Skin depth $\delta = 427\ \mu$m.

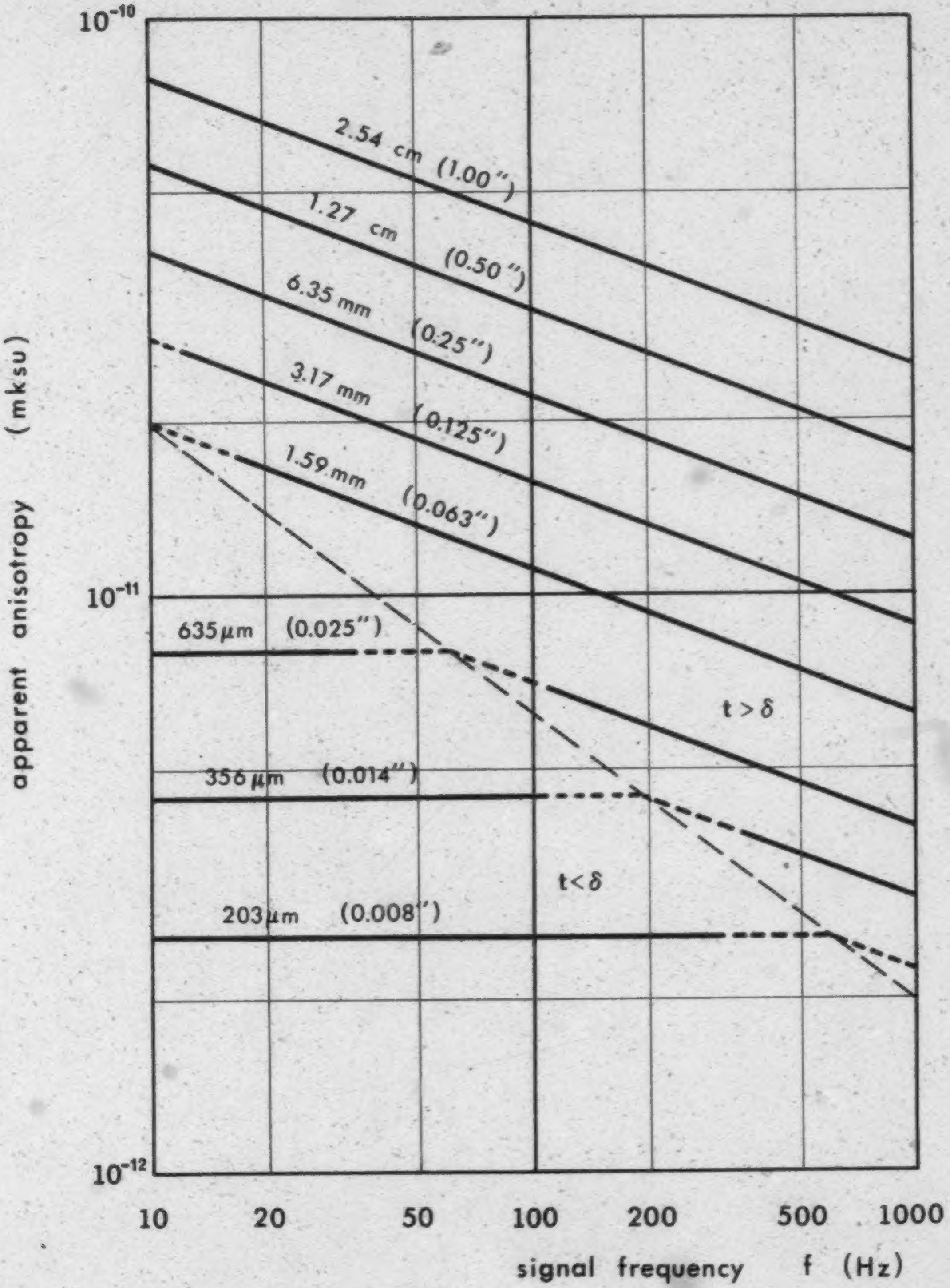
10^-10
10^-11
10^-12
apparent anisotropy (mksu)
2.54 cm (1.00")
1.27 cm (0.50")
6.35 mm (0.25")
3.17 mm (0.125")
1.59 mm (0.063")
635μm (0.025")
356μm (0.014")
203μm (0.008")
t > δ
t < δ
10
20
50
100
200
500
1000
signal frequency f (Hz)

in setting up an alternating field of suitable magnitude would be prohibitive and the resulting stresses could not be tolerated. Furthermore, Barkhausen noise associated with an alternating field was expected to have become the dominant noise component. Having decided on a direct field, it remained to choose between solenoid and permanent magnet excitation. Compactness and large-field capability would favor use of a solenoid. However, the problem of I^2R power losses in the coil windings and the difficulty of generating noise-free current, even at zero frequency, prompted the use of permanent magnets.

Because of the shape of the specimen gap, where most of the magnetostatic energy is stored, it was decided to use anisotropic barium ferrite magnets. These have a ratio B_d/H_d at maximum energy product B_dH_d such that no area-changing polepieces are required between the air gap and the magnet blocks. Furthermore, barium ferrite is inexpensive per unit energy capacity and has negligibly small eddy current losses.

For several reasons, it was decided that the magnet blocks would be magnetized after assembly of the transducer block:

1. Since the blocks are magnetically "open-circuited" before assembly, and since their magnetic hysteresis loops are not reversible in the second quadrant, they cannot attain

maximum energy product after assembly unless they are remagnetized. Different magnet materials are so affected to different degrees, but the only materials not strongly affected, such as isotropic barium ferrites, have rather small energy products even at optimal conditions.

2. It was desired to be able to vary the magnitude of the bias field in order to examine the effect on susceptibility anisotropy of different values of bias field. Thus magnetizing/demagnetizing coils had to be included.
3. While magnetized, the magnet blocks exert such large forces on each other and on magnetically permeable components, that they are extremely difficult to work with and assemble.
4. There is an irreversible loss in magnetization when the magnet blocks undergo the temperature changes incurred during the epoxy casting process.(Tenzer, 1956).

By following the procedure now to be outlined for several thicknesses of magnet blocks, it was determined that 1.9 cm thick blocks of Arnox 5 would provide a field of sufficient intensity. The maximum gap flux aimed for was

0.1 tesla. The magnet blocks are actually only 1.75 cm thick because of the optional surface grinding which was done.

Figure 4.7 indicates qualitatively the approximate flux leakage paths around both the magnet blocks and the specimen gap. The leakage factor, defined in Section 3.1, for a pair of cylindrical polepieces with dimensions as indicated in Figure 4.8, can be interpolated from the family of curves given in Figure 4.9. These curves give the leakage factor for air gaps as a function of the two ratios of dimensions x/d and r_g/d .

For the specimen gap:

$$d = 2.54 \text{ cm}$$

$$x \sim 2.5 \text{ cm}$$

$$r_g \sim 8.6 \text{ cm} \tag{4.9}$$

$$\frac{x}{d} \simeq 1.0$$

$$\frac{r_g}{d} \simeq 3.4$$

Therefore the specimen gap leakage factor is

$$\xi_g \cong 0.45 \tag{4.10}$$

The leakage factor for the permanent magnet blocks is equal to that of an air gap of equal dimensions, divided by a factor $B_d/\mu_0 H_d$ which is simply the normal relative permeability of the permanent magnets at their operating

Figure 4.7 Approximate direct-flux leakage paths (shown for half of the main magnetic bridge circuit).

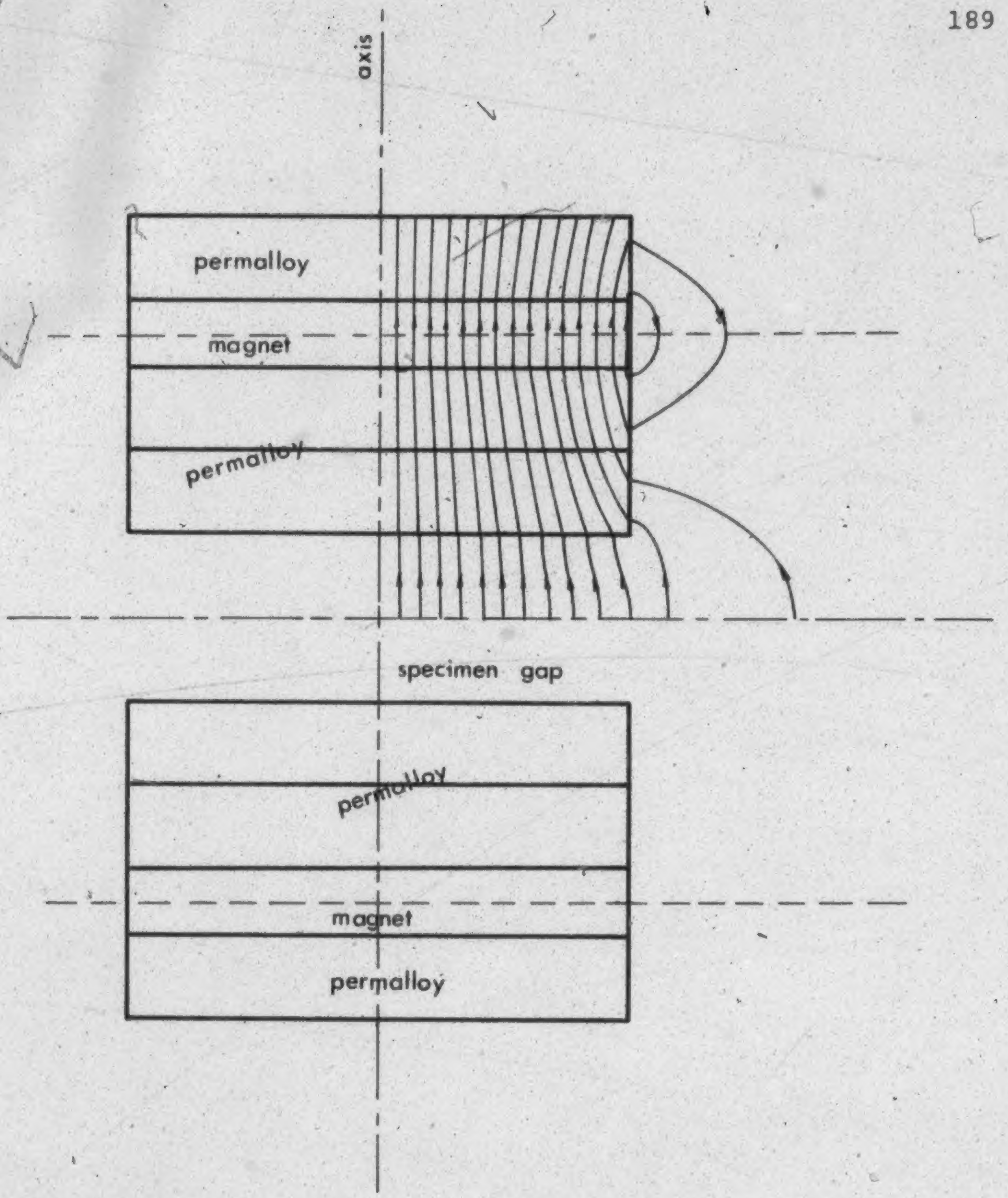
axis
permalloy
magnet
permalloy
specimen gap
permalloy
magnet
permalloy

Figure 4.8 Generalized polepiece dimensions for estimating air gap flux leakage factor.

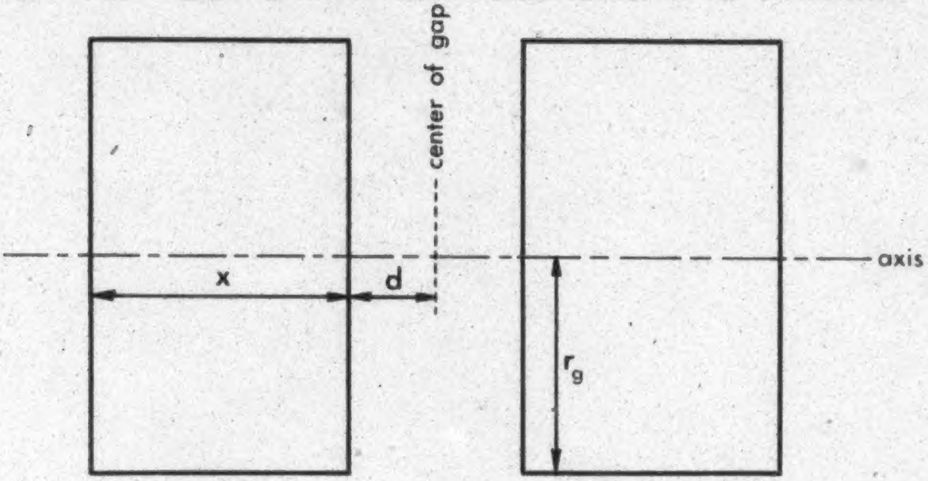
center of gap
axis
x
d
r_g

Figure 4.9 Flux leakage factor for a pair of cylindrical polepieces, as a function of dimensional ratios $\frac{x}{d}$ and $\frac{r_g}{d}$. (After Kroon, 1968)

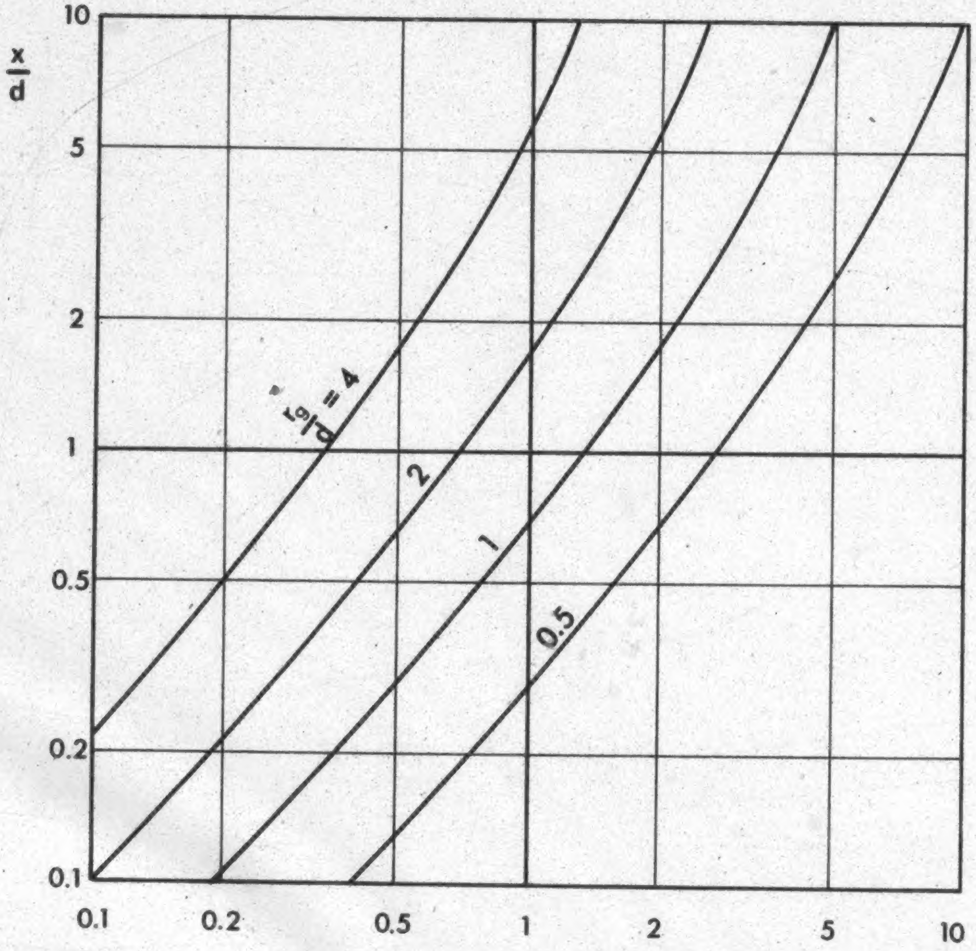

leakage ξ

point. The equivalent air gap has dimensions:

$$\begin{aligned} d &= 0.875 \text{ cm} \\ x &\sim 2.5 \text{ cm} \\ r_g &\sim 8.6 \text{ cm} \\ \frac{x}{d} &\sim 2.9 \\ \frac{r_g}{d} &\sim 9.8 \end{aligned} \tag{4.11}$$

Therefore the leakage factor is

$$\xi_m \cong 0.28 \tag{4.12}$$

At its operating point, the magnet block was estimated to have a normal relative permeability:

$$\frac{B_d}{\mu_0 H_d} \cong 1.1 \tag{4.13}$$

Therefore the effective leakage factor for the magnet block is

$$\xi_m' = 0.25 \tag{4.14}$$

Note that since the outer surface of the outer magnet gap is considerably larger than the corresponding inner surface, the magnet blocks are made to protrude 2.5 cm past the outer surfaces to avoid increased leakage. It is assumed that the leakage due to the short air gaps between the adjacent polepiece stacks is negligible. The total leakage factor is simply the sum of the component leakage factors, which is 0.70.

To find the operating point (B_d, H_d) of the permanent magnets on their hysteresis curve, one computes $B_d/\mu_0 H_d$ from:

$$\frac{B_d}{\mu_0 H_d} = \left\{\frac{A_g\ \ell_m}{A_m\ \ell_g}\right\} \frac{B_g}{\mu_0 H_g} \tag{4.15}$$

where: A_g = area of air gap

ℓ_g = length of air gap

A_m = area of magnet block

ℓ_m = length of magnet block

B_g = $\mu_0 H_g$ in air

For the air gap:

A_g = (physical area of gap)(1 + total leakage factor)

and since μ_r = 1.00

ℓ_g = physical length of gap

For the magnet A_m and ℓ_m are the physical area and physical length, respectively. Hence:

$$\frac{B_d}{\mu_0 H_d} = \frac{(2.32 \times 10^{-2}\ \mathrm{m}^2)(1.70)(1.75 \times 10^{-2}\ \mathrm{m})}{(2.32 \times 10^{-2}\ \mathrm{m}^2)(2.69 \times 10^{-2}\ \mathrm{m})}$$

$$= 1.11 \tag{4.16}$$

This slope yields optimum energy product $B_d H_d$ of 2.75×10^4 joules/m^3 for Arnox 5, as shown in Figure 4.10.

$$\begin{aligned} H_d &= 1.41 \times 10^5\ \mathrm{A/m} \quad (1770\ \mathrm{oe}) \\ B_d &= 0.195\ \mathrm{T} \quad (1950\ \mathrm{gauss}) \end{aligned} \tag{4.17}$$

Figure 4.10 Demagnetizing curve for Arnox 5. Second quadrant only is shown. (From data published by Allegheny Ludlum Steel Corp.).

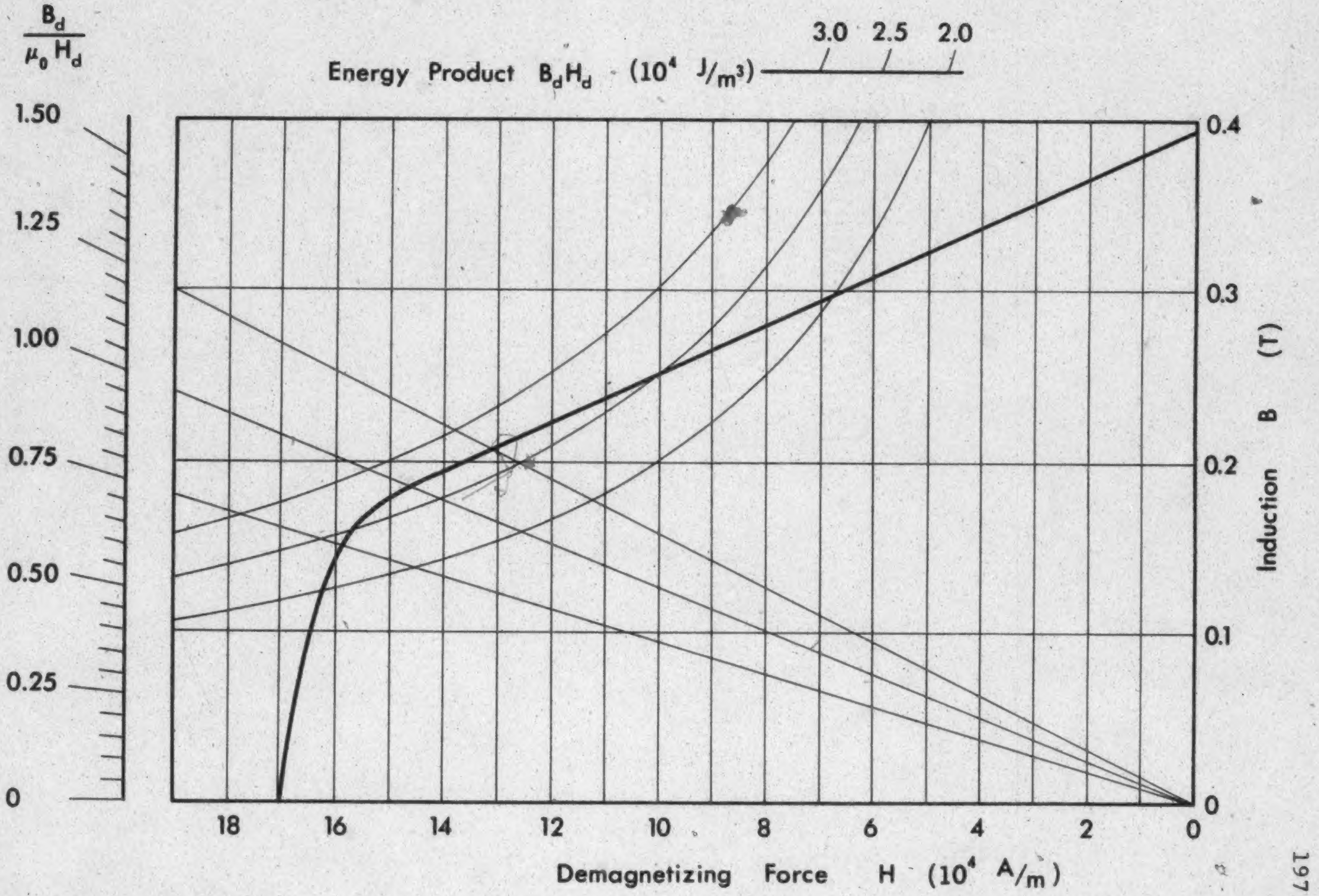
$\frac{B_d}{\mu_0 H_d}$
1.50
1.25
1.00
0.75
0.50
0.25
0
Energy Product B_dH_d (10^4 J/m^3)
3.0
2.5
2.0
0.4
0.3
0.2
0.1
0
Induction B (T)
18
16
14
12
10
8
6
4
2
0
Demagnetizing Force H (10^4 A/m)

Therefore the total flux density in the specimen gap is:

$$B_g = \frac{B_d}{1 + \text{total leakage factor}}$$

$$= \frac{0.195}{1.70}$$

$$= 0.115 \text{ tesla} \qquad (4.18)$$

4.2.2 Magnetizing Requirements and Magnetizing Coils

Having decided to include magnetizing coils, it was necessary to design these to operate without producing excessive thermal stresses or requiring impracticably large power supplies.

The manufacturer of the barium ferrite blocks recommends that they be subjected to a magnetizing force of 6.4×10^5 A/m to give a saturation flux density of 1.27 teslas. However, the permalloy core pieces saturate at 0.87 teslas and would have to be taken well beyond saturation to generate the required field. The hysteresis curve for Arnox 5 in Figure 4.11 shows that very little is lost by taking the magnets to a flux density of only 0.87 teslas. They are still virtually saturated. Thus the coils are designed to produce a uniform 0.87 tesla flux density throughout the core and gaps. This requires a magnetic field intensity of about 3.4×10^5 A/m for the magnets and 6.9×10^5 A/m for the air gaps. We assume that

Figure 4.11 Magnetizing curve for Arnox 5. (From data published by Allegheny Ludlum Steel Corp.).

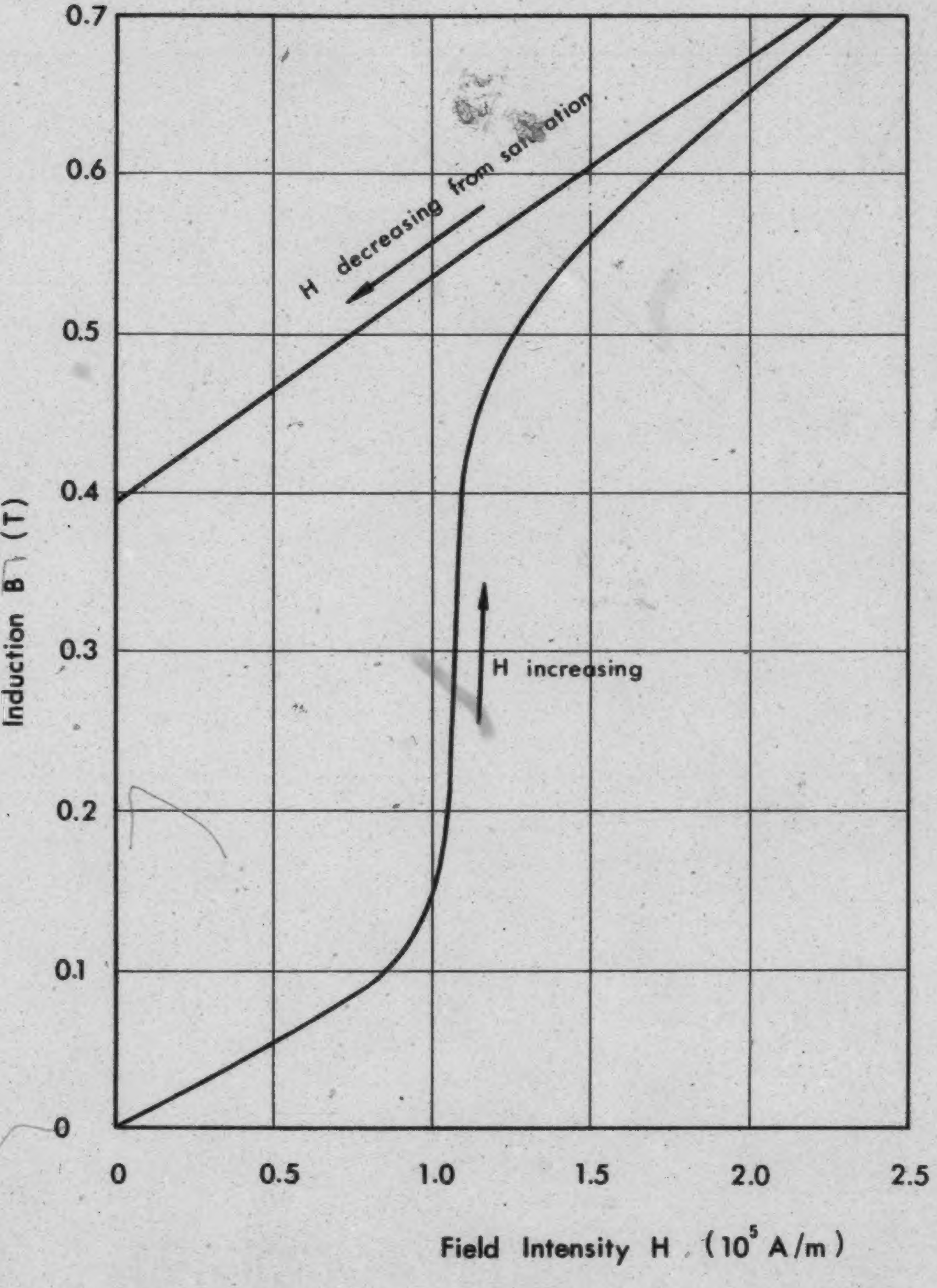
0.7
0.6
0.5
0.4
0.3
0.2
0.1
0
Induction B (T)
0
0.5
1.0
1.5
2.0
2.5
Field Intensity H (10⁵ A/m)
H decreasing from saturation
H increasing

the permalloy polepieces require negligible field intensity.

A flux density of 0.87 teslas throughout the core means a total flux of 19.5 milliwebers. However, the outer permalloy shell shown in Figure 4.3 saturates at a total flux of about 6.5 milliwebers for both halves. Thus an outer magnetizing frame is required to carry the remaining 13.0 milliwebers, if the huge reluctance of the outer air path is to be avoided. Since a good magnetic shield is also desirable, the two functions are combined in a closed box constructed of mild steel and made an integral part of the transducer. Since mild steel saturates at about 1.9 teslas, a total cross section of 68.5 cm^2 throughout is an absolute minimum. This implies a minimum thickness of 1.14 cm on the pieces normal to the core axis, and 0.44 cm on the pieces parallel to the axis. To keep the material out of saturation while still allowing for leakage flux not accounted for, the outer box pieces are made with thicknesses of 1.90 cm and 1.27 cm, respectively. The end pieces of the shield box had to be spaced away from the outer permalloy shell so that thermal noise currents would not affect the signal coils, and so that the box could act effectively as a shield. This gap was arbitrarily set at 1.25 cm on each side. The gap requires a field intensity of about 5×10^5 A/m during magnetizing.

We can now determine the total magnetizing force required from the coils. Figure 4.12 shows that the total

Figure 4.12   Magnetizing force requirements of the main magnetic circuit elements.

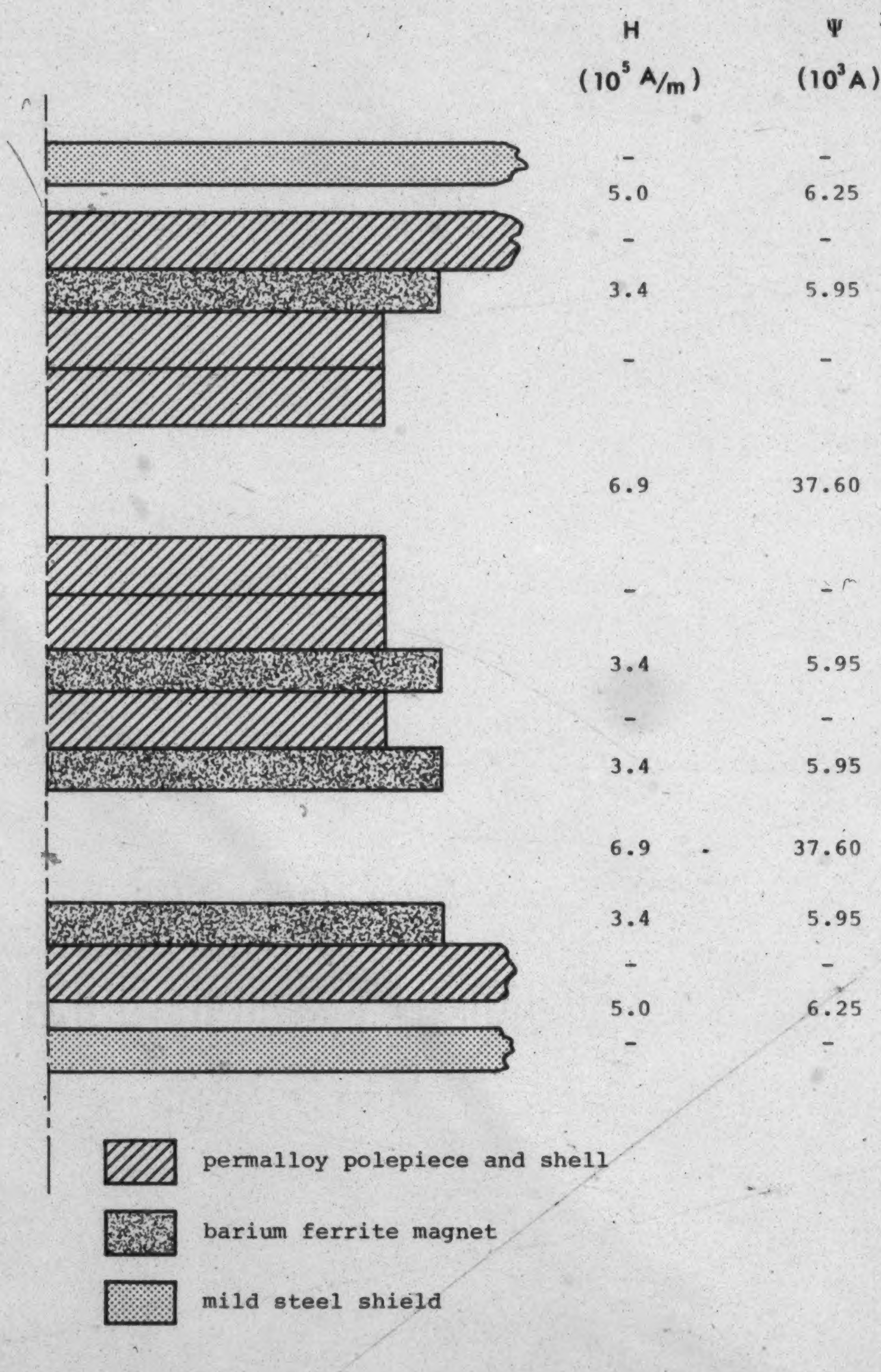
H
(10^5 A/m)
Ψ
(10^3 A)
5.0
6.25
3.4
5.95
6.9
37.60
3.4
5.95
3.4
5.95
6.9
37.60
3.4
5.95
5.0
6.25
permalloy polepiece and shell
barium ferrite magnet
mild steel shield

is 1.12 x 10^5 ampere turns. Effects of air gap leakage would reduce reluctance, hence relaxing the magnetizing force requirement. Thus 1.12 x 10^5 ampere turns is a liberal figure.

4.2.3 The Magnetizing Power Supply

Simple calculation indicated that the large number of ampere turns required for magnetizing could not be provided from the mains supply into a coil of reasonable size. Therefore it was decided to construct a pulse-discharge capacitor-bank supply.

To avoid important eddy current losses in the solid steel outer magnetizing frame, the current rise in the magnetizing coils must be relatively slow. This outer frame has thickness of twice the skin depth at 14 Hz, assuming a relative permeability of 50. A long rise time also prevents damage to stress-sensitive magnetic components by minimizing the rate of change of stress. Large stresses that could result from elastic nonlinearities are thus avoided. Furthermore, slow rise times allow multiple coils to be switched by simple inexpensive relays rather than electronic switching arrangements, because synchronization and contact-bounce problems are minimized. The rise time cannot be made arbitrarily large because of increasing ohmic losses during the magnetizing pulse and hence larger capacitor bank energy storage requirements.

Still neglecting air gap leakage, the magnetic energy required is:

$$E = \Sigma \tfrac{1}{2} BHV \qquad (4.19)$$

where: B = induction

= 0.87 teslas everywhere

H = magnetic field intensity

= 6.9×10^5 A/m in the main air gaps

= 5×10^5 A/m in the end gaps

= 3.4×10^5 A/m in the magnets

V = volumes of the gaps

= 2.42×10^{-3} m^3 for the main air gaps

= 5.62×10^{-4} m^3 for the end gaps

= 1.57×10^{-3} m^3 for the magnets.

Thus we obtain that

$$E = 1080 \text{ joules} \qquad (4.20)$$

To allow for leakage, ohmic losses, and residual energy in the capacitor bank at peak magnetizing current, a total energy storage capacity of 4000 joules was decided on. Electrolytic capacitors suitable for pulse discharge appear to minimize the size, weight and cost per joule of energy storage for ratings of about 400 volts. Since the capacitor stored energy is

$$E = \tfrac{1}{2} CV^2 \qquad (4.21)$$

therefore, at 400 volts

$$C = \frac{2E}{V^2}$$

$$= \frac{(2)(4000)}{(400)(400)}$$

$$= 0.05 \text{ farad} \qquad (4.22)$$

Accordingly, fifty electrolytic capacitors rated at 1000 microfarads, 400 volts D.C. are used.

There was sufficient space within the permalloy magnetic circuit for a solenoid consisting of 6800 turns of #17 AWG enameled wire. This wire gauge was chosen because it allows the wire to conform readily to the contours of the noncircular solenoids and permits a sufficiently large number of turns to allow the solenoid to be used as a signal winding without requiring transformer matching to the amplifier.

In order to get 1.12×10^5 ampere turns from a 6800-turn solenoid, the coil must carry a current of 16.5 amperes. Rough calculation showed that the solenoid could be "matched" to the capacitor bank by dividing it into 8 paralleled sections of equal resistance and approximately equal inductance. Thus the total current required from the power supply is (8)(16.5) = 132 amperes.

We can now calculate the inductance of the solenoid.

$$L = \frac{\text{inductance of 6800-turn series winding}}{(\text{number of sections})^2}$$

$$= (1 + \text{leakage factor})(\frac{n\phi_0}{i_0})(\frac{1}{8})^2 \qquad (4.23)$$

$$= (1 + \text{leakage factor})(\mu_0 n^2)\frac{(\text{area of gap})}{(64)(\text{gap length})}$$

Since a leakage factor is included, the area of the gap is simply the physical area of the polepieces. The leakage factor is estimated to be 0.40. It is different from the leakage factor previously calculated because the leakage flux due to the magnetizing coils has a different geometry from that due to the permanent magnets. The length of the gap is the sum of the effective lengths of the individual gaps. For the air gaps with μ_r = 1.00, this is simply their physical length. For the magnet blocks, the physical length is multiplied by $1/_{\mu_r}$, for convenience evaluated at peak magnetization.

$$\frac{1}{\mu_r} = \frac{\mu_0 \hat{H}}{\hat{B}}$$

$$= \frac{(4\pi \times 10^{-7})(3.4 \times 10^5)}{0.87}$$

$$= 0.49 \qquad (4.24)$$

For the end gaps, only two thirds of the total flux passes, since the remainder is carried by the permalloy shell. This is equivalent to increasing their area by 50% or decreasing their length by 33%, for purposes of inductance. Thus the effective gap length is

$$\ell_g = \text{length of main air gaps} + (0.49)(\text{magnet gaps}) + (0.67)(\text{end gaps})$$

$$= 0.108 + (0.49)(0.070) + (0.67)(0.025)$$

$$= 0.159\ \text{m} \tag{4.25}$$

Substituting this back into Eq. 4.23 gives

$$L = 0.181\ \text{henry} \tag{4.26}$$

Resistance of the solenoid was computed for the eight parallel sections, each measured individually

$$R = 1.438\ \text{ohms} \tag{4.27}$$

The maximum magnetizing current may now be calculated. The equivalent circuit of the magnetizing solenoid and capacitor bank is shown in Figure 4.13. When the switch is closed, we have a single series RLC loop for which, in general:

$$L\frac{di}{dt} + Ri + \frac{q}{C} = 0 \tag{4.28}$$

In this case, $\frac{1}{LC} > \left\{\frac{R}{2L}\right\}^2$, therefore the discharge is oscillatory. The solution to Eq. 4.28 is (Standard Handbook for Electrical Engineers, 1968, p. 2-138)

Figure 4.13 Equivalent circuit of solenoid and capacitor bank just before starting the magnetizing pulse.

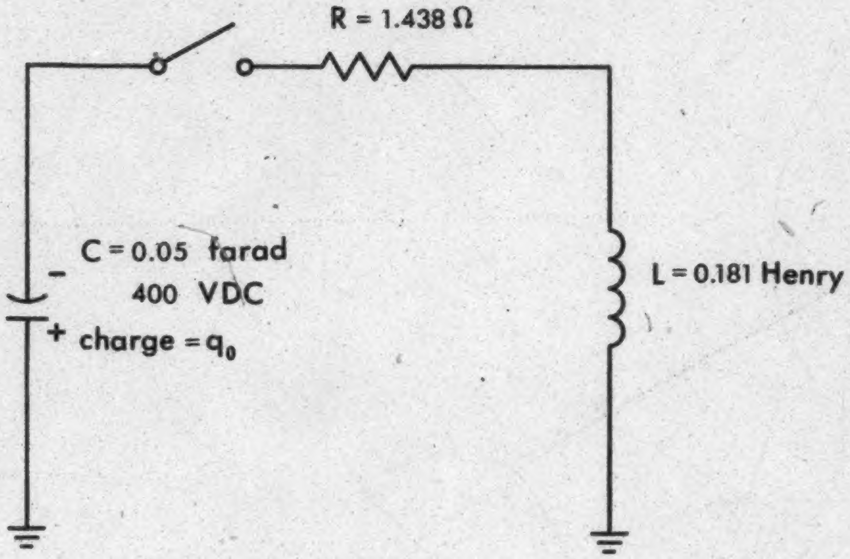
R = 1.438 Ω
C = 0.05 farad
400 VDC
charge = q0
L = 0.181 Henry
–
+

$$i = -\frac{q_0}{LC_g}\epsilon^{-at} \sin gt \tag{4.29}$$

where: $q_0 = CV_0$

$= 20$ coulombs

$$g = \left(\frac{1}{LC} - \frac{R^2}{4L^2}\right)^{1/2}$$

$$= 9.67 \text{ sec}^{-1} \tag{4.30}$$

$$a = \frac{R}{2L}$$

$$= 3.91 \tag{4.31}$$

For maximum current, differentiate and equate to zero:

$$\frac{di}{dt} = -\frac{q_0}{LCg}\left\{\epsilon^{-at} g \cos gt - a\,\epsilon^{-at} \sin gt\right\} = 0 \tag{4.32}$$

$$g \cos gt = a \sin gt$$

$$\tan gt = g/a = 3.47$$

$$gt = 1.29 \text{ radians}$$

$$t = 0.1335 \text{ sec} \tag{4.33}$$

Substituting the values for q_0, g, a and t into Eq. 4.29:

$$i_{max} = 129 \text{ amperes} \tag{4.34}$$

which is satisfactory.

The magnetic circuit is arranged to make a bridge configuration for reasons cited in Section 3.5. In order that the bridge be balanced to direct magnetic flux, it is necessary to have independent control of the state of magnetization of the magnets on either side of the bridge. Accordingly the pulse-discharge power supply is divided into two independent capacitor banks with an independent voltage regulator on each, as shown in Figure 4.14.

4.2.4 Power Supply Circuit Description

The circuits of the primary power supply, shown in Figure 4.15, and the regulators, shown in Figure 4.16, are relatively conventional. The diode decoupling network shown in Figure 4.17 is included with the capacitor bank so that in case of failure-by-shorting of one of the capacitors in the array, the other capacitors cannot discharge through it. An energy of 4000 joules could otherwise produce a serious explosion. It will also be noted that there is an array of rectifier diodes between the output relay bank and the solenoids. The diodes from output to ground clamp the output, and hence the capacitor voltage, essentially at zero after the capacitors have totally discharged. If this were not done, the oscillatory nature of the discharge would cause the capacitors to recharge in the reverse polarity, and would cause a reverse, or demagnetizing, current through the coils. Furthermore, the reverse charge would cause serious deterioration of the polarized dielectric of the electrolytic capacitors in the bank. This could lead to high leakage and ultimately to failure. The diode pairs in series with the solenoid windings ensure a unidirectional

Figure 4.14 Block diagram of the pulse-discharge magnetizing power supply.

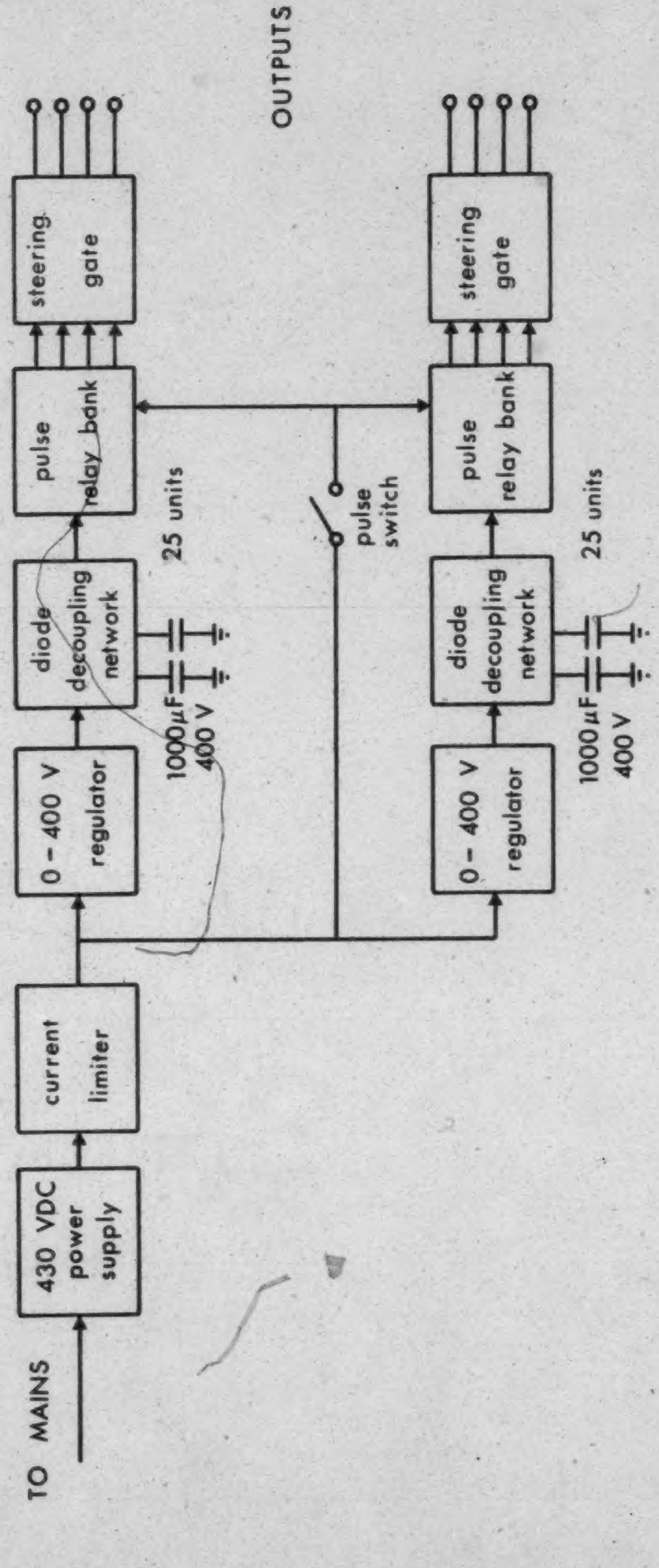
TO MAINS
430 VDC power supply
current limiter
0 - 400 V regulator
diode decoupling network
1000 μF 400 V
25 units
pulse relay bank
steering gate
pulse switch
0 - 400 V regulator
diode decoupling network
1000 μF 400 V
25 units
pulse relay bank
steering gate
OUTPUTS

Figure 4.15 Schematic of primary power supply for capacitor bank.

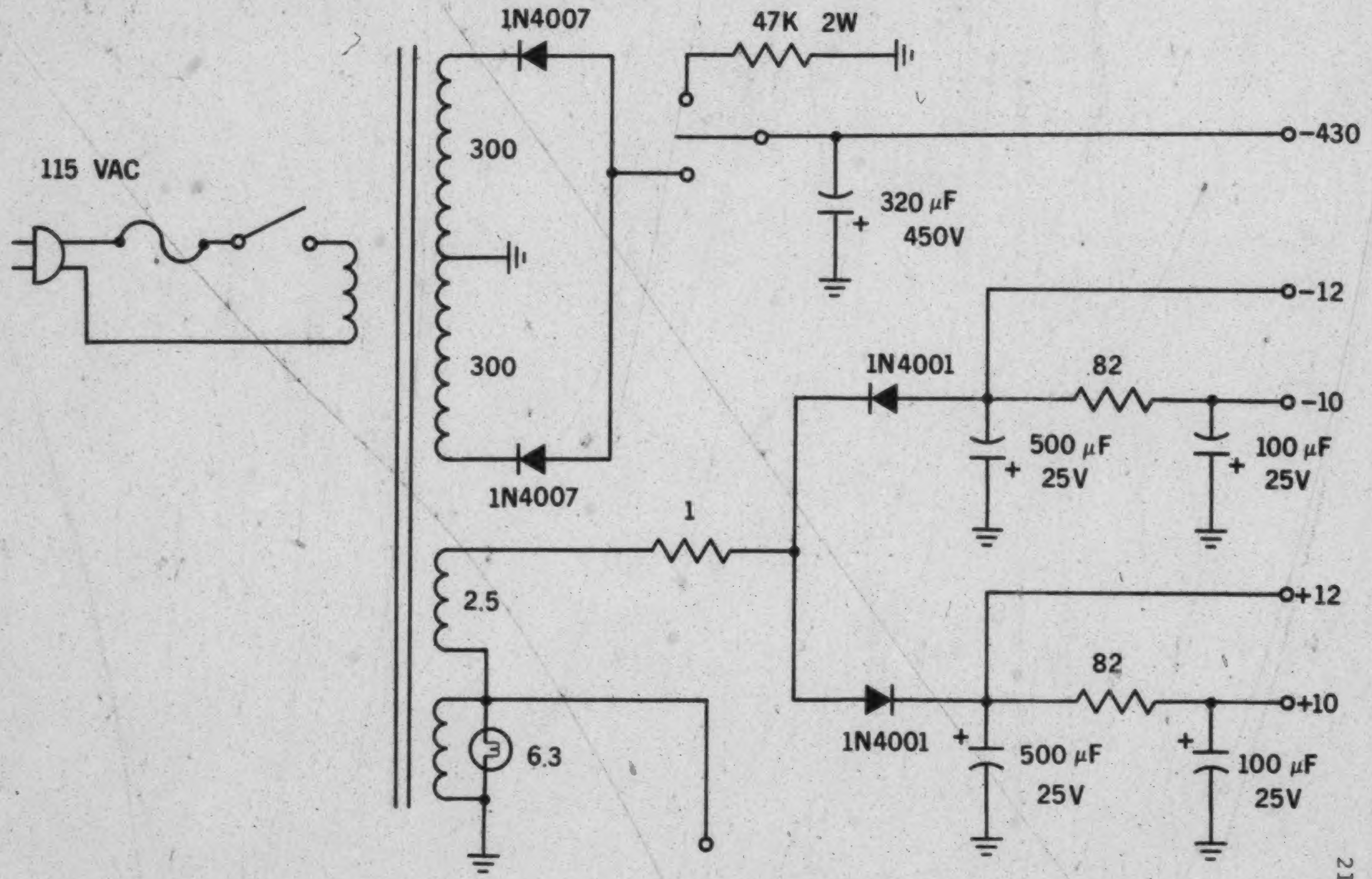

115 VAC
1N4007
300
300
1N4007
47K 2W
-430
320 µF
450V
-12
1N4001
82
-10
500 µF
25V
100 µF
25V
1
2.5
6.3
+12
82
+10
1N4001
500 µF
25V
100 µF
25V

Figure 4.16 Schematic of voltage regulator for pulse-discharge capacitor bank power supply.

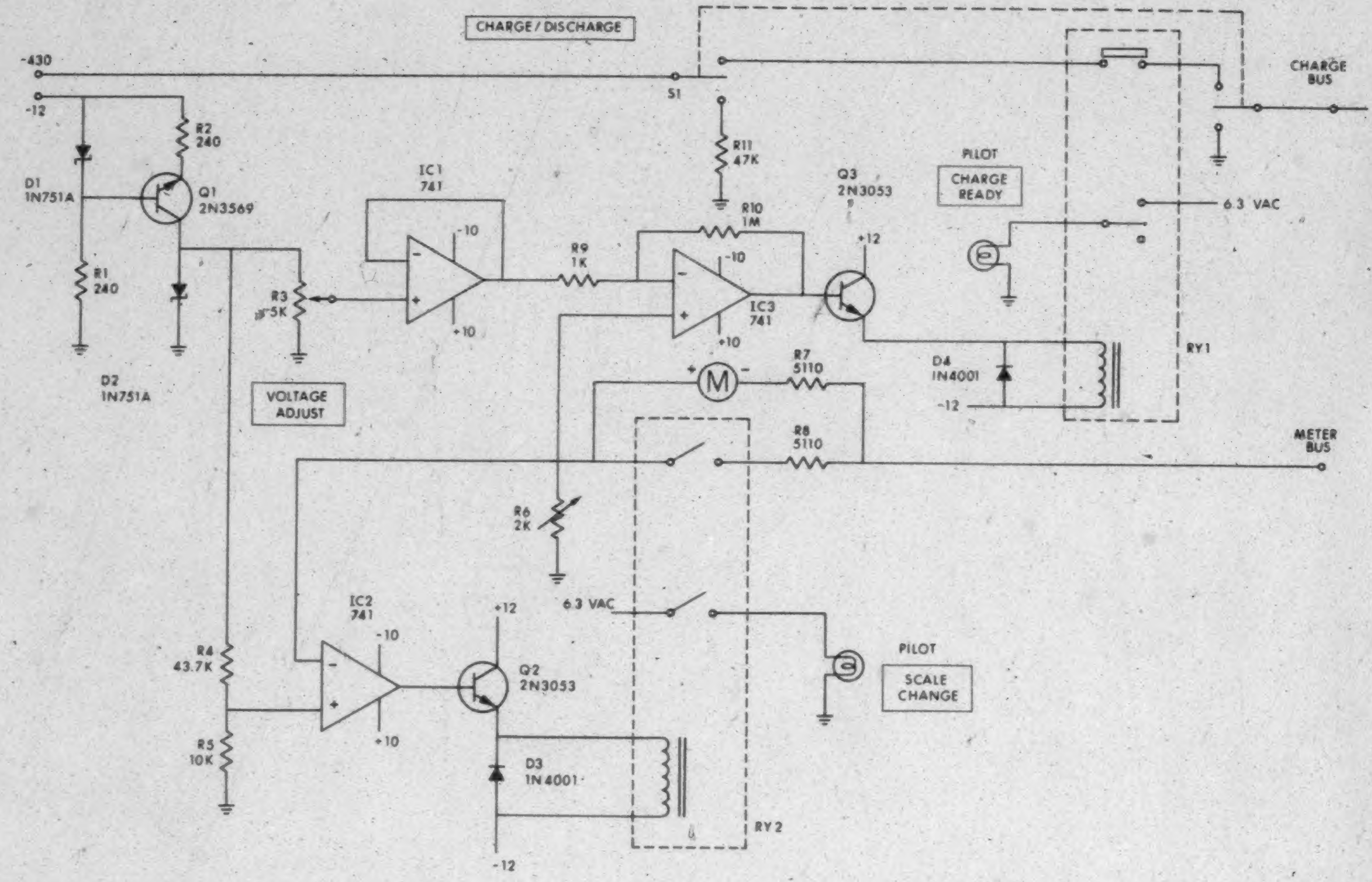
CHARGE / DISCHARGE
-430
-12
S1
CHARGE BUS
R2 240
D1 1N751A
Q1 2N3569
R1 240
D2 1N751A
R3 5K
VOLTAGE ADJUST
IC1 741
-10
+10
R9 1K
R11 47K
R10 1M
IC3 741
Q3 2N3053
+12
PILOT
CHARGE READY
6.3 VAC
RY1
D4 1N4001
-12
M
R7 5110
R8 5110
METER BUS
R6 2K
R4 43.7K
R5 10K
IC2 741
Q2 2N3053
D3 1N4001
RY2
6.3 VAC
PILOT
SCALE CHANGE

Figure 4.17 Diode decoupling network for the capacitor bank.

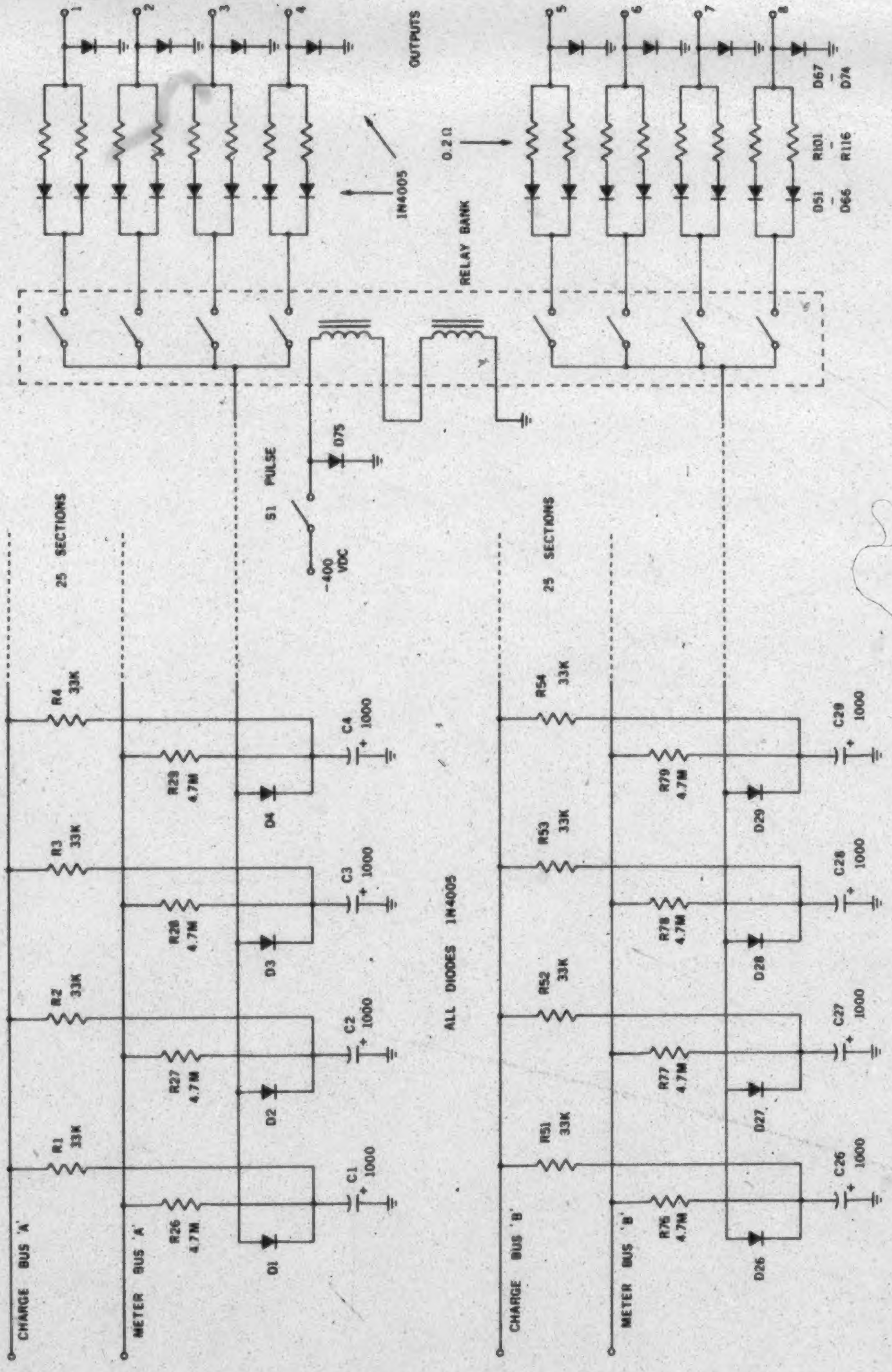
CHARGE BUS 'A'
METER BUS 'A'
R1 33K
R2 33K
R3 33K
R4 33K
R26 4.7M
R27 4.7M
R28 4.7M
R29 4.7M
D1
D2
D3
D4
C1 1000
C2 1000
C3 1000
C4 1000
25 SECTIONS
ALL DIODES 1N4005
CHARGE BUS 'B'
METER BUS 'B'
R51 33K
R52 33K
R53 33K
R54 33K
R76 4.7M
R77 4.7M
R78 4.7M
R79 4.7M
D26
D27
D28
D29
C26 1000
C27 1000
C28 1000
C29 1000
25 SECTIONS
S1 PULSE
-400 VDC
D75
RELAY BANK
1N4005
0.2 Ω
OUTPUTS
1
2
3
4
5
6
7
8
D51 – D66
R101 – R116
D67 – D74

current, even if the inductances of the individual windings do not exactly match. Otherwise, one winding could effectively "short out" another higher-inductance winding by carrying a reverse current.

The temperature rise of the solenoids, assuming a total mass of 50 kg, specific thermal capacity of 385 joules/kg °K, and total adiabatic absorption of 2000 joules, is 0.10 C°. This temperature rise is insufficient to cause differential thermal stress problems, provided pulses are not started in rapid succession.

4.3 Electrical Interference and Shielding

4.3.1 Types of Interference and Methods of Shielding

Electric and magnetic interference is coupled into the transducer windings and low-level electronics by conduction, by near-field induction, and by radiation. The transducer windings are more susceptible to interference than the amplifier and wiring because of their large physical size and high inductance.

Conducted interference between two circuits can occur through any impedance common to both. Frequently, conducting paths exist between circuits because these circuits share a common power supply and common ground path. There are a number of ways to arrange power supply wiring and insert filters to minimize conductive feedthrough. However, it is most effective to provide a separate dry-cell power supply for the first stage of amplification. This is done here. The magnetizing power supply is, of course, disconnected while the instrument is being used for measurements.

Near-field induction results from mutual inductance and mutual capacitance between circuits. Its effects normally diminish with distance from the interference source as the inverse square or inverse cube. On the other hand, the electromagnetic radiation field diminishes as the simple inverse of distance so that, at great distances from the source, the radiation field will predominate. At a distance $r = \frac{\lambda}{2\pi}$ the induction and radiation fields are equal in magnitude. At smaller distances interference is largely induction, at larger distances it is radiation. Since $\frac{\lambda}{2\pi}$ at 400 Hz is about 119 km, it is clear that near-field induction predominates for this instrument.

Electromagnetic shielding is a very effective technique for suppressing both near-field induction and far-field radiation. The attenuation of electromagnetic fields as they pass through a permeable, conductive shield is directly related to the skin effect. The attenuation is precisely the same for electric current, magnetic induction and electromagnetic field intensity. The rate of attenuation is given by

$$\alpha = 15.4 \left(\frac{f\mu_0\mu_r}{\rho}\right)^{1/2} \text{ dB/m} \qquad (4.35)$$

This attenuation is caused by transformation of electric energy into heat. Using a mild steel having $\mu_r = 150$ and $\rho = 10^{-7}$ ohm meters, the attenuation rate at 100 Hz is

$$\alpha = 0.67 \times 10^4 \text{ dB/m} \qquad (4.36)$$

Another source of attenuation from shield materials is that due to reflection as a wave passes from one medium into the next. The impedance of any medium to an electromagnetic wave is given by:

$$Z = \frac{E}{H} \qquad (4.37)$$

Thus for free space we have an impedance:

$$\begin{aligned} Z_0 &= \frac{E}{H} \\ &= \left(\frac{\mu_0}{\epsilon_0}\right)^{1/2} \\ &= 377 \text{ ohms} \qquad (4.38) \end{aligned}$$

In metals this impedance is related to frequency, permeability and resistivity by

$$\begin{aligned} Z_s &= (j\omega\mu_0\mu_r\rho)^{1/2} \\ &= (\pi f\mu_0\mu_r\rho)^{1/2}(1 + j) \qquad (4.39) \end{aligned}$$

Using mild steel with $\mu_r = 150$ and $\rho = 10^{-7}$ ohm meters,

$$Z_s = 7.70 \times 10^{-6} f^{1/2} \quad (1 + j) \tag{4.40}$$

For distances r smaller than $\frac{\lambda}{2\pi}$ from an interfering source (the near-field induction region), the ratio E/H is not equal to 377 ohms. Rather, near an electric field source, the impedance of free space is given approximately by

$$Z_0 \approx -\frac{j}{2\pi f \epsilon_0 r}$$

$$= -1.80 \times 10^{10} \frac{j}{fr} \tag{4.41}$$

Similarly for distances $r \ll \frac{\lambda}{2\pi}$ from a magnetic field source, the impedance of free space is approximately

$$Z_0 \approx -j(2\pi f \mu_0 r)$$

$$= 7.90 \times 10^{-6} jfr \tag{4.42}$$

In all cases, the reflection loss in dB is given by

$$\mathbf{R} = 10 \log \left| \frac{(Z_s + Z_0)^2}{4 Z_s Z_0} \right| \text{dB} \tag{4.43}$$

Considering first electric interference in the near-field region, we see from Eqs. 4.40 and 4.41 that $|Z_s| \ll |Z_0|$ for $f < 10^4$ Hz and $r < 10^3$ meters. Thus the reflection loss becomes:

$$\mathbf{R}_E = 10 \log \left| \frac{(Z_s + Z_0)^2}{4 Z_s Z_0} \right| \quad \text{dB}$$

$$\approx 10 \log \left| \frac{Z_0}{4 Z_s} \right|$$

$$= 10 \log \left[\frac{1.80 \times 10^{10} \ (fr)^{-1}}{4 \sqrt{2} \ (7.70 \times 10^{-6}) \ f^{1/2}} \right]$$

$$= 10 \log (4.13 \times 10^{14} \ f^{-3/2} \ r^{-1}) \qquad (4.44)$$

Setting $f = 100$ Hz and $r = 10$ m, one obtains

$$R_E = 10 \log (4.13 \times 10^{9})$$

$$= 106.2 \ \text{dB} \qquad (4.45)$$

Similarly, for near-field magnetic interference, we see from Eqs. 4.40 and 4.42 that $|Z_s| << |Z_o|$ for $f \sim 100$ Hz and $r \geq 1$ meter. Therefore reflection loss is

$$R_M \sim 10 \log \left| \frac{Z_o}{4 Z_s} \right|$$

$$= 10 \log \left[\frac{7.89 \times 10^{-6} fr}{4 \sqrt{2} \ (7.70 \times 10^{-6}) f^{1/2}} \right]$$

$$= 10 \log (0.181 \ f^{1/2} r) \qquad (4.46)$$

Again, setting $f = 100$ Hz and $r = 10$ meters,

$$R_M = 10 \log 18.1$$

$$= 12.6 \ \text{dB} \qquad (4.47)$$

Thus reflection losses for electric fields are very high while those for magnetic fields are quite low, especially at smaller distances.

The total shielding effectiveness, in terms of insertion loss $\mathbf{S}$, in dB, of the shield is given by

$$\mathbf{S} = \alpha t + \mathbf{R} \tag{4.48}$$

where t is the shield thickness. In Section 4.2 it was shown that a shield thickness of 1.25 cm satisfies its double requirement as a magnetizing frame. With this thickness

$$\begin{aligned} \mathbf{S} &= (0.67 \times 10^4)(1.25 \times 10^{-2}) + \mathbf{R} \\ &= 84 \text{ dB} + \mathbf{R} \end{aligned} \tag{4.49}$$

Substituting values of $\mathbf{R}$ from Eqs. 4.45 and 4.47, one obtains the shielding factors for $f = 100$ Hz and $r = 10$ m.

$$\begin{aligned} \mathbf{S}_E &= 190 \text{ dB} \quad \text{(electric interference)} \\ \mathbf{S}_M &= 97 \text{ dB} \quad \text{(magnetic interference)} \end{aligned} \tag{4.50}$$

4.3.2 Effects of a Hole in the Shield

It is necessary that the transducer shield have at least one hole in one side to admit the spinning shaft and rock specimen. The effect of this hole on the shielding effectiveness of the enclosure is now considered.

As a preliminary, we must determine whether the apparent reluctance of the transducer block, as measured between any two opposite faces, is materially different with or without the presence of the shield. If it were, the total spurious flux passing through the transducer cross-section would depend on the shield's presence. We consider a cubic shield of side 40 cm. Using a mild steel with $\mu_r = 100$ and $\rho = 10^{-7}$ ohm meters, we get at 100 Hz a skin depth of

$$\delta = 504 \left[\frac{\rho}{\mu_r f}\right]^{1/2}$$

$$= 1.59 \times 10^{-3} \text{ m} \tag{4.51}$$

Therefore the effective cross-sectional area is

$$A_s = (\delta)(\text{shield perimeter})$$

$$= (1.59 \times 10^{-3})(1.60)$$

$$= 2.55 \times 10^{-3} \text{ m}^2 \tag{4.52}$$

The effective cross-sectional area without the shield is simply $(0.40)(0.40) = 0.16 \text{ m}^2$. Thus the shield reduces the area by a factor of 63. However, this reduced area is approximately balanced by the relative reversible permeability of the shield of 100. Thus the reluctance of the block at 100 Hz is essentially the same regardless of the shield's presence. Therefore the noise flux is only minimally disturbed outside the shield.

Consider a spurious, spatially uniform magnetizing force H_N in the vicinity of the transducer. The noise flux to be passed by a cubic magnetic shield of side x can be roughly approximated by:

$$\phi_N = \mu_0 H_N \text{ (cross-sectional area of shield box)}$$

$$= \mu_0 H_N x^2 \qquad (4.53)$$

For the present calculation it may be assumed that flux passes passes with uniform density to a depth equal to the skin depth δ below the outward-facing surfaces of the shield, with no flux penetrating below that depth. For this approximation to be valid it is required that all joints in the enclosure be magnetically "tight". This would require closely-fitting, overlapping panels, or a welded enclosure.

Because of the non-vanishing reluctance of the shield walls, there is a magnetic potential gradient along the walls in the direction of the spurious magnetizing force. Although the equipotentials are somewhat distorted by the presence of the hole, we may assume, as a first approximation, that the magnetic field intensity H_N' within the hole is equal to that in the flux-carrying skin of the shield wall, away from the immediate vicinity of the hole, as shown in Figure 4.18. This field intensity is

$$H_N' = \frac{\text{flux density in the flux-carrying skin}}{(\mu_0)\text{(reversible permeability of shield material)}}$$

$$= \frac{\phi_N}{\{4x\delta\ \mu_0 \mu_r\}} \qquad (4.54)$$

As a further approximation, we may replace the magnetic effect of the hole with that of a current loop with its

Figure 4.18 Approximate equipotentials and flux lines in a magnetic-shield wall containing a hole.

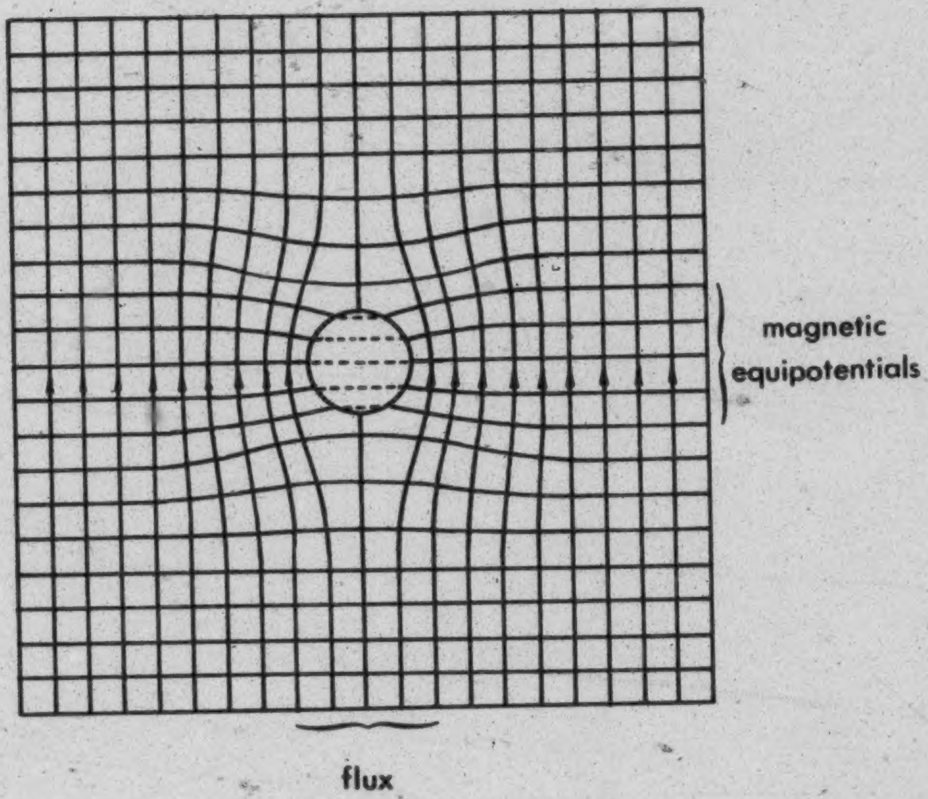
magnetic equipotentials
flux

axis in the z-direction, radius a equal to that of the hole, and carrying a current $2aH_N'$. In general, the axial field intensity in the plane of a current loop of radius a and carrying a current i, at a distance d from its center is

$$H = \frac{i}{2a}\left[\frac{a^3}{2d^3} + \frac{9a^5}{16d^5} + \ldots\ldots\right] \tag{4.55}$$

If $\frac{a^2}{d^2} << 1$, then the second and succeeding terms are negligible. Therefore

$$H \simeq \frac{ia^2}{4d^3} \tag{4.56}$$

Thus, substituting $i = 2aH_N'$, and using Eqs. 4.53 and 4.54, we get the effective noise field intensity H_N''

$$\begin{aligned} H_N'' &= \frac{2aH_N'a^2}{4d^3} \\ &= \mu_0 H_N x^2 \left[\frac{2a^3}{4d^3}\right]\left[\frac{1}{4x\mu_0\mu_r}\right]\left[\frac{1}{504}\right]\left[\frac{\mu_r f}{\rho}\right]^{1/2} \\ &= 2.5 \times 10^{-4}\ \frac{xa^3}{d^3}\left(\frac{f}{\mu_r \rho}\right)^{1/2} H_N \end{aligned} \tag{4.57}$$

Thus the noise field leakage due to the hole is

$$\begin{aligned} L_H &= \frac{H_N''}{H_N} \\ &= 2.5 \times 10^{-4}\ \frac{xa^3}{d^3}\left[\frac{f}{\mu_r \rho}\right]^{1/2} \end{aligned} \tag{4.58}$$

Specifically, at the center of the shield where $d = x/2$

$$L_H = 2.0 \times 10^{-3} \frac{a^3}{x^2} \left[\frac{f}{\mu_r \rho} \right]^{1/2} \tag{4.59}$$

Taking a minimum value of 2.5 cm for the hole radius a, setting $x = 40$ cm as a maximum reasonable shield size, and substituting $\mu_r = 100$ and $\rho = 10^{-7}$ ohm meter for the mild steel used, we get for the leakage at a frequency of 100 Hz

$$L_H = 6.2 \times 10^{-4} \tag{4.60}$$

This corresponds to shielding of 64 dB. Thus the existence of the hole clearly limits the shield's effectiveness.

There are also holes required for mounting the electrical connectors, but these are smaller and may be placed immediately behind the outer shell of the permalloy magnetic circuit. Hence they cause no problems.

Where external noise is serious enough, the leakage factor of the hole can be materially reduced by placing a laminated silicon steel or permalloy collar around the hole, as in Figure 4.19. This results in a large reduction in magnetic potential gradient in the immediate vicinity of the hole, at the expense of a larger gradient elsewhere on the shield, where it is harmless.

It should be noted that noise leakage through the hole depends on the orientation of the spurious magnetizing force. If it is perpendicular to the plane of the shield

Figure 4.19 Change in magnetic equipotential distribution due to collared hole.

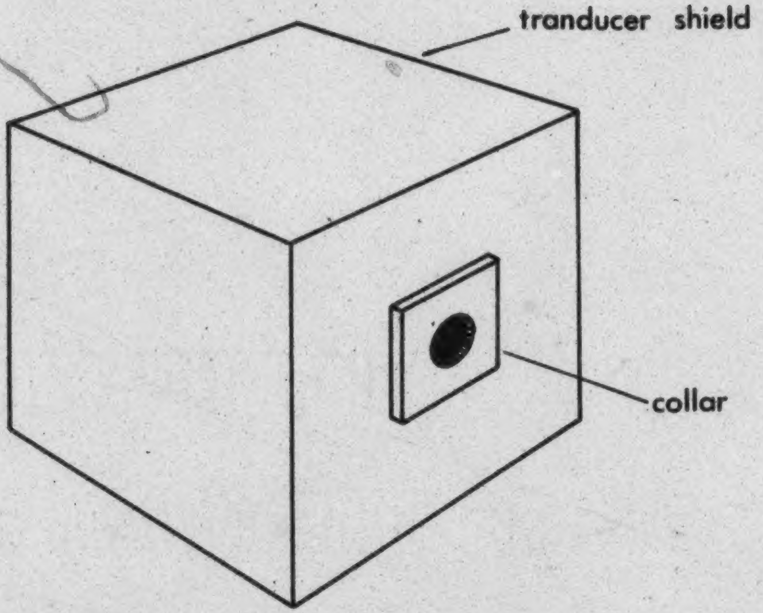
tranducer shield
collar

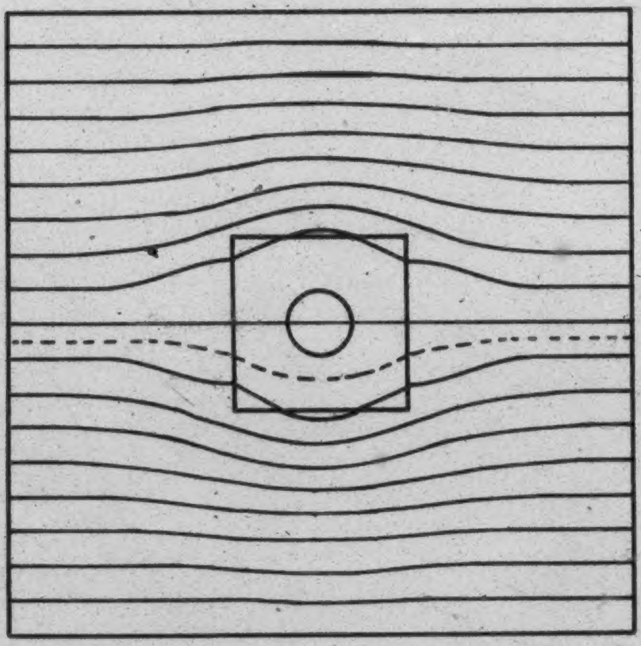

wall containing the hole, there will be only a very small potential gradient across the hole and hence a small leakage factor. Leakage becomes maximum where H_N is in the plane of the shield wall containing the hole.

4.4 Encapsulation of the Transducer

4.4.1 Encapsulation Requirements

It was decided to cast the entire transducer into a single solid block for three main reasons:

1. To minimize vibrations which would generate spurious signals.
2. To minimize thermal fluctuations and their effects on transducer components.
3. To sustain the large mechanical forces which act during and after magnetizing.

Simple coherent vibration of the whole transducer is reduced by encapsulation only by virtue of the increased mass. Such vibration is important only in relation to the relatively small external electric and magnetic fields. These are largely controlled by extensive electrostatic and magnetic shielding; by suitable differential configuration of the magnetic bridge circuit, signal coils, and electronic amplifiers; and by sensing field gradients rather than field intensity or its time rate of change.

Differential vibration of component parts of the transducer assembly can produce enormous noise effects by virtue of the very large magnetic fields existing virtually everywhere inside the transducer shield. The permalloy, ferrite, and copper portions of the transducer are the main components which will produce signal in response to differential vibration. All have internal mechanical resonances. They also resonate, usually at much lower frequencies and behaving approximately as simple masses, with their supporting structures which provide a spring constant. In minimally supported structures both types of resonance can have a very high Q-factor because of the relatively small mechanical losses within the materials involved.

Inevitably all transducer elements are mechanically excited at the signal frequency. The rotating shaft exerts radial forces onto its supporting structure because of its imbalance. This imbalance results largely from nonuniformity of rock specimens and uncertainty in positioning them within the specimen cup. Only the second and higher harmonics of the rotational frequency are of importance, but even if the shaft imbalance were so distributed as to produce only a fundamental-frequency force, the harmonics would be generated by the stress-strain nonlinearities present in virtually any mechanical bearing or support system. The magnitude of the forces transmitted may be minimized by mounting the shaft assembly and the transducer block separately on lossy rubber springs. There is also airborne (acoustic) noise from the rotating shaft because of imperfect geometrical symmetry about the axis of rotation. This results from the practical necessity of using nonspherical specimens. The drive motor and coupling ball bearings also tend to produce considerable acoustic noise. Noise from the necessarily large main shaft bearings near the specimen cup was virtually eliminated by using aerostatic journal bearings, as will be discussed in Section 4.6.

Both acoustically and mechanically transmitted noise apply a driving force to the external shield structure. In order to minimize the effects of this force, it is necessary to:

1. Mechanically support all transducer components in such a way that differential movement is minimized. This is best accomplished by filling all waste spaces within the transducer with a suitable stiff and lossy encapsulant substance.
2. Ensure that the effective spring constant k of the total support of each circuit element must give, with the mass of that element, a resonant frequency $\frac{1}{2\pi}\sqrt{\frac{k}{m}}$ well above 400 Hz. This is the highest fundamental signal frequency anticipated and is limited by the maximum

shaft speed of 200 Hz.

3. Ensure that the mechanical supports have sufficiently great internal losses to make the Q-factors of the various resonances small, preferably smaller than unity.

In regions where there is a thickness greater than 3 cm or so of supporting encapsulant between two circuit elements, the effective modulus of the support is raised by embedding into it high-modulus ceramic pillars, strategically positioned relative to the circuit elements supported. One of the lowest-frequency resonances remaining will be that of the entire magnetic-circuit-with-coils acting as a simple mass and supported by the encapsulating material between the outer surface of the magnetic circuit and the enclosing shield structure (see Figure 4.20). The internal structure has a total mass of about 200 kg. The encapsulating material is assumed to act as a simple spring with rectangular geometry indicated in the diagram. Its spring constant is given by

$$k = Y \frac{A}{d} \tag{4.61}$$

where: Y = Young's modulus of encapsulant

A = total cross-sectional area of spring

d = depth of spring in direction of compression.

Figure 4.20 Delineation of effective mass and spring for calculating the lowest mechanical resonance frequency of the transducer block.

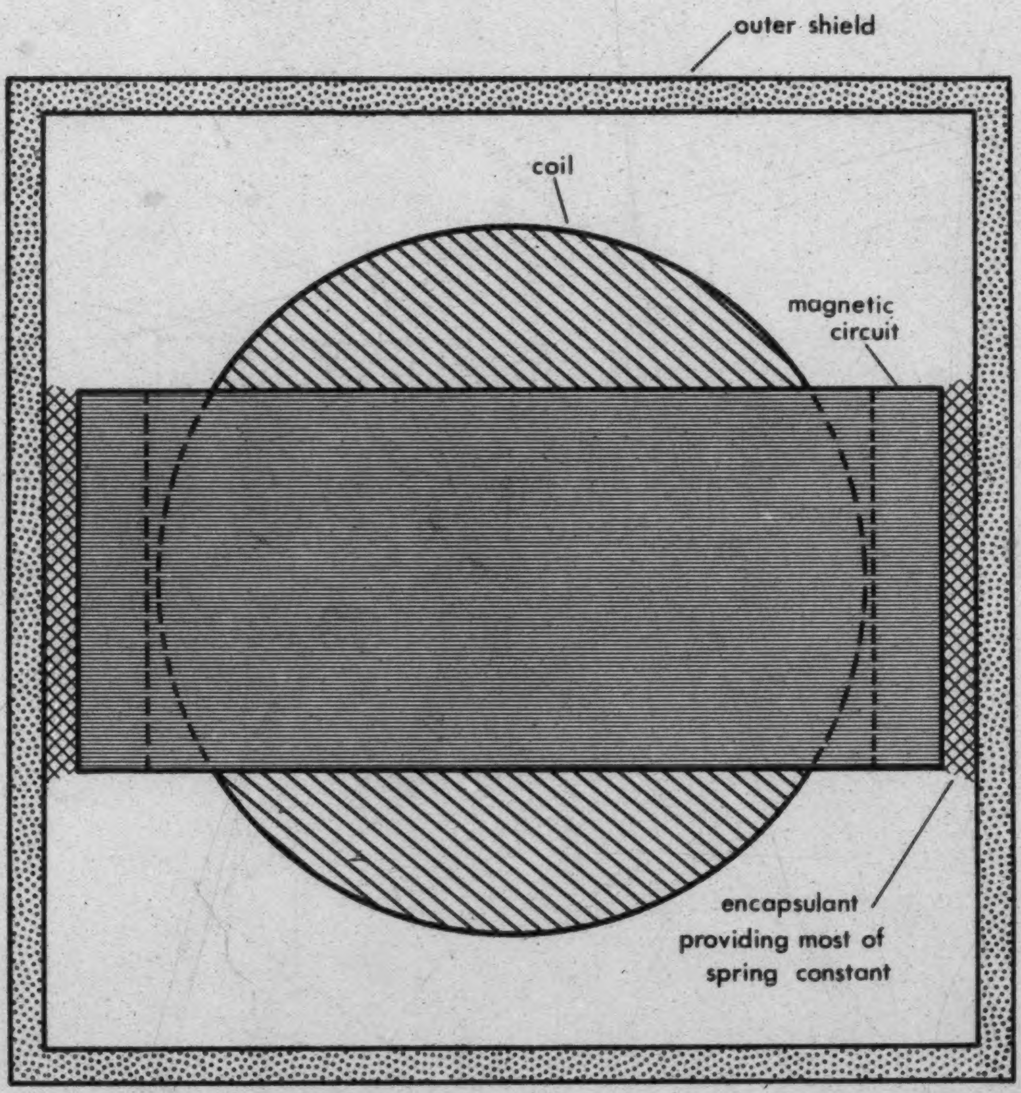
outer shield
coil
magnetic circuit
encapsulant providing most of spring constant

If the resonant frequency f_0 is to be made larger than, say, 1000 Hz, then

$$k \geq 4\pi^2 f_0^2 m$$

$$= 7.9 \times 10^9 \ \text{N/m} \qquad (4.62)$$

Thus we find the modulus required:

$$Y \geq \frac{kd}{A}$$

$$\geq \frac{(7.9 \times 10^9 \ \text{N/m})(1.25 \times 10^{-2} \ \text{m})}{0.107 \ \text{m}^2}$$

$$= 0.92 \times 10^9 \ \text{N/m}^2 \qquad (4.63)$$

The presence of encapsulant in all spaces other than the two shaded in the diagram will further raise k and thereby f_0. Since all other resonances are expected to be of higher frequency, a modulus of 10^9 N/m² is appropriate for the encapsulant.

4.4.2 Encapsulant Limitations

One could not simply specify a casting resin of the required Young's modulus because of two limitations:

1. Epoxy resins are powerful adhesives and contract considerably during and after cure, thus exerting large stresses on contained and containing surfaces. While the permalloy components must be held by the encapsulant, they

must not be permanently stressed beyond about 10^7 N/m^2 or there will be a considerable reduction of the initial and reversible permeabilities. Furthermore, even temporary stresses must not exceed about 10^8 N/m^2 as they would take the permalloy into its elastically nonlinear region and would result in permanent irreversible loss of initial and reversible permeabilities (see Figure 3.11).

2. Stress due to temperature changes in a block made of materials with differing coefficients of thermal expansion could similarly be harmful and must be kept to less than 10^7 N/m^2.

A first approximation to the magnitude of stresses applied to embedded components may be obtained by casting small pressure transducers into the encapsulant material being considered. After cooling to room temperature, pressures as high as 2.3 x 10^8 N/m^2 have been observed in so-called "rigid" epoxy systems (Stucki et al., 1967). It is worth considering that for any given encapsulant material, stresses produced on embedded components are anisotropic and depend on the aspect ratio or geometry of the embedded part. Indeed, if the aspect ratio becomes extremely large, as in a thin filament or film, the linear spring constant of the embedded component becomes much less than that of the body of encapsulant imparting a stress to it. This being the case, the component is subjected to the same linear strain as the encapsulant, and the resulting linear stress is simply the product of strain and Young's modulus of the component. Thus, given a typical cure-induced linear strain of 1% in epoxy resins, and a Young's modulus of about 2×10^{11} N/m^2 for permalloy, we get maximum stresses of about 2×10^{9} N/m^2.

In epoxies cure-induced strain occurs while the epoxy/curing-agent system is in a liquid state, while it is in a thermoplastic state, and after it has gelled. The strain is of two kinds: that caused by the reaction and rearrangement of the molecules into a more compact configuration; and thermal shrinkage, brought about by the cooling of the cured resin from higher reaction temperatures. Most of the reaction-produced strain occurs before gellation, so that the effect can be largely offset by feeding in additional resin while the reaction progresses. Clearly, no stresses are developed before gellation. After gellation starts and for the remainder of the cure process, stresses are produced on embedded components. One very effective way to keep these stresses small is to incorporate so-called "flexibilizing agents" into the epoxy resin. Although the name suggests production of a true elastomer, one actually obtains a visco-elastic "solid". Thus, even after gellation commences, there is sufficient flow to largely relieve stresses as they are generated. Optimal stress relief is predicated upon curing at an optimum temperature which is high enough to keep viscosity sufficiently low for flow to occur, but low enough to keep the reaction rate and hence rate of reaction-produced strain build-up low. After curing is completed and the casting cools, the viscosity increases very rapidly and the epoxy becomes essentially an elastic solid. The lower Young's modulus of the flexibilized epoxy will keep stress due to thermal shrinkage from becoming excessive. A typical plot of pressure vs. temperature as measured by a pressure transducer during cooling is shown in Figure 4.21.

A disadvantage of "flexibilized" systems is that some viscous behaviour remains even after cooling to room temperature. Thus, given large pressure and long periods of time, some flow will occur. It is thus necessary to provide nonviscous supports, embedded into the resin, to keep all components from shifting due to gravitational effects.

Particulate filler materials may be used with the epoxy resin to further reduce cure-induced strain, reduce the coefficient of thermal expansion of the cured composite to bring it nearer to that of encapsulated components and hence reduce thermal stresses, and to raise the

Figure 4.21 Pressure exerted on encapsulated pressure transducers by a flexible epoxy resin formulation after curing and cooling. (After Hanson and Tuzinski, 1959).

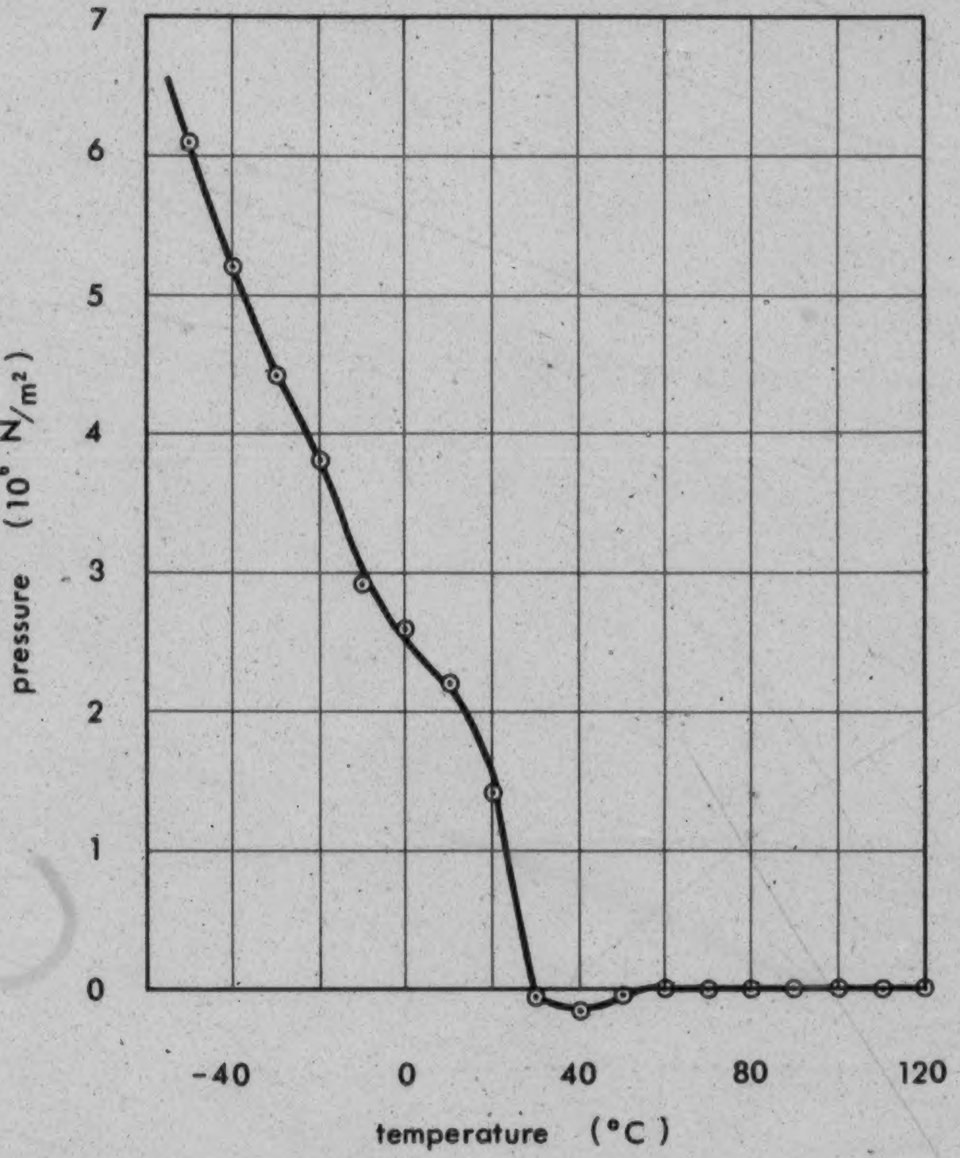
pressure (10^6 N/m^2)
7
6
5
4
3
2
1
0
-40
0
40
80
120
temperature (°C)

Young's modulus of the composite encapsulant. Young's modulus for a typical flexible epoxy is about 10^8 N/m^2. In this application the modulus must be larger by one order of magnitude.

For small loading volumes of filler, the cure-induced volume strain is reduced in proportion to the filler loading volume. The reduction in strain is brought about by bulk displacement of the resin with an inert compound which does not undergo permanent dimensional change during the cure process. In addition, the filler also absorbs exotherm heat and thereby moderates extremes of temperature change during curing. As loading volumes approach the maximum possible, volume strain decreases faster than the percentage of resin in the mixture. This is because a large proportion of the resin receives a positive mechanical volume strain from the filler particles to partially compensate for the negative volume strain due to the curing reaction. Indeed, if for a filler one used equal-sized spheres of infinite modulus and in a closest-packed array, then it is clear that the two volume strains would completely cancel because a net volume strain of zero would have to result. For completely analogous reasons, the coefficient of thermal expansion and the compressive modulus approach those of the filler material when extremely high loading volumes of filler are used.

Unfortunately, the viscosity of a resin-filler system increases rapidly at large loading volumes. By considering a system of rigid, non-solvated spheres dispersed in a viscous Newtonian fluid, Mooney (quoted by Seymour, 1972) arrived at a semi-empirical modification of Einstein's equation for relative viscosity:

$$\frac{\nu}{\nu_0} = \frac{2.5C}{1 - \beta C} \qquad (4.64)$$

where: ν = viscosity

C = partial volume occupied by filler

β = hydrodynamic factor.

The factor β is itself a function of partial volume occupied by the filler, but approaches 1.91 for loosely packed spheres and 1.35 for close-packed spheres. Viscosity tends to infinity as maximum loading is approached.

The problem is solved by putting the filler particles in place before the resin, and then impregnating the entire unit with filler-in-situ. Even then, a very low-viscosity resin must be found and the impregnation must be done in vacuum. This also ensures that all non-filled voids, such as spaces between turns of wire on the coils, are completely impregnated. Various reactive diluents may be used with epoxies to reduce their pouring viscosity while not causing serious deterioration of mechanical properties after cure. Several proprietary resin systems were tested.

The resin selected was 3-M Scotchcast No. 237, which has a viscosity of 30 centipoise at 120°C, one of the lowest available. Gel time is about 90 minutes at 90°C and cure time is about 8 hours at the same temperature. Young's modulus is about 2 x 10^8 N/m^2 after cure. Typical cure-induced stress curves are given in Figure 4.22. Inverse viscosity is plotted against time for two curing temperatures in Figure 4.23.

To raise Young's modulus by the necessary factor of five and reduce stress during curing, a filler had to be found which would admit the resin to a depth of 30 cm well within the gel time under a pressure of 10^5 N/m^2. This pressure is convenient since the atmosphere can be used to apply it with the transducer assembly in vacuum. Larger pressures would tend to disturb transducer components during the initial stages of impregnation and might cause strain in parts of the permalloy. Silica sand was tried and found to exclude the resin. Solid glass spheres were eventually chosen as a filler. Those used range in diameter from 0.1 to 1.0 mm. They allowed rapid and complete impregnation. Stress gradients which remain between filler particles are not harmful over distances less than 1 mm. The glass beads were easy to handle and readily flowed into all cavities requiring filler.

For reasons including the awkward curing cycle and the relatively high viscosity, the Scotchcast No. 237

Figure 4.22 Pressure due to cure-induced strain for Scotchcast No. 237 epoxy resin.

1. Cure 2 hours at 120°C.
2. Cure 16 hours at 95°C.
3. 40% filler, cure 2 hours at 120°C.

(After data published by 3-M Company).

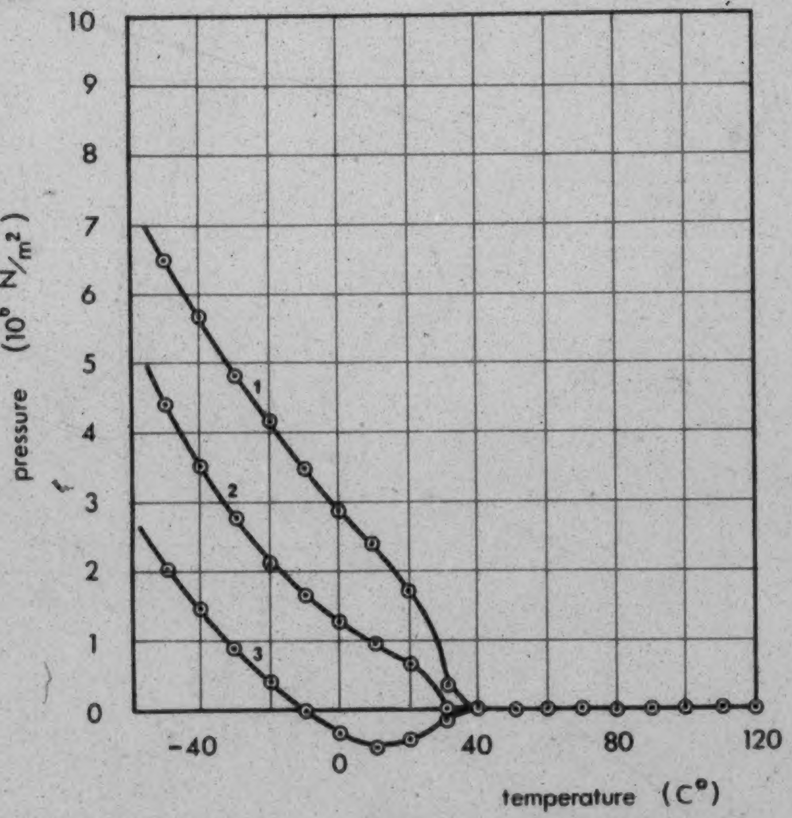
pressure (10^6 N/m^2)
10
9
8
7
6
5
4
3
2
1
0
-40
0
40
80
120
temperature (C°)
1
2
3

Figure 4.23 Decrease in inverse viscosity with time during the curing process of Scotchcast No. 237 epoxy resin. Curves are plotted for two curing temperatures. (After data published by 3-M Company).

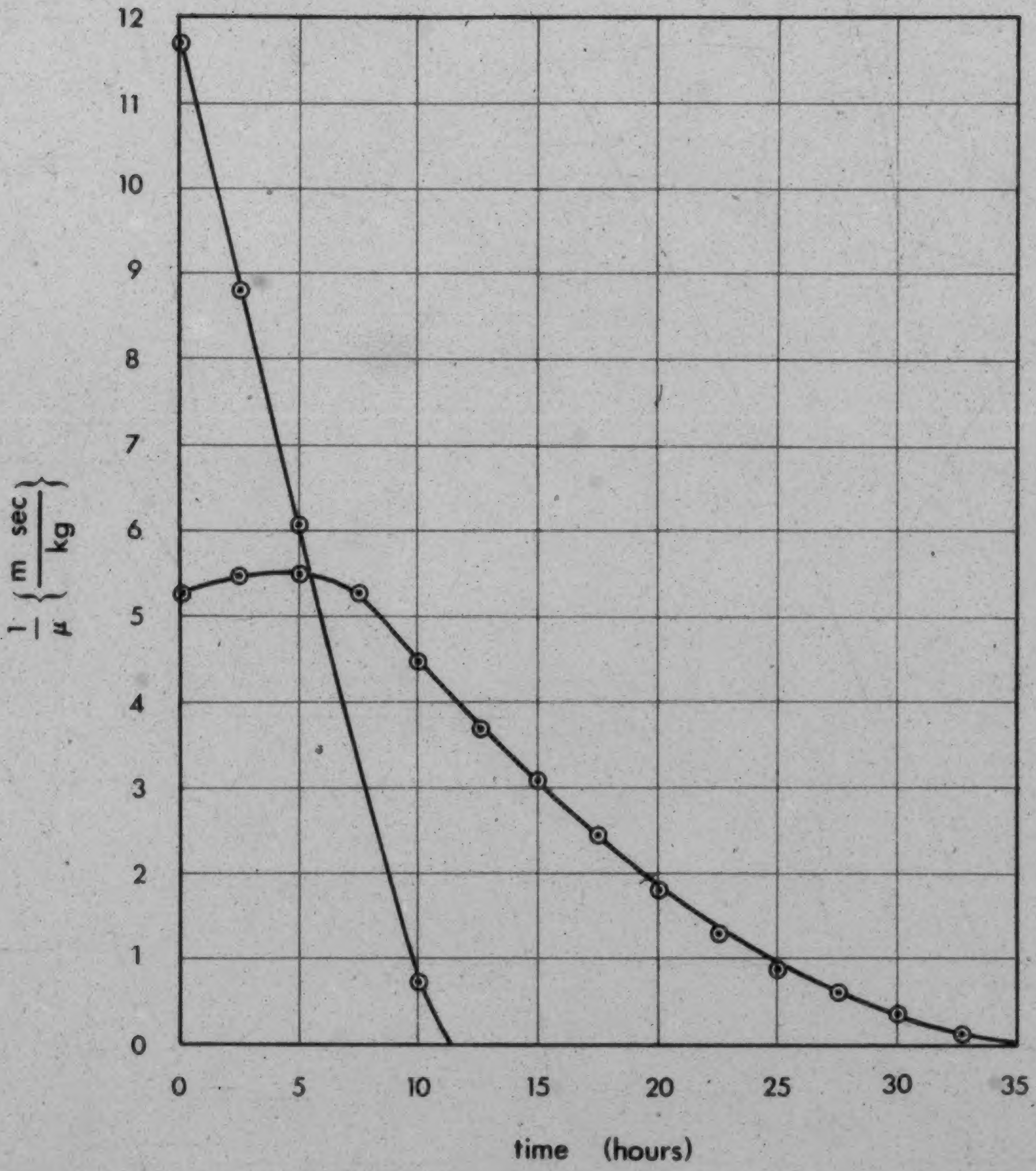
12
11
10
9
8
7
6
5
4
3
2
1
0
$\frac{1}{\mu}\left\{\frac{m\ sec}{kg}\right\}$
0
5
10
15
20
25
30
35
time (hours)

was not used for some subassemblies of small size or requiring only thin films of resin. Thus the signal coils, some of which are wound with #35 AWG wire, were individually impregnated with a low-viscosity polyester casting resin thinned with styrene monomer, and cured with promoter and catalyst at room temperature. Stress produced by the curing resin does not affect the copper and strengthens the coil. Also, so-called "rigid" room-temperature-curing epoxies were used in thin films to bond similar materials within the transducer structure, in particular to bond stacks of permalloy laminations. Where film thickness is much smaller than lamination thickness, virtually all strain is in the epoxy, rather than in the bonded material.

It was essential that various portions of the magnetic circuit be in accurate alignment with the outer casing during and after casting. Also, it was essential that component sections not move while the epoxy was being injected. Thus rigid supports had to be provided for most parts. These supports had to withstand gravitational and viscous forces on the parts supported, but transmit no thermal expansion stresses to them. To this end, only one of any two opposite sides of any magnetic component is rigidly connected to the outer frame. The supports are ceramic pillars made from blocks of hydrous aluminum silicate, available commercially under the trade name LAVA.

This material works easily with a jig saw and disc sander while it is still "green" or unfired. The fired pieces were cemented in place with small quantities of room-temperature-curing epoxy resin.

The support of the many connecting wires presented further problems. The very fine wires of the signal coils were soldered to #17 AWG wire quite near the coil concerned. The soldered joint and the free part of the thin wire were then cemented to the coil itself with rigid epoxy. Thus the wires were strong enough to resist breakage by small shifts in the filler during impregnation. Temperature-sensing diodes were similarly affixed to rigid portions of the structure. All wires were routed to two eighteen-pin sockets mounted on the outer shield. They were attached to the structure every ten to fifteen cm in dabs of flexible RTV silicone rubber. This material served admirably to keep the individual leads apart, yet was sufficiently flexible to prevent wire breakage in case of shifting filler.

4.5 Electronics

A block diagram of the signal electronics is shown in Figure 4.24. The two pairs of signal coils and two pairs of nulling coils are connected to a selector switch. In one position, "direct", one measures specimen magnetization parallel to the applied field. In the other position, "cross-field", magnetization normal to the applied field is measured. The signal and noise outputs then go to separate low-noise preamplifiers of equal gain. Both inputs and outputs of the preamplifiers are differential. Since the Q-factor of the specimen-gap coils is low ($Q \simeq 2$) at a frequency of 100 Hz, the coils are not tuned. Thus phase shift as a function of operating frequency is not a problem. Also, nonlinear magnetization effects can be seen, since the harmonic content of the signal remains intact.

The outputs from the preamplifiers pass through low-pass filters having variable cut-off frequency. They are then amplified by separate variable-gain direct-coupled differential amplifiers with single-ended outputs. The two outputs are then mixed by a differential amplifier which has variable gain for the null channel to effect an interference-nulling control. The mixed signal then passes through a high-pass filter having a variable cut-off fre-

Figure 4.24 Block diagram of the signal electronics.

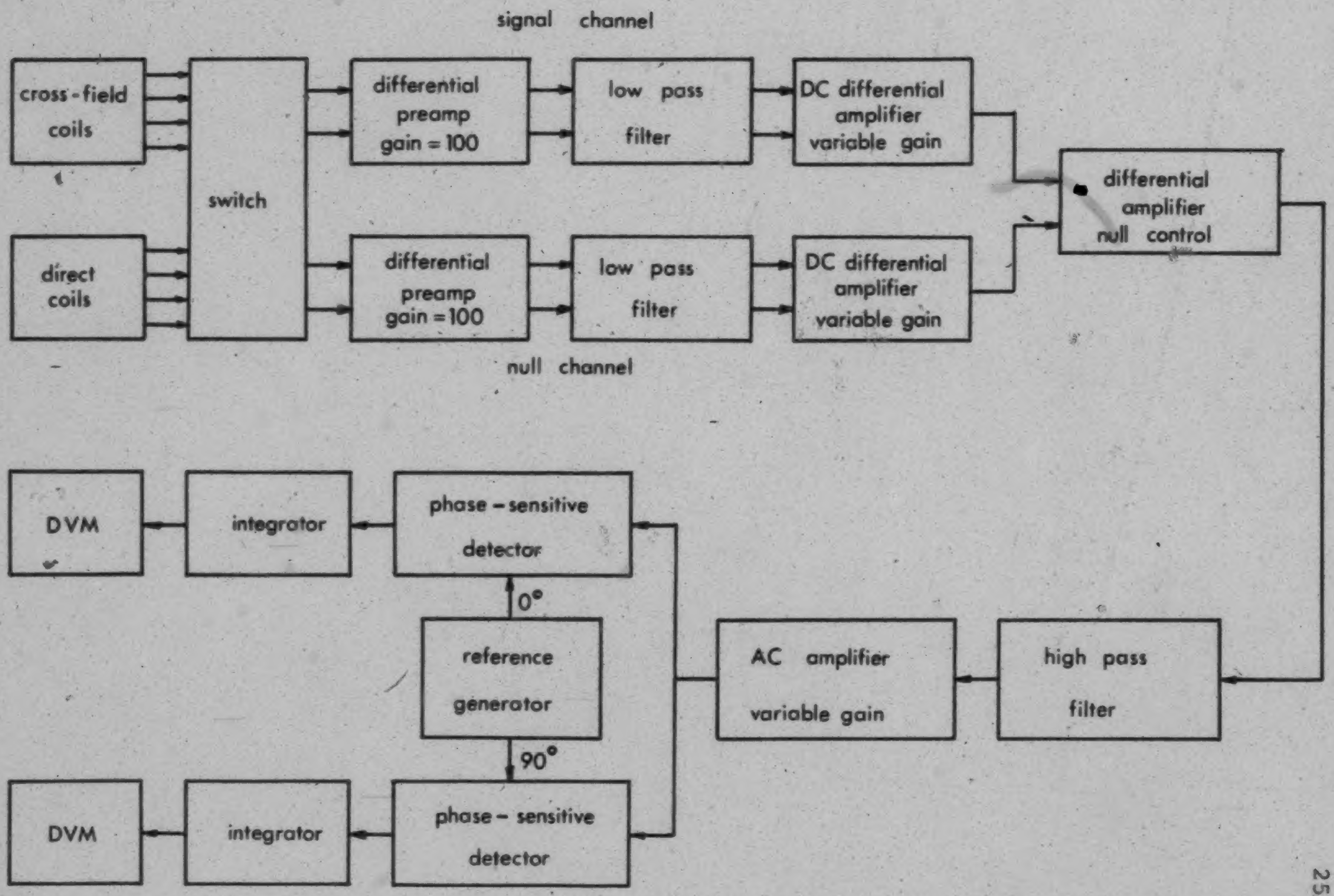
signal channel
cross-field coils
direct coils
switch
differential preamp gain = 100
low pass filter
DC differential amplifier variable gain
differential preamp gain = 100
low pass filter
DC differential amplifier variable gain
null channel
differential amplifier null control
high pass filter
AC amplifier variable gain
phase - sensitive detector
0°
reference generator
90°
phase - sensitive detector
integrator
integrator
DVM
DVM

quency. It goes to the input of a variable-gain A.C. amplifier.

From the output of the A.C. amplifier the signal goes to the inputs of two phase-sensitive detectors which are gated by quadrature signals from a photocell generator on the spinner shaft. The signal output of the detectors is D.C. on which are superimposed A.C. components due to gated noise and spurious signals. The D.C. component is filtered by means of an integrator, one for the in-phase output and one for the quadrature. The integrated outputs are then measured by a pair of digital voltmeters.

4.5.1 Preamplifier

All signal coils are connected in pairs, balanced with respect to ground. This arrangement minimizes electrostatic noise pickup and requires that the amplifier have a differential input. It is important that all electrostatic pickup be minimized, even if its frequency differs appreciably from the signal frequency. This is because the high gain signal amplifiers could otherwise overload or the noise input could nonlinearly mix with itself or other noise in the amplifier to produce spurious output at the signal frequency.

There are two sets of signal coils in the specimen gap, one set to detect magnetic flux variations parallel to the applied field, another set for variations normal to the field. Each set consists of two pairs of coils located with respect to each other and electrically connected in such a way that gradients of signal flux variation are detected. Thus spurious magnetic variations, usually from external sources such as 60 Hz power lines, transformers and rotating machinery, can be nulled out since their relative gradient is different from that of the signal flux. Both coil pairs feed separate differential amplifiers, as shown in Figure 4.24.

The minimum signal detectable is theoretically limited by the random thermal (Johnson) noise generated in the coil windings and noise generated within the first stages of the amplifier. It was shown in Chapter 3 that, for a given set of coil dimensions, the signal-to-noise ratio is independent of the number of turns on the coil. The number of turns is important, however, insofar as it affects the relative noise generated by the first stages of the amplifier.

The best low-noise low-frequency amplifiers employ a parametric amplification mechanism and are quite complex. It was decided that, as a first trial at least, a simple active device would be used for the first amplifier stage. The noise figure of an amplifier is defined as the ratio between the signal-to-noise ratio at the output of the amplifier and the signal-to-noise ratio at its input, expressed in decibels. Field effect transistors have the lowest noise figures at low frequencies between 10 Hz and 100 Hz. However, in order to achieve a low noise figure with a field effect device, it is necessary that the generator have a relatively large resistance, typically about one megohm. For an untuned signal coil, such a resistance requires typically 100,000 turns. Not only is such a coil difficult to wind and encapsulate, but also the coil's self-capacitance may approach resonance with the self-inductance at the signal frequency or lower. In this case large currents flow internally, but the external signal is small and has phase sharply dependent on frequency. Thus self-resonance limits the useable number of turns per coil. It is also possible to match a low-resistance coil to a field effect device through an elegant low-noise step-up transformer. Such a device would employ a thin-tape-wound nickel alloy core and sectionalized high impedance secondary winding.

Fortunately silicon junction transistors are available which have very good noise figures, at least in the upper part of the 10 Hz to 100 Hz frequency range, and operate optimally with generator resistances of about 1000 ohms. The signal coils were made to have resistances of between 300 and 700 ohms per section. The number of turns is then small enough that there are no self-resonances below about 3000 Hz. The active devices chosen for the first amplifier stage are 2N3906 PNP silicon annular transistors. Their typical noise characteristics are shown in Figure 4.25 (A) and (B). If for any reason, such as avoiding self-resonance, it were necessary to wind the coils with even fewer turns and therefore lower resistance, it would be possible to parallel the first-stage transistors in such a way that the optimum generator resistance is decreased by an amount depending on the number of devices paralleled (Walton and Liu, 1971). At frequencies for which the coil reactance due to inductance is appreciable with respect to its resistance, the coil's positive reactance should be cancelled by the negative reactance of a capacitor if optimum noise figure is to be maintained. If series tuning is used, the impedance of the tuned coil simply equals its resistance R. If parallel tuning is used, the tuned impedance Z_T is given by

$$Z_T = Q^2 R \tag{4.65}$$

$$\text{where } Q = \frac{\text{coil reactance}}{\text{coil resistance}}$$

The signal voltage is simultaneously multiplied by Q. Thus one would not use parallel tuning where Q was less than unity.

A circuit diagram for the preamplifier is shown in Figure 4.26. Transistor Q5 and resistors R15, R16 and

Figure 4.25 (A) Noise figure for 2N3906 transistor vs. generator resistance R_g.

$f = 1000$ Hz

$I_c = 200\ \mu A$

$V_{CE} = 5.0$ V

$T_A = 25°C$.

(B) Noise figure for 2N3906 transistor vs. frequency f.

$R_g = 500\,\Omega$

Other parameters are as in (A).

(After Motorola data).

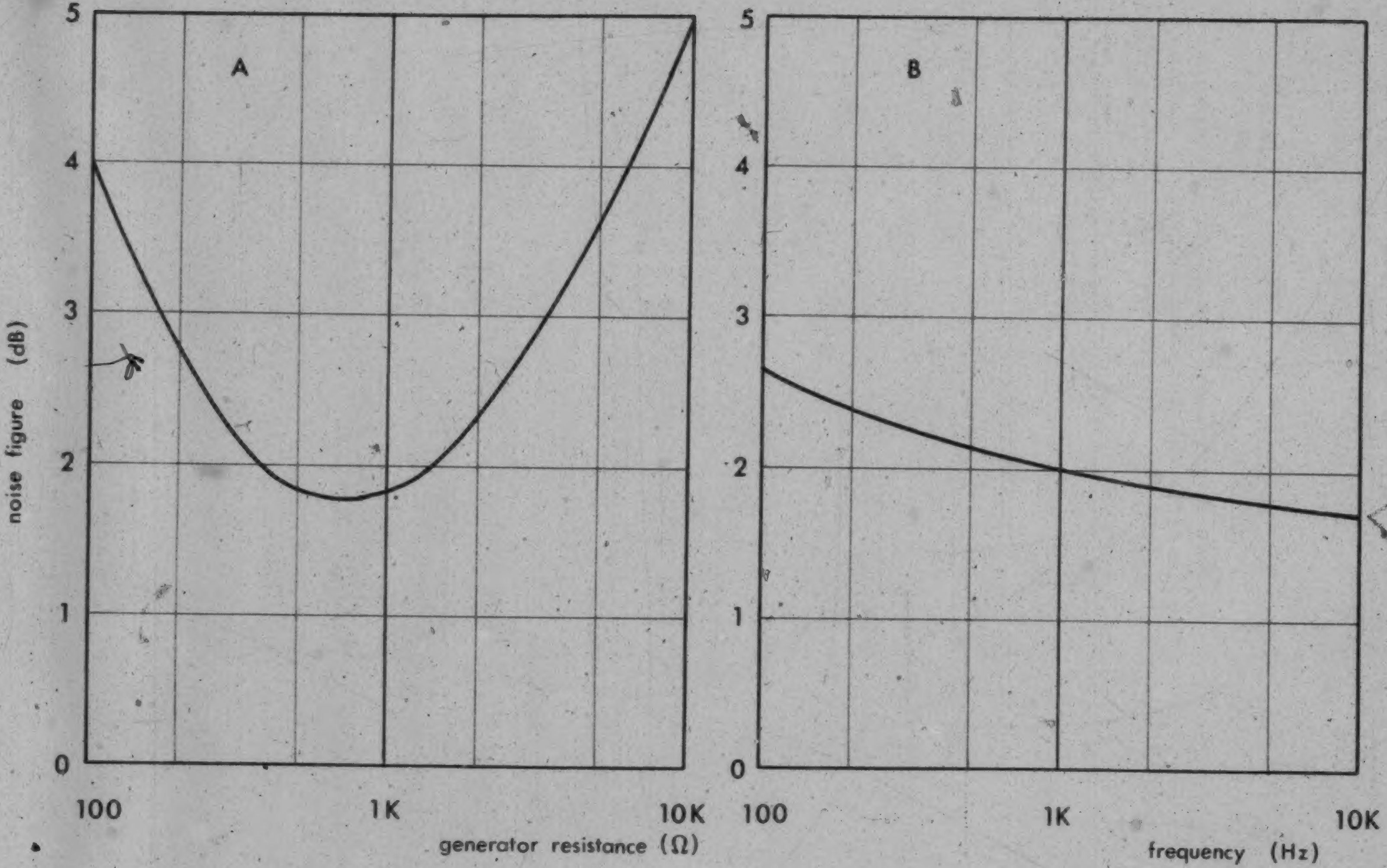
A
B
noise figure (dB)
0
1
2
3
4
5
100
1K
10K
generator resistance (Ω)
frequency (Hz)

Figure 4.26 Schematic of the preamplifier. Resistances are in ohms, capacitances in microfarads.

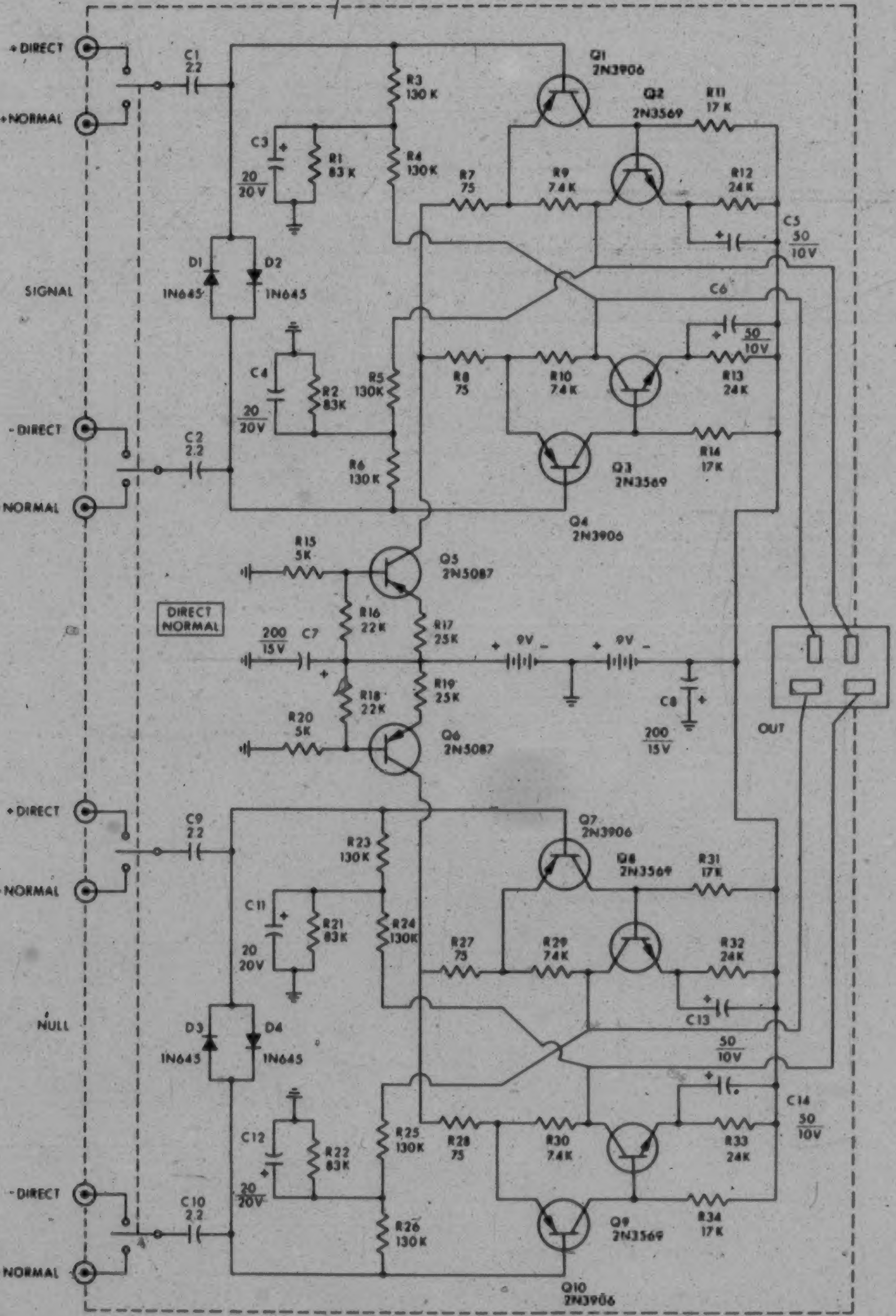
+DIRECT
+NORMAL
SIGNAL
-DIRECT
-NORMAL
DIRECT NORMAL
+DIRECT
+NORMAL
NULL
-DIRECT
-NORMAL
C1 2.2
C2 2.2
C3 20 20V
C4 20 20V
R1 83K
R2 83K
D1 1N645
D2 1N645
R3 130K
R4 130K
R5 130K
R6 130K
Q1 2N3906
Q2 2N3569
R11 17K
R7 75
R9 7.4K
R12 24K
C5 50 10V
C6 50 10V
R8 75
R10 7.4K
R13 24K
R14 17K
Q3 2N3569
Q4 2N3906
R15 5K
Q5 2N5087
R16 22K
R17 25K
200 15V C7
9V
9V
C8 200 15V
R18 22K
R19 25K
R20 5K
Q6 2N5087
OUT
C9 2.2
Q7 2N3906
Q8 2N3569
R31 17K
R23 130K
C11 20 20V
R21 83K
R24 130K
R27 75
R29 7.4K
R32 24K
C13 50 10V
D3 1N645
D4 1N645
C12 20 20V
R22 83K
R25 130K
R28 75
R30 7.4K
R33 24K
C14 50 10V
C10 2.2
R26 130K
Q9 2N3569
R34 17K
Q10 2N3906

R17 form a current source which supplies 280 μA. By circuit symmetry, the transistor pair Q1 and Q2 draws 140 μA, as does the pair Q3 and Q4. Resistors R11 and R12 determine the distribution of this current in the former pair. Resistors R13 and R14 serve the same function for the latter pair. Thus transistors Q1 and Q4 carry a collector current of 100 μA each, while Q2 and Q3 carry 40 μA each. This optimizes noise figure for the transistors used. Q1 and Q2 form a cascaded common emitter pair. Capacitor C5 shunts the emitter resistor for Q2 keeping its signal frequency gain high. Negative feedback is applied to the cascaded pair via R7 and R9. The closed-loop gain is approximately equal to

$$K = \frac{R7 + R9}{R7} = 100 \qquad (4.66)$$

since the open-loop gain is much larger than this ratio. Transistors Q3 and Q4 are connected similarly to form the other half of the balanced differential amplifier. R1 through R6 provide heavy crossover negative feedback to balance and stabilize the operating points of the two halves of the differential circuit. This negative feedback is restricted to D.C. by shunt capacitors C3 and C4. The signal coils are coupled to the input through C1 and C2. The circuit is protected from damage due to high voltage transients from the signal coils by diodes D1 and D2.

Under normal operating conditions these diodes do not conduct and therefore do not interfere with circuit operation. Power for the circuit is provided by a pair of 9V zinc-carbon batteries. This eliminates the 60 Hz feedthrough which comes from mains-operated power supplies.

4.5.2 Main Amplifier

The circuit for the main amplifier is shown in Figure 4.27. Resistors R1 through R4 and capacitors C1 through C8 make up a low pass filter having variable cutoff frequency. For the signal channel, IC1 and IC2 constitute a high-input-impedance amplifier having both differential input and output. Gain is controlled by feedback resistors R5 and R6 and bridging resistors R13 through R15. R23 optimizes the common-mode rejection ratio of the amplifier. IC5 then provides a single-ended output for the signal channel. IC6 does likewise for the null channel. The two outputs are mixed by IC7. The null input is gain-controlled by R31 and R32 to optimize interference nulling. The mixing amplifier is followed by a variable-cutoff-frequency high-pass filter which serves to reject the accumulated offset voltages of the operational amplifiers preceding it. The high-pass filter is followed by an A.C. coupled variable-gain amplifier. Because of the large-value feedback resistors, the operational amplifier for this stage must have very low offset current.

Figure 4.27 Schematic of the main amplifier. Resistances are in ohms, capacitances in microfarads.

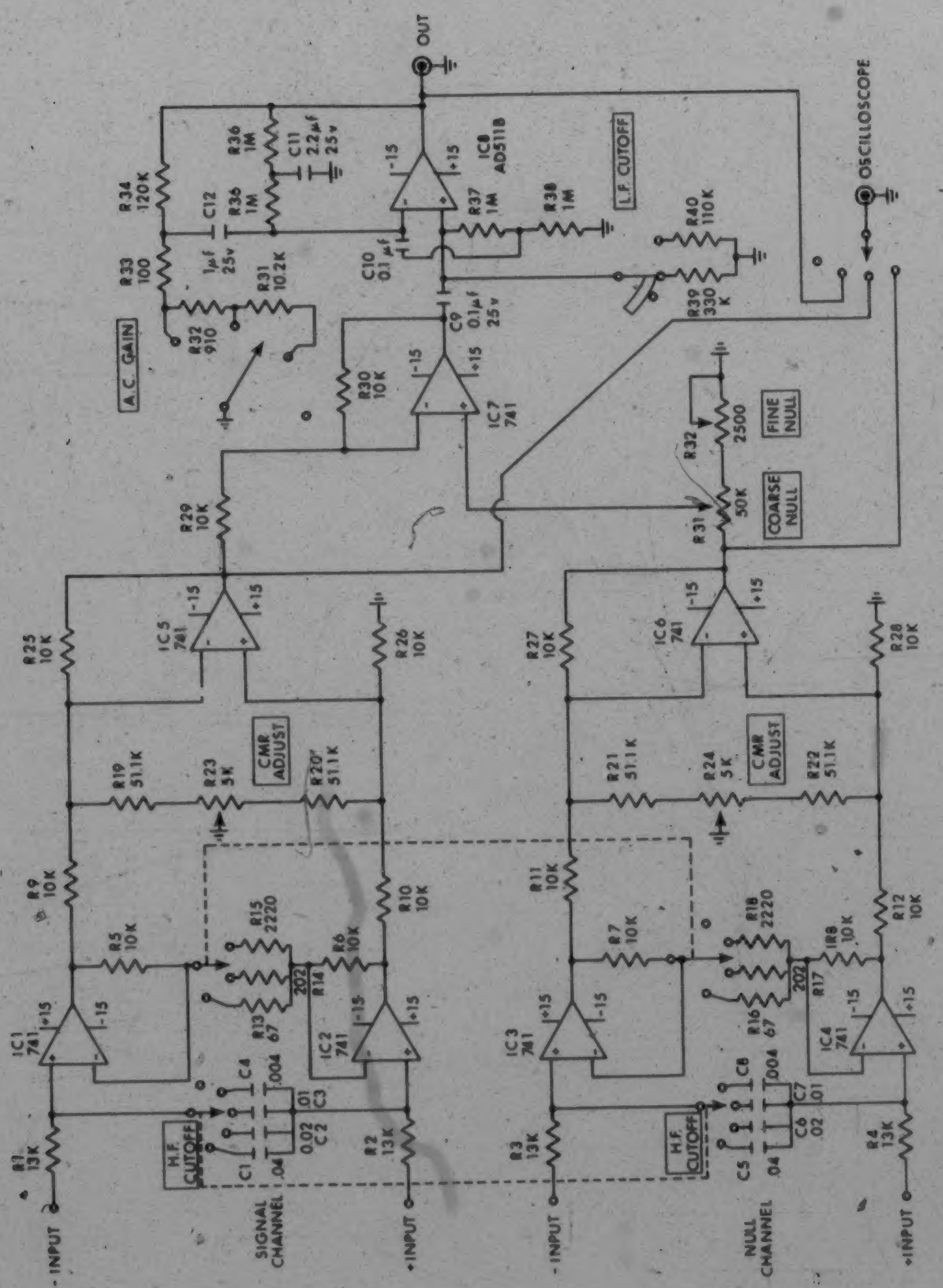
OUT
OSCILLOSCOPE
-INPUT
+INPUT
SIGNAL CHANNEL
NULL CHANNEL
H.F. CUTOFF
CMR ADJUST
A.C. GAIN
L.F. CUTOFF
COARSE NULL
FINE NULL
IC1 741
IC2 741
IC3 741
IC4 741
IC5 741
IC6 741
IC7 741
IC8 AD511B
R1 13K
R2 13K
R3 13K
R4 13K
R5 10K
R6 10K
R7 10K
R8 10K
R9 10K
R10 10K
R11 10K
R12 10K
R13 67
R14 202
R15 2220
R16 67
R17 202
R18 2220
R19 51.1K
R20 51.1K
R21 51.1K
R22 51.1K
R23 5K
R24 5K
R25 10K
R26 10K
R27 10K
R28 10K
R29 10K
R30 10K
R31 50K
R32 2500
R31 10.2K
R32 910
R33 100
R34 120K
R36 1M
R36 1M
R37 1M
R38 1M
R39 330 K
R40 110K
C1 .04
C2 0.02
C3 .01
C4 .004
C5 .04
C6 .02
C7 .01
C8 .004
C9 0.1µf 25v
C10 0.1µf
C11 2.2µf 25v
C12 1µf 25v
+15
-15

A FET-input amplifier is therefore used. Oscilloscope monitoring is provided for the outputs of IC5, IC6, and IC8.

4.5.3 Phase Sensitive Detectors

The circuit diagram for one channel of the phase-sensitive detector is shown in Figure 4.28. It is an adaptation of the gating-type detector. This configuration is relatively insensitive to reference-voltage variations, unlike linear-multiplier-type detectors. In its usual form, the gating type circuit is limited by nonlinearities in the bridge transformer and gating diodes. In this circuit, the bridge transformer functions are performed by operational amplifiers in precision closed loops. The effects of diode nonlinearities are greatly reduced by suitably placing the diodes in feedback paths. A similar circuit was described by Marzetta (1971).

In order that a small signal may be detected in the presence of high-amplitude noise, it is required that the detector have a good operating precision and hence wide dynamic range. For an operating precision of 0.01% one should be able to measure down to about 10^{-4} volts with a noise level of 1 volt. To achieve this precision it is necessary that the diodes have a reverse leakage current less than 10^{-4} times the maximum forward signal current. Also the critical feedback resistors (marked by asterisks in the circuit) must have ratios accurate to

Figure 4.28 Schematic of one channel of the phase-sensitive detector. Resistances are in ohms, capacitances in microfarads. Resistances marked with an asterisk are specially selected units with 0.01% tolerance (see text).

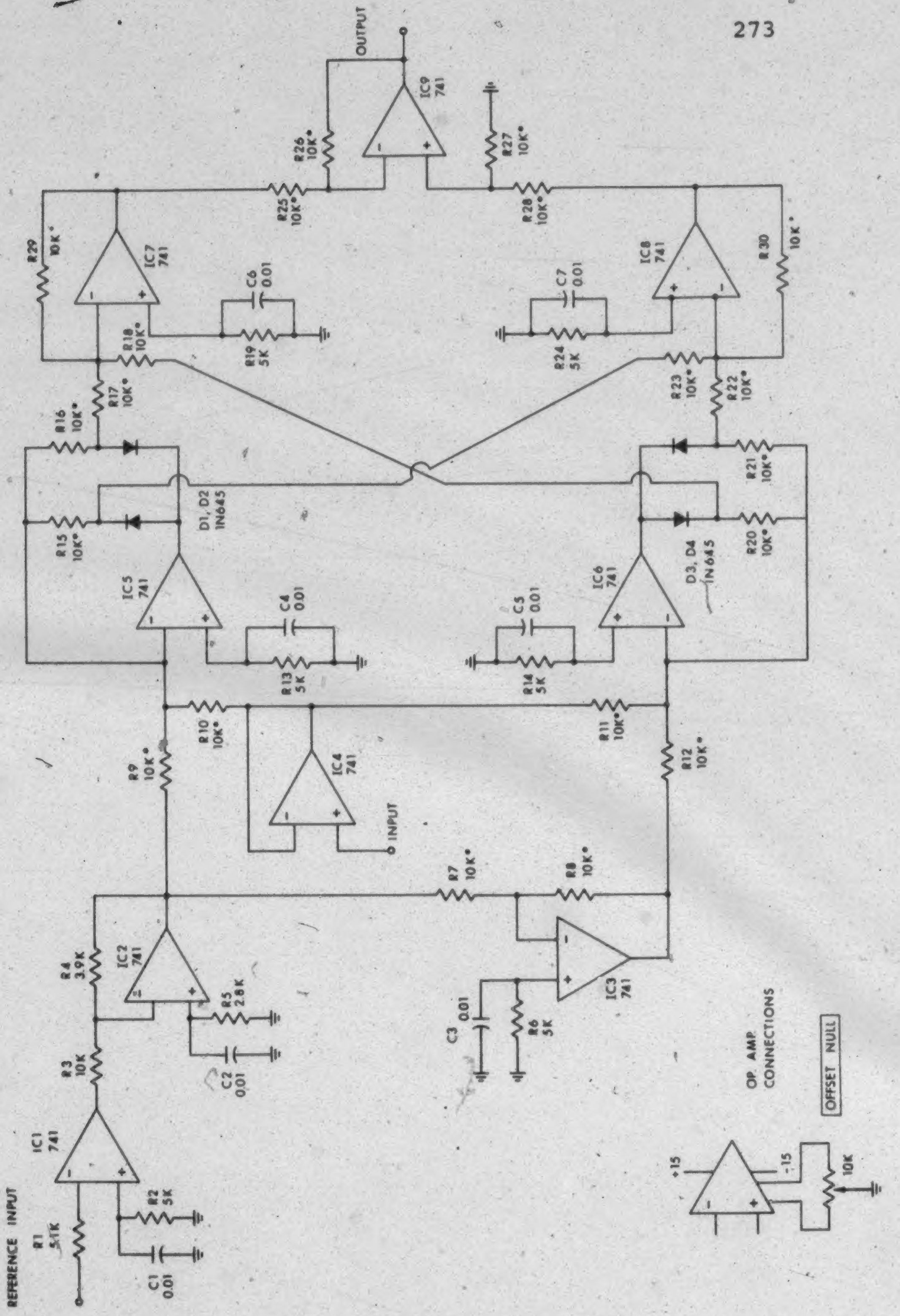
REFERENCE INPUT
R1 5.1K
R2 5K
C1 0.01
IC1 741
R3 10K
R4 3.9K
IC2 741
R5 2.8K
C2 0.01
R6 5K
C3 0.01
IC3 741
R7 10K*
R8 10K*
R9 10K*
R10 10K*
R11 10K*
R12 10K*
IC4 741
INPUT
IC5 741
C4 0.01
R13 5K
R14 5K
C5 0.01
IC6 741
R15 10K*
R16 10K*
D1, D2 1N645
D3, D4 1N645
R20 10K*
R21 10K*
R17 10K*
R18 10K*
R22 10K*
R23 10K*
C6 0.01
R19 5K
C7 0.01
R24 5K
IC7 741
IC8 741
R29 10K*
R30 10K*
R25 10K*
R26 10K*
R27 10K*
R28 10K*
IC9 741
OUTPUT
OP. AMP. CONNECTIONS
OFFSET NULL
+15
-15
10K

better than 0.01%. The latter requirement was met by selecting resistors in sets from a batch of 100 1% units. They were matched to better than 0.01% by bridge measurement.

The circuit shown in Figure 4.28 employs full-wave detection, unlike the more common half-wave detector. Full-wave detection offers immunity to any D.C. component present in the signal input and permits easier filtering of the detector output. Internal offset voltages are minimized by providing offset-nulling potentiometers for all operational amplifiers.

4.5.4 Integrator

The generalized integrator circuit used is shown in Figure 4.29 (A). It provides a 12 dB/octave ultimate high-frequency roll-off. For the particular ratio of capacitors in the feedback path, the settling time of the circuit is minimized. The output approaches its final value somewhat more rapidly than with equal-valued capacitors, and does so with negligible overshoot. Because large resistors are required for long integrating times, it is necessary that the operational amplifier have very low input offset current. Hence a unit with a FET input is used.

Figure 4.29 (A) Generalized schematic of integrator.

(B) Schematic of one channel of the signal integrator. Resistances are in ohms.

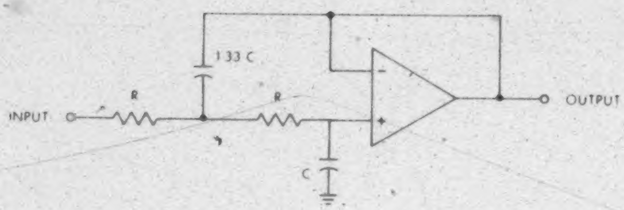
133 C
R
R
INPUT
OUTPUT
C
-
+

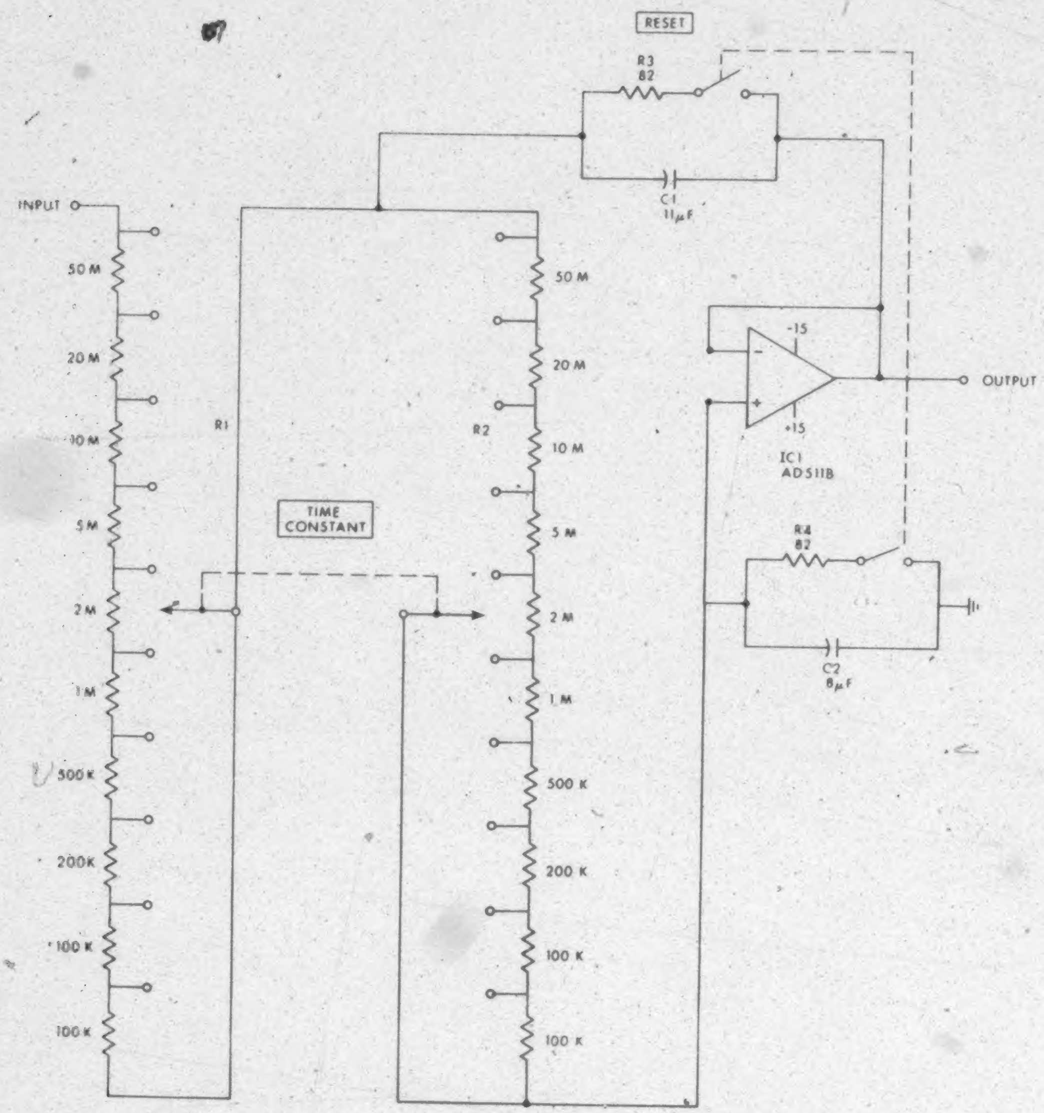
RESET
R3
82
C1
11μF
INPUT
50 M
20 M
10 M
5 M
2 M
1 M
500 K
200 K
100 K
100 K
R1
R2
TIME
CONSTANT
50 M
20 M
10 M
5 M
2 M
1 M
500 K
200 K
100 K
100 K
-15
+15
-
+
OUTPUT
IC1
AD511B
R4
82
C2
8μF

4.6 Design of Spinner Shaft and Motor Drive

For all signal-sensing arrangements other than the magnetic modulator, the signal sensitivity is directly proportional to the rotational speed of the spinner shaft. Thus, given that mechanically and acoustically transmitted vibrations from the shaft do not become a dominant noise source, the frequency for maximum sensitivity should be as high as possible. The structural strength of most rock specimens suggests that a rotational frequency of 200 Hz could be used.

4.6.1 Shaft Bearings

The choice of type and location of bearings for the shaft presented several problems. Ball bearings are suited to meet the mechanical requirements but cannot be used near or within the transducer assembly because of the magnetic noise they generate. It is necessary, however, to have bearings quite near the position of the specimen on the shaft because of limitations imposed by uncontrolled oscillation, or "whipping", of the free end of the shaft. In general a shaft of circular cross-section which is clamped at one end has a fundamental allowed frequency of vibration equal to (Morse and Ingard, 1968)

$$f_1 = \frac{0.560}{\ell^2}\left[\frac{Y\gamma^2}{\rho}\right]^{1/2} \tag{4.67}$$

where: ℓ = length of bar

Y = Young's modulus

y = radius of gyration = ¼ diameter

ρ = density

Therefore the critical shaft length for rotational frequency f is

$$\ell_c = 0.748\left(\frac{y}{f}\right)^{\frac{1}{2}}\left(\frac{Y}{\rho}\right)^{\frac{1}{4}} \tag{4.68}$$

Nonconductive materials must be used for the rotating shaft. Those with high specific modulus typically have $Y/\rho \sim 10^7\ \mathrm{m}^2/\mathrm{sec}^2$. Allowing a maximum shaft diameter of 2.5 cm and a rotational frequency of 200 Hz, critical length becomes

$$\ell_c = 0.235\ \mathrm{m} \tag{4.69}$$

The actual shaft extension must be considerably shorter than this because of the mass of the specimen and holder at its end, which do not contribute to shaft stiffness. Suppose 10 cm is a permissible length. This places the outermost bearing within the gap fringing area. Thus use of ball bearings is precluded, especially since the inside diameter would have to be 2.5 cm. Hydrodynamic bearings, even with smaller inside diameters, are impractical at these speeds because of high friction losses involved in shearing the lubricant. Hydrostatic bearings, though allowing smaller friction losses, incur such problems as providing a sump for the lubricant. Also, any bearing using a liquid lubricant is very much restricted in the types of bearing materials which are useable. Aerostatic bearings were chosen because they could provide a reasonable load capacity, use a readily available lubricant, and run with exceedingly low friction losses, even with a large bearing diameter. Aerostatic journals can be situated immediately adjacent to the rotating specimen without any magnetically deleterious effects. The principal requirement for bearing materials is that they be dimensionally stable. See Figure 4.30.

The load capacity of the journal bearings is dictated by the centrifugal forces produced by an off-balance specimen. It is assumed that as a worst case, the entire imbalance is that of a 2.5 cm diameter, 2.5 cm length cylinder with a specific gravity of 3.0, spun about a diametral axis 1.0 mm away from its geometrical center. This is equivalent to 3.68 gm suspended 1 cm off-axis. Therefore the radial force incurred at 200 Hz is

$$
\begin{aligned}
F_r &= 4\pi^2 f^2 mr \\
&= 4\pi^2(4 \times 10^4)(3.68 \times 10^{-3})(10^{-2}) \\
&= 58.2 \text{ newtons} \qquad (4.70)
\end{aligned}
$$

The air pressure available on the compressed air mains supply is 1.7×10^5 N/m^2. Based on this pressure and load

Figure 4.30 Aerostatic journal bearings for the spinner shaft.

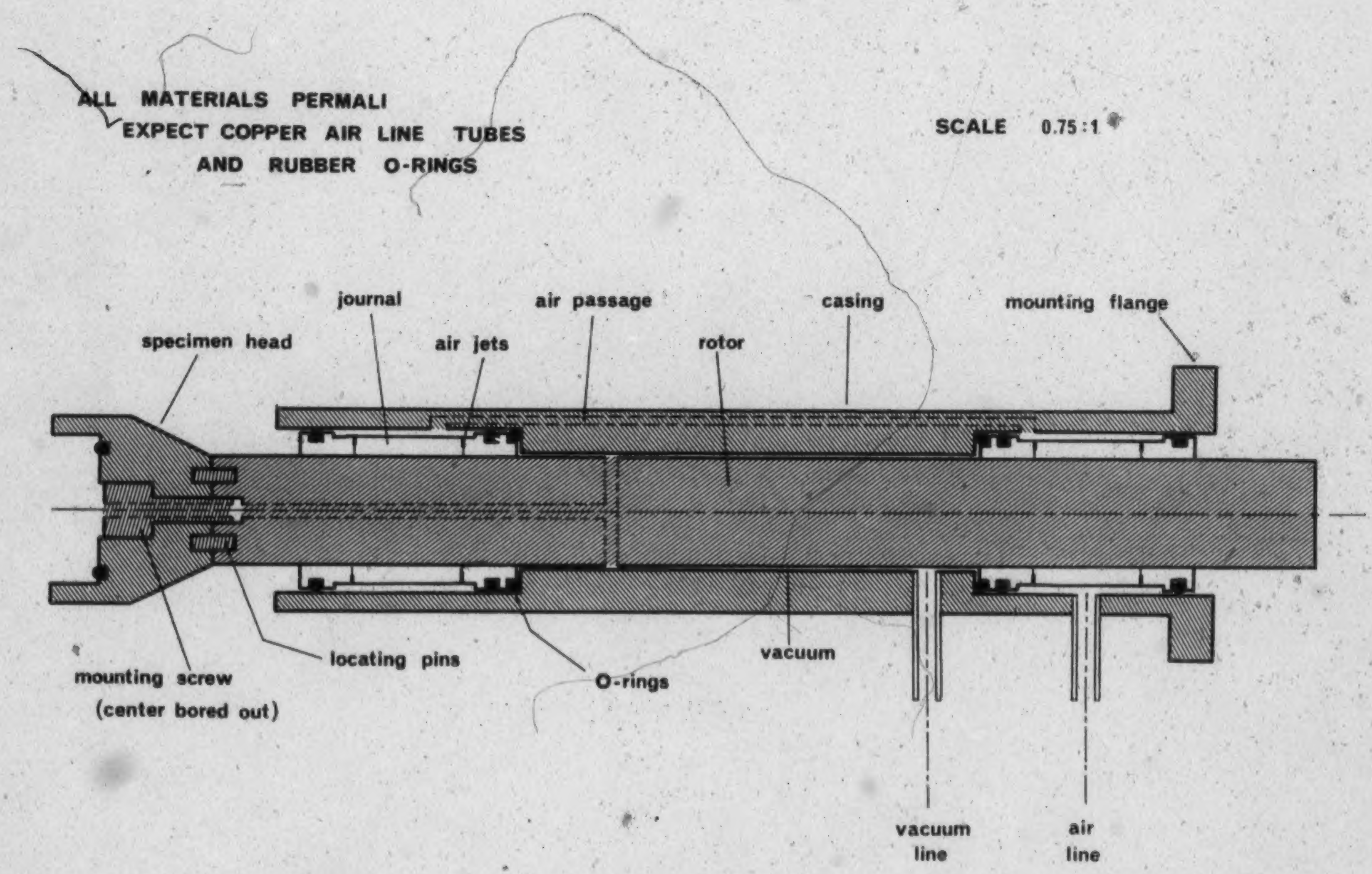
ALL MATERIALS PERMALI
EXPECT COPPER AIR LINE TUBES
AND RUBBER O-RINGS
SCALE 0.75:1
journal
air passage
casing
mounting flange
specimen head
air jets
rotor
mounting screw
(center bored out)
locating pins
O-rings
vacuum
vacuum line
air line

capacity, bearing journal dimensions can then be chosen from the general performance graph of Figure 4.31 (Powell, 1970). It has been experimentally shown by Powell (1970) that radial geometric errors (manufacturing tolerances) of less than one third the mean radial clearance h_0 reduce the load rating less than 10%. Underdamped resonances of the suspended shaft mass M on the radial bearing stiffness K also reduce the load capacity. Thus we ensure that shaft speed is always below the first critical frequency

$$f_1 = \frac{1}{2\pi}\left(\frac{K}{M}\right)^{\frac{1}{2}}$$

$$\simeq \frac{1}{2\pi}\left(\frac{1.7\, F_r}{M h_0}\right)^{\frac{1}{2}} \qquad (4.71)$$

Assuming an effective suspended mass of 0.2 kg per bearing and a radial clearance of 2.5×10^{-5} m, the first critical frequency becomes 719 Hz, which is quite satisfactory.

The air flow required per journal is taken from Figure 4.31. At 90 cm^3/sec each, the total flow is only 180 cm^3/sec. This is readily provided.

Friction power loss in a journal bearing is

$$P_f = \frac{\nu \pi^3 D^3 L f^2}{h_0} \qquad (4.72)$$

where ν = viscosity of air

$= 1.81 \times 10^{-5}\ {}^{kg}/_{m\ sec}$

Figure 4.31 General performance of air journal bearings with simple orifice feeding at quarter stations.

$\epsilon = 0.8$ (eccentricity ratio)

$K_{go} = 0.4$

$n = 8$ jets per row

$\ell = 0.25 L$

(where L is the length of the journal and ℓ is the separation of the jets from the bearing edge)

$P_a = 10^5$ N/m^2

$P_0 - P_a = 1.7 \times 10^5$ N/m^2

$h_0 = 2.5 \times 10^{-3}$ cm (bearing clearance)

Airflow is given in free volume at 15°C.

(After Powell, 1970).

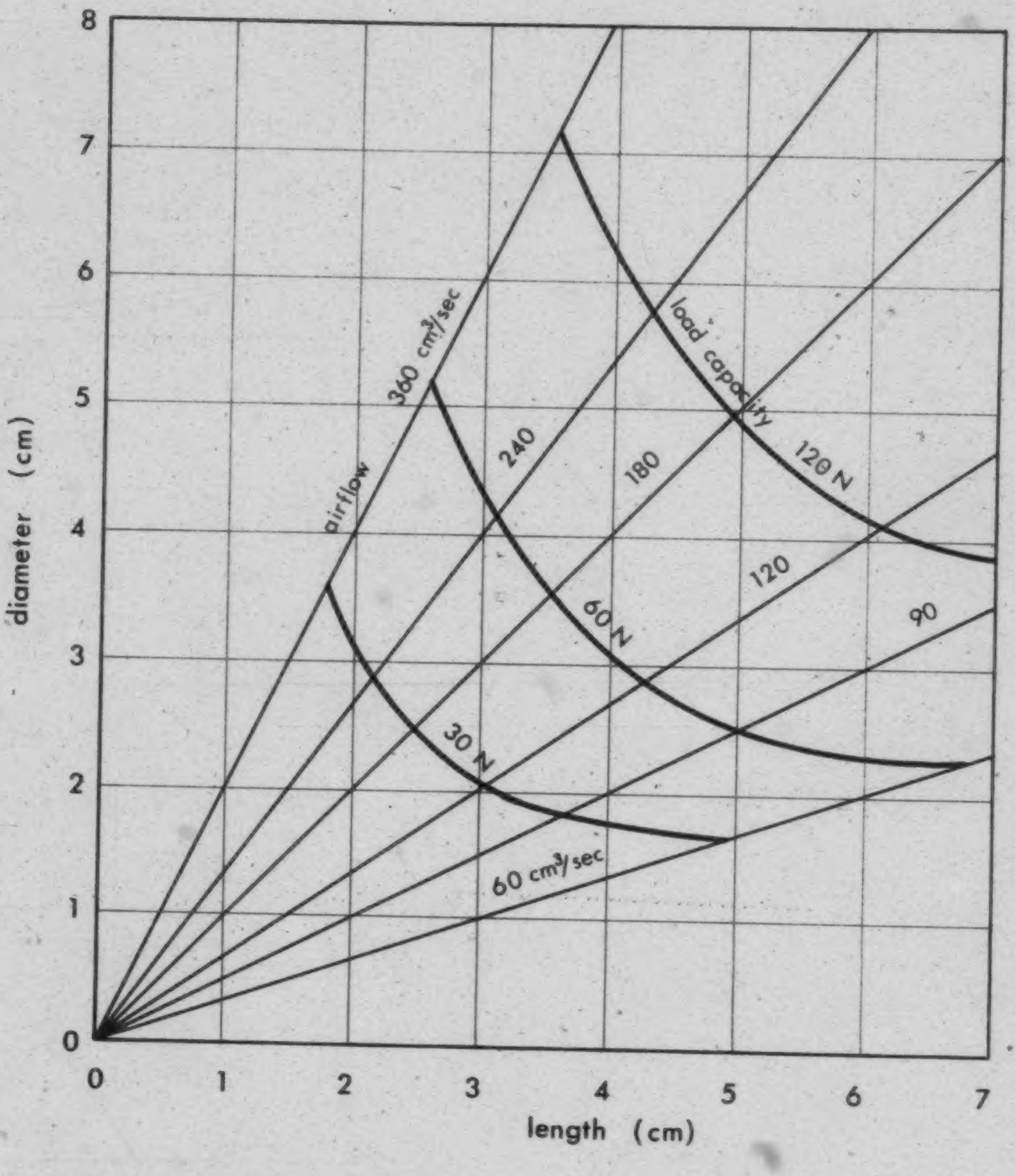
diameter (cm)
length (cm)
0
1
2
3
4
5
6
7
8
airflow
360 cm³/sec
240
180
120
90
60 cm³/sec
load capacity
120 N
60 N
30 N

Thus for each bearing

$$P_f = \frac{1.81 \times 10^{-5} (\pi^3)(2.5 \times 10^{-2})^3 (0.05)(4 \times 10^4)}{2.5 \times 10^{-5}}$$

$$= 0.701 \text{ watts} \qquad (4.73)$$

This amount of power is readily supplied by a very small motor.

The dimensions of the air jets are determined from the required value of gauge pressure ratio:

$$K_{go} = \frac{P_d - P_a}{P_0 - P_a} \qquad (4.74)$$

where: P_d = pressure immediately downstream from the jets

P_0 = line pressure

P_a = exhaust pressure

Figure 4.32 shows the effect of K_{go} on load coefficient for three values of eccentricity ratio. The curves suggest that optimum values of K_{go} lie between 0.3 and 0.6, with a maximum at 0.4. A factor which places a lower limit on K_{go} is the consideration of choking of the feed holes. Bearings with choked feed holes often exhibit aerostatic instability. For air, the critical pressure ratio is

$$\frac{P_d}{P_0} = 0.528 \qquad (4.75)$$

Figure 4.32 Typical load coefficient vs. gauge pressure ratio for an aerostatic journal bearing. ϵ is the rotor deflection as a fraction of the total radial clearance. (After Powell, 1970).

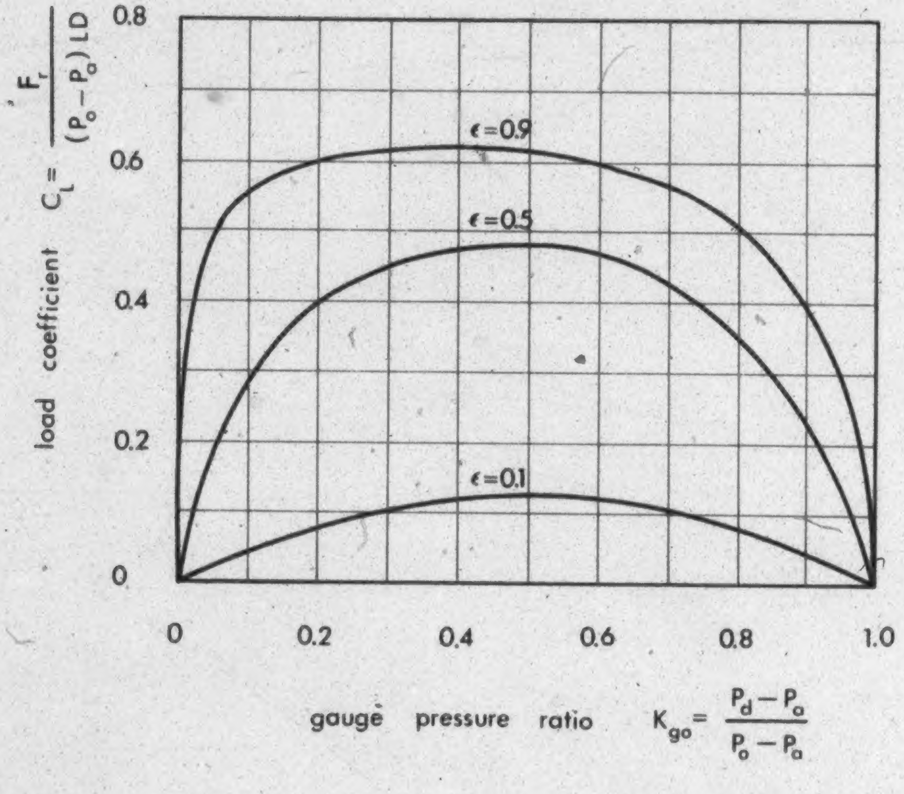
load coefficient $C_L = \frac{F_r'}{(P_o - P_a)LD}$
0.8
0.6
0.4
0.2
0
ϵ=0.9
ϵ=0.5
ϵ=0.1
0
0.2
0.4
0.6
0.8
1.0
gauge pressure ratio $K_{go} = \frac{P_d - P_a}{P_o - P_a}$

Substituting this ratio into Eq. 4.74 we get a lower limit on K_{go}

$$K_{go_{min}} = \frac{0.528 - \frac{P_\circ}{P_0}}{1 - \frac{P_\circ}{P_0}} \qquad (4.76)$$

For reasons discussed later in this section, the facing ends of the journals exhaust into a vacuum line. This further raises the lower limit on K_{go}. Assuming perfect vacuum:

$$K_{go_{min}} = 0.528 \qquad (4.77)$$

Figure 4.33 gives the relationship between jet diameter and clearance for annular orifices. A value of $K_{go} \sim 0.6$ is obtained by using $d = 3.43 \times 10^{-2}$ cm (the diameter of a #80 drill - the smallest standard size) and $h_0 = 2.5 \times 10^{-5}$ m. Annular jets were chosen for simplicity of machining, since simple orifices invariably demand a smaller bore d.

4.6.2 Spinner Shaft

One major requirement in designing the spinner shaft was to keep the motor's time-varying and rotating magnetic fields from inducing objectionable signal levels in the transducer. Accordingly, the separation of the motor and transducer shield was set at 50 cm, measured between their closest surfaces. Provisions were made for

Figure 4.33 Relation between jet diameter and clearance for annular orifices. (After Powell, 1970).

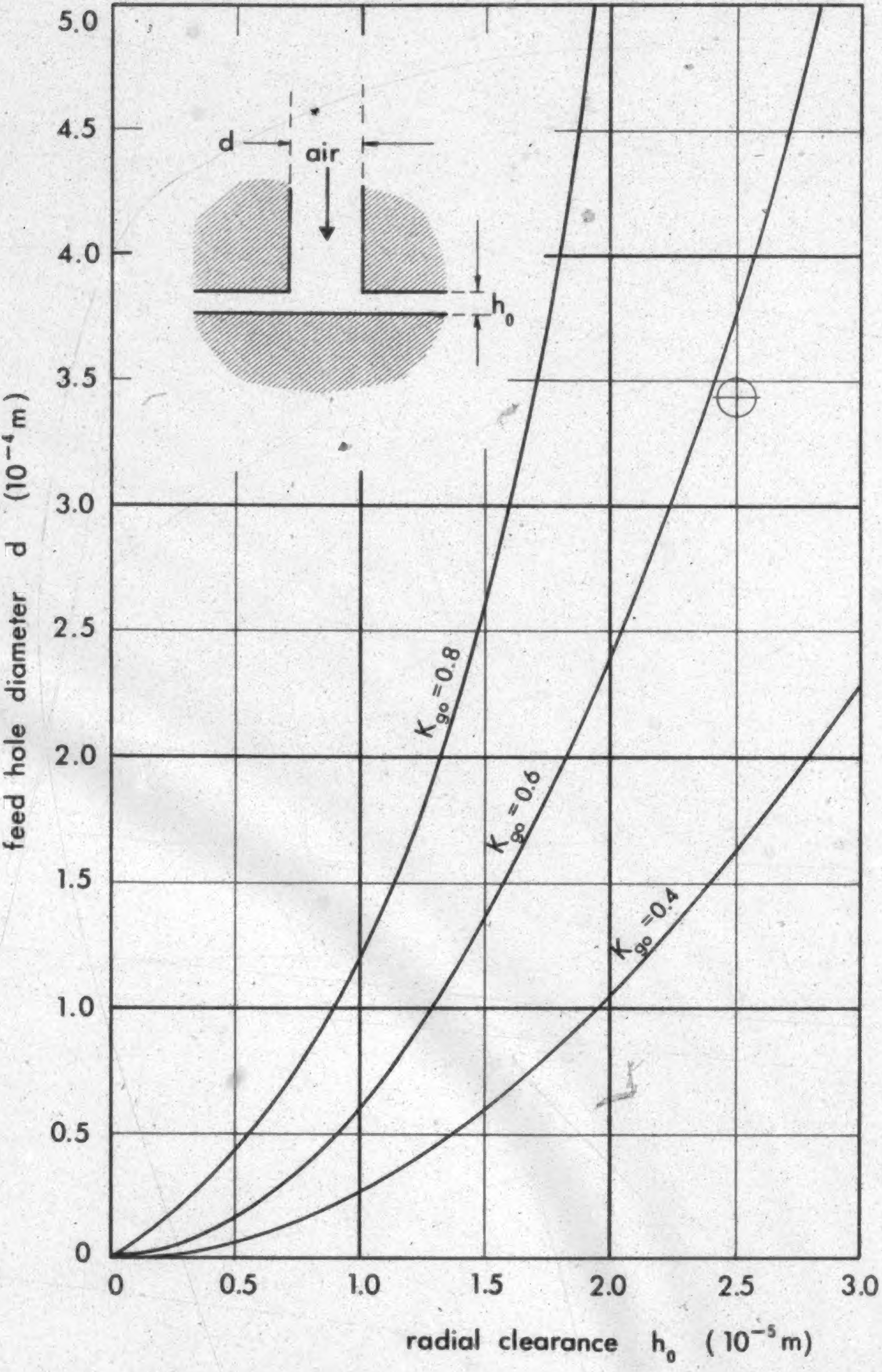
d
air
h_0
$K_{go}=0.8$
$K_{go}=0.6$
$K_{go}=0.4$
feed hole diameter d (10^{-4} m)
5.0
4.5
4.0
3.5
3.0
2.5
2.0
1.5
1.0
0.5
0
0
0.5
1.0
1.5
2.0
2.5
3.0
radial clearance h_0 (10^{-5} m)

attaching a motor shield, should such have proven necessary. The 50 cm separation requires an extension shaft 35 cm long spanning the gap between the Permali rotor and the brass motor extension, the latter in ball bearings. The extension shaft was to be kept of small diameter to minimize induced signal due to eddy currents. A minimum diameter is set by the requirement that the shaft not be resonant at any of its rotational speeds. The fundamental frequency of a bar, whether clamped at both ends or free at both ends, is

$$f_0 = \frac{3.56}{\ell^2}\left[\frac{Y\gamma}{\rho}\right]^{\frac{1}{2}} \qquad (4.78)$$

If aluminum is used, the critical radius of gyration for a frequency of 200 Hz is

$$= \frac{f_0\,\ell^2}{3.56}\left[\frac{\rho}{Y}\right]^{\frac{1}{2}}$$

$$= \frac{200(0.35)^2\,(2.71 \times 10^3)^{\frac{1}{2}}}{3.56\,(6.90 \times 10^{10})^{\frac{1}{2}}}$$

$$= 1.36 \times 10^{-3} \text{ meters} \qquad (4.79)$$

Therefore the critical diameter is 5.45 mm. To allow for a generous safety factor, the shaft diameter is 12.5 mm.

All components of the spinner shaft and housing which enter the main transducer block are made of beechwood laminations impregnated at high pressure with a phenolic resin. This material is commercially available under the trade name "Permali" from Permali, Inc. Even the stator components cannot be made of metals because the eddy currents which result when a conductor vibrates in a magnetic field gradient induce currents in the signal windings. These currents can be much larger than the coils' Johnson noise. Lucite was tried as a shaft rotor material. It was found that residual magnetic and electrostatic moments within the material rendered it useless. Coating the component with a conductive film did not help sufficiently. Also, lucite did not have sufficient dimensional stability to keep the aerostatic journals within their required tolerances for extended periods of time. Figure 4.34 shows the overall arrangement of the spinner shaft and drive motor.

The specimen cube shown in Figure 4.35 is also made of Permali. The specimen is aligned with a slot in the side of the cube and is held with a nylon set-screw. The cube is balanced about its three orthogonal axes by removing material from its bottom corners. The cube is held in place in the specimen head by vacuum. Air is exhausted through an axial hole in the rotor and the rubber O-ring on which the specimen sits serves as a vacuum seal. This mounting arrangement holds the cube securely in place while spinning, although a slight tug is sufficient to remove it.

4.6.3 Spinner Motor

The motor is a four-pole two-phase induction machine designed to run with electrical input of 115 V at

Figure 4.34 Overall arrangement of the spinner shaft and drive motor.

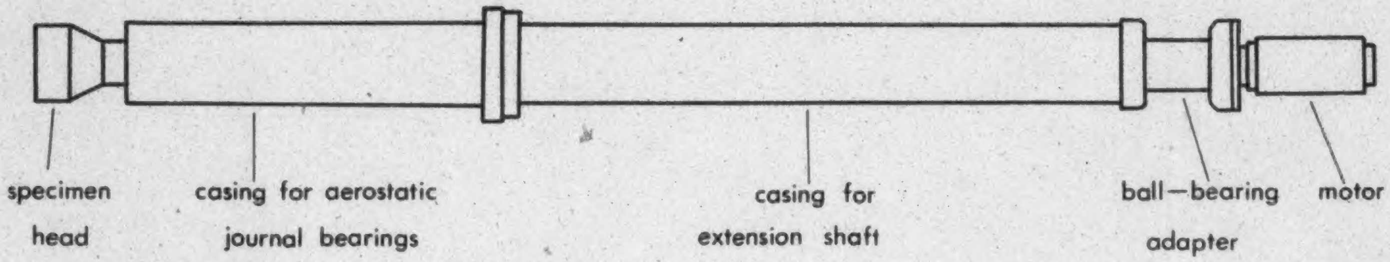
specimen
head
casing for aerostatic
journal bearings
casing for
extension shaft
ball—bearing
adapter
motor

scale = 1 : 4

Figure 4.35 Three views of the Permali cube which holds the specimen.

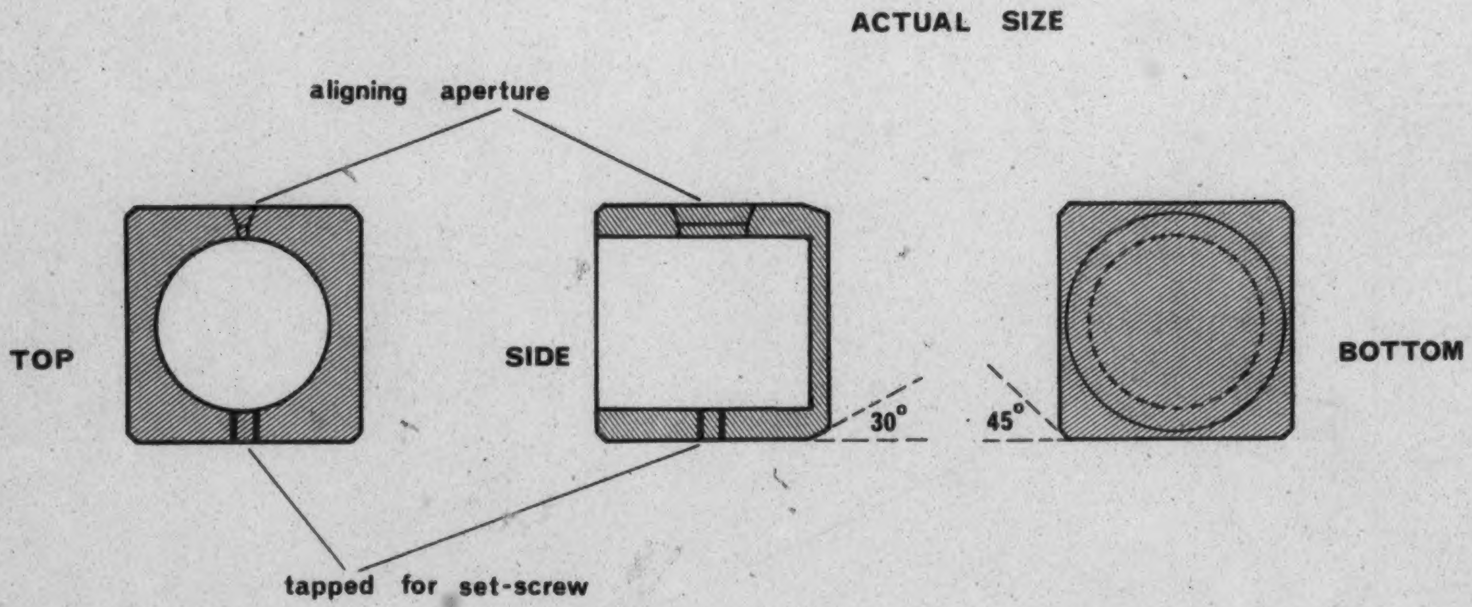
ACTUAL SIZE
aligning aperture
TOP
SIDE
30°
45°
BOTTOM
tapped for set-screw

400 Hz. An induction machine was chosen in preference to other types because of the nature of its stray magnetic fields. The stray field due to each stator winding is, of course, time variant at the input frequency and, to some extent, at its harmonics. Because there are four poles on the stator, the motor's gap has a field which rotates at exactly half the input frequency, with again some harmonic content. Part of this rotating field also leaks out. In order that a current be induced into the rotor windings it is necessary for the rotor to "slip" with respect to the rotating field. That is, the shaft actually turns at somewhat less than half the input frequency. Thus, none of the major stator leakage effects are synchronous with the shaft rotation.

The rotor is excited at the slip frequency, typically about 5 Hz. Therefore its field rotates at the slip frequency plus the shaft frequency, which is just the input frequency. Therefore the rotor's leakage field has dominant components at slip frequency and at input frequency, neither of which is synchronous with shaft rotation. Synchronous interference could, however, result from second-order effects such as a permanent polarization or magnetic asymmetry of the rotor. Other frequency components must also be minimized to keep amplifiers from overloading and to keep integrating times required for noise rejection reasonable. The motor is physically small since only minimal mechanical power is required. It still allows the shaft to reach top speed in about five seconds.

4.6.4 Motor Drive Electronics

Because the signal from the instrument has amplitude proportional to the motor speed, and because there are slight phase shifts within the electronic circuitry as a function of signal frequency, it was decided that a motor speed regulator would be required. The normal expedient of using a stable oscillator and amplifier with some form of synchronous motor was not permissible because of the signal-synchronous magnetic interference which the motor windings would create. For similar reasons a D.C. servo motor was ruled out. The characteristics of the small induction motor which is used for the shaft drive suggest that a servo which varies the frequency of the drive to the motor, but at constant amplitude, is the most desirable regulatory mechanism.

A block diagram for the regulator is shown in Figure 4.36. Figure 4.37 shows the circuit diagram. The motor speed is sensed by the photoelectric tachometer which is also used for gating the phase-sensitive detectors in the signal circuit. The buffered output is used as a reference to which the oscillator within a phase-

Figure 4.36 Block diagram of the drive-motor speed regulator.

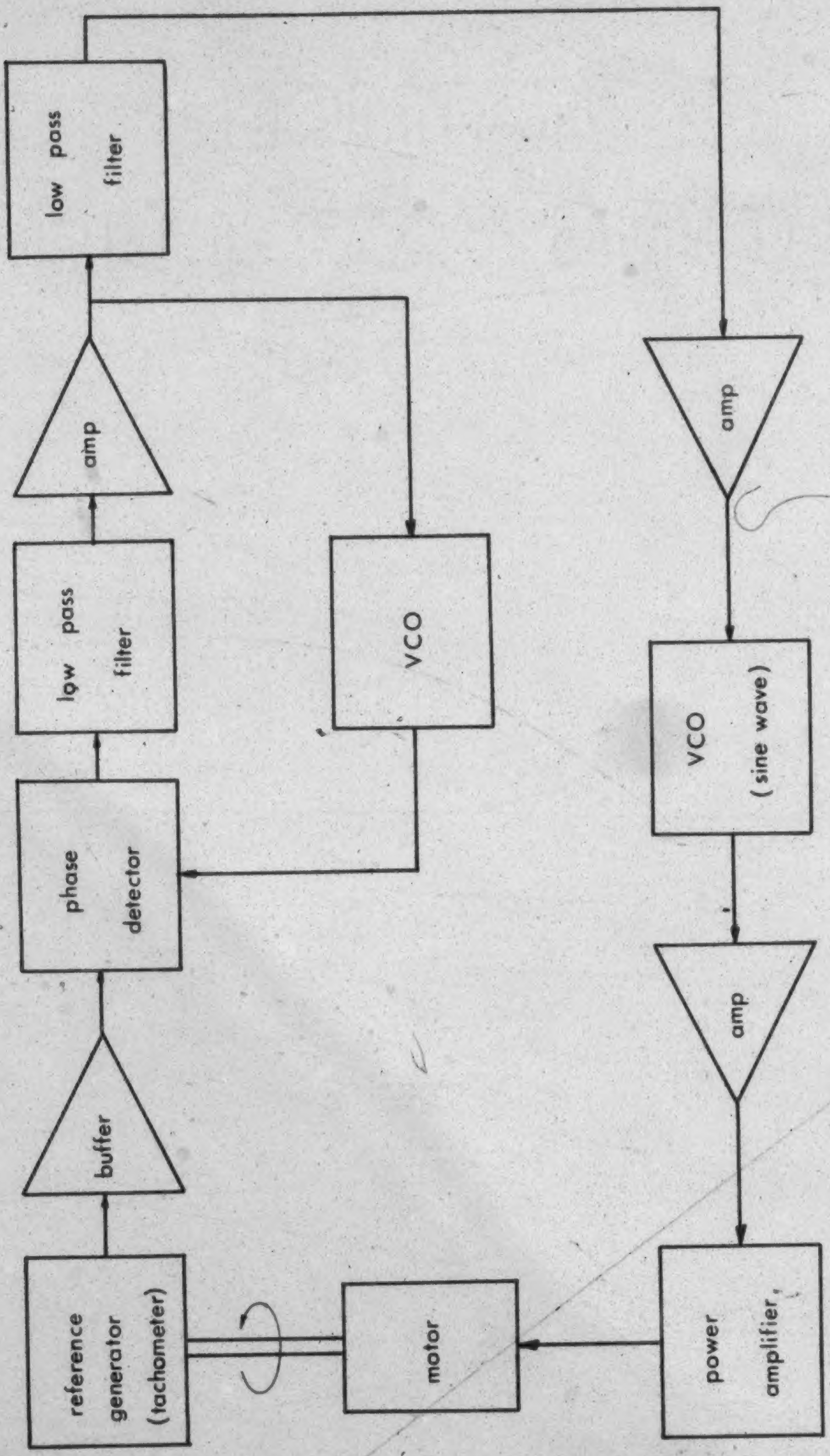
reference generator (tachometer)
buffer
phase detector
low pass filter
amp
low pass filter
VCO
motor
power amplifier
amp
VCO (sine wave)
amp

Figure 4.37 Schematic of the drive-motor speed regulator.
All resistances are in ohms (K = 1000).
All capacitances are in microfarads.

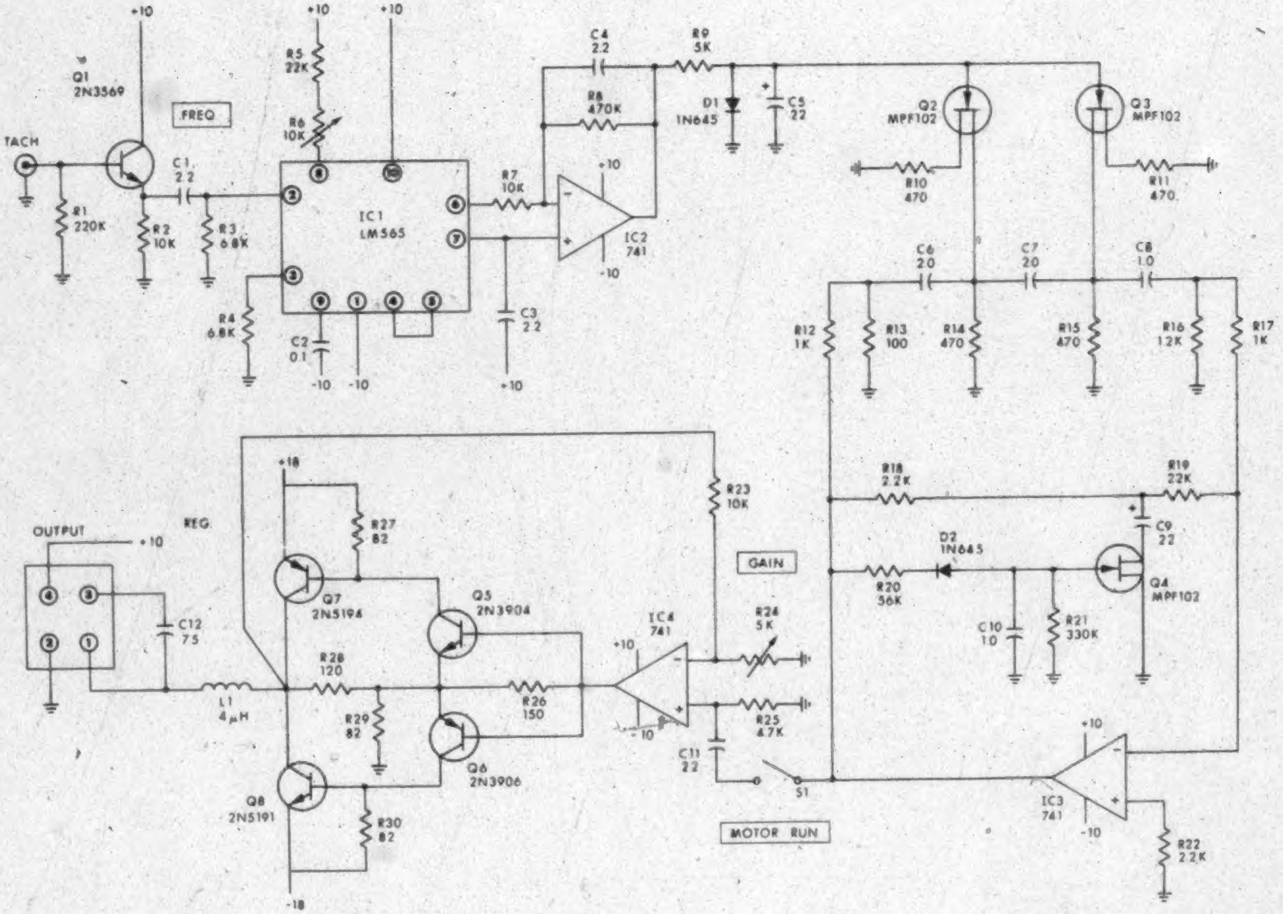
TACH
Q1
2N3569
+10
FREQ
R1
220K
R2
10K
C1
2.2
R3
6.8K
R4
6.8K
R5
22K
R6
10K
+10
+10
IC1
LM565
C2
0.1
-10
-10
C3
2.2
+10
R7
10K
IC2
741
+10
-10
C4
2.2
R8
470K
R9
5K
D1
1N645
C5
22
Q2
MPF102
R10
470
Q3
MPF102
R11
470
C6
20
C7
20
C8
1.0
R12
1K
R13
100
R14
470
R15
470
R16
1.2K
R17
1K
R18
2.2K
R19
22K
C9
22
D2
1N645
R20
56K
C10
1.0
R21
330K
Q4
MPF102
IC3
741
+10
-10
R22
2.2K
S1
MOTOR RUN
GAIN
R23
10K
R24
5K
R25
4.7K
C11
22
IC4
741
+10
-10
R26
150
Q5
2N3904
Q6
2N3906
+18
R27
82
Q7
2N5194
R28
120
R29
82
Q8
2N5191
R30
82
-18
L1
4 μH
C12
75
REG
OUTPUT
+10

locked loop is synchronized. The error voltage which varies the frequency of this oscillator is amplified and varies the frequency of an independent voltage-controlled oscillator, but over a much greater frequency deviation. The output of this oscillator is then amplified, phase shifted, and fed to the motor windings. For the gains chosen, a 1 Hz change from natural running frequency of the oscillator within the phase-locked loop causes a change of about 50 Hz within the oscillator driving the motor. During normal running, the frequency of drive goes to its maximum of about 150 Hz until the motor reaches its desired running speed. The servo then rapidly reduces the frequency of drive to its normal 115 Hz. This allows approximately 10 Hz of slip frequency between the motor windings and the shaft rotation. During normal running, the shaft drive frequency does not vary more than about 0.1 Hz, or about 0.1%. Even this effect is largely oscillatory and its consequences are rejected by the phase sensitive detectors. Only long term drift within the frequency-determining elements of the phase-locked loop requires periodic calibration with a standard susceptibility specimen.

CHAPTER 5

CONSTRUCTION OF THE MAIN TRANSDUCER BLOCK

5.1 Preparation of the Permalloy Strips

The laminations for the main magnetic circuit and polepieces were taken from 2.5 cm wide, 356 micron thick moly-permalloy tape coated with magnesia. They were cut to length before annealing. For the outer portion of the magnetic circuit all pieces are 33.0 cm long. The pieces for constructing the polepieces are 15.2 cm long. The polepiece laminations were also punched with four centered holes of 0.64 cm diameter and spaced 4 cm apart. Steel jigs were constructed to support the stacks of laminations in the annealing oven and thereby minimize warping and bending. The 15.2 cm laminations were laid horizontally in a steel channel bar with a 2.5 cm square, 15 cm long steel bar placed on top of them. The 33 cm laminations could not be placed horizontally because of the inside diameter of the oven. For this reason a jig was constructed in which a wedge-shaped piece of steel, forced down an incline by gravity, holds the stack flat in a vertical position. This method avoids the effects of thermal expansion and resultant strain incurred with screw-held pieces.

5.2 Annealing of the Moly-permalloy

All transducer components made of Permalloy 80 were annealed in hydrogen after the final cutting process, but before the assembly of the laminations. For alloys having percentages of molybdenum greater than 2½% to 3%, a single slow furnace cooling from about 1000°C at a rate of 1°C/minute produces higher values of maximum and initial permeability than are obtained with the double treatment of a slow furnace cooling and partial reheating followed by air quenching at 1000°C/minute. The latter process is preferable for alloys having lower percentages of molybdenum (Bozorth, 1951). For alloys having about 4% molybdenum, cooling rates intermediate between slow furnace cooling and air quenching produce optimum initial permeability. Accordingly, cooling rates of about 10°C/minute were used.

The hydrogen atmosphere used for annealing serves as a deoxidizer. It is preferable to deoxidizers added to the alloy melt because the latter leave fine-grained precipitates in the alloy and thereby depress permeability.

During the annealing process the laminations were brought to a temperature of 1100°C in a period of about one hour. After another hour at this temperature the cooling at about 10°C/minute was started.

5.3 Assembly of the Polepieces

The polepieces were assembled as 15 cm stacks of the 15.2 cm by 2.5 cm, 356 micron thick laminations. They were coated with a very low viscosity thermosetting epoxy resin (Hysol #2046), then stacked and bolted together with threaded nylon rods passed through the four punched holes in each lamination. Before tightening down the nuts on these rods, the lamination edges which were to constitute the poleface were aligned with a very flat block which was covered with a thin sheet of polyvinyl chloride. The nuts were then tightened to squeeze out the excess epoxy resin. Another flat block faced with a sheet of vinyl was then placed on the opposite side of the poleblock and the resin allowed to cure. Before further assembly, the four polepieces which were to be used in pairs on each side of the specimen gap were joined together with epoxy and 0.5 mm spacers.

5.4 Assembly of the Magnetizing and Sensing Coils

Since the main magnetizing coils could not be wound in situ, they had to be wound in six separate self-supporting sections. Each is rectangular in cross-section. In plan view they had to be made quite rounded, rather than rectangular, in order that the wire would wrap properly around the core without requiring excessive tension.

By improvising a controlled-tension electrical winding rig for the job, it was possible to approach closest-spacing throughout the coils.

The coils were made self-supporting through spot application of a rigid room-temperature-curing epoxy resin throughout the winding. Care was taken that no completely enclosed voids were thus created. These would have prevented complete vacuum impregnation with the flexible resin. PVC film served as a release agent to keep the coils from attaching themselves to the plywood coil forms. Two of these coils are shown in Plate 1.

All but one of the smaller sensing coils were also wound on plywood coil forms. Because of the small size of the wire and the large number of turns per coil, no attempt was made to achieve closest spacing. The coils were made self-supporting by winding them directly onto pieces of electrical tape placed adhesive-side-out on the coil forms. Between 4 and 8 pieces of tape per coil kept each one quite reasonably rigid. See Plates 2 and 3.

Because of the very small size of the wire and the great importance of avoiding vibrations within these coils, it was considered necessary to vacuum-impregnate them individually with a very-low-viscosity polyester thermosetting resin. The resin was poured onto the coils under a reduced air pressure of about 1500 N/m^2. Just

Plate 1 Two of the magnetizing coils used in the main magnetic circuit. The white material is the epoxy resin which was applied in spots to make the coils self-standing.

Plate 2 Two specimen-gap sensing coils. This pair is used to sense flux variations parallel to the bulk field, and is connected to null externally-produced fields.

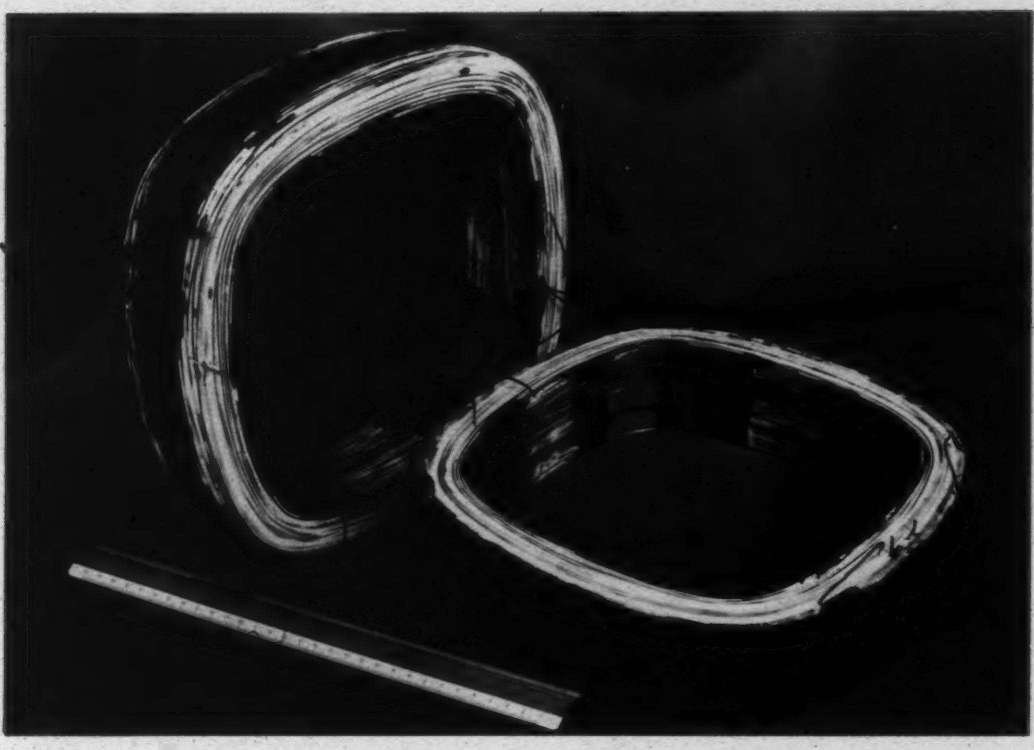

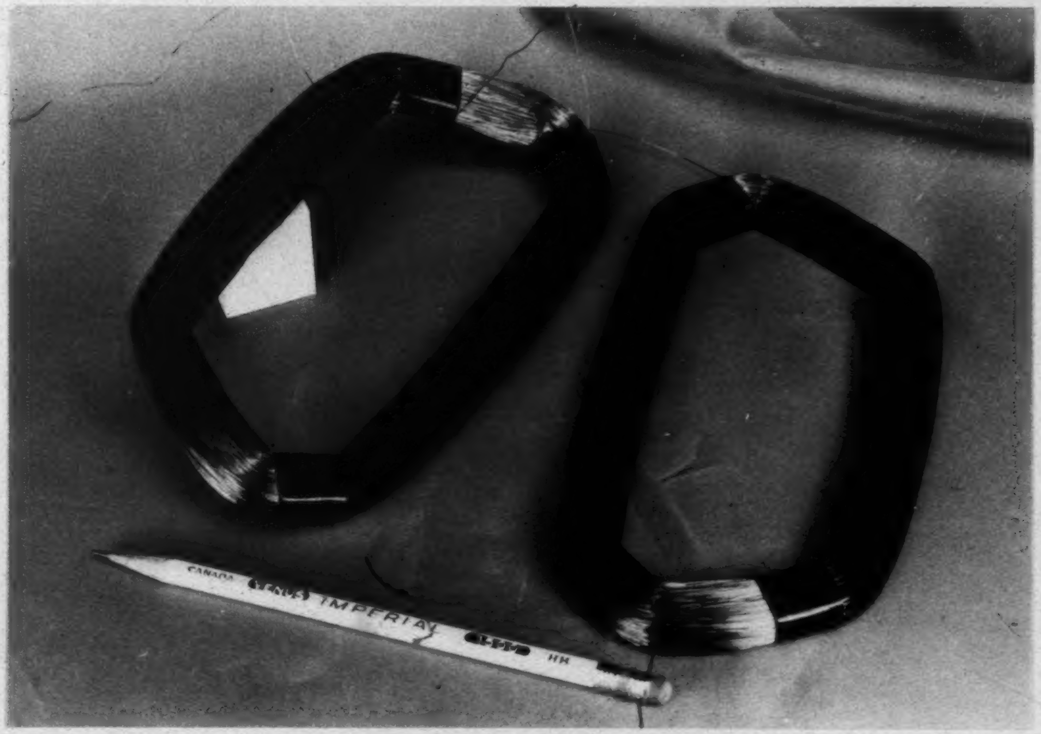
CANADA
IMPERIAL
HH

Plate 3	One of the pair of specimen-gap sensing coils which provides the main signal for flux variations parallel to the bulk field.
Plate 4	An unencapsulated subassembly consisting of a pair of permalloy polepieces, a pair of barium ferrite permanent magnet blocks, and one of the magnetizing coils.

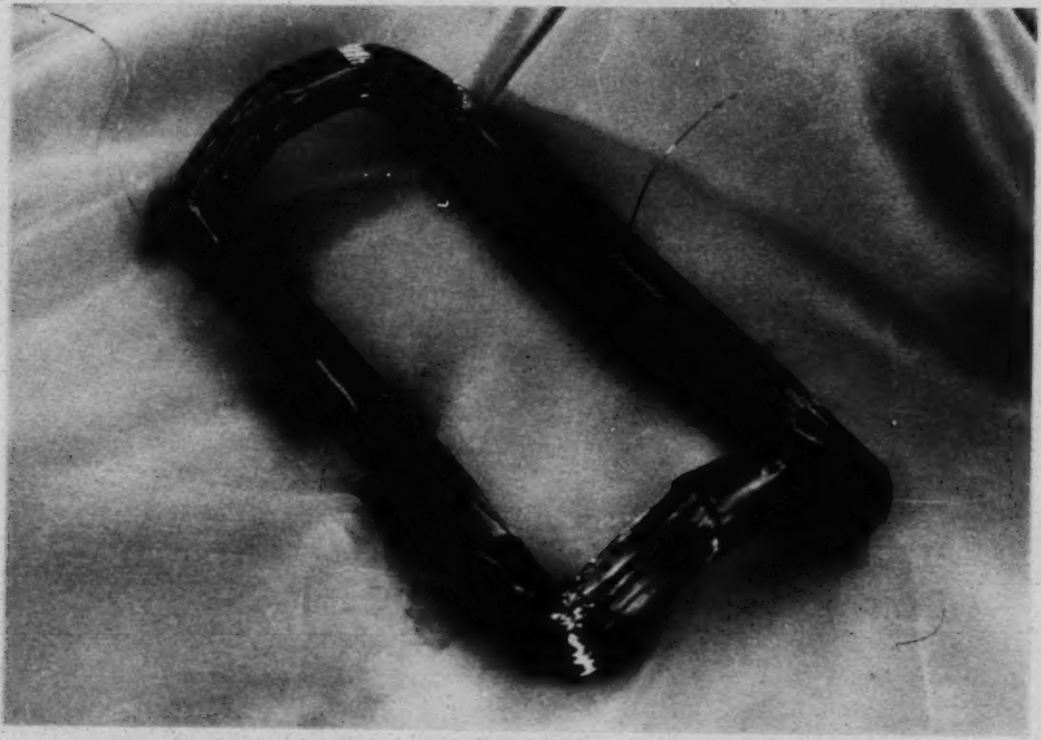

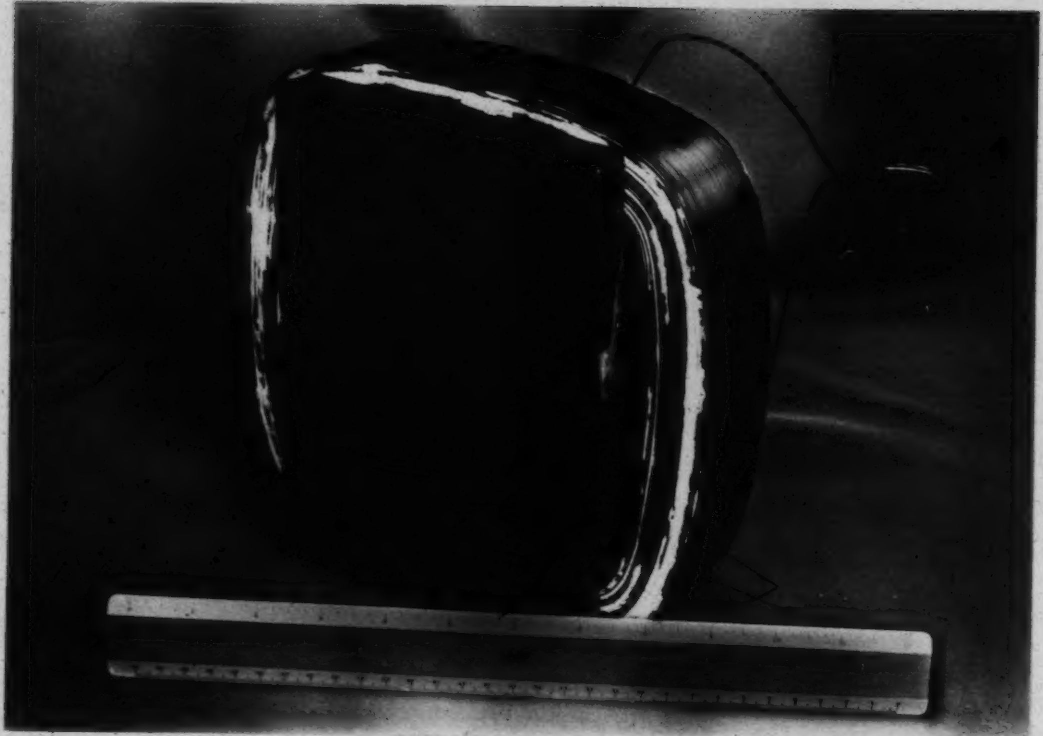

before the resin started to gel the coils were quickly extracted and placed on sheets of PVC film. After the cure was complete the coils were removed from the PVC film. The electrical tape could then be removed since polyester resin does not adhere to it.

5.5 Magnetic Bridge Subassembly

A subassembly was made of the balancing gap and the thin-tape polepieces. It consists of four permanent magnet blocks (arranged in pairs and separated by ceramic pillars to form the balancing gap), one 15.2 cm square, 2.5 cm thick polepiece assembly, and associated magnetizing coils. Also included are the alternating-flux-only magnetic signal cores which go to the magnetic-sensor cavities.

Figure 5.1 shows the components without the coils and spacers. The smaller polepiece assemblies consist of strips of 100 micron Permalloy 80 are were assembled and vacuum impregnated in separate molds before their use in this subassembly. Two concentric magnetizing coils are used to make maximum use of available space.

The individual parts were assembled in a plywood mold of the shape indicated in Figure 5.1. The walls were made of 3.8 cm fir plywood. They were bolted to avoid distortion given the pressure gradients present during the vacuum impregnation. All parts were initially located by

Figure 5.1 Magnetic bridge subassembly.

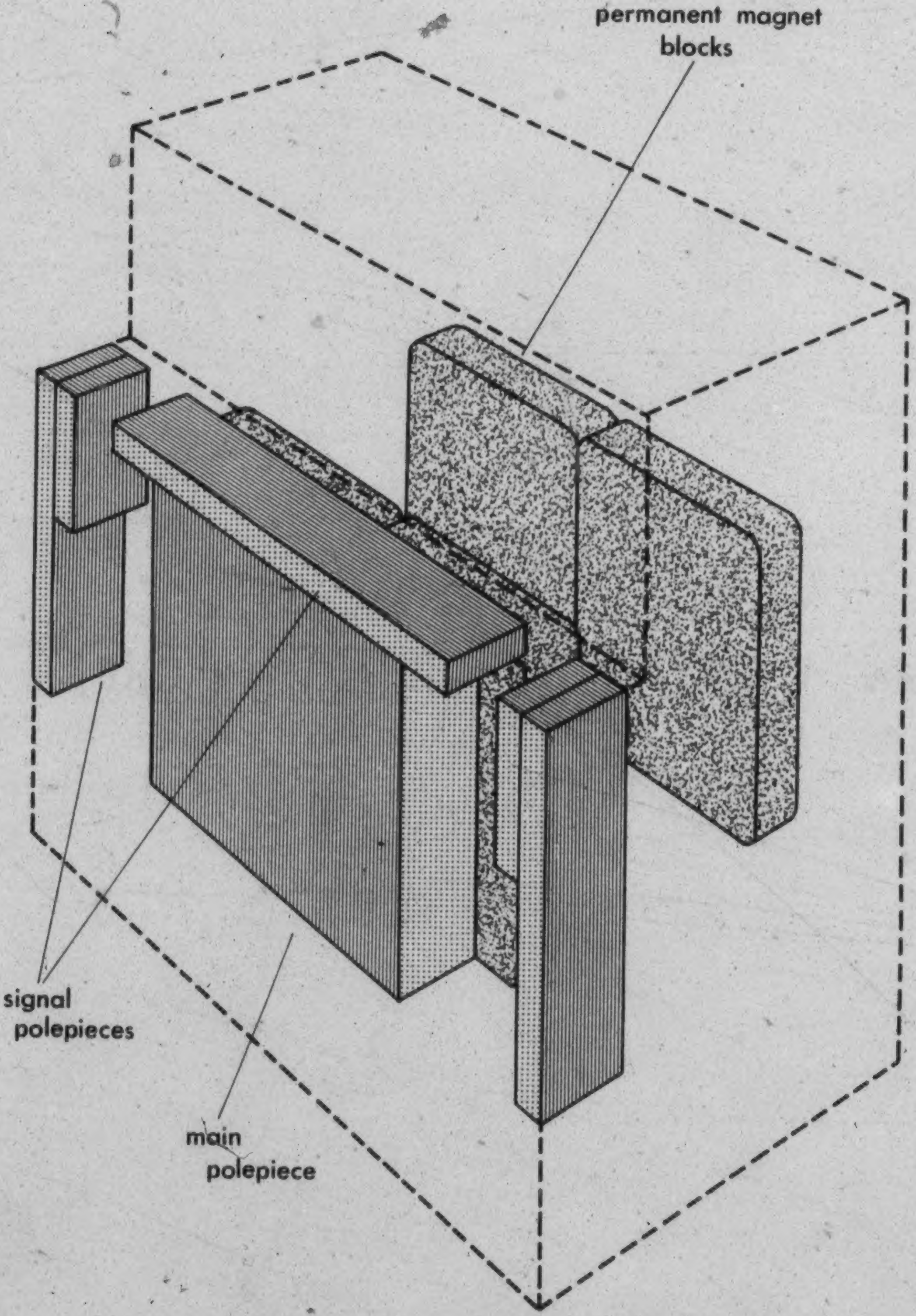
permanent magnet blocks
signal polepieces
main polepiece

ceramic spacers cemented in place with epoxy. After all main parts were in place, four temperature-sensing diodes were placed in various locations within the cavity, and their leads were passed through the mold walls. The magnetizing coils also had their leads passed through the mold walls to enable them to be used as heaters during the casting procedure and to facilitate their subsequent connection to the rest of the circuits. The remaining cavities were then filled with glass beads and the mold sealed. It was then vacuum-impregnated following essentially the same procedure as will be described for the main casting. The completed subassembly is shown in Plates 5 and 6. Another subassembly consisting of a pair of polepiece blocks, a pair of magnet blocks, and one of the magnetizing coils is shown in Plate 4. The pieces were cemented together but not cast.

5.6 Assembly of the Main Magnetic Circuit

Using the magnetic bridge subassembly as a base, the central polepiece blocks, magnetizing coils, and the ceramic specimen gap spacers were cemented in place, as shown in Plate 7. The addition of one of the direct signal coils is shown in Plate 8. Allowance was then made for the spinner shaft by cementing in a 5.0 cm diameter solid PVC cylinder. This piece was first turned to a 1.5 mm taper and was coated with a release agent consisting of RTV

Plates 5 and 6	Two views of the magnetic bridge subassembly. Note the thin-tape signal polepieces and the ceramic bars used to position the magnetizing coils within the mold and also those used to anchor the wire leads coming from the casting.

Plate 7 One polepiece block and magnetizing coil has been added to the magnetic bridge subassembly. The four ceramic spacers used to define the specimen gap are also shown.

Plate 8 One of the direct specimen-gap signal coils has been added.

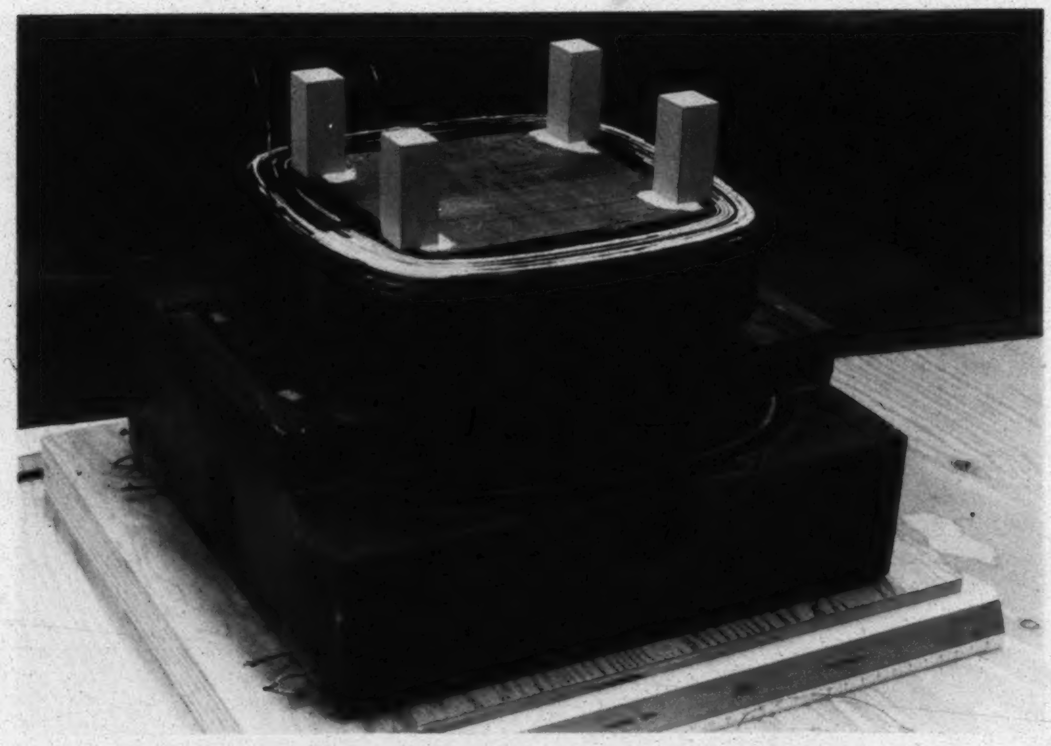

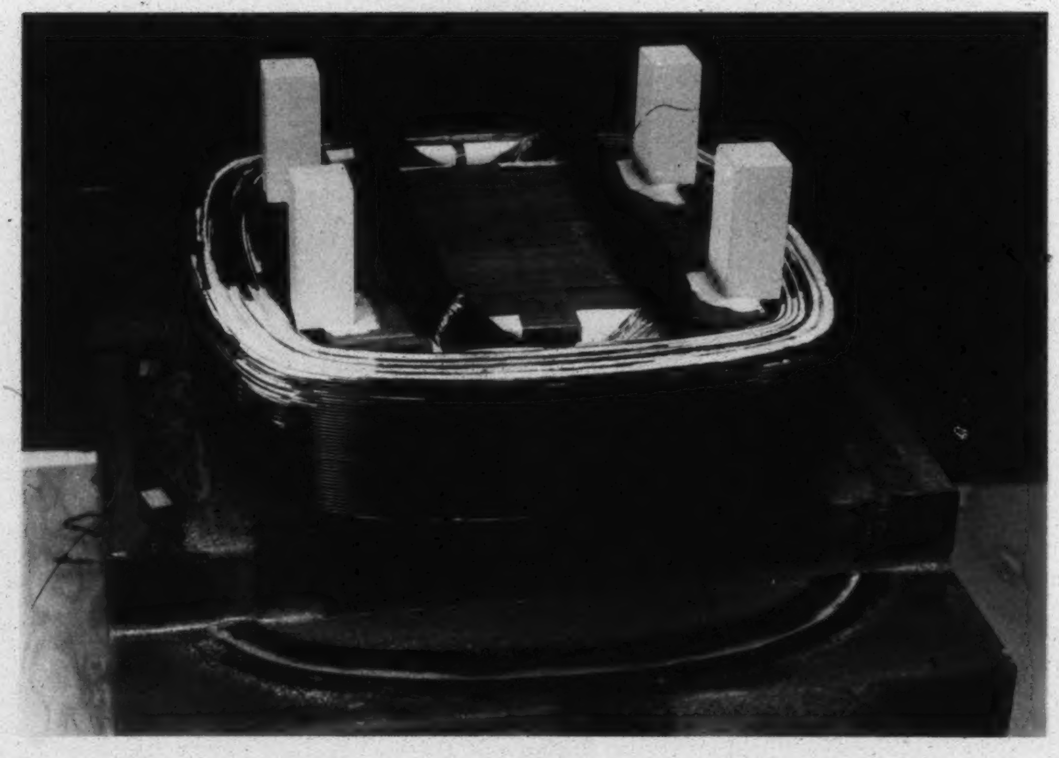

silicone rubber dissolved in toluene. Both the taper and the coating facilitate the cylinder's removal after casting. The cylinder was then covered with a thixotropic epoxy resin which forms the inner surface of the shaft opening and also serves to locate the two cross-field signal coils, as is shown in Plate 9. The two direct nulling coils were then added (Plate 10), followed by the cross-field nulling coils and outer polepiece assembly (Plates 11 and 12). After the last magnetizing coil was in place the entire structure was placed on its side and cemented to one of the outer shield walls, using suitable ceramic spacers, as is shown in Plate 13. The same picture also shows the wooden frame which was to be used to hold the outer magnetic circuit in place as it was being cemented in. The laminations of the outer frame were individually cemented into place with a room-temperature-curing epoxy. The ends of all the laminations were overlapped to afford a low-reluctance magnetic frame. Because of nonuniformity in placing the epoxy resin, the laminations would not lie flat after they had been laid to a thickness of about 2 cm. Therefore another wooden frame was periodically placed on top of the partly completed magnetic frame and weighted down with heavy steel bars until the epoxy had cured. When the entire frame was completed and the epoxy cured, the wooden frame supporting the structure was removed and replaced with

Plate 9 The slightly-tapered PVC cylinder has been added. It is to form the cylindrical cavity to accommodate the specimen shaft. The cylinder has been coated with a thixotropic epoxy resin into which the pre-impregnated cross-field signal coils are embedded.

Plate 10 The direct nulling coils have been added.

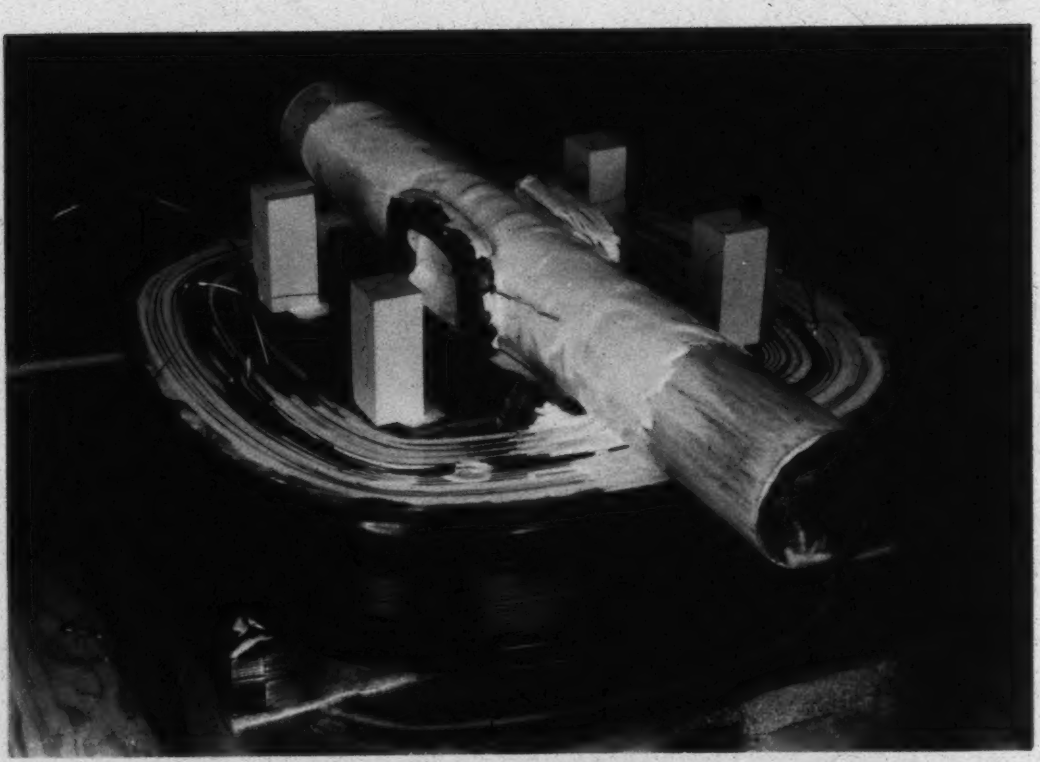

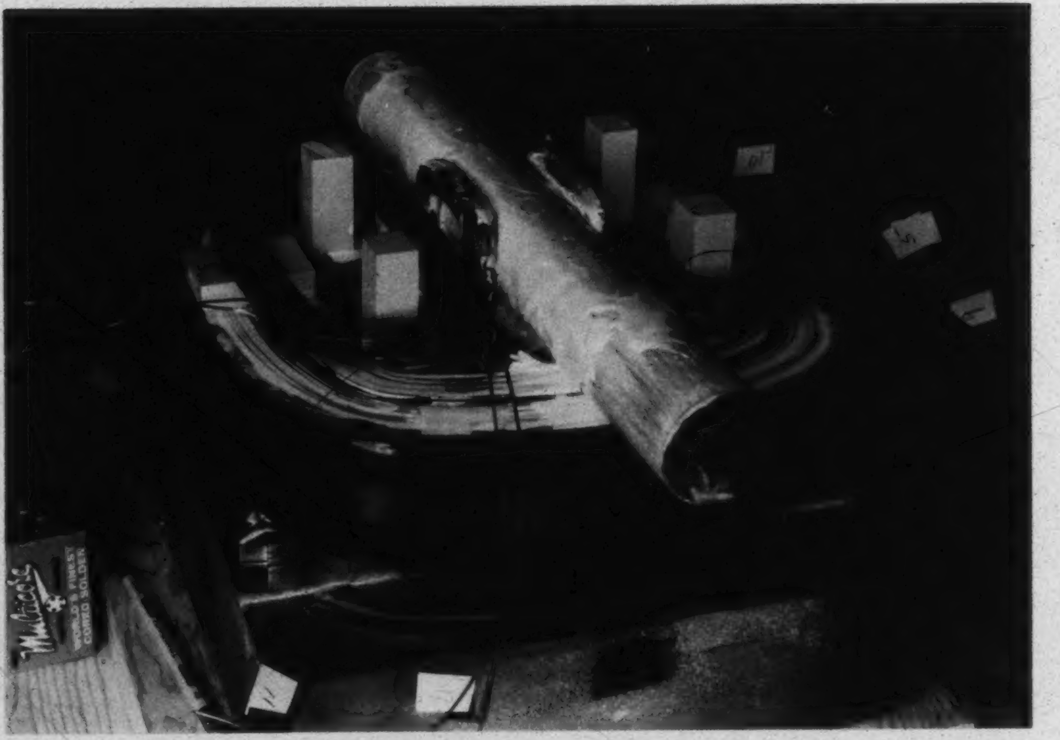
Multicore
WORLD'S FINEST CORED SOLDER

Plate 11 The outer polepiece subassembly has been added. A large outer magnetizing coil is seen in the background.

Plate 12 The cross-field nulling coils have been added.

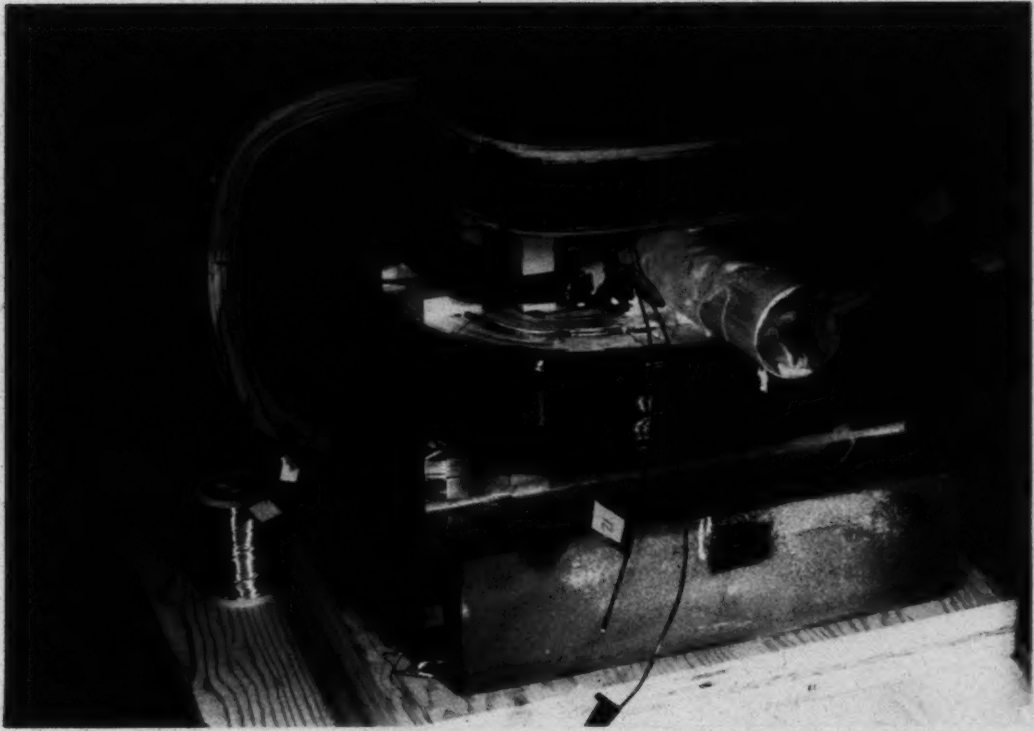

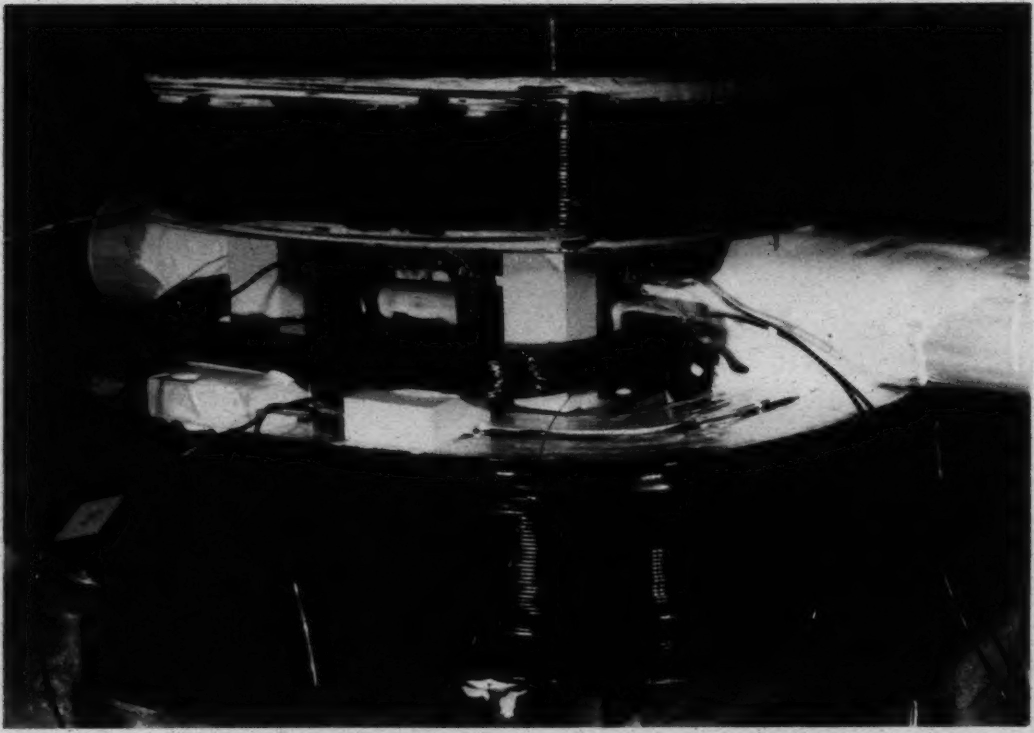

ceramic pillars, as shown in Plate 14.

After the main magnetic circuit was completed, the 38 wires which accommodate the magnetizing coils, signal coils and temperature-sensing diodes were assembled as shown in Plate 15. They are held to the shield wall with dabs of RTV silicone rubber. This shield wall was then bolted into place and all the wiring completed. Four views of the wired structure are shown in Plates 16 through 19. Also visible in these photographs is the 20-turn coil of #30 AWG wire which was wrapped onto one of the outer magnetic circuit legs in order to measure its effective permeability of the outer yoke both before and after encapsulation.

After the other three sides of the magnetic shield were bolted on to form a box, the entire remaining volume was filled with glass beads to within 2 cm of the top, as shown in Plate 20. The box was rocked back and forth while being filled to ensure that the glass beads would fill every void they could. Plate 20 also shows the two tapered wooden plugs which are used to form the cavities for the magnetic flux sensors.

The top of the transducer box was filled with ceramic bars rather than glass beads, as shown in Plate 21. This was done so that the epoxy resin, which was admitted through the top, would flow freely across the top of the

Plate 13 The completed inner magnetic circuit assembly has been placed on its side and, by means of ceramic spacers and epoxy resin, is attached to one of the outer magnetic shield walls. A wooden frame has been constructed on which the outer permalloy yoke will be assembled.

Plate 14 The outer permalloy yoke has been assembled and the wooden frame which supported it has been removed and replaced with ceramic pillars.

Plate 15 All signal coil, magnetizing coil, and temperature-sensing diode leads have been routed to two 18-pin electrical connectors. The wires are supported by means of dabs of RTV silicone rubber.

Plate 16 All electrical connections have been made and the shield wall holding the electrical connectors is bolted into place. Note the twenty-turn permeability-monitoring winding about one leg of the outer permalloy yoke.

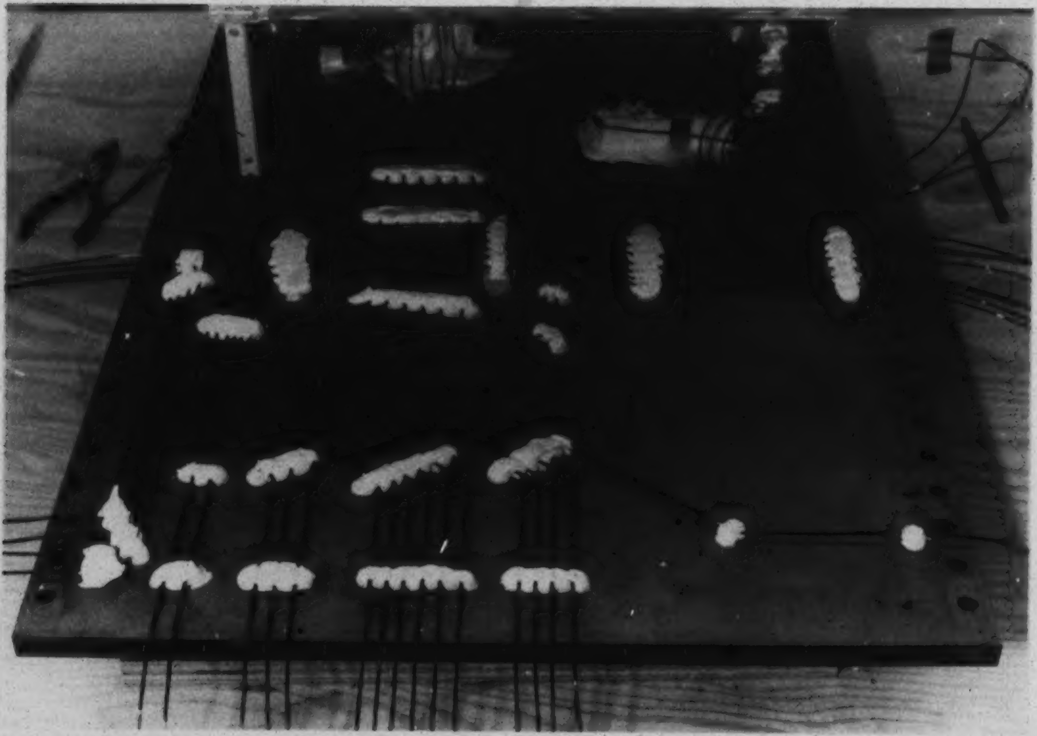

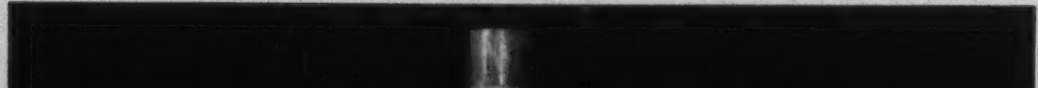

Plates 17 and 18 Two views of the completed internal transducer assembly.

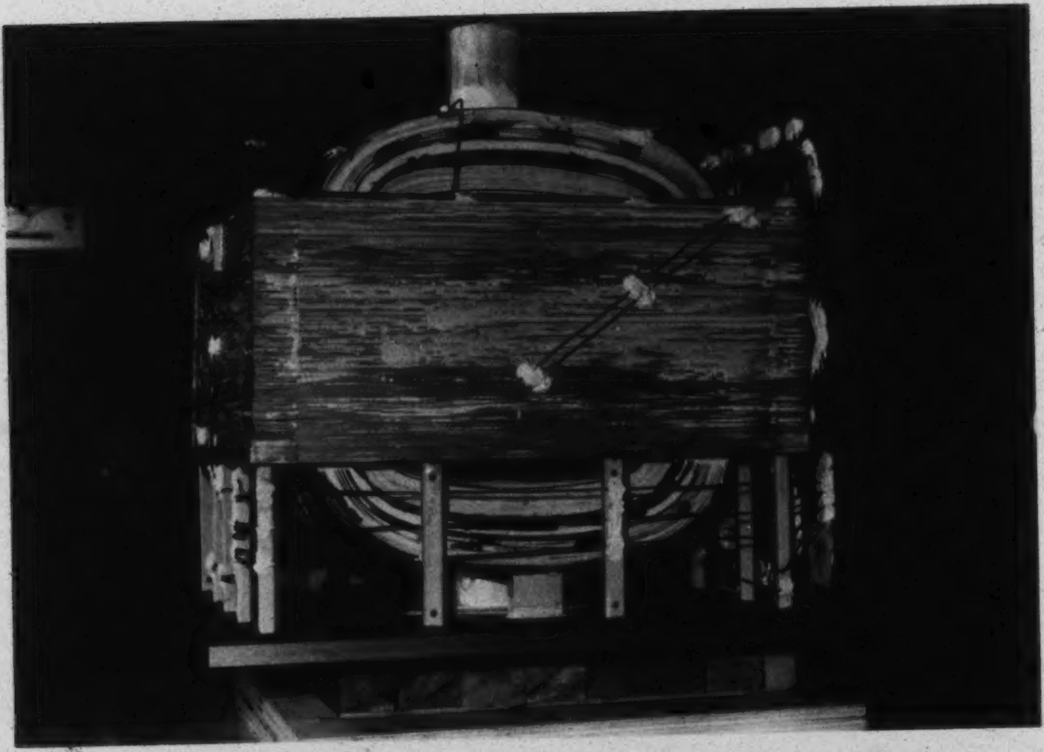

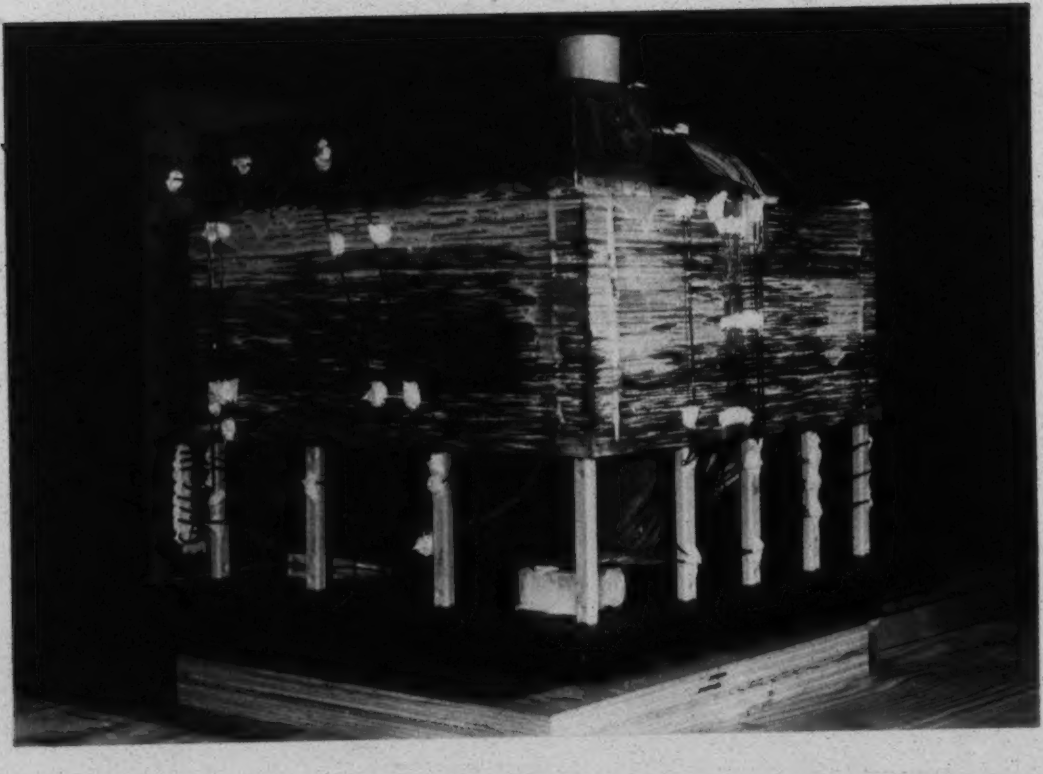

Plate 19 Top view of the completed internal transducer assembly.

Plate 20 Three of the remaining shield walls have been bolted into place and the voids in the resulting box are filled with glass beads. Note the two wooden plugs which have been inserted to form the cavities for the magnetic bridge sensors.

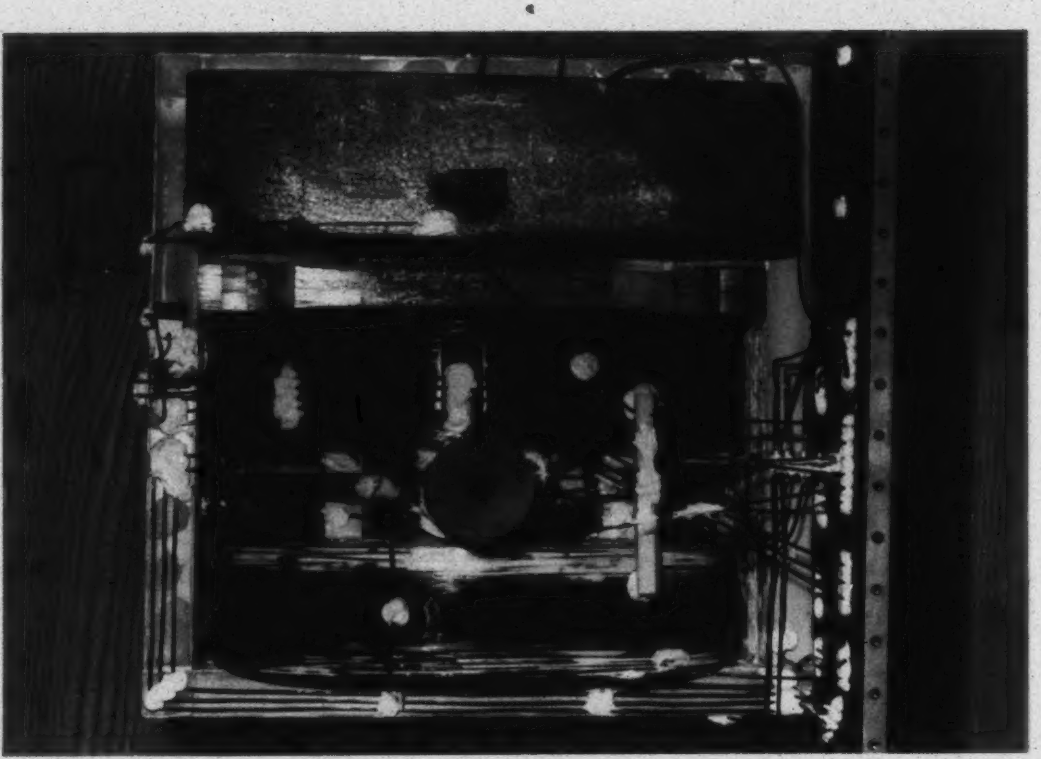

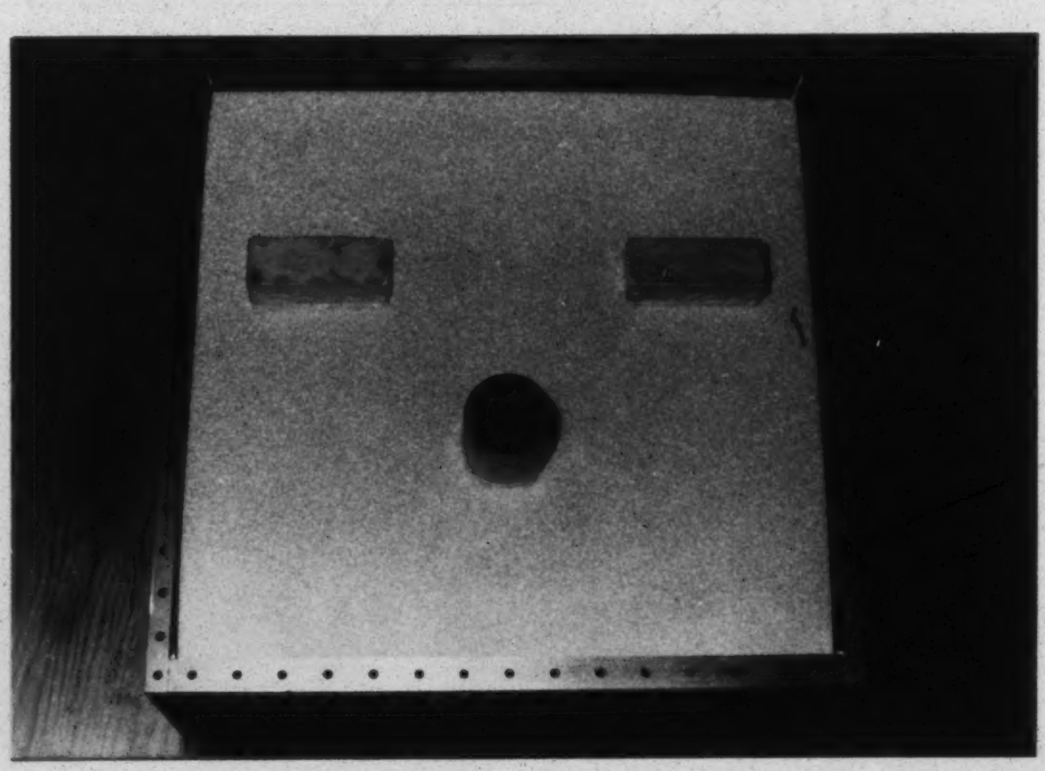

cavity and then uniformly force its way down through the glass beads. The top of the box does not contain any critical magnetic components which would require filling it with glass beads.

5.7 The Vacuum Impregnation Procedure

After the shield top had been bolted into place the transducer block was lowered into a vacuum chamber. Two plate heaters were placed against the sides of the block and held with plywood braces, as shown in Plate 22. Electrical connections to the plate heaters, and to the magnetizing coils which would act as heaters, were brought out through the vacuum chamber walls. Connections were also provided for four temperature-sensing diodes strategically placed within the transducer block.

A schematic diagram of the hydraulic circuit used for encapsulation is shown in Figure 5.2. Premeasured quantities of the two epoxy resin components were simultaneously mixed and heated to 90°C in container A. At the same time chambers C and H were evacuated by opening valves F and G and closing B, D, and M. A pressure of about 1000 N/m^2 was maintained. After the resin was thoroughly mixed, valve E was shut and B opened slightly to admit the resin into vacuum chamber C. Here it was allowed to deaerate for approximately 10 minutes. Only a relatively small quantity of resin could be introduced into the tank at one

Plate 21 The inside of the top of the shield box is lined with ceramic bars which act as a filler while allowing for easier penetration of the epoxy resin during encapsulation.

Plate 22 The shield box is sealed and placed in a large vacuum chamber. Heater panels are put into place and all hydraulic and electrical connections are made in preparation for vacuum impregnation.

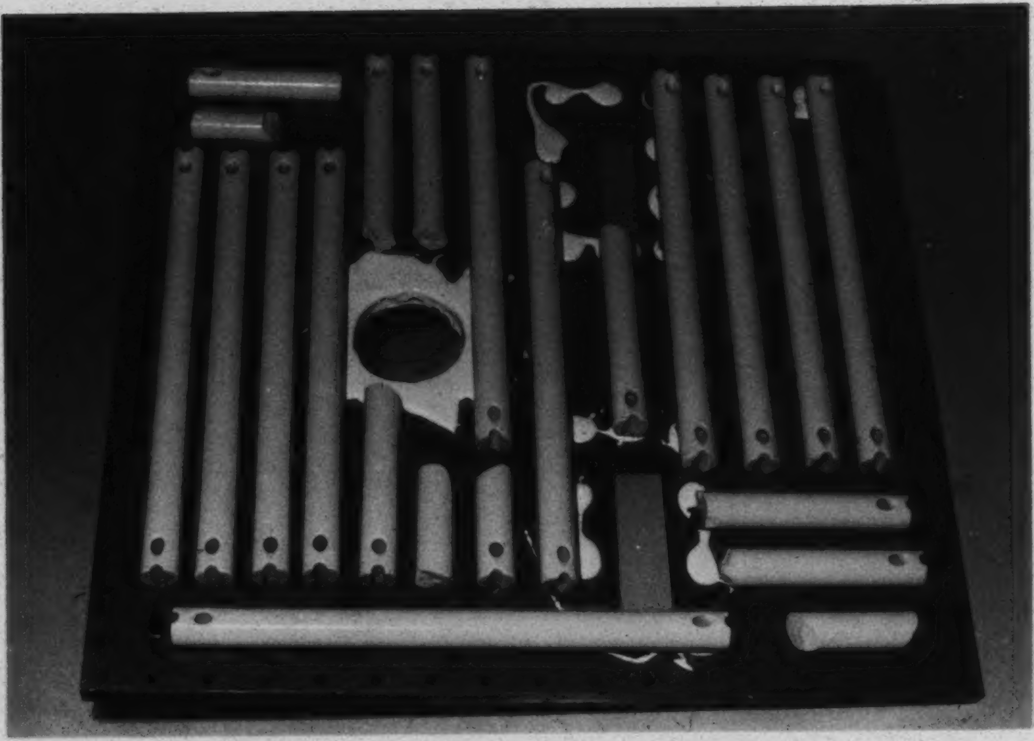

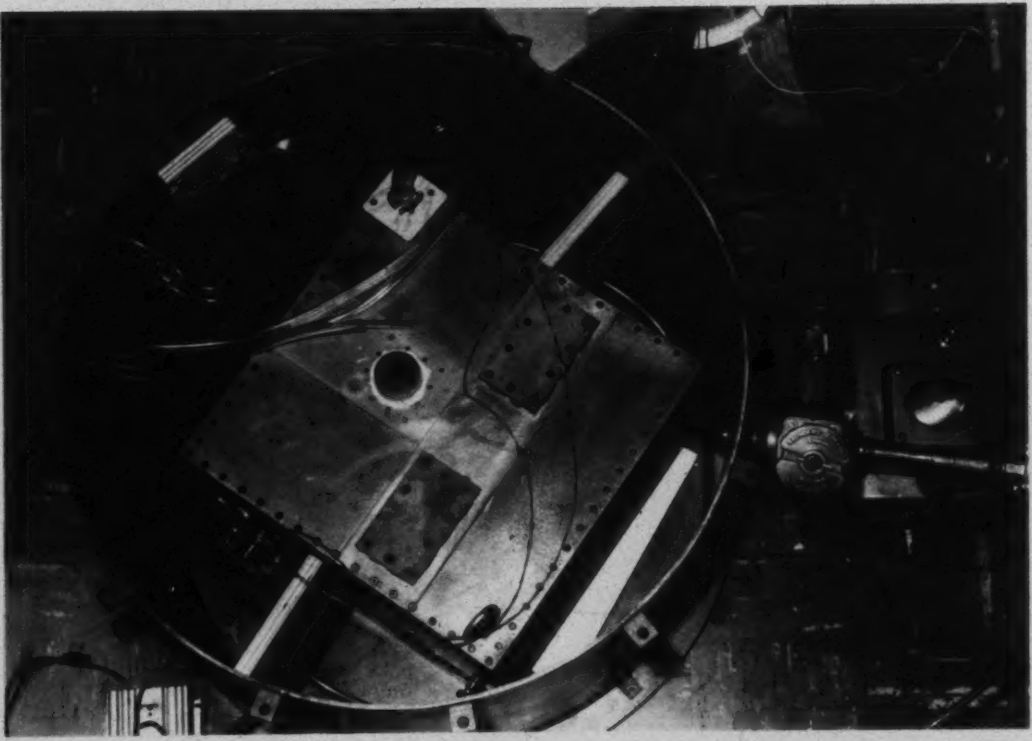

Figure 5.2 Schematic of the hydraulic circuit used for encapsulating the main transducer.

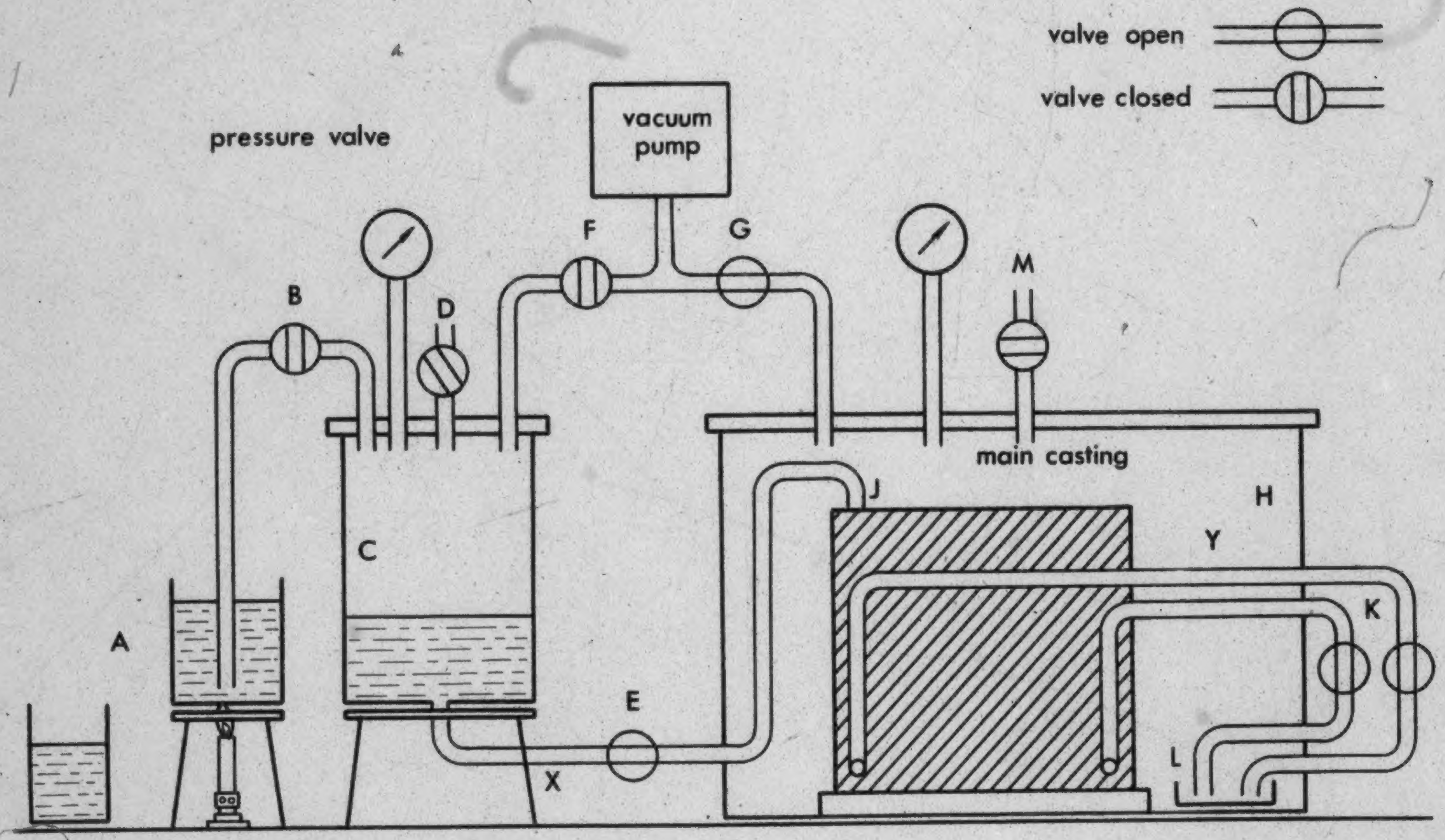
pressure valve
vacuum pump
valve open
valve closed
A
B
C
D
E
F
G
H
J
K
L
M
X
Y
main casting

time because of the large volume occupied by the froth which results from deaerating and also to keep the hydrostatic pressure at the bottom of the container reasonably low. Valve B was closed just before container A was empty. After the resin had thoroughly deaerated, valve F was shut and valves E and D opened, the latter only slightly. This allowed the increased air pressure in chamber C to force the resin through hose X and into the evacuated transducer block at J. The block was kept evacuated through four smaller hoses Y which were connected to four holes near the bottom of the shield box, passed twice through the vacuum chamber walls in order that valves might be put on each, and opened into the main vacuum chamber just over an overflow container L. When tank C had almost emptied, valve D was shut and F opened to reevacuate the chamber. It was then ready to receive another batch of resin which had been mixed in container A while the previous batch was being forced into the transducer block. In all, five of these overlapping cycles were required to completely fill the block. The uniformity of epoxy flow within the block was evident from the fact that no resin appeared in any of the overflow hoses Y until 95% of the free volume within the block had been filled. As soon as resin did start flowing through one of the hoses Y, the appropriate valve K was shut to prevent excessive leakage while still allowing vacuum to be applied via the hoses not overflowing.

After impregnation was complete the hoses X and Y were removed and the corresponding holes in the block were closed with threaded plugs.

The temperature of the transducer block had to be carefully regulated throughout the epoxy curing process in order that it cure properly with a minimum curing stress. Also temperature changes had to be slow and uniform so that thermal stresses would not be excessive. After the block was placed into the vacuum chamber, its temperature was raised to 95°C over a time period of about 24 hours. After impregnation was complete, it was removed from the vacuum chamber and placed into an insulated box consisting of 10 cm thick styrofoam. Here the block was allowed to remain at 95°C for another 24 hours. It was then allowed to return to room temperature over a time period of about 48 hours. The temperatures within the block were continuously monitored by four temperature-sensing diodes. It was noted that temperature differences of as much as ±5°C existed within the block throughout the curing process, and curing times were extended to allow for this.

After the transducer block had cooled, the PVC cylinder and wooden plugs were easily removed by tapping them with a hammer.

The permeability of the outer permalloy yoke was measured by means of the twenty-turn monitoring winding which was placed on one leg of the yoke after the latter had been assembled. Measurements were made before the vacuum impregnation and again after the transducer encapsulation was complete and the block had cooled. Both measurements indicated an effective permeability of about 25,000. This indicates that the sensitive permalloy components were not seriously strained, either elastically or inelastically, during the encapsulating process.

Plate 23 Overall view of the spinner instrument with its associated electronics. At the far left is the transducer block with its preamplifier. The block is mounted on a sturdy table and is isolated from the table by four rubber pads. Nothing else save the preamplifier is mounted on this table. The spinner shaft assembly (center) is mounted on the adjacent workbench. Right of center can be seen the signal electronics, the motor speed regulator, and the pulse-discharge power supply.

Plates 24 and 25 Two views of the spinner shaft assembly. The shaft casing is rubber-isolated from a wooden frame which is mounted on two ball-bearing slides. The slides are mounted on wooden brackets which are bolted to the workbench. The slides allow more than adequate movement to permit easy access to the specimen head. Also visible are the air and vacuum hoses and electrical cables to the motor and tachometer.

Plate 26	The standard solenoid, described in Chapter 7, is shown with four standard-size specimens and the specimen cube.
Plate 27	The instrument for bulk susceptibility. It is described in Chapter 6.

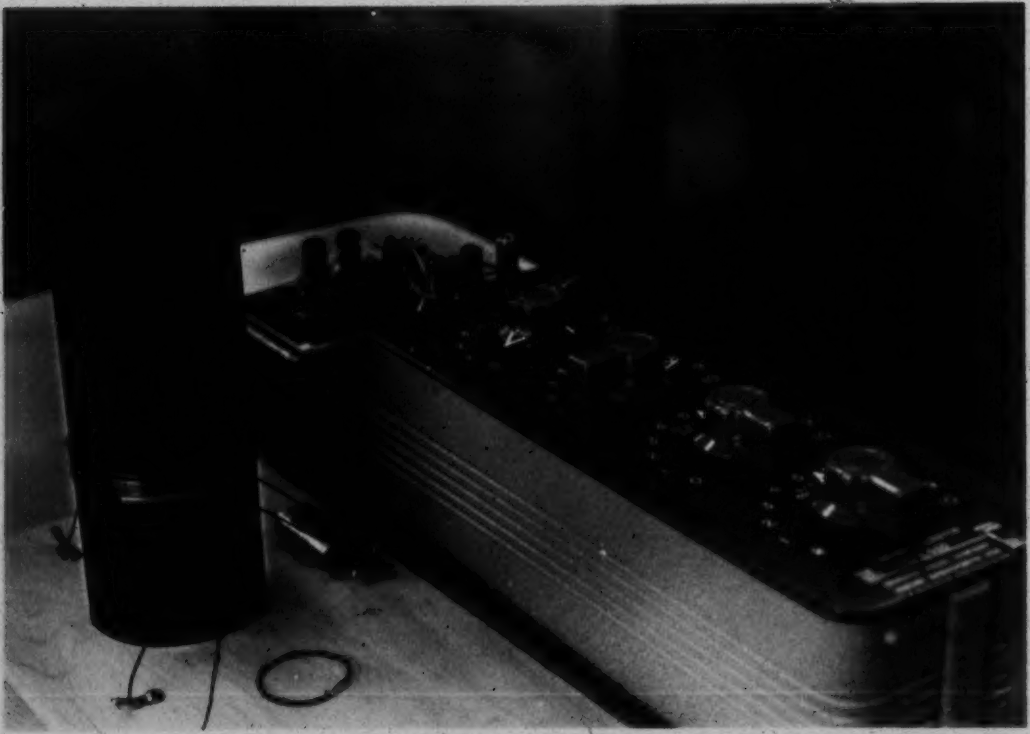

CHAPTER 6

INSTRUMENT FOR BULK SUSCEPTIBILITY

Bulk susceptibility or, more accurately, axial susceptibility of the rock specimens is measured by means of a double-tuned differential transformer. No ferromagnetic core materials are used, except for trace amounts to establish balance. The instrument is shown schematically in Figure 6.1. The two secondary halves are relatively tightly coupled to a portion of the primary, but quite loosely to each other. The transformer windings are tuned to 9.8 kHz and are excited at that frequency. Equal and opposite voltages are induced in the two identical secondary windings. Thus, when the transformer is balanced, the output is zero. Upon inserting a specimen into the holder, the coupling between the primary and the nearby secondary is increased (if the specimen is paramagnetic or ferromagnetic) or decreased (if the specimen is diamagnetic). In either case the off-balance voltage is proportional to the susceptibility of the specimen multiplied by its volume.

Fine-balancing of the transformer is accomplished by moving a piece of ferrite and a piece of lead along the base plate upon which the transformer block is mounted. For rough-balancing, a loosely-coupled 6-turn winding is

Figure 6.1 Schematic of the bulk susceptibility instrument.

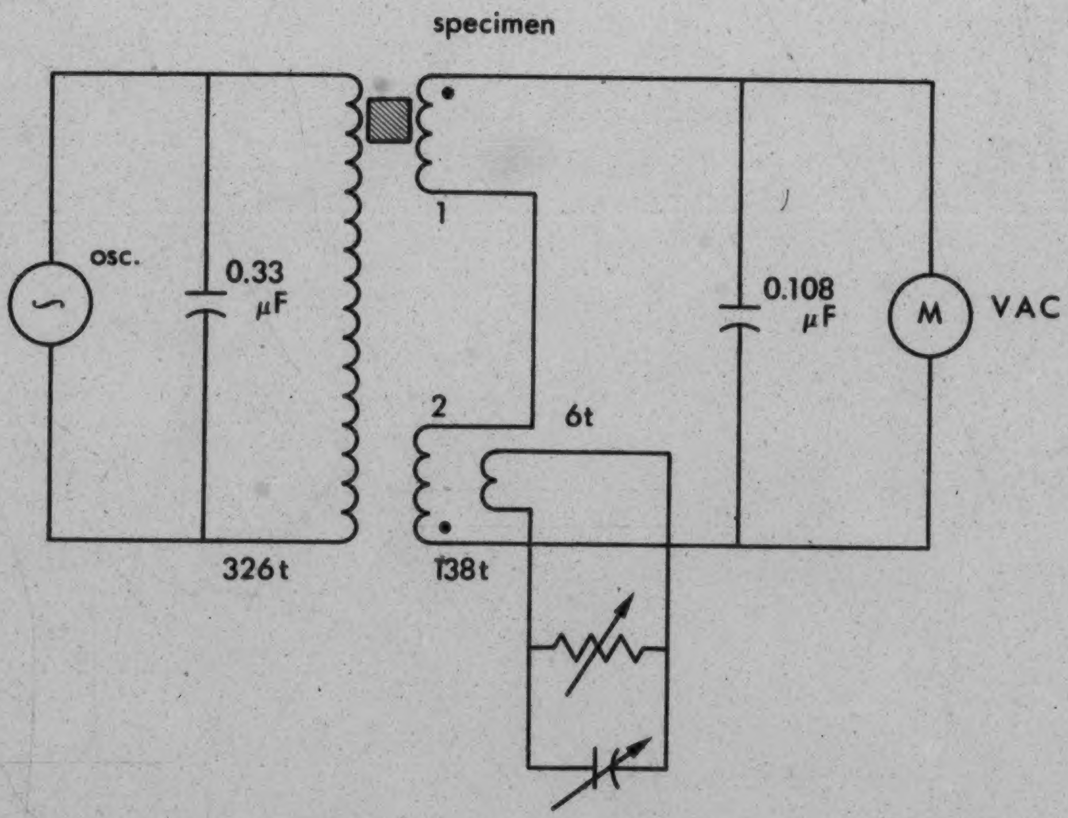
specimen
osc.
0.33
μF
326t
1
2
138t
6t
0.108
μF
M
VAC

placed near secondary 2. Varying the resistance across this winding effects resistive balance while varying the capacitance effects reactive balance.

A cross-sectional view of the differential transformer is shown in Figure 6.2. The primary and secondary coils were wound on phenolic coil forms of the dimensions indicated. The coils were placed, with their tuning capacitors, inside a PVC cylinder. The cavity within the cylinder was then vacuum-impregnated with an epoxy resin, leaving only a small cavity near the top to accept the specimen. Primary and secondary leads are brought out through the sides of the cylinder and the balancing winding is placed outside it.

The balance has been found to be acceptably stable to a few microvolts with a 10 V drive. The instrument is capable of measuring, in 2.5 cm by 2.5 cm cylindrical specimens, a susceptibility of less than 10^{-6} mksu. Since this is considerably less than the diamagnetic susceptibility of most materials, virtually any specimen may be measured.

Diamagnetic susceptibility is readily distinguished from ferromagnetic susceptibility by noting the different direction in which the ferrite slug must be moved in order to reestablish balance after the specimen is inserted.

Figure 6.2 Actual-size cross-section of the bulk susceptibility instrument.

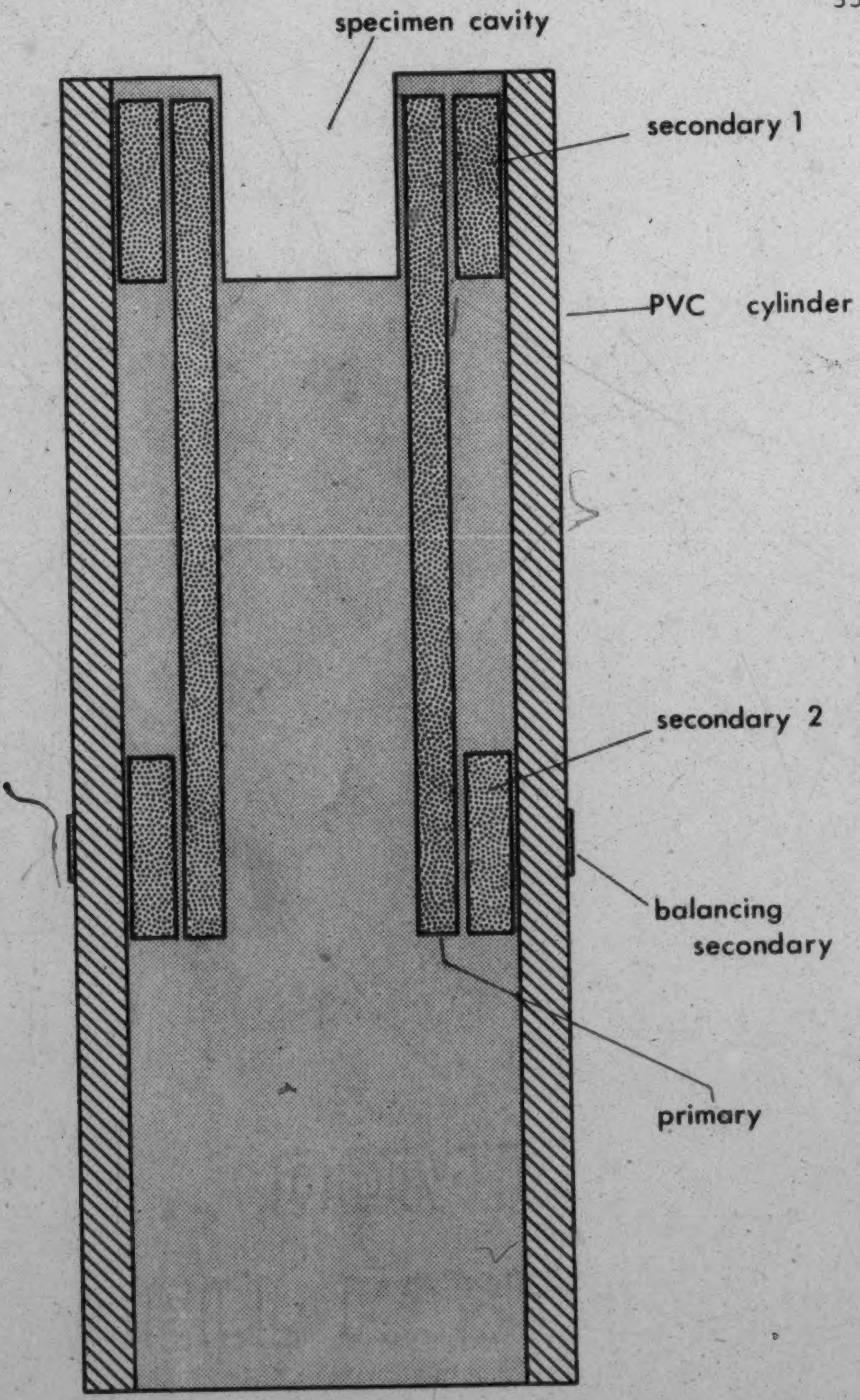
specimen cavity
secondary 1
PVC cylinder
secondary 2
balancing secondary
primary

CHAPTER 7

OBSERVATIONS WITH THE NEW INSTRUMENT

7.1 Noise Levels in the Spinner Instrument

For the observations presented in this chapter, the specimen-gap coils with axes parallel to the applied field direction were used as flux sensors. It was shown in Eq. 3.130 that the Johnson noise generated by these coils is equivalent to an apparent susceptibility anisotropy of 4.4 x 10^{-11} mksu measured in a bandwidth of 0.1 Hz. This noise amplitude is increased somewhat if coil reactances are not tuned out. The first stage of the amplifier also increases the noise level.

Figure 7.1 shows an actual 15-minute observation of apparent susceptibility anisotropy vs. time. Only the fluctuating component of the observation is shown. The fluctuation is superimposed on a relatively stable D.C. output, typically equivalent to a susceptibility anisotropy of about 4 x 10^{-10} mksu. This D.C. level results largely from offsets developed by the operational amplifiers in the main amplifier and phase-sensitive detectors. Their effect is easily deducted from observed signal levels.

The shaft was spun without a specimen and outside the specimen gap. The RC time constant of the integrators

Figure 7.1 Apparent susceptibility anisotropy versus time in a typical 15-minute observation. The shaft is spun outside the specimen gap, so the fluctuations are due to transducer and amplifier noise.

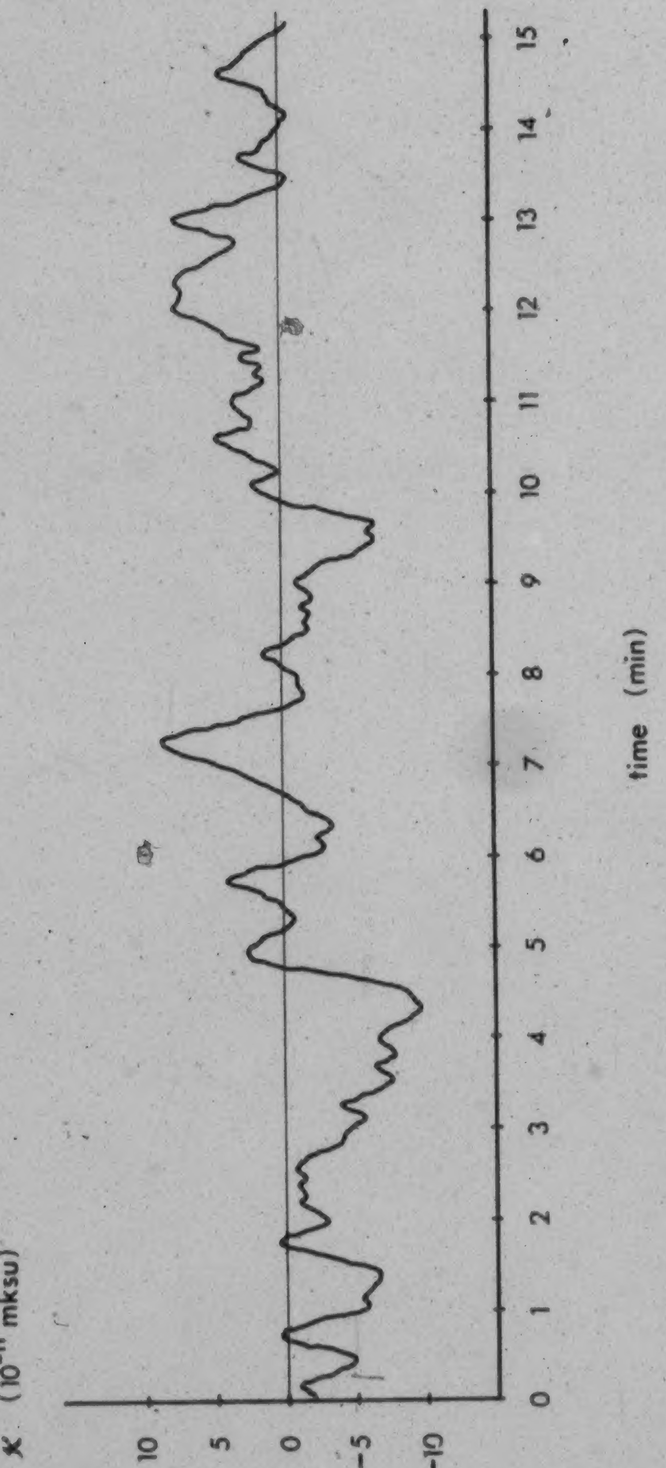
κ (10⁻¹¹ mksu)
10
5
0
-5
-10
0
1
2
3
4
5
6
7
8
9
10
11
12
13
14
15
time (min)

was set at 10 seconds, and therefore the observed bandwidth was about 0.03 Hz. For this bandwidth the theoretically predicted noise from the signal coils used, assuming zero net reactance, would be about 2.4 x 10^{-11} mksu. The signal was sampled at 10-second intervals for the 15-minute duration of the trace in Figure 7.1. From these observations the rms fluctuation was computed and was found to be 4.1 x 10^{-11} mksu (3.3 x 10^{-12} emu/cm^3). This is only 4.7 dB above the theoretical minimum. The difference can be ascribed to the coils' inductive reactance and to noise from the first stage of the amplifier.

The noise seen ahead of the phase-sensitive detectors is dominated by power mains interference, mainly at 60 Hz and 180 Hz, with considerable noise from cyclic switching transients produced by line-operated electrical equipment. The actual voltage at the signal-sensing coils is about 20 microvolts rms. This corresponds to a level equivalent to a susceptibility anisotropy of about 2 x 10^{-7} mksu. Adjustment of the nulling control will reduce this level, but not by more than a factor of three, since the wideband noise due to cyclic switching transients is not readily nulled out completely with circuitry having unbalanced reactances.

The output from the phase-sensitive detectors shows no detectable change when the nulling control is taken through its full range, except that the amplitude calibration changes due to the gain change in the null channel of the main amplifier. Some signal is picked up by the nulling coils and varying the gain of the null channel will change the output signal. It is therefore necessary to recalibrate the output amplitudes with the standard solenoid whenever a considerable change in the null-control setting is made.

The ratio between the power-mains interference level of 2×10^{-7} mksu and the observed rms fluctuation of 4.1×10^{-11} mksu indicates that the dynamic range of the phase-sensitive detectors is about 5000, or 74 dB. It is therefore concluded that, if no tuned circuits or other narrow-band filtering is to be used, the efforts to give the phase-sensitive detectors a wide dynamic range have been useful.

7.2 Operating Sensitivity of the Spinner

When the shaft with specimen cube is spun in the specimen gap, a rather large and steady susceptibility anisotropy is indicated, even if the specimen cube is empty. This anisotropy is typically 3×10^{-8} mksu and results from the nonvanishing magnetic susceptibility of the shaft materials. The signal from the shaft can be deducted from the signal with the shaft-plus-specimen to obtain the specimen signal.

In addition to the steady offset due to shaft magnetism, there is a fluctuation in the signal which is attributable to both the specimen and the shaft. Figure 7.2 shows an actual 15-minute observation of susceptibility anisotropy vs. time. As in Figure 7.1, only the fluctuating component is shown. The shaft was spun with the specimen cube and a rock specimen having a bulk susceptibility of about 3 x 10^{-5} mksu and an **h**-factor of about 1%. It can be seen that the output would be relatively steady for a period of minutes and then go through similar periods of essentially monotonic change. The relatively small fluctuations during the periods of "steady" signal are similar in magnitude to those shown in Figure 7.1, and probably represent thermal noise. The larger amplitude variations, which tend to be monotonic for periods of one to four minutes, are possibly due to trace quantities of ferromagnetic debris adhering to the surfaces of the shaft, specimen cube, and rock specimen. When the shaft rotates in the specimen gap, such ferromagnetic particles are subjected to considerable magnetic and aerodynamic forces, and their resulting movement could change the observed susceptibility variations.

The output signal was sampled at 10-second intervals for the 15-minute duration of the trace in Figure 7.2. From these observations the rms fluctuation was computed

Figure 7.2 Apparent susceptibility anisotropy versus time in a typical 15-minute observation. The shaft is spun with a rock specimen in the specimen gap. Therefore magnetic fluctuations intrinsic to the shaft and specimen appear in the output.

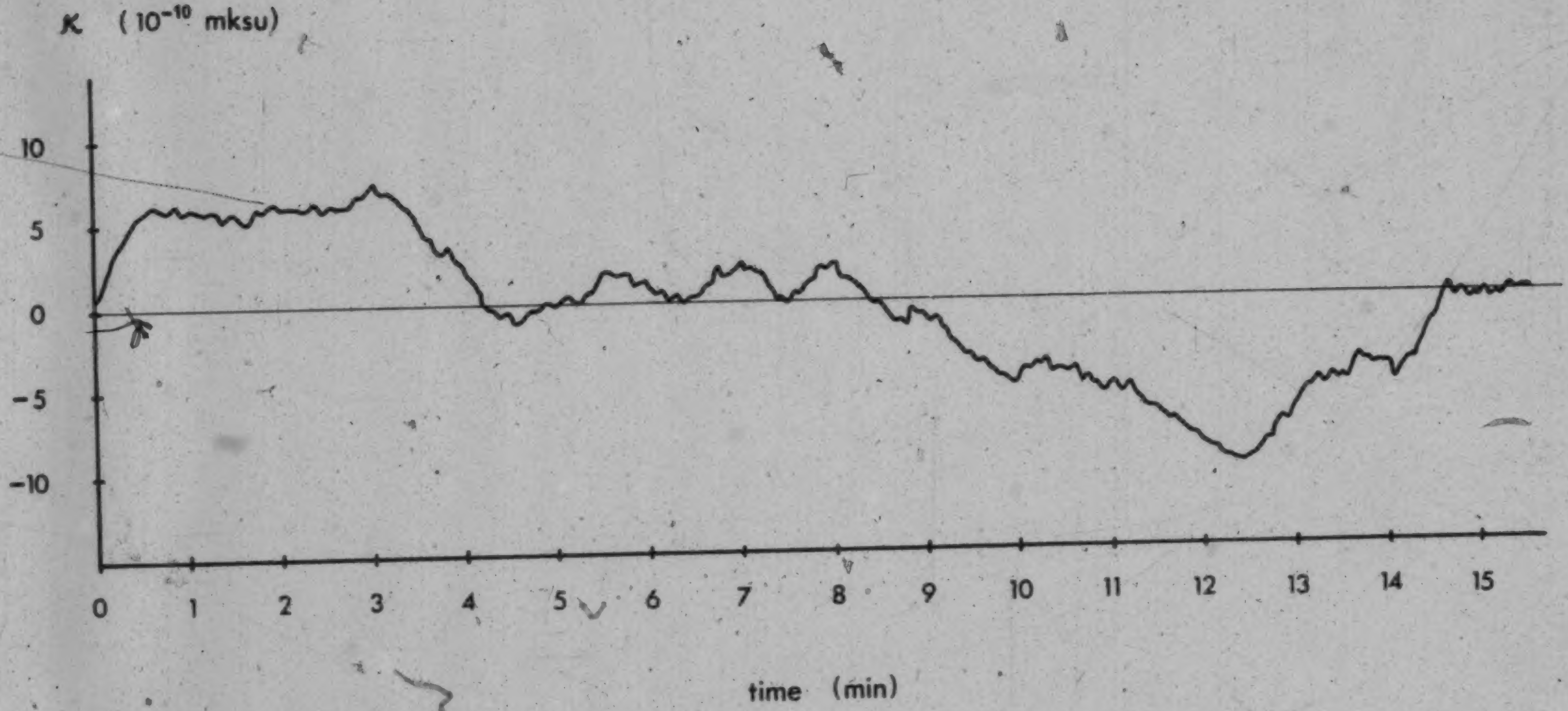

κ (10^{-10} mksu)
10
5
0
-5
-10
0
1
2
3
4
5
6
7
8
9
10
11
12
13
14
15
time (min)

and found to be 4.4 x 10^{-10} mksu, or about ten times the observed transducer noise.

When the specimen cube is re-oriented to spin about a different axis the handling which is required constitutes another source of signal fluctuation. This fluctuation could also be caused by the forced movement of trace quantities of ferromagnetic debris on the surface of the specimen cube. This hypothesis is supported by the fact that the observed fluctuations decreased by approximately an order of magnitude after the specimen cube had been cleaned by soaking it in dilute hydrochloric acid for twenty minutes. This treatment is also given to all rock specimens before measurements are taken.

A series of 20 sets of measurements was taken on the shaft with an empty specimen cube. The normal procedure of stopping the shaft and re-orienting the cube after every measurement was followed. The observed in-phase and quadrature components of susceptibility anisotropy were tabulated according to specimen cube orientation. This gives a good indication of the repeatability of the shaft signal. Results for the three spin axes are shown in Tables 7.1 A, B and C. In each table, means and standard deviations are computed for both in-phase and quadrature signal, as well as for their vector sum. These standard deviations are equivalent to rms "noise" occasioned by handling the specimen cube. The noise levels computed for the three spin axes agree quite well.

TABLE 7.1 Results of a series of 20 sets of measurements taken on the spinner shaft with an empty specimen cube. The routine measurement sequence was followed. Readings are tabulated according to spin axis. Standard deviations are also shown.

TABLE 7.1A

Observations with shaft and empty specimen holder (Axis 1). All readings are in mks units.

Reading number	I (10^{-10})	Q (10^{-10})	X (10^{-10})	$[I-\overline{I}]^2$ (10^{-20})	$[Q-\overline{Q}]^2$ (10^{-20})	$[X-\overline{X}]^2$ (10^{-20})
1	445	206	490	900	144	1024
2	406	189	448	81	25	100
3	416	182	454	1	144	16
4	424	184	462	81	100	16
5	406	187	447	81	49	121
6	402	182	441	169	144	289
7	433	200	477	324	36	361
8	406	193	449	81	1	81
9	404	203	452	121	81	36
10	427	194	469	144	0	121
11	402	199	449	169	25	81
12	429	218	481	196	576	529
13	431	205	477	256	121	361
14	425	180	462	100	196	16
15	396	180	435	361	196	529
16	387	177	426	784	289	1024
17	406	183	445	81	121	169
18	423	192	464	64	4	36
19	424	201	469	81	49	121
20	407	217	461	64	529	9
Mean values	415	194	458	207	141	252

$X = [I^2 + Q^2]^{1/2}$

rms noise: $\left\{[X-\overline{X}]^2\right\}^{1/2} = 1.59 \times 10^{-9}$ mksu

$\left\{[I-\overline{I}]^2\right\}^{1/2} = 1.44 \times 10^{-9}$ mksu

$\left\{[Q-\overline{Q}]^2\right\}^{1/2} = 1.19 \times 10^{-9}$ mksu

TABLE 7.1B

Observations with shaft and empty specimen holder (Axis 2). All readings are in mks units.

Reading number	I (10^{-10})	Q (10^{-10})	X (10^{-10})	$[I-\bar{I}]^2$ (10^{-20})	$[Q-\bar{Q}]^2$ (10^{-20})	$[X-\bar{X}]^2$ (10^{-20})
1	673	351	759	16	64	0
2	671	346	755	36	9	16
3	669	352	756	64	81	9
4	675	348	759	4	25	0
5	668	325	743	81	324	256
6	645	338	728	1024	25	961
7	700	348	782	529	25	529
8	696	317	764	361	676	25
9	676	350	761	1	49	4
10	694	352	778	289	81	361
11	681	347	764	16	16	25
12	675	342	757	4	1	4
13	683	343	764	36	0	25
14	664	341	746	169	4	169
15	694	346	776	289	9	289
16	676	338	756	1	25	9
17	685	351	770	64	64	121
18	673	337	753	16	36	36
19	675	342	757	4	1	4
20	677	344	759	0	1	0
Mean values	677	343	759	150	77	142

$X = [I^2 + Q^2]^{1/2}$

rms noise: $\left\{[X-\bar{X}]^2\right\}^{1/2} = 1.19 \times 10^{-9}$ mksu

$\left\{[I-\bar{I}]^2\right\}^{1/2} = 1.23 \times 10^{-9}$ mksu

$\left\{[Q-\bar{Q}]^2\right\}^{1/2} = 0.88 \times 10^{-9}$ mksu

TABLE 7.1C

Observations with shaft and empty specimen holder (Axis 3). All readings are in mks units.

Reading number	I (10^{-10})	Q (10^{-10})	X (10^{-10})	$[I-\bar{I}]^2$ (10^{-20})	$[Q-\bar{Q}]^2$ (10^{-20})	$[X-\bar{X}]^2$ (10^{-20})
1	215	222	309	484	49	484
2	257	230	345	400	1	196
3	254	216	333	289	169	4
4	252	258	361	225	841	900
5	238	221	325	1	64	36
6	246	234	340	81	25	81
7	213	266	369	576	1369	1444
8	222	229	319	225	0	144
9	239	244	341	4	225	100
10	254	236	347	289	49	256
11	222	219	312	225	100	361
12	222	233	322	225	16	81
13	255	207	328	324	484	9
14	233	217	318	16	144	169
15	257	210	332	400	361	1
16	262	236	353	625	49	484
17	214	218	306	529	121	625
18	222	231	321	225	4	100
19	235	217	320	4	144	121
20	232	228	325	25	1	36
Mean values	237	229 ✓	331	259	211	282

$X = [I^2 + Q^2]^{1/2}$

rms noise: $\left\{[X-\bar{X}]^2\right\}^{1/2} = 1.68 \times 10^{-9}$ mksu

$\left\{[I-\bar{I}]^2\right\}^{1/2} = 1.61 \times 10^{-9}$ mksu

$\left\{[Q-\bar{Q}]^2\right\}^{1/2} = 1.45 \times 10^{-9}$ mksu

For the vector sum the average noise is 1.49×10^{-9} mksu. The salient theoretically-predicted and observed noise levels are shown in Figure 7.3.

For routine measurements, the shaft signals are recorded with the specimen cube in its three positions. A sequence of five to ten rock specimens is then measured. After this the empty-shaft measurements are repeated. If they are within normal fluctuation limits of the previous set, the means of the two are used as corrections to be deducted from the readings taken with the rock specimens. If they should show a large variance with the preceding set, any intervening rock measurements of sufficiently low amplitude are discarded. The specimen cube is then cleaned and another set of readings is attempted.

7.3 Instrument Output for a General Susceptibility Matrix

If a process has aligned the magnetic crystal or grain axes in a rock, or there exists a statistical alignment of crystal or grain axes, then bulk specimens will be anisotropic. Assuming linear, reversible magnetization of the specimen, the magnetization along a set of three orthogonal coordinate axes is

$$\begin{aligned} M_1 &= \kappa_{11}H_1 + \kappa_{12}H_2 + \kappa_{13}H_3 \\ M_2 &= \kappa_{21}H_1 + \kappa_{22}H_2 + \kappa_{23}H_3 \qquad (7.1) \\ M_3 &= \kappa_{31}H_1 + \kappa_{32}H_2 + \kappa_{33}H_3 \end{aligned}$$

Figure 7.3 A comparison of theoretically-predicted thermal noise levels with levels of noise and interference observed in the instrument. Power mains noise is wideband, before phase-sensitive detection. Other noise is measured with a bandwidth of 0.03 Hz, or is predicted for that bandwidth.

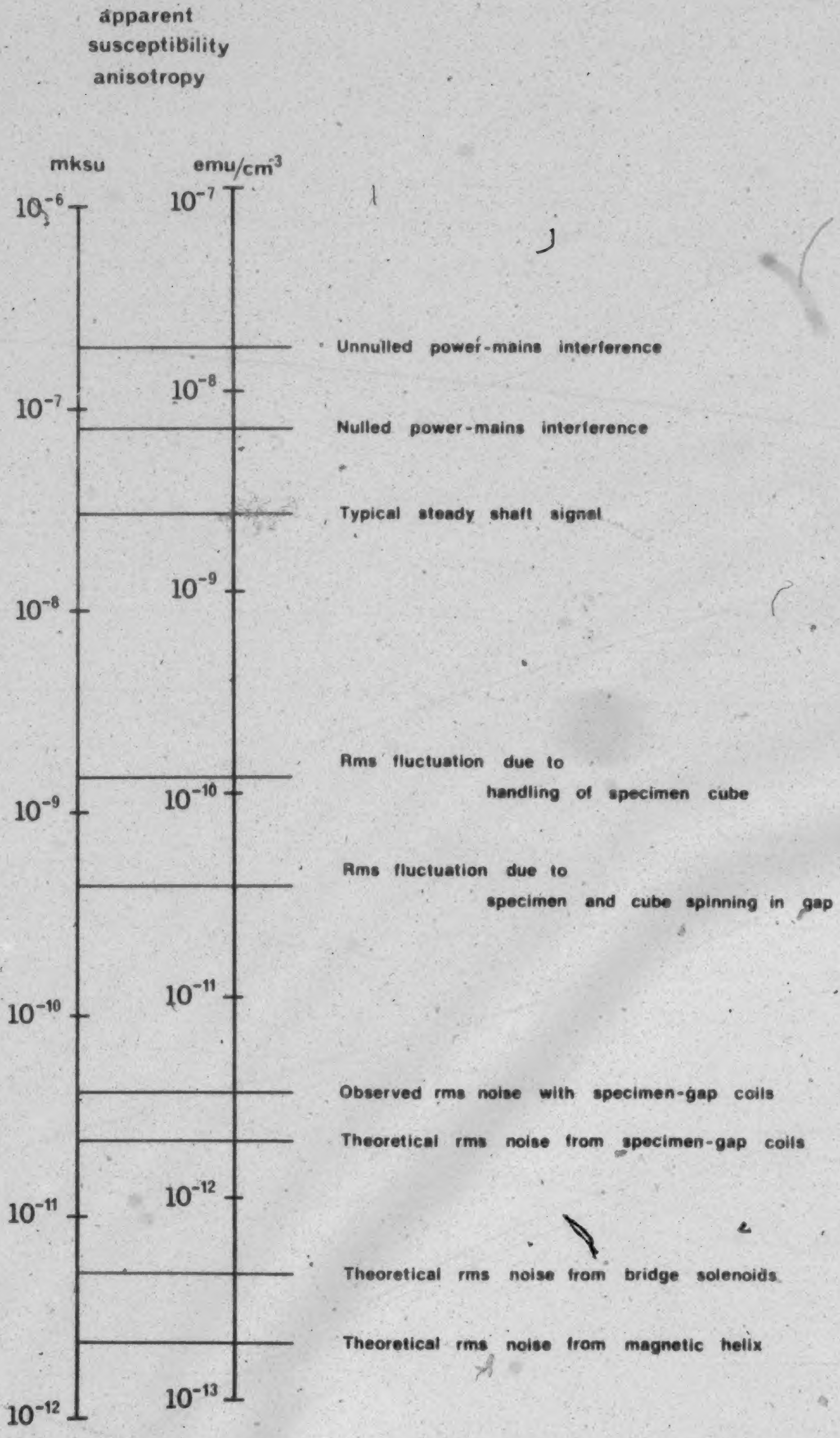
apparent susceptibility anisotropy
mksu
emu/cm^3
10^{-6}
10^{-7}
10^{-8}
10^{-9}
10^{-10}
10^{-11}
10^{-12}
10^{-7}
10^{-8}
10^{-9}
10^{-10}
10^{-11}
10^{-12}
10^{-13}
Unnulled power-mains interference
Nulled power-mains interference
Typical steady shaft signal
Rms fluctuation due to handling of specimen cube
Rms fluctuation due to specimen and cube spinning in gap
Observed rms noise with specimen-gap coils
Theoretical rms noise from specimen-gap coils
Theoretical rms noise from bridge solenoids
Theoretical rms noise from magnetic helix

Figure 7.4 shows the generalized magnetization and applied field vectors, as well as the coordinate axes of standard specimens. Suppose the field is applied in the x_1 direction. Then $\overrightarrow{H} = [H_1, 0, 0]$. Therefore:

$$\left.\begin{aligned} M_1 &= \kappa_{11} H_1 \quad \text{(direct component)} \\ M_2 &= \kappa_{21} H_1 \\ M_3 &= \kappa_{31} H_1 \end{aligned}\right. \quad \begin{matrix} \\ \left.\begin{matrix} \\ \\ \end{matrix}\right\} \text{(transverse components)} \end{matrix} \qquad (7.2)$$

The anisotropic susceptibility is a property of the specimen and is a tensor of second rank:

$$[\kappa_{ij}] = \begin{bmatrix} \kappa_{11} & \kappa_{12} & \kappa_{13} \\ \kappa_{21} & \kappa_{22} & \kappa_{23} \\ \kappa_{31} & \kappa_{32} & \kappa_{33} \end{bmatrix} \qquad (7.3)$$

where i, j = 1, 2, 3 refer to the three axes about which the specimen rotates. The matrix is symmetrical about the diagonal. Hence:

$$\begin{aligned} \kappa_{12} &= \kappa_{21} \\ \kappa_{13} &= \kappa_{31} \\ \kappa_{23} &= \kappa_{32} \end{aligned} \qquad (7.4)$$

When a specimen is rotated in the (i,j) plane, with the i-axis aligned with the shaft reference mark and perpendicular to the applied field at time $t = 0$, the magnetic moment of the specimen is

Figure 7.4 Generalized magnetization and applied field vectors.

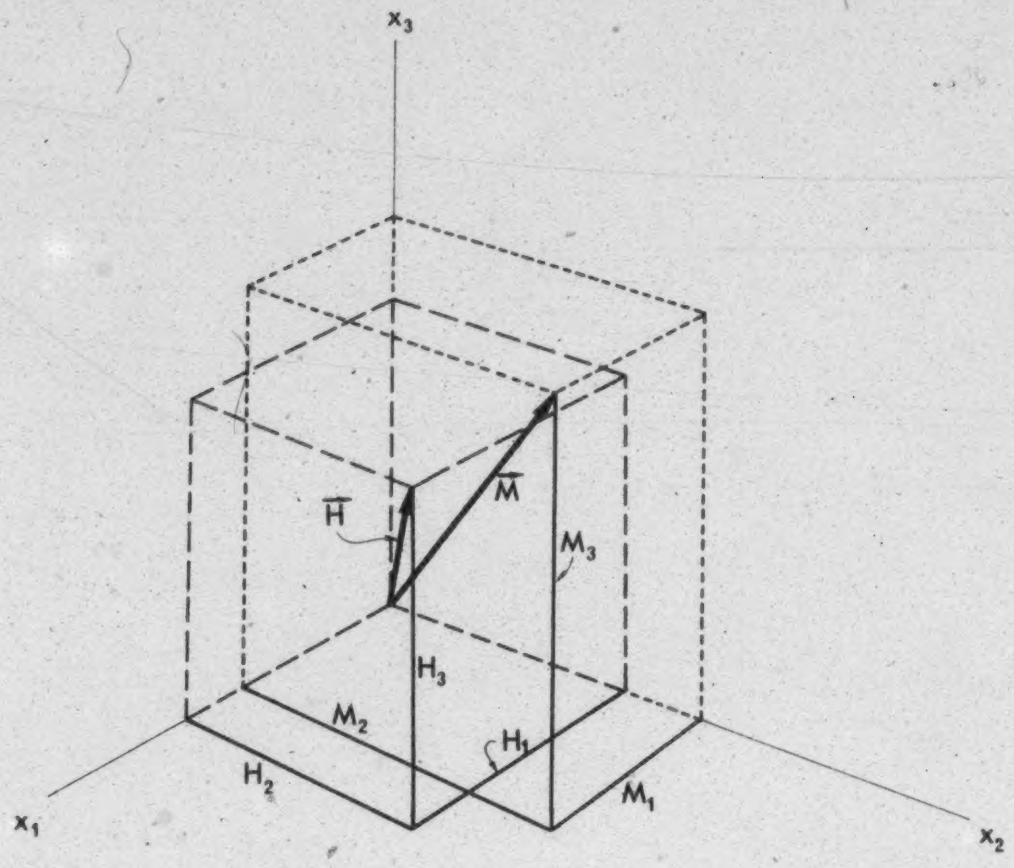
x_3
$\overline{H}$
$\overline{M}$
M_3
H_3
M_2
H_1
H_2
M_1
x_1
x_2

$$m_{\overline{ij}} = -\frac{VH}{2}\left\{(\kappa_{ii} - \kappa_{jj})^2 + 4\kappa_{ij}^2\right\}^{1/2} \cos 2(\omega t + \delta_{\overline{ij}}) \tag{7.5}$$

$$\sin 2\delta_{\overline{ij}} = \frac{2\kappa_{ij}}{\left\{(\kappa_{ii} - \kappa_{jj})^2 + 4\kappa_{ij}^2\right\}^{1/2}} \tag{7.6}$$

$$\cos 2\delta_{\overline{ij}} = \frac{\kappa_{ii} - \kappa_{jj}}{\left\{(\kappa_{ii} - \kappa_{jj})^2 + 4\kappa_{ij}^2\right\}^{1/2}} \tag{7.7}$$

where: V = volume of specimen

H = applied field intensity

$\delta_{\overline{ij}}$ = phase angle of κ_{ii} in the rock with respect to maximum susceptibility

The $\overline{ij}$ subscript is used to distinguish the terms involved from tensor elements.

Let $\omega t = 0$ and $\delta_{\overline{ij}}$ = arbitrary. Then Eq. 7.5 becomes:

$$m_{\overline{ij}} = -\frac{VH}{2}\left\{(\kappa_{ii} - \kappa_{jj})^2 + 4\kappa_{ij}^2\right\}^{1/2} \cos 2\delta_{\overline{ij}} \tag{7.8}$$

One can now substitute Eq. 7.7 to obtain:

$$m_{\overline{ij}} = -\frac{VH}{2}(\kappa_{ii} - \kappa_{jj}) \tag{7.9}$$

This is the in-phase output. Call it I_{ij}.

Similarly, let $\omega t = \pi/4$ and $\delta_{\overline{ij}}$ = arbitrary. Then from Eqs. 7.5 and 7.6 one obtains:

$$m_{\overline{ij}} = -\frac{VH}{2}\left\{(\kappa_{ii} - \kappa_{jj})^2 + 4\kappa_{ij}^2\right\}^{1/2} \sin 2\delta_{\overline{ij}}$$

$$= VH\kappa_{ij} \tag{7.10}$$

This is the quadrature output. Call it Q_{ij}. Thus from Eqs. 7.9 and 7.10:

$$\kappa_{ii} - \kappa_{jj} = -\frac{2I_{\overline{ij}}}{VH} \tag{7.11}$$

$$\kappa_{ij} = \frac{Q_{\overline{ij}}}{VH} \tag{7.12}$$

Spinning the rock specimen about its three orthogonal axes will yield the following set of measured values:

$$\begin{bmatrix} \Delta_1 = \kappa_{11} - \kappa_{22} & \kappa_{12} & \kappa_{13} \\ \kappa_{21} & \Delta_2 = \kappa_{22} - \kappa_{33} & \kappa_{23} \\ \kappa_{31} & \kappa_{32} & \Delta_3 = \kappa_{33} - \kappa_{11} \end{bmatrix} \tag{7.13}$$

One then measures bulk susceptibility $\bar{\kappa}$

$$\bar{\kappa} = \frac{\kappa_{11} + \kappa_{22} + \kappa_{33}}{3} \tag{7.14}$$

Thus one gets:

$$\begin{aligned} \kappa_{11} &= \bar{\kappa} + \tfrac{1}{3}(\Delta_1 - \Delta_3) \\ \kappa_{22} &= \bar{\kappa} + \tfrac{1}{3}(\Delta_2 - \Delta_1) \\ \kappa_{33} &= \bar{\kappa} + \tfrac{1}{3}(\Delta_3 - \Delta_2) \end{aligned} \tag{7.15}$$

This, then, yields the susceptibility matrix of Eq. 7.3.

In order to determine the principal susceptibility magnitudes and directions, we must transform this latter matrix into a diagonal matrix:

$$[K] = \begin{bmatrix} K_a & 0 & 0 \\ 0 & K_b & 0 \\ 0 & 0 & K_c \end{bmatrix} \qquad (7.16)$$

Here K_a, K_b, and K_c are the principal susceptibilities, and the coordinate system of the transformed matrix defines the orientation of the susceptibility ellipsoid.

7.4 Geometrical Representation of a Tensor

A tensor can be usefully represented by a second-degree surface ellipsoid or hyperboloid (Runcorn, 1967). This surface is defined by:

$$K_{ij} x_i x_j = 1 \qquad (7.17)$$

For a symmetrical tensor this becomes

$$K_{11} x_1^2 + K_{22} x_2^2 + K_{33} x_3^2 + 2K_{23} x_2 x_3 + 2K_{31} x_3 x_1 + $$
$$+ 2K_{12} x_1 x_2 = 1 \qquad (7.18)$$

When referred to the principal axes, Eq. 7.18 becomes

$$K_a x_1^2 + K_b x_2^2 + K_c x_3^2 = 1$$

or

$$\frac{x_1^2}{\left\{\frac{1}{\sqrt{K_a}}\right\}^2} + \frac{x_2^2}{\left\{\frac{1}{\sqrt{K_b}}\right\}^2} + \frac{x_3^2}{\left\{\frac{1}{\sqrt{K_c}}\right\}^2} = 1 \qquad (7.19)$$

Thus the semi-axes of the representation surface have lengths $1/\sqrt{\kappa_a}$, $1/\sqrt{\kappa_b}$, and $1/\sqrt{\kappa_c}$. Thus if κ_a, κ_b, and κ_c are positive, the surface is an ellipsoid.

Following the derivation by Runcorn (1967), it is seen that the susceptibility ellipsoid has two useful properties:

1. The length of the radius vector is the inverse square root of the susceptibility in that direction.
2. If the applied field is in the direction of a radius vector extending from the center of the ellipsoid to a point P on its surface, then the normal at P is parallel to the magnetization.

7.5 Calibration

The in-phase and quadrature outputs of the instrument are calibrated with a standard solenoid having n turns, cross-sectional area A, and resistance R. The method is similar to one using wire loops described by Noltimier (1964).

Let the solenoid axis be aligned with the shaft reference mark. The solenoid is spun in the (i,j) plane with its axis normal to the applied field at time $t = 0$. The voltage induced in the solenoid as it spins is then equal to

$$e_L = -n \frac{d\phi}{dt}$$

$$= -nA \frac{d}{dt} (B_0 \sin \omega_r t)$$

$$= -nA \omega_r B_0 \cos \omega_r t \qquad (7.20)$$

where B_0 is the bulk flux density in the specimen gap. The coil is terminated by a fixed resistance, normally that of a precision resistor connected across the coil. This resistance is assumed to be much larger that the reactance of the coil at the signal frequencies used. Then the solenoid current is

$$i_L = \frac{e_L}{R}$$

$$= -\frac{nA\omega_r B_0 \cos \omega_r t}{R} \qquad (7.21)$$

Therefore the induced magnetic moment is

$$m_L = n i_L A$$

$$= -\frac{n^2 A^2 \omega_r B_0}{R} \cos \omega_r t \qquad (7.22)$$

The sensing coils "see" only the component of magnetic moment parallel to the applied field

$$m_L' = m_L \sin \omega_r t$$

$$= - \frac{n^2 A^2 \omega_r B_0}{2R} \sin 2\omega_r t \qquad (7.23)$$

The angular relationships of flux ϕ, voltage e_L, current i_L and moment m_L are shown in Figure 7.5. It can be seen that m_L' is maximum for the quadrature output ($\omega t = \pi/4$). Therefore:

$$I_c = 0 \qquad (7.24)$$
$$Q_c = - \frac{n^2 A^2 \omega_r B_0}{2R}$$

The values of n, A, and R are, of course, known parameters of the standard solenoid. The angular velocity of the shaft, ω_r, is readily measured. The specimen-gap flux density may either be measured independently or it may be calculated from observations taken with the standard solenoid.

One standard solenoid which was made for calibration has 50 turns, a diameter of 2.29 cm, and a series resistance of 3400 ohms. From inductance tables by Grover (1946) it is seen that the coil has an inductance of 42.9 microhenries. Its reactance at 100 Hz is therefore 0.027 ohms and is completely negligible in view of the large series resistance.

In order to calibrate the spinner, one turns the shaft housing in its mounting cradle while the shaft spins, until the in-phase output is zero and the quadrature output

Figure 7.5 The angular relationships of flux ϕ, induced voltage e_ℓ, current i_ℓ and moments m_ℓ and m_ℓ'.

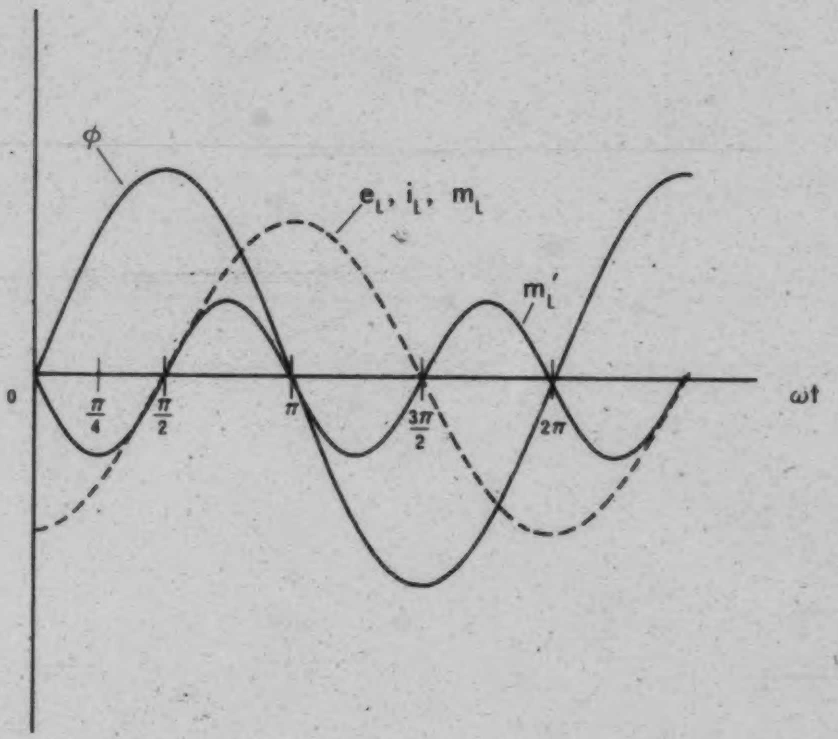
ϕ
e_L, i_L, m_L
m_L'
0
$\frac{\pi}{4}$
$\frac{\pi}{2}$
π
$\frac{3\pi}{2}$
2π
ωt

is negative. The instrument is then calibrated for phase. It is calibrated for amplitude by comparing the observed quadrature output with that given by Eq. 7.24. This establishes the ratio between an output voltage and the magnetic moment which produces it. Then, from Eqs. 7.11 and 7.12 one can establish a ratio between output voltage and susceptibility anisotropy.

In order to calculate bulk field B_0, one places the standard solenoid in alignment with the signal coils (i.e. with its axis parallel to the applied field if the signal coils for parallel magnetization are being used). While keeping the solenoid stationary, a current $i_0 \sin 2\omega_r t$ is passed through it. Then the solenoid has a magnetic moment

$$m_l'' = n i_0 A \sin 2\omega_r t \qquad (7.25)$$

Then combining Eqs. 7.23 and 7.25, it follows that

$$B_0 = \frac{m_l'}{m_l''}\left\{\frac{2 i_0 R}{n A \omega_r}\right\} \qquad (7.26)$$

Since both magnetic moments m_l' and m_l'' have equal frequency, the ratio of the moments is simply the ratio of their respective maximum output signals. Thus

$$B_0 = \frac{\text{signal with rotating solenoid}}{\text{signal with stationary solenoid}}\left\{\frac{2 i_0 R}{n A \omega_r}\right\} \qquad (7.27)$$

The maximum gap induction was thus found to be 0.125 tesla.

7.6 Correction for Orientation of the Specimens in the Outcrop

A computer program which derives principal susceptibility magnitudes and directions from the output and calibration information outlined in Sections 7.3 and 7.5 was written by Dr. D. I. Gough. The directions are given by an azimuth measured clockwise from the downdip direction of the specimen, and a dip measured downward from the specimen's downdip direction. A transformation is included which expresses directions also in terms of the North-West-vertical field coordinate axes.

Figure 7.6 shows a specimen having generalized orientation with respect to the field coordinate axes. The measured susceptibility vector $\vec{K}$ shown in Figure 7.7 has directional cosines ℓ, m, and n relative to axes referred to the specimen axis and marks. Then the horizontal projections of ℓ and m, and the vertical projection of n onto the field horizontal plane and vertical axis are

$$\begin{aligned} \ell' &= \ell \cos d + m \sin d \\ m' &= m \cos d - \ell \sin d \qquad (7.28) \\ n' &= n \end{aligned}$$

If the horizontal projection ℓ' of the down-dip component makes an angle θ with North, measured clockwise from North, then the directional cosines of $\vec{K}$ on North-West-vertical axes are:

Figure 7.6 A rock specimen having generalized orientation with respect to the field coordinate axes.

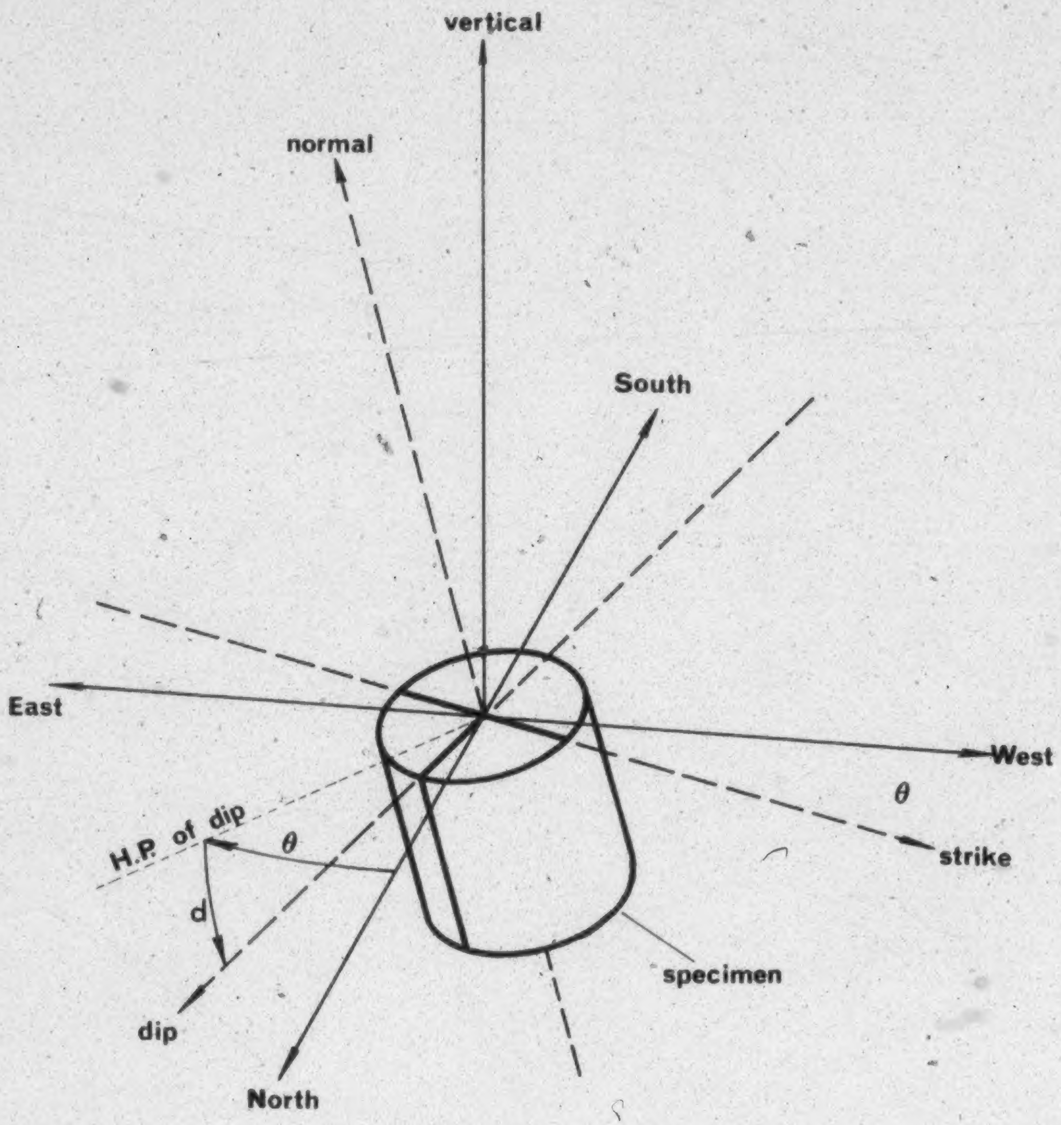
vertical
normal
South
East
West
θ
strike
H.P. of dip
θ
d
dip
specimen
North

(H.P = horizontal projection)

Figure 7.7 The measured susceptibility vector $\vec{\kappa}$ and its components in three reference frames:

1. Strike, dip, normal-to-bedding.
2. Strike, horizontal projection of dip, vertical.
3. North, west, vertical.

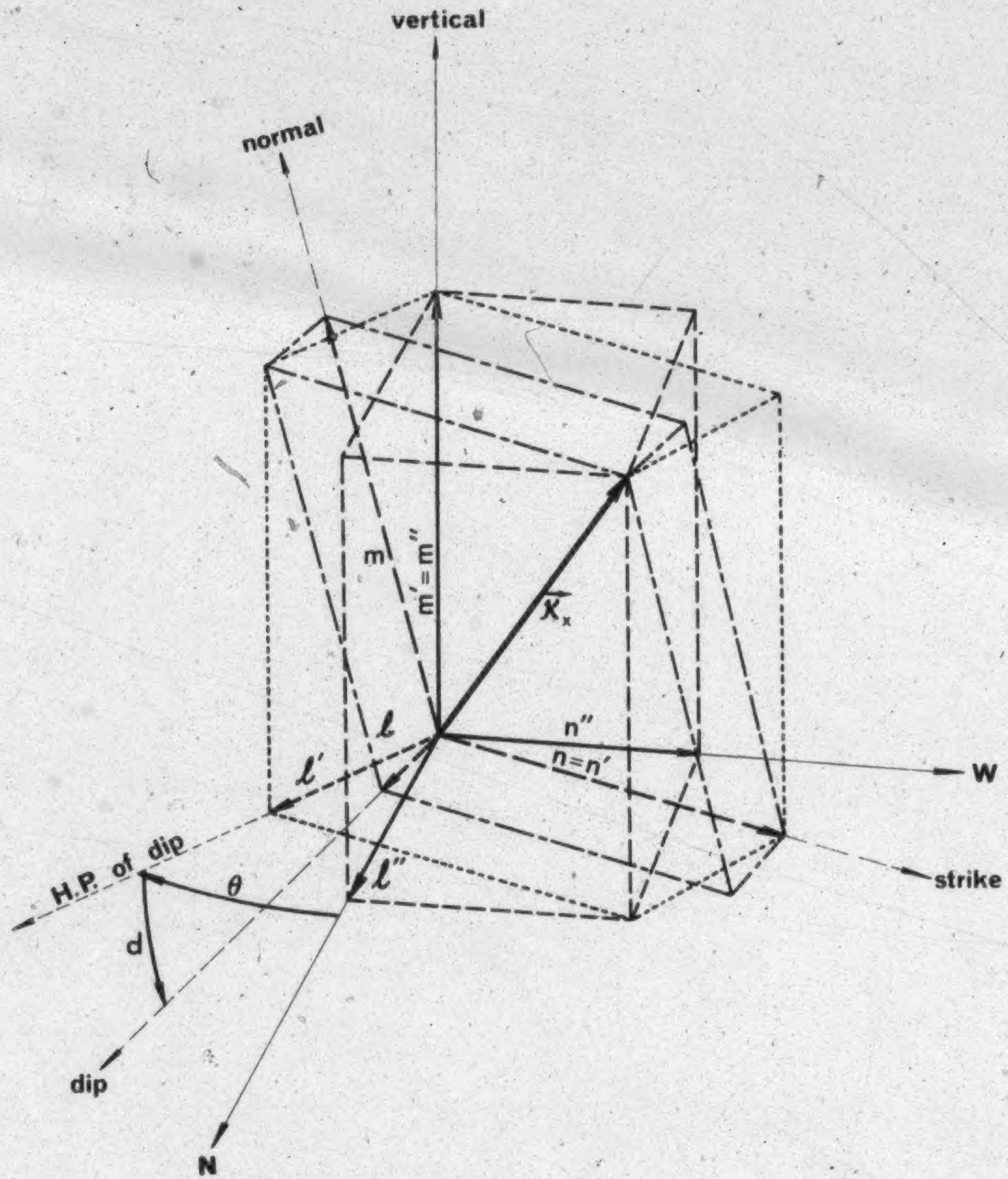
vertical
normal
m
m' = m''
$\bar{X}_x$
ℓ
ℓ'
n''
n = n'
W
strike
H.P. of dip
θ
d
ℓ''
dip
N

(H.P = horizontal projection)

$$\begin{aligned}
\ell'' &= \ell' \cos\theta + n' \sin\theta \\
&= \ell \cos d \cos\theta + m \sin d \cos\theta + n \sin\theta \\
m'' &= m' \\
&= m \cos d - \ell \sin d \qquad (7.29) \\
n'' &= n' \cos\theta - \ell' \sin\theta \\
&= n \cos\theta - \ell \cos d \sin\theta - m \sin d \sin\theta
\end{aligned}$$

Relative to the specimen axes, $\vec{\kappa}$ has an inclination, positive downwards, of

$$\theta_1 = -\sin^{-1} m \qquad (7.30)$$

and an azimuth θ_2 clockwise from ℓ of

$$\theta_2 = \tan^{-1}\left(-\frac{n}{\ell}\right) \qquad (7.31)$$

Relative to north-west-vertical axes, $\vec{\kappa}$ has an inclination

$$\begin{aligned}
\theta_1'' &= -\sin^{-1} m'' \\
&= -\sin^{-1} (m \cos d - \ell \sin d) \qquad (7.32)
\end{aligned}$$

and an azimuth of

$$\begin{aligned}
\theta_2'' &= \tan^{-1}\left(-\frac{n''}{\ell''}\right) \\
&= \tan^{-1}\left\{-\frac{\ell \cos d \cos\theta + m \sin d \cos\theta + n \sin\theta}{n \cos\theta - \ell \cos d \sin\theta - m \sin d \sin\theta}\right\}
\end{aligned}$$

$$(7.33)$$

7.7 Comparison with Torque-meter Measurements

A set of nine specimens which had been measured on torquemeters were kindly provided by Dr. W. H. Owens of the University of Birmingham. The directional information provided by the torquemeters, both low-field and high-field, and the spinner are shown in Figures 7.8 A, B, C and D. The observed lineation, foliation, and other characteristic amplitude parameters are compared in Table A-1 in Appendix 1. In general, very good agreement with the torquemeter readings was obtained.

It will be seen that for the NIB specimens (all alpha-numeric specimen designations are Dr. Owens') the readings from the spinner agree quite well with those from the low-field torquemeter. The high-field torquemeter values, however, agree with neither. For the KA13 specimens, in contrast, there is agreement with the high-field values. These results are not surprising since the field employed in the spinner (0.125 T) is intermediate between the field in the low-field torquemeter (0.01 T) and that in the high-field torquemeter (0.50 T). For the SI and SF specimens both torquemeters and the spinner are substantially in agreement.

Figure 7.8 Directional plots of the maximum, intermediate, and minimum susceptibilities of the specimens supplied by Dr. Owens. Suffixes H, L, and S indicate whether the measurement was made with the high-field torquemeter, low-field torquemeter, or spinner magnetometer, respectively.

(A) SI specimens
(B) SF specimens
(C) NIB specimens
(D) KA13 specimens

■ maximum
▲ intermediate
○ minimum

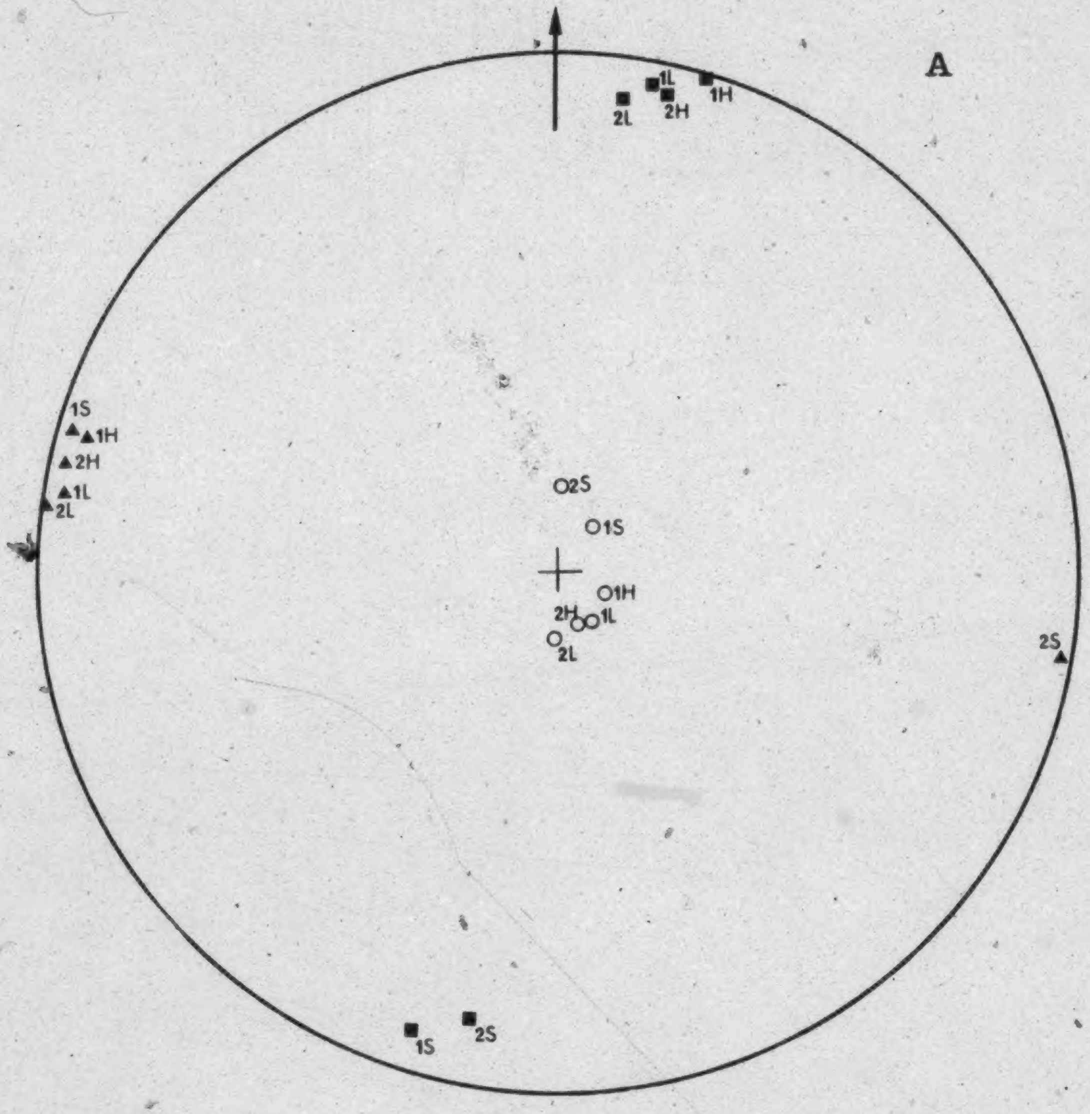
A
1L
2L
2H
1H
1S
1H
2H
1L
2L
2S
1S
1H
2H
1L
2L
2S
1S
2S

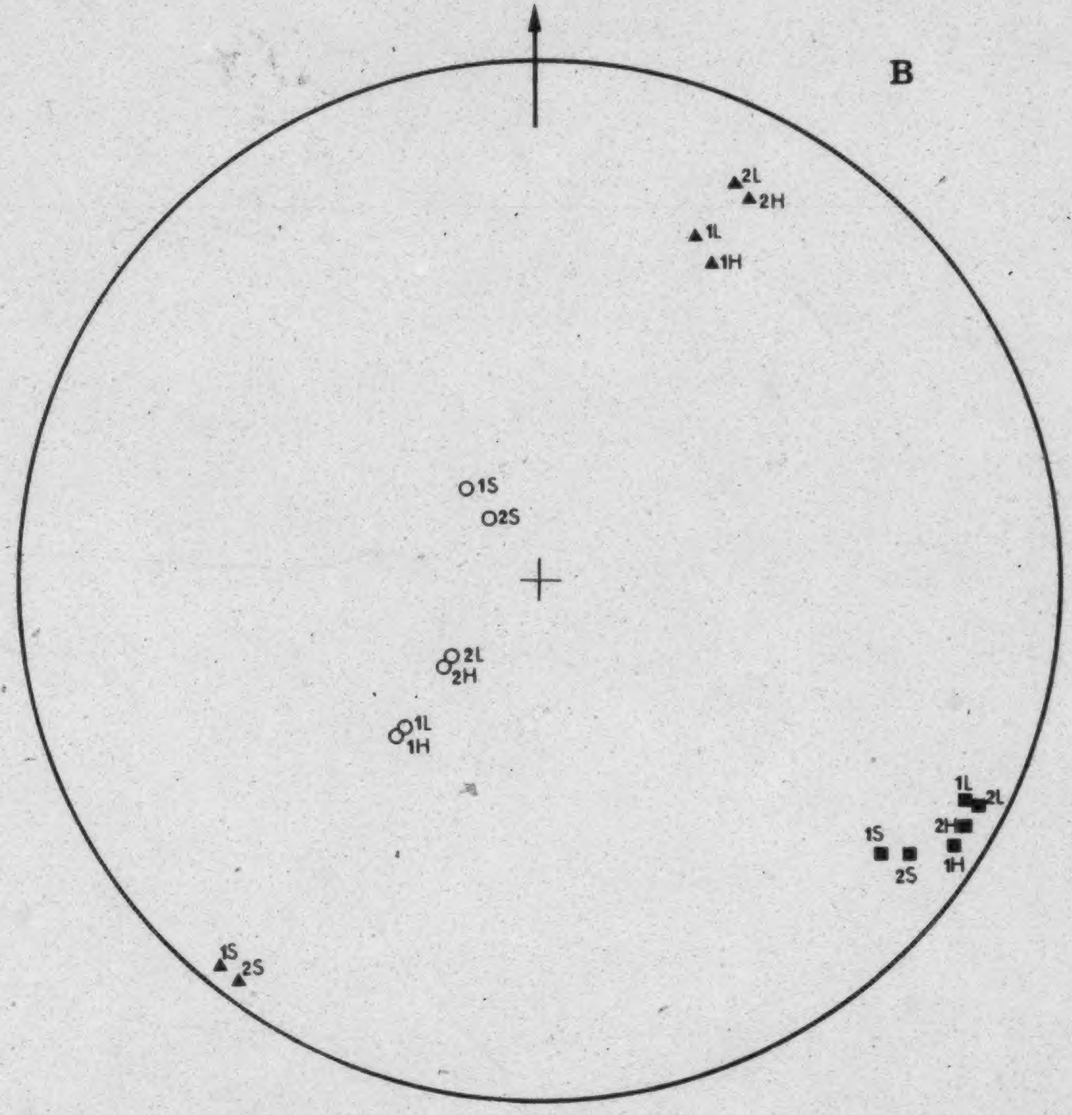
B
2L
2H
1L
1H
1S
2S
2L
2H
1L
1H
1L
2L
2H
1S
2S
1H
1S
2S

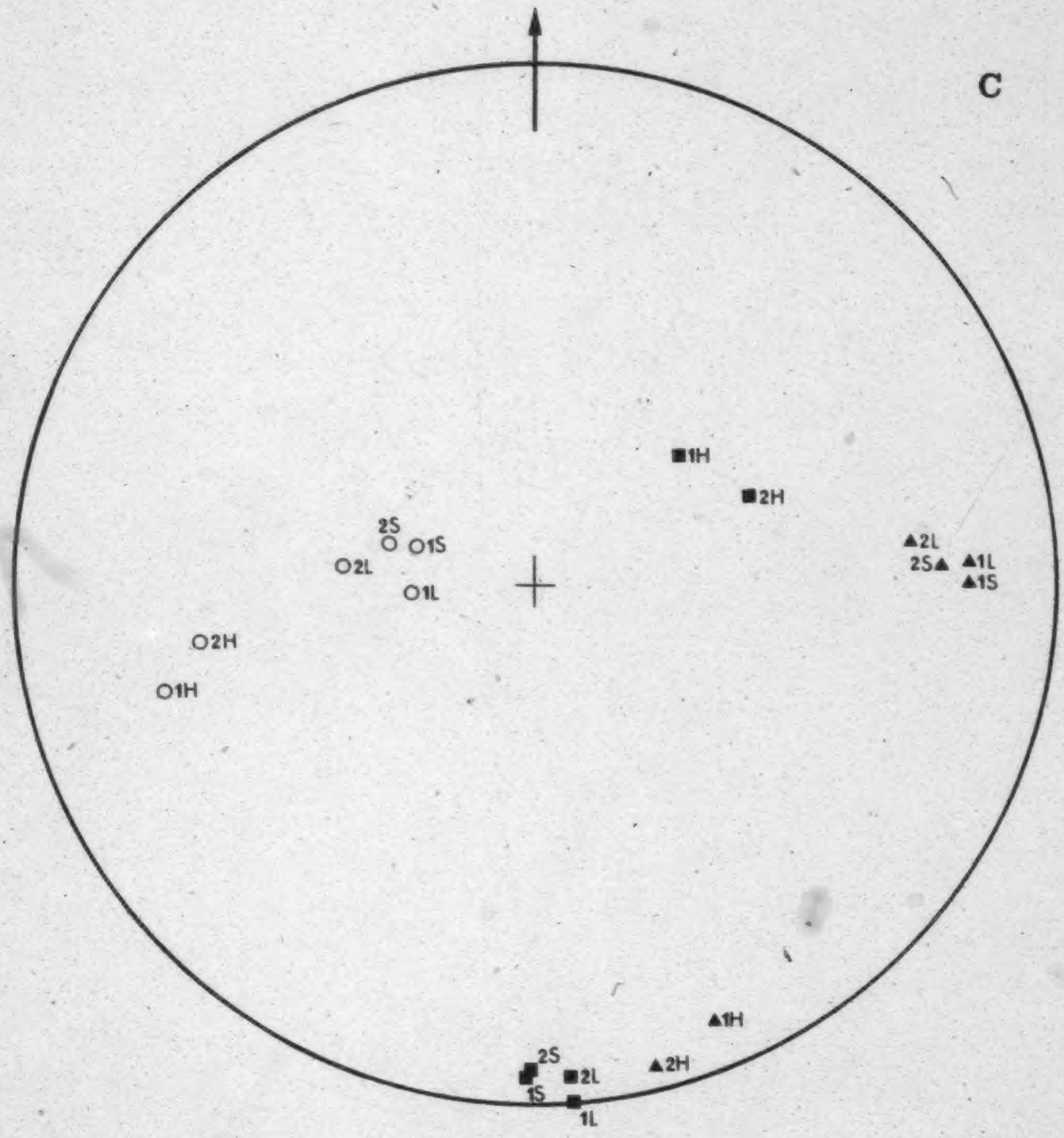
C
1H
2H
2S
1S
2L
1L
2H
1H
2L
2S
1L
1S
1H
2S
2L
1S
2H
1L

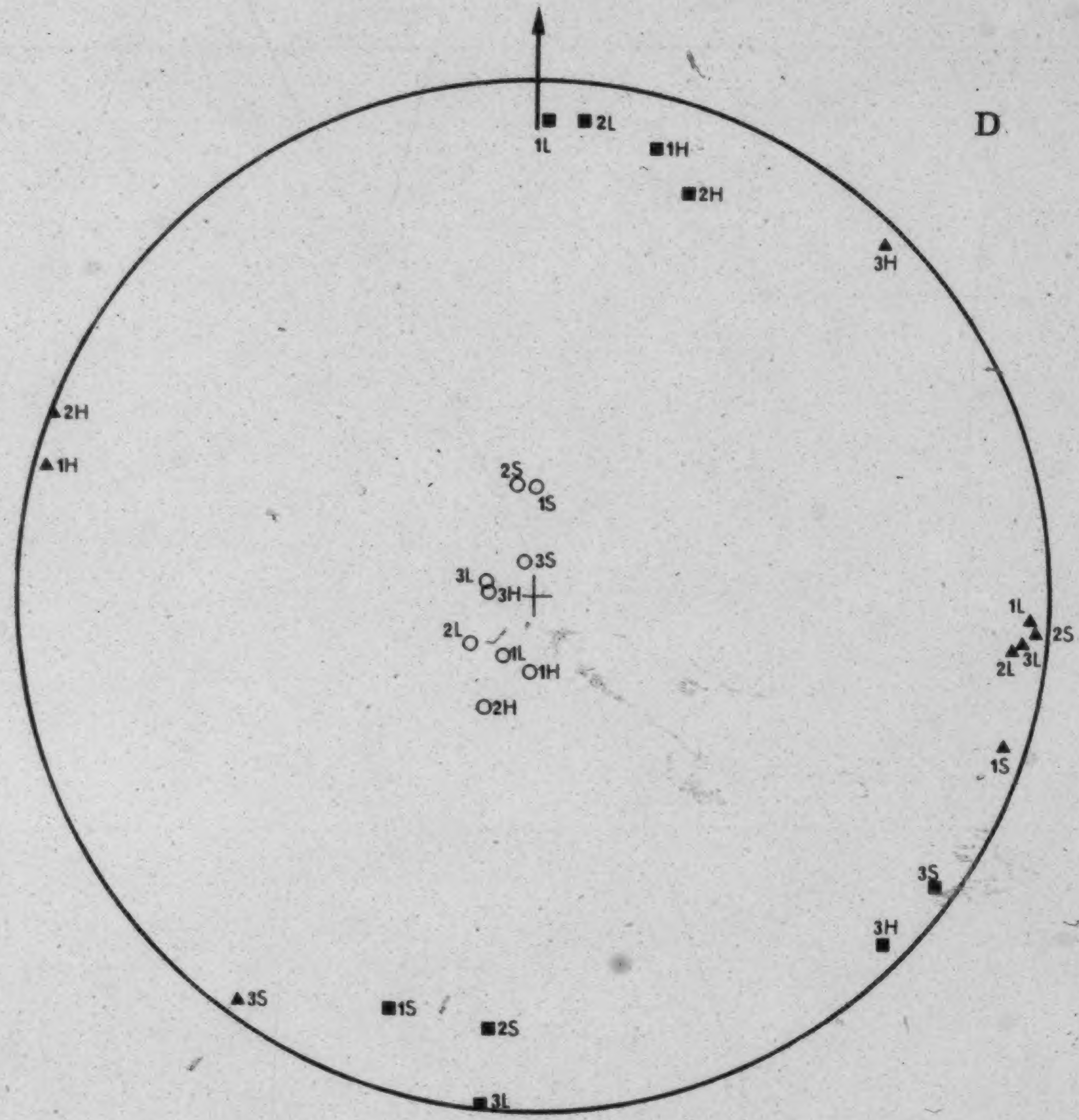
D
1L
2L
1H
2H
3H
2H
1H
2S
1S
3S
3L
3H
2L
1L
1H
2H
1L
2S
3L
2L
1S
3S
3H
3S
1S
2S
3L

7.8 Measurements on Cardium Specimens

A suite of specimens was collected from the Cardium Sandstone formation of the Rocky Mountains foothills. It was initially tried to make measurements on these specimens using Dr. J. W. Graham's A.C. bridge spinner instrument. However, it was found that many of the specimens produced signals not much greater than the noise level of the instrument and proper measurements were therefore impossible.

The directional values, as measured by the new spinner are listed in Appendix 2. The amplitude parameters are given in Appendix 3. The fold which was sampled is shown on the map in Figure 7.9. It was noted that the susceptibility maxima and intermediate values were scattered around the bedding plane, while the minima clustered about the normal to the bedding plane. This is commonly seen with sedimentary rocks. To examine the output for any correlation with the deformation pattern, the specimens were divided into groups according to which limb of the fold they came from (refer to map). It was then seen that there was a very strong clustering of the susceptibility maxima as referred to the specimen axes. This implies that the deformation had a major effect on the susceptibility patterns. The correlation of the maxima with the down-dip direction of the specimen, rather

Figure 7.9 Map showing locations from which the Cardium Sandstone specimens were taken.

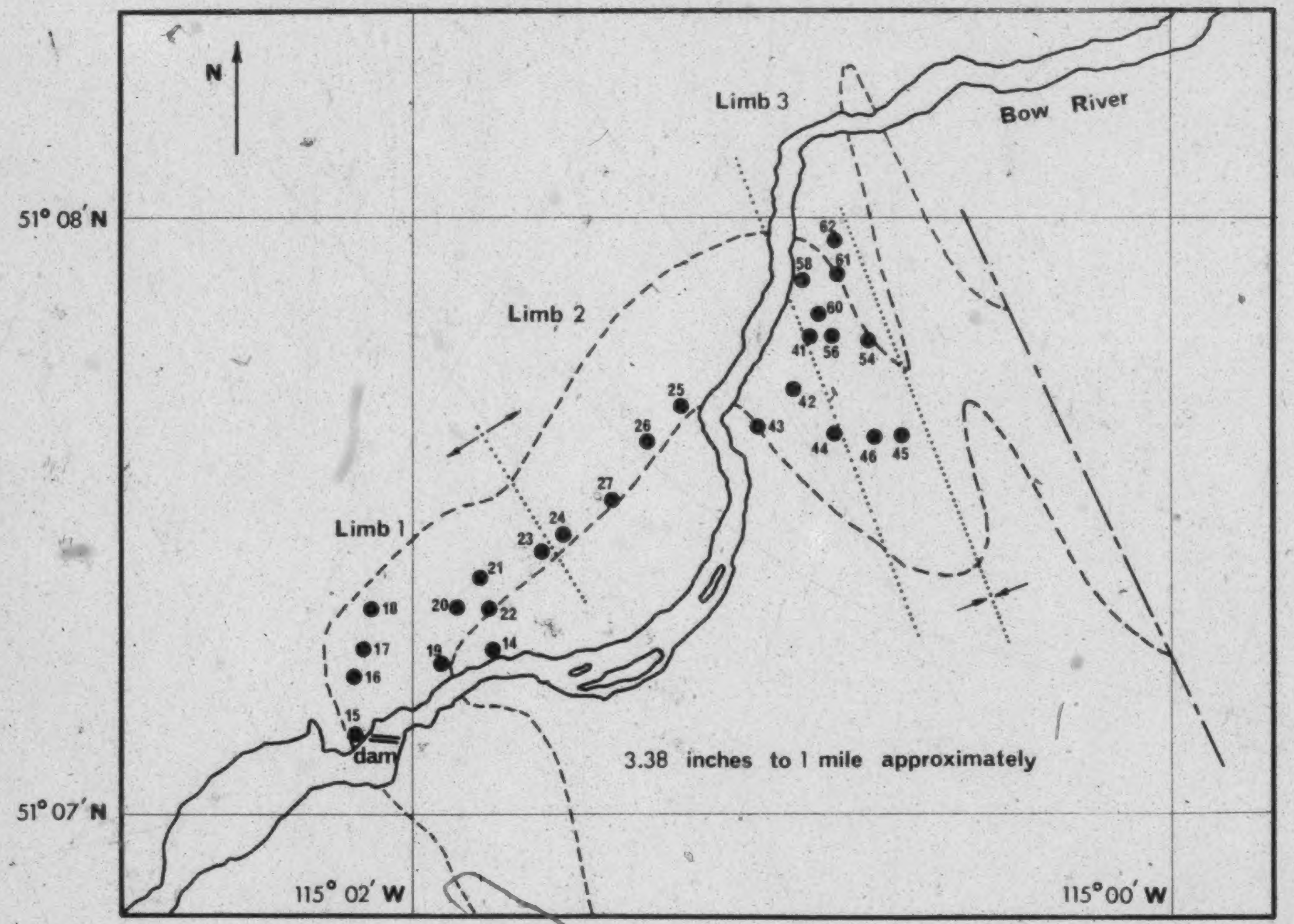
N
Limb 3
Bow River
51° 08′ N
Limb 2
Limb 1
dam
3.38 inches to 1 mile approximately
51° 07′ N
115° 02′ W
115° 00′ W
62
58
61
60
41
56
54
42
25
43
26
44
46
45
27
24
23
21
18
20
22
17
19
14
16
15

than with field orientation implies that gravitational effects during or subsequent to folding contributed to the grain-aligning mechanism. These effects are possibly related to the gravity-sliding mechanism proposed by Graham (1966). Since the orientation of the maxima with respect to the dip is not constant along the fold, it seems that another aligning mechanism is superimposed on the gravitational one. Perhaps the original depositional alignment was involved in this way. The maxima for limbs 1, 2 and 3 of the fold are shown in Figures 7.10, 7.11 and 7.12, respectively.

The orientation of all susceptibility minima and intermediate values for specimens having q less than unity are shown in Figures 7.13 and 7.14. For those specimens having q greater than unity, the minima and intermediate values are not well defined and show considerable scatter. It is worth noting that the six minima not included in the tight cluster about the bedding normal are located in the bedding plane, rather than being randomly distributed. For these specimens, the intermediate values are aligned with the normal to bedding. All maxima observed lie on or near the bedding plane. Possibly two grain alignment mechanisms were involved and one or the other tends to be dominant. Alternatively, the grain alignment mechanism might have permitted the short axes of grains to have two stable orientations, or, more likely, one stable orientation and

Figure 7.10 Directional plot of susceptibility maxima of specimens from Limb 1 of the fold. The maxima cluster about a direction about 45° counter-clockwise from the down-dip direction.

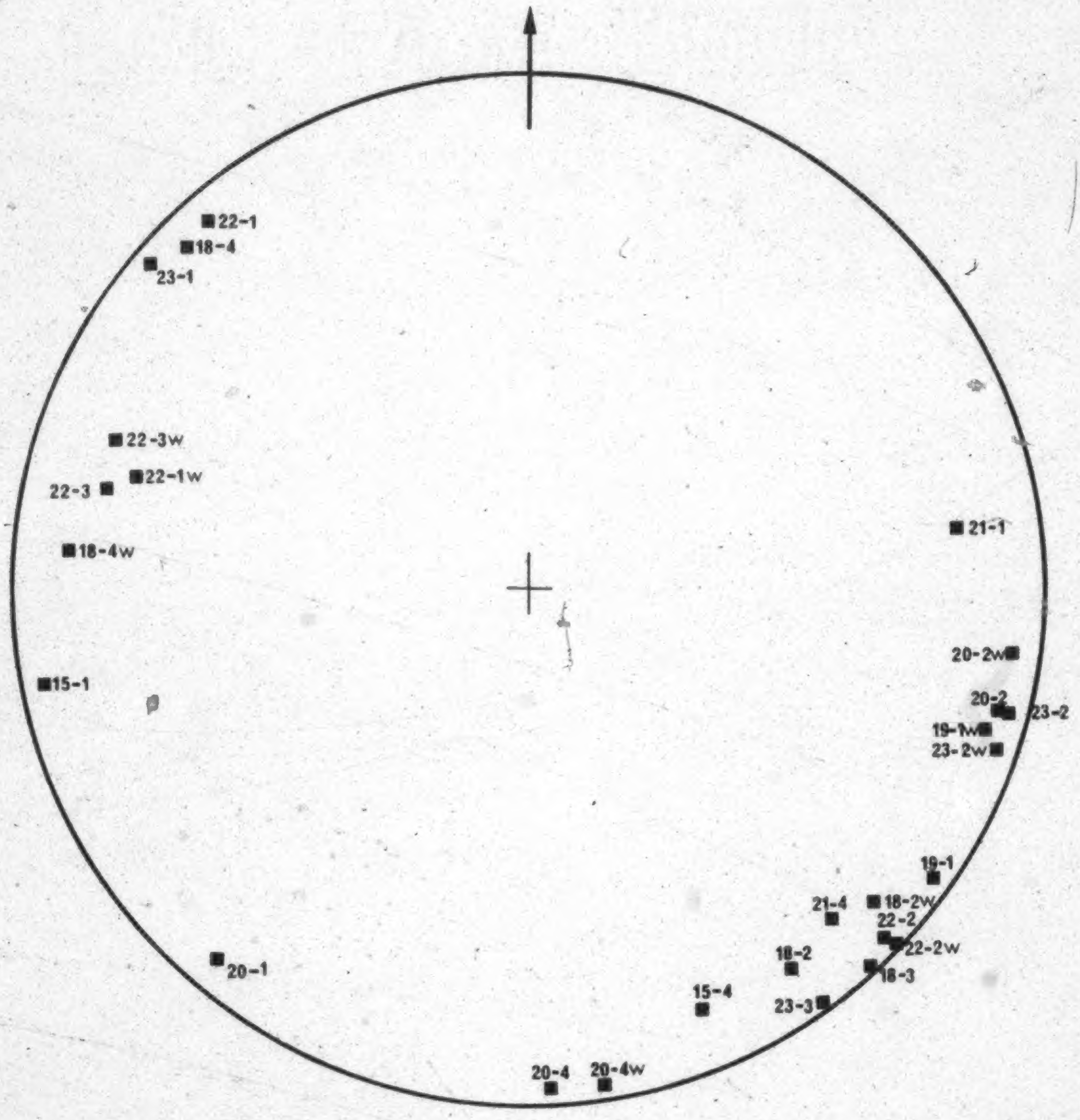
22-1
18-4
23-1
22-3w
22-1w
22-3
18-4w
15-1
20-1
21-1
20-2w
20-2
23-2
19-1w
23-2w
19-1
21-4
18-2w
22-2
22-2w
18-2
18-3
15-4
23-3
20-4
20-4w

Figure 7.11 Directional plot of susceptibility maxima of specimens from Limb 2 of the fold. The maxima cluster about a direction approximately parallel to the down-dip direction.

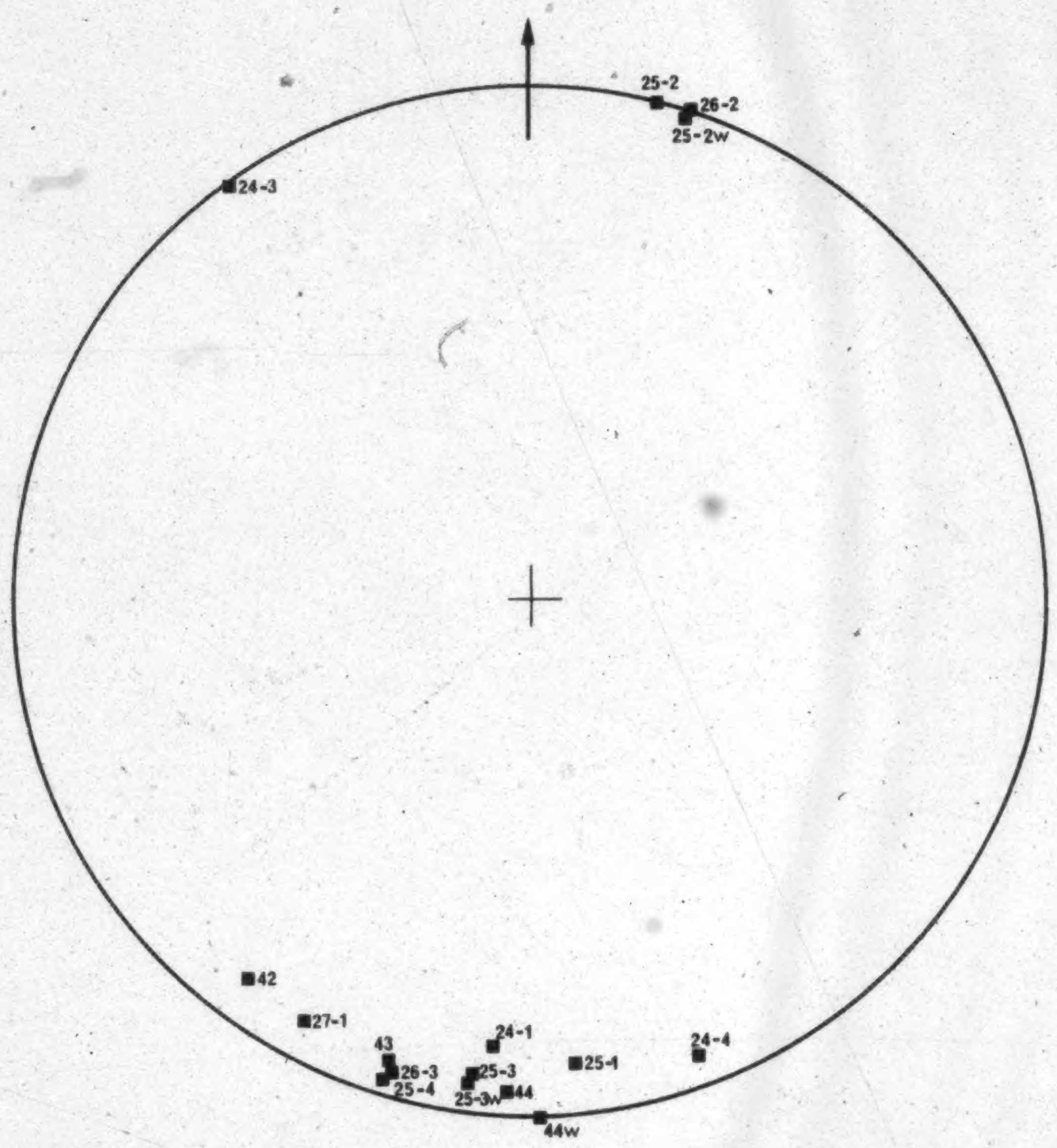
25-2
26-2
25-2w
24-3
42
27-1
43
26-3
25-4
24-1
25-3
25-3w
44
44w
25-1
24-4

Figure 7.12 Directional plot of susceptibility maxima of specimens from Limb 3 of the fold. The maxima cluster about a direction about 45° clockwise from the down-dip direction.

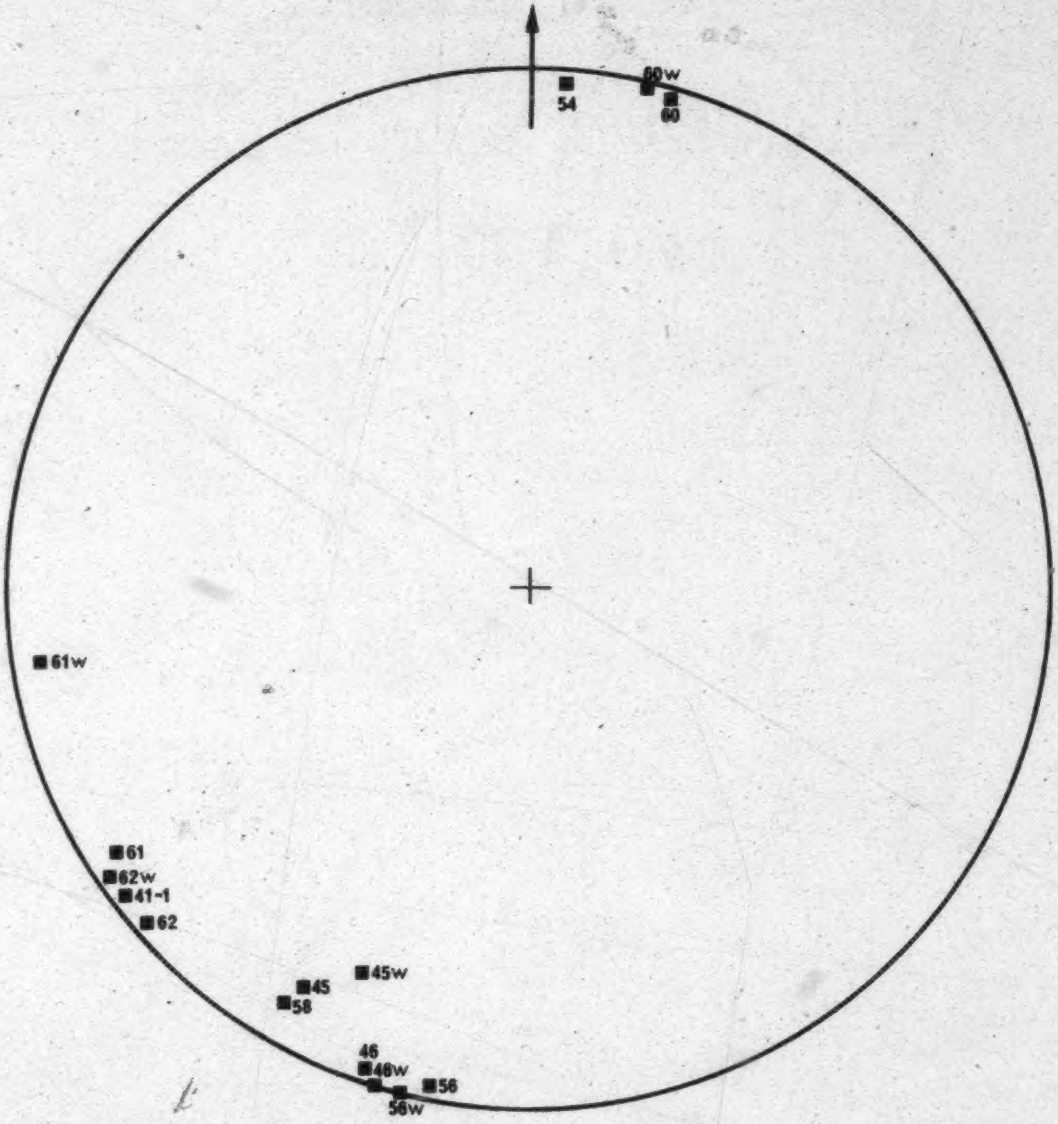
60w
54
60
61w
61
62w
41-1
62
45w
45
58
46
46w
56
56w

Figure 7.13 Directional plot of intermediate values of susceptibility of the Cardium Sandstone specimens. Most intermediate directions are in the bedding plane, with a few clustering about the normal to bedding.

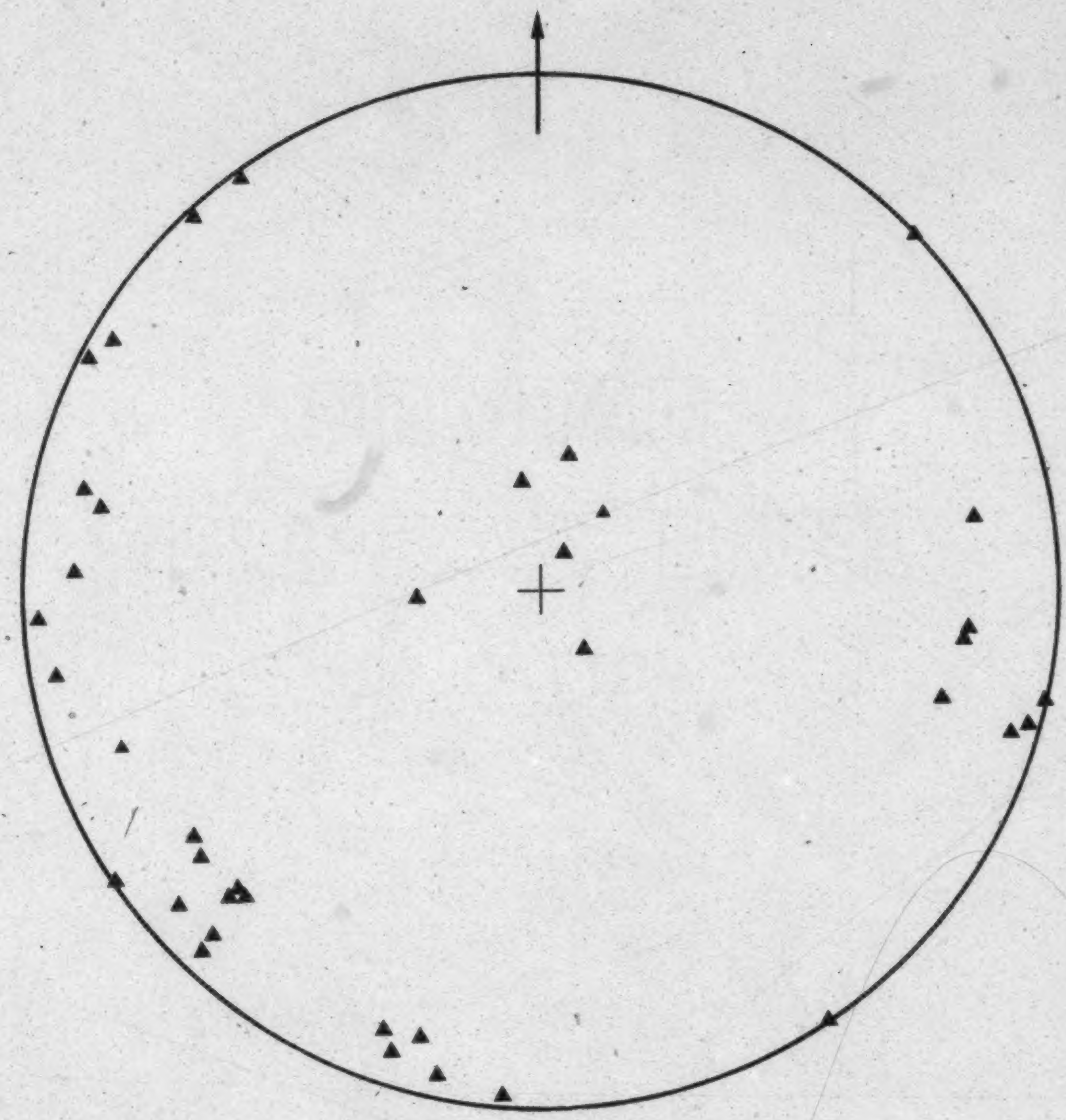

Figure 7.14 Directional plot of susceptibility minima of the Cardium Sandstone specimens. Most of the directions of minimum susceptibility cluster around the normal to bedding. A few minima, however, appear near the plane of bedding.

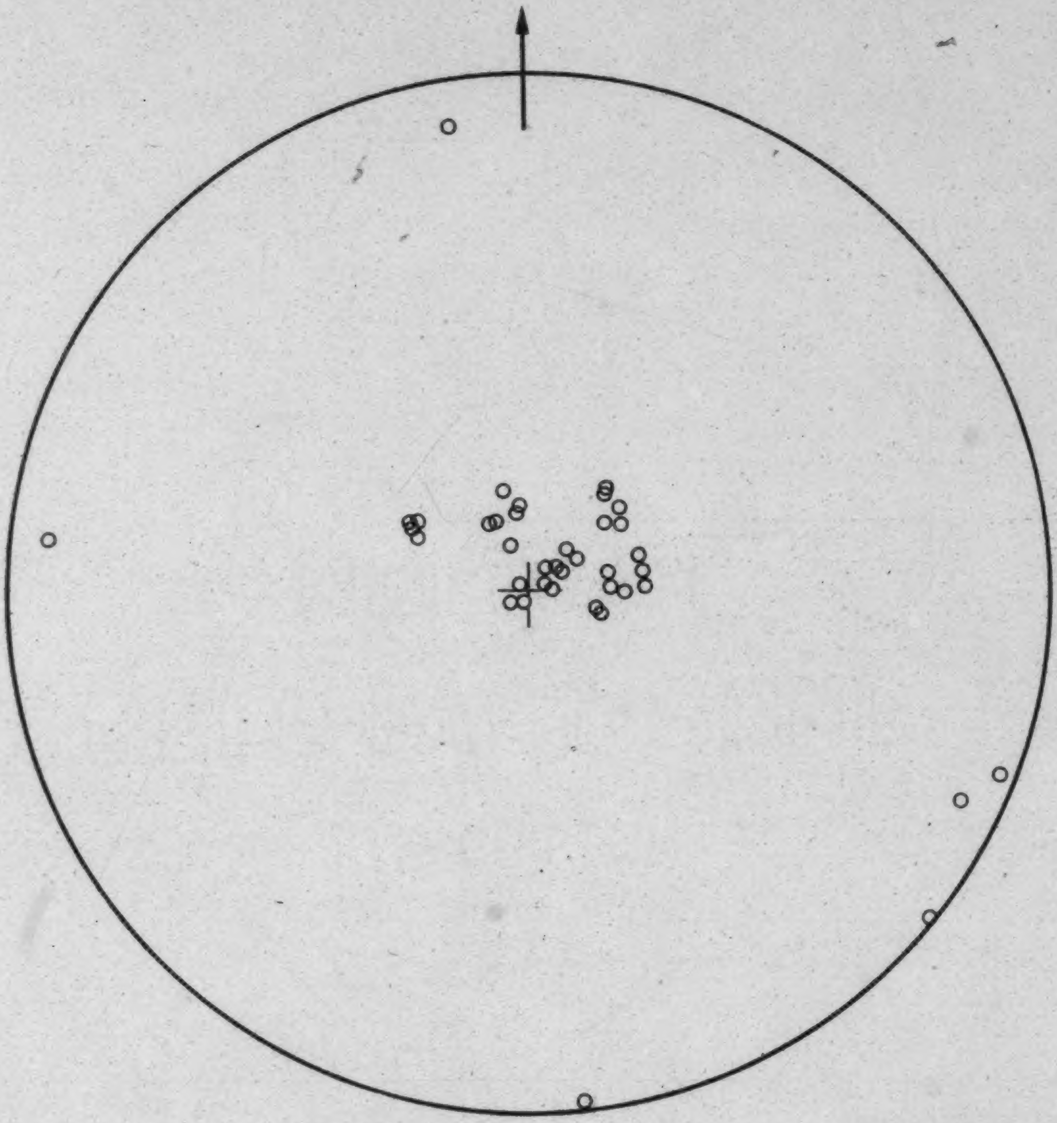

one which was metastable.

All specimen numbers with suffix "W" indicate a second core from a single block sample. Thus two cores having the same numerical designation were in essentially the same bedding plane and were quite close together in the rock formation. They should therefore have essentially the same susceptibility parameters, at least if the magnetic fabric is an extensive one. It can be seen from Figures 7.10 through 7.14 that there is excellent agreement between the orientations of the susceptibility ellipsoids of such core pairs, usually within a few degrees. Appendix 3 shows that the amplitude parameters derived from the susceptibility ellipsoids of these specimen pairs are, in general, closely comparable.

This is not intended to be a definitive study of this rock exposure, but only to be a test of the practical utility of the instrument. The results demonstrate that further work on the Cardium Sandstones should be rewarding.

BIBLIOGRAPHY

Balsley, J. R. and A. F. Buddington (1958): Iron-titanium oxide minerals, rocks and aeromagnetic anomalies of the Adirondack area, New York; Econ. Geology, 53, p. 777-805.

Beranek, L. L. (1954): Acoustics; McGraw-Hill, New York, 481 pp.

Bhattacharya, P. K. (1950): Magnetic anisotropy of sedimentary rocks; thesis, California Institute of Technology.

Bittel, H. (1969): Noise of ferromagnetic materials; IEEE Trans. Magnetics, 5, p. 359-365.

Bozorth, R. (1951): Ferromagnetism; D. Van Nostrand Co., Princeton, N. J., 968 pp.

Brophy, J. J. (1958): Magnetic fluctuations in molybdenum permalloy; J. Appl. Phys., 29, p. 483-484.

Callen, H. B. and T. A. Welton (1951): Irreversibility and generalized noise; Phys. Rev., 83, p. 34-40.

Clark, H. A. and P. B. Vanderlyn (1949): Double-ratio A. C. bridges with inductively-coupled ratio arms; Proc. Instn. Elect. Engrs., 96, Pt II, p. 365-378.

Crimes, T. P. and M. A. Oldershaw (1967): Palaeocurrent determinations by magnetic fabric measurements on the Cambrian rocks of St. Tudwal's Peninsula, North Wales; Geol. J., 5, p. 217-232.

Della Torre, E. and C. V. Longo (1969): The Electromagnetic Field; Allyn and Bacon, Inc., Boston, Mass., 739 pp.

Enoch, R. D. and A. R. Winterborn (1967): The effect of sheet thickness on the magnetic properties of a high permeability Ni-Fe-Cu-Mo alloy; in Magnetic Materials and their Applications, The Institution of Electrical Engineers, London, p. 123-139.

Evans, B. A. (1960): Temperature-controlled permanent magnet for high-resolution nuclear magnetic resonance; J. Sci. Instrum., 37, p. 353-355.

Fuller, M. D. (1967): The A. C. bridge; in Methods in Palaeomagnetism; ed. D. W. Collinson, K. M. Creer, and S. K. Runcorn, Elsevier Publishing Company, Amsterdam, p. 403-408.

Fuller, M. D. (1963): Magnetic anisotropy and paleomagnetism; J. Geophys. Res., 68, p. 293-309.

Fuller, M. D. (1962): A magnetic fabric in till; Geol. Mag., 99, p. 233-237.

Fuller, M. D. (1960): Anisotropy of susceptibility and the natural remanent magnetization of some Welsh slates; Nature, 186, p. 790-792.

Galehouse, J. S. (1968): A test of the method using the anisotropy of magnetic susceptibility as a palaeocurrent indicator; Geol. Soc. Amer. Bull., 79, p. 387-390.

Girdler, R. W. (1961): The measurement and computation of anisotropy of magnetic susceptibility of rocks; Geophys. J., 5, p. 34-44.

Graham, J. W. (1967): Preliminary account of a refined technique for magnetic susceptibility anisotropy measurements of rocks; in Methods in Palaeomagnetism; ed. D. W. Collinson, K. M. Creer, and S. K. Runcorn, Elsevier Publishing Company, Amsterdam, p. 409-424.

Graham, J. W. (1966): Significance of magnetic anisotropy in Appalachian sedimentary rocks; in The Earth Beneath the Continents, ed. J. S. Steinhart and T. J. Smith, American Geophysics Union Monograph, 10, p. 627-648.

Graham, J. W. (1954): Magnetic susceptibility anisotropy, an unexploited petrofabric element; Geol. Soc. Amer. Bull., 65, p. 1257-1258.

Granar, L. (1958): Magnetic measurements on Swedish varved sediments; Arkiv Geofysik, 3, p. 1-40.

Grover, F. W. (1946): Inductance Calculations; D. Van Nostrand Co., Inc., New York, 286 pp.

Hamilton, N. (1967): The effect of magnetic and hydrodynamic control on the susceptibility anisotropy of redeposited silt; Jour. Geology, 75, p. 738-743.

Hamilton, N. (1963): Susceptibility anisotropy measurements on some Silurian siltstones; Nature, 197, p. 170-171.

Hamilton, N. and A. I. Rees (1971): The anisotropy of magnetic susceptibility of the Franciscan rocks of the Diablo Range, central California; Geologische Rundschau, 60, p. 1103-1124.

Hamilton, N., W. H. Owens, and A. I. Rees (1968): Laboratory experiments on the production of grain orientation in shearing sand; Jour. Geology, 76, p. 465-472.

Hanson and Tuzinski (1959): Strain gage evaluation of flexible epoxy resins; NEMA and AIEE, Second National Conference on Application of Electrical Insulation; Washington, D. C.

Hargraves, R. B. (1959): Magnetic anisotropy and remanent magnetism in hemo-ilmenite from ore deposits at Allard Lake, Quebec; J. Geophys. Res., 64, p. 1565-1578.

Higuchi, T. (1970): A statistical model of core noise in half-wave push-pull magnetic amplifiers; IEEE Trans. Magnetics, 6, p. 847-849.

Hrouda, F. and F. Janak (1971): A study of the hematite fabric of some red sediments on the basis of their magnetic susceptibility anisotropy; Sedimentary Geology, 6, p. 187-199.

Irving, E. (1964): Paleomagnetism; John Wiley & Sons, Inc., New York, 399 pp.

Irving, E. and A. Major (1964): Post-depositional detrital remanent magnetization in a synthetic sediment; Sedimentology, 3, p. 135-143.

Ising, G. (1942): On the magnetic properties of varved clay; Arkiv Mat. Astron. Fysik, 29A(5), p. 1-37.

Kawanishi, K., K. Iwasawa, and A Sasaki (1972): Noise reduction in magnetic modulators by using two frequency excitation; IEEE Trans. Magnetics, 8, p. 361.

Khan, M. A. (1962): The anisotropy of magnetic susceptibility of some igneous and metamorphic rocks; J. Geophys. Res., 67, p. 2873-2885.

King, R. F. (1966): The magnetic fabric of some Irish granites; Jour. Geology, 5, p. 43-66.

King, R. F. and A. I. Rees (1962): The measurement of the anisotropy of magnetic susceptibility of rocks by the torque method; J. Geophys. Res., 67, p. 1565-1572.

Kirke, H. L. (1945): Radio frequency bridges; J. Instn. Elect. Engrs., 92, Pt III, p. 2-7.

Kroon, D. J. (1968): Electromagnets; Boston Technical Publishers, Cambridge, Mass., 252 pp.

Latimer, K. E. (1953): Non-linearity in magnetic core materials at low field strengths; in Soft Magnetic Materials for Telecommunications, ed. C. E. Richards and A. C. Lynch, Pergamon Press Ltd., London, p. 38-50.

Macfarlane, G. G. (1950): The spectrum of Barkhausen noise in a magnetic modulator; Appendix 9.2, in The fundamental limitations of the second-harmonic type of magnetic modulator as applied to the amplification of small D. C. signals, F. C. Williams and S. W. Noble, Proc. Instn. Elect. Engrs., London, 97, p. 459.

Marzetta, L. A. (1971): A high performance phase-sensitive detector; IEEE Trans. Instrum. Meas., 4, p. 296-301.

Michelson, P. E. (1952): Electrical Engineering Proseminar Course Work; Carnegie Inst. Wash. Publ., Dept. Terr. Mag.

Mooney, H. M. and R. Bleifuss (1953): Magnetic susceptibility measurements in Minnesota, part II, analysis of field results; Geophysics, 18, p. 383-393.

Morrish, A. H. and S. P. Yu (1955): Dependence of the coercive force on the grain size and the density of some iron oxide powders; J. Appl. Phys., 26, p. 1049-1055.

Morse, P. M. and K. U. Ingard (1968): Theoretical Acoustics; McGraw-Hill, New York, 927 pp.

Noltimier, H. C. (1967): Use of the spinner magnetometer for anisotropy measurements; in Methods in Paleomagnetism, ed. D. W. Collinson, K. M. Creer, and S. K. Runcorn, Elsevier Publishing Company, Amsterdam, p. 399-402.

Noltimier, H. C. (1964): Calibration of a spinner magnetometer with a wire loop; J. Sci. Instrum., 41, p. 55.

Polder, D. (1953): Physical aspects of losses in soft magnetic materials; in Soft Magnetic Materials for Telecommunications, ed. C. E. Richards and A. C. Lynch, Pergamon Press Ltd., London, p. 74-89.

Porath, H. and F. H. Chamalaun (1966): The magnetic anisotropy of hematite bearing rocks; Pure and Applied Geophysics, 64, p. 81-88.

Potter, P. E. and F. J. Pettijohn (1963): Paleocurrents and Basin Analysis; Academic Press Inc., N. Y., 298 pp.

Powell, J. W. (1970): Design of Aerostatic Bearings, Machinery Publishing; Brighton, 280 pp.

Rayleigh, Lord (1919): On the problem of random vibrations and of random flights in one, two, or three dimensions; Phil. Mag., Ser. 6, 37, p. 321-347.

Rees, A. I. (1968): The production of preferred orientation in a concentrated dispersion of elongated and flattened grains; Jour. Geology, 78, p. 457-465.

Rees, A. I. (1966): The effect of depositional slopes on the anisotropy of magnetic susceptibility of laboratory deposited sands; Jour. Geology, 74, p. 856-867.

Rees, A. I. (1965): The use of anisotropy of magnetic susceptibility in the estimation of sedimentary fabric; Sedimentology, 4, p. 257-271.

Rees, A. I. (1961): The effect of the water currents in the magnetic remanence and anisotropy of susceptibility of some sediments; Geophys. J., 5, p. 235-251.

Rees, A. I., U. von Rad, and F. P. Shepard (1968): Magnetic fabric of sediments from the La Jolla Submarine Canyon and Fan, California; Marine Geology, 6, p. 145-178.

Runcorn, S. K. (1967): The anisotropy of magnetization of rocks; in Methods in Paleomagnetism, ed. D. W. Collinson, K. M. Creer, and S. K. Runcorn, Elsevier Publishing Company, Amsterdam, p. 353-360.

Rusnak, G. A. (1957): Sand grains under "unidirectional" fluid flow conditions; Jour. Geology, 65, p. 384-409.

de Sa, A. and L. Molyneux (1963): A spinner magnetometer; J. Sci. Instrum., 40, p. 162-164.

Scouten, D. C. (1972): Sensor noise in low-level flux-gate magnetometer; IEEE Trans. Magnetics, 8, p. 223-231.

Seymour, R. B. (1972): Fillers for polymers; Modern Plastics Encyclopedia, 49, p. 382-388.

Spotts, M. F. (1964): Mechanical Design Analysis; Prentice-Hall, Inc., Englewood Cliffs, N. J., 428 pp.

Stacey, F. D. (1967): The Koenigsberger ratio and the nature of thermoremanence in igneous rocks; Earth Planet. Sc. Letters, 2, p. 67-68.

Stacey, F. D. (1963): Physical theory of rock magnetism; Advances in Physics, 12, p. 45-133.

Stacey, F. D. (1960): Magnetic anisotropy of dispersed powders; Australian J. Phys., 13, p. 196-201.

Stacey, F. D. (1960 - a): Magnetic anisotropy of igneous rocks; J. Geophys. Res., 65, p. 2429-2442.

Stacey, F. D., G. Joplin, and J. Lindsay (1960): Magnetic anisotropy and fabric of some foliated rocks from S. E. Australia; Geofisica Pura e Applicata, 47, p. 30-40.

Stone, D. B. (1963): Anisotropic magnetic susceptibility measurements on a phonolite and on a folded metamorphic rock; The Geophysical Journal of the R. A. S., 7, p. 375-390.

Stoner, E. C. (1945): The demagnetizing factors for ellipsoids, Phil. Mag., Ser. 7, 36, p. 803-821.

Strangway, D. W. (1967): Mineral magnetism; in Mining Geophysics, Volume II, Theory; The Society of Exploration Geophysicists, Tulsa, p. 437-445.

Stucki, F. F., W. D. Fuller, and R. D. Carpenter (1967): Internal stress measurement of encapsulated electronic modules; Electronic Packaging and Producing, 7, p. 39-46.

Tenzer, R. K. (1956): Effects of temperature variations on the remanence of permanent magnets; in Conference on Magnetism and Magnetic Materials, American Institute of Electrical Engineers, p. 203-211.

Uyeda, S., M. D. Fuller, J. C. Belshe, and R. W. Girdler (1963): Anisotropy of magnetic susceptibility of rocks and minerals; J. Geophys. Res., 68, p. 273-291.

Walton, C. A. and C. C. Liu (1971): A low-noise amplifier with parallel integrated-circuit transistors; IEEE J. Solid State Circuits, 6, p. 415-417.

Watton, W. L. and M. E. Pemberton (1949): A direct-capacitance aircraft altimeter; Proc. Instn. Elect. Engrs., 96, Pt II, p. 379-389.

Weiner, M. M. (1969): Magnetostrictive offset and noise in flux gate magnetometers; IEEE Trans Magnetics, 5, p. 98-105.

Williams, F. C. and S. W. Noble (1950): The fundamental limitations of the second-harmonic type of magnetic modulator as applied to the amplification of small D. C. signals; Proc. Instn. Elect. Engrs, London, 97, p. 445-459.

APPENDIX 1 OWENS SPECIMENS

(Susceptibilities in mksu)

Specimen Number	$\bar{K}$			h (%)			P			q		
	LFTM	HFTM	S	LFTM	HFTM	S	LFTM	HFTM	S	LFTM	HFTM	S
SI 57C	.62	.62	.65	8.67	8.13	7.55	.32	.37	.38	.28	-	.32
SI 57D	.72	.72	.69	9.19	8.90	8.27	.39	.43	.40	.32	-	.33
SF 22.3	1.37	1.37	.86	4.64	5.08	6.36	.43	.49	1.29	.35	-	.78
SF 22.4	1.07	1.07	.72	5.56	-	6.96	.51	-	.74	.41	-	.54
NIB 3.1	1.49	1.49	.97	.84	.47	.84	.38	.41	.46	.32	.34	.38
NIB 3.2	1.41	1.41	.99	.82	.81	.89	.81	.32	.53	.58	.28	.42
KA13 3.1	4.25	4.25	2.01	1.40	.92	1.76	.86	.29	.24	.60	.25	.22
KA13 3.2	4.13	4.13	2.01	1.28	.75	1.58	.83	.20	.10	.58	.18	.09
KA13 3.3	3.75	3.75	1.87	1.98	1.72	2.72	.37	.05	.03	.31	.05	.03

Specimen Number	l			l_{rel} (%)			f			f_{rel} (%)		
	LFTM	HFTM	S	LFTM	HFTM	S	LFTM	HFTM	S	LFTM	HFTM	S
SI 57C	1.32	-	1.37	2.13	-	2.09	5.09	-	4.31	7.73	-	6.59
SI 57D	1.87	-	1.65	2.60	-	2.39	6.10	-	4.96	8.02	-	7.18
SF 22.3	1.92	-	3.07	1.40	-	3.57	5.53	-	3.91	3.97	-	4.56
SF 22.4	2.01	-	2.14	1.88	-	2.97	5.13	-	3.96	4.65	-	5.50
NIB 3.1	.34	.21	.26	.23	.14	.26	1.08	.61	.68	.72	.40	.70
NIB 3.2	.52	.28	.30	.37	.20	.31	.91	1.01	.73	.64	.71	.73
KA13 3.1	2.76	.85	.70	.65	.20	.35	4.62	3.47	3.20	1.08	.81	1.60
KA13 3.2	2.39	.50	.28	.58	.12	.14	4.11	2.86	3.04	.99	.69	1.51
KA13 3.3	1.99	.30	.15	.53	.08	.08	6.51	6.43	5.05	1.72	1.70	2.70

APPENDIX 2: CARDIUM SPECIMENS

(Angles in degrees)

Spec. No.	Specimen Axes						North-West-Vertical Axes						Orientation	
	Azimuth			Dip			Azimuth			Dip			Azim	Dip
	Max	Int	Min	Max	Int	Min	Max	Int	Min	Max	Int	Min		
15-1	-100	- 36	- 9	5	-79	10	-177	- 92	- 86	2	-65	25	284	15
15-4	- 23	-109	-148	-13	18	-68	- 87	-176	-178	0	13	-77	296	14
18-2W	- 47	44	157	-11	- 5	-78	-142	- 51	- 64	2	8	-81	264	18
18-2	- 34	-123	152	-12	1	-78	-129	142	- 59	3	- 9	-81	264	18
18-3	- 42	-132	128	- 2	0	-88	-114	156	- 63	6	- 8	-80	288	11
18-4W	- 84	5	- 92	12	- 2	-77	-171	- 80	-145	13	6	-75	275	8
18-4	- 44	-135	-101	7	10	-77	-130	139	-151	12	5	-77	275	8
19-1W	- 72	27	11	- 8	-48	41	-140	- 44	- 57	- 6	-43	47	291	6
19-1	- 54	51	35	- 4	-76	13	-123	- 32	- 33	0	-72	18	291	6
20-1	- 40	-145	- 50	- 7	-83	- 1	- 56	-126	-147	3	-82	8	264	13
20-2W	- 82	10	176	- 5	-22	-67	170	-100	61	- 3	- 8	-81	251	14
20-2	- 75	37	13	- 6	-73	15	177	- 88	- 95	- 3	-61	29	251	14
20-4W	- 9	- 99	-134	- 3	5	-84	- 67	-158	- 90	7	3	-82	302	11
20-4	- 3	- 92	-143	- 4	3	-85	- 61	-151	- 83	7	3	-82	302	11
21-1	- 97	88	- 6	-18	-71	- 2	165	- 52	-110	-20	-66	13	257	15
21-4	- 42	-130	169	-14	8	-74	-135	135	- 54	1	- 4	-85	265	19
22-1W	- 73	- 99	13	22	-66	- 9	-137	-110	- 41	26	-61	11	306	21
22-1	- 40	-133	-107	7	17	-72	- 98	171	-104	23	2	-67	306	21
22-2W	- 45	45	-140	- 1	-19	-71	-126	- 37	-144	12	- 4	-77	281	20
22-2	- 45	46	-142	- 2	-19	-70	-125	- 36	-150	12	- 5	-77	281	20
22-3W	- 69	19	- 98	16	- 8	-72	-149	- 56	-128	21	8	-67	285	17
22-3	- 75	13	- 92	17	- 5	-72	-156	- 61	-124	21	12	-66	285	17
23-1	- 49	38	-136	3	-45	-45	-147	- 64	136	10	-36	-52	263	11
23-2W	- 70	21	175	- 5	-11	-78	-174	- 84	- 92	1	5	-85	256	17
23-2	- 75	16	176	- 4	-12	-77	-178	- 88	- 91	0	4	-86	256	17
23-3	- 35	-124	-131	- 2	19	-71	-108	160	-139	13	8	-74	288	19
24-1	5	-143	- 83	-14	-74	8	- 53	- 99	-145	10	-75	10	302	24

Spec. No.	Specimen Axes						North-West-Vertical Axes						Orientation	
	Azimuth			Dip			Azimuth			Dip			Azim	Dip
	Max	Int	Min	Max	Int	Min	Max	Int	Min	Max	Int	Min		
24-3	-36	-127	-124	1	18	-72	-104	165	-141	12	9	-75	294	14
24-4	-20	-109	-130	-6	15	-74	-76	-167	-118	10	9	-76	305	17
25-1	-5	-98	117	-11	-16	-71	-37	-126	37	5	-18	-71	328	16
25-2W	19	-72	-67	2	29	-61	7	-92	-64	13	32	-54	347	12
25-2	16	-74	-70	1	21	-69	4	-92	-60	13	23	-63	347	12
25-3W	9	-83	119	-7	-19	-70	-14	-102	57	6	-16	-72	337	13
25-3	9	-84	124	-8	-18	-70	-14	-103	61	4	-16	-74	337	13
25-4	17	-73	119	-2	-8	-82	2	-87	34	8	-5	-81	345	10
26-2	19	-71	104	0	-5	-85	14	-76	20	12	-1	-78	355	12
26-3	18	-74	121	-5	-20	-69	7	-82	82	5	-17	-72	349	10
27-1	28	-62	-136	-9	2	-81	33	-59	-23	8	11	-76	5	19
41-1	-128	-38	159	2	-8	-82	-111	-22	31	-9	7	-78	16	19
42	37	-53	178	-8	-6	-80	63	-27	29	6	4	-83	26	17
43	19	-72	161	-7	-5	-82	22	-68	112	0	-3	-87	3	7
44W	-2	89	-92	0	-57	-33	-42	37	-126	8	-56	-33	320	8
44	3	96	-91	-4	-46	-44	-37	48	-123	4	-46	-43	320	8
45W	23	-167	-68	-21	-69	-3	25	-148	-65	-10	-80	1	3	12
45	29	173	-63	-13	-73	-9	32	160	-59	-3	-85	-4	3	12
46W	17	-72	-73	0	26	-64	13	-81	-61	8	28	-60	356	9
46	18	-71	-78	-3	26	-64	14	-79	-66	6	29	-61	356	9
54	4	-86	-73	3	11	-78	-47	-139	-93	12	12	-73	309	9
56W	14	-76	-76	0	11	-79	-35	-129	-86	12	14	-71	310	13
56	11	-78	-89	-3	15	-75	-38	-132	-100	10	17	-70	310	13
58	30	-59	-121	-8	4	-81	38	-55	-20	9	14	-73	7	20
60W	13	-77	25	2	0	-88	-14	-105	-24	14	2	-75	333	13
60	16	-73	60	2	-2	-87	-10	-100	-15	15	1	-75	333	13
61W	-99	-81	-8	6	-84	2	-179	-95	-88	2	-67	23	281	21
61	-123	-33	-121	6	0	-84	158	-114	-96	-5	18	-71	281	21
62W	-125	-35	-110	3	1	-87	141	-132	-104	-8	16	-72	265	19
62	-132	-42	-97	3	2	-86	134	-139	-106	-10	16	-71	265	19

APPENDIX 3: CARDIUM SPECIMENS

(Susceptibilities in mksu)

Specimen Number	$\bar{K}$ (x 10^{-4})	l (x 10^{-6})	l_{rel} (%)	f (x 10^{-6})	f_{rel} (%)	h (%)	P	q
15-1	.316	.221	.70	.706	2.24	2.58	.37	.31
15-4	.227	.497	2.19	.495	2.18	3.29	2.02	1.00
18-2W	.147	.236	1.61	.483	3.29	4.08	.65	.49
18-2	.169	.243	1.44	.520	3.07	3.78	.61	.47
18-3	.182	.103	.56	.454	2.50	2.76	.25	.23
18-4W	.210	.060	.29	.485	2.31	2.44	.13	.12
18-4	.201	.058	.29	.492	2.45	2.57	.13	.12
19-1W	.398	.277	.70	.203	.51	.86	4.31	1.37
19-1	.373	.756	2.03	.559	1.50	2.52	4.17	1.35
20-1	.504	.300	.59	.790	1.57	1.86	.47	.38
20-2W	.351	.563	1.60	.428	1.22	2.03	3.84	1.31
20-2	.350	.638	1.82	.364	1.04	1.96	14.03	1.75
20-4W	.378	.312	.83	.404	1.07	1.48	1.26	.77
20-4	.365	.281	.77	.318	.87	1.26	1.58	.88
21-1	.382	.383	1.00	.966	2.53	3.02	.49	.40
21-4	.184	.092	.50	.437	2.37	2.61	.23	.21
22-1W	.378	.310	.82	.195	.51	.93	7.83	1.59
22-1	.346	.278	.80	.679	1.96	2.36	.52	.41
22-2W	.299	.226	.75	.657	2.20	2.56	.42	.34
22-2	.285	.229	.80	.646	2.27	2.66	.43	.35
22-3W	.201	.085	.43	.485	2.41	2.61	.19	.18
22-3	.210	.104	.50	.476	2.27	2.50	.25	.22
23-1	.207	.261	1.26	.231	1.11	1.75	2.61	1.13
23-2W	.212	.152	.72	.536	2.53	2.87	.33	.28
23-2	.212	.140	.66	.548	2.59	2.90	.29	.26
23-3	.232	.153	.66	.631	2.72	3.03	.28	.24
24-1	.252	.331	1.31	.622	2.47	3.12	.72	.53

Specimen Number	$\bar{\kappa}$ (x 10^{-4})	l (x 10^{-6})	l_{rel} (%)	f (x 10^{-6})	f_{rel} (%)	h (%)	P	q
24-3	.271	.185	.68	.632	2.33	2.66	.34	.29
24-4	.318	.341	1.07	.795	2.50	3.03	.55	.43
25-1	.229	.261	1.14	.412	1.80	2.37	.93	.63
25-2W	.182	.343	1.88	.339	1.86	2.81	2.04	1.01
25-2	.201	.331	1.65	.285	1.42	2.25	2.76	1.16
25-3W	.182	.353	1.94	.363	2.00	2.98	1.89	.97
25-3	.212	.355	1.67	.365	1.72	2.56	1.89	.97
25-4	.196	.307	1.57	.244	1.25	2.04	3.38	1.26
26-2	.154	.369	2.40	.290	1.88	3.10	3.49	1.27
26-3	.161	.271	1.68	.290	1.80	2.65	1.76	.94
27-1	.224	.104	.46	.353	1.57	1.80	.35	.29
41-1	.220	.338	1.54	.315	1.43	2.21	2.32	1.07
42	.258	.337	1.31	.282	1.09	1.75	2.96	1.19
43	.392	.595	1.52	.746	1.90	2.66	1.33	.80
44W	.304	.451	1.48	.363	1.19	1.94	3.29	1.24
44	.313	.339	1.08	.325	1.04	1.58	2.18	1.04
45W	.439	.402	.92	.631	1.44	1.89	.94	.64
45	.542	.430	.79	.760	1.40	1.80	.79	.57
46W	.290	.364	1.25	.222	.76	1.40	9.14	1.64
46	.243	.279	1.15	.208	.85	1.43	4.09	1.34
54	.196	.098	.50	.610	3.11	3.33	.18	.16
56W	.149	.114	.76	.434	2.91	3.27	.30	.26
56	.154	.145	.94	.428	2.78	3.24	.41	.34
58	.166	.254	1.53	.557	3.35	4.11	.59	.46
60W	.182	.237	1.30	.546	3.00	3.64	.56	.43
60	.156	.228	1.46	.558	3.58	4.29	.51	.41
61W	.270	.527	1.95	.524	1.94	2.92	2.02	1.01
61	.205	.256	1.25	.434	2.12	2.74	.83	.59
62W	.210	.171	.81	.574	2.73	3.13	.35	.30
62	.210	.119	.57	.564	2.68	2.95	.24	.21

APPENDIX 4 A LISTING OF IMPORTANT SYMBOLS WITH THE PHYSICAL QUANTITY REPRESENTED AND THE UNITS EMPLOYED

A = cross-sectional area (m^2)

a = major semi-axis of a grain (m)

a = diameter (m)

B = magnetic induction (T)

b = minor semi-axis of a grain (m)

C = capacitance (F)

C = mechanical compliance (m/N)

C_L = load coefficient (numeric)

c = velocity of sound in air (m/s)

d = diameter (m)

d = half-depth of specimen gap (m)

E = energy (J)

e = electrical potential (volts)

F = force (N)

f = frequency (Hz)

f = magnetic foliation (numeric)

H = magnetic field intensity (A/m)

h_0 = air bearing clearance (m)

h = thickness (m)

h = axial length (m)

h = alignment factor (numeric)

I = moment of inertia (kg$\cdot$m^2)

I_{ij} = in-phase induced magnetic moment ($A \cdot m^2$)

i = electric current (A)

J = intensity of induced magnetization (A/m)

K_{go} = gauge pressure ratio (numeric)

K = effective spring constant (N/m)

k = Boltzmann's constant (1.38×10^{-23} J/°K)

L = inductance (H)

L_H = noise-field leakage (numeric)

l = magnetic lineation (numeric)

ℓ = length (m)

M = number of Barkhausen transitions between zero magnetization and saturation (numeric)

M = mutual inductance (H)

M = mass (kg)

m = magnetic moment ($A \cdot m^2$)

m = mass (kg)

N = demagnetizing factor (numeric)

N = number of laminations in a magnetic circuit element (numeric)

N = number of turns in half of the helix (numeric)

n = number of turns on solenoid (numeric)

n = number of randomly distributed magnetic grains in a rock specimen (numeric)

P = pressure (N/m^2)

P = power (W)

$\mathbf{P}$ = prolateness factor (numeric)

p = pressure (N/m^2)

Q = ratio of energy stored in a tuned circuit to the energy dissipated per radian at resonance (numeric)

Q_{ij} = quadrature induced magnetic moment (A·m^2)

q = filling factor (numeric)

q = electric charge (C)

q = ratio of lineation to foliation (numeric)

$\mathcal{R}$ = magnetic reluctance (A/Wb)

R = reflection loss (dB)

R = electrical resistance (ohms)

r = general linear dimension (m)

r = radius (m)

S = stress (N/m^2)

S = insertion loss (dB)

s = standard deviation (units of measured quantity)

T = torque (N·m)

T = absolute temperature (°K)

t = time (s)

t = lamination thickness (m)

V = volume (m^3)

V = electrical potential (volts)

W = spectral power density (W/Hz)

w = width (m)

x = general linear dimension (m)

Y = Young's modulus (N/m^2)

y = radial dimension (m)

Z = impedance (ohms)

z = axial dimension (m)

α = rate of attenuation (dB/m)

β' = angle of central disc of Airy pattern (rad)

β = hydrodynamic factor (numeric)

γ = radius of gyration (m)

δ = skin depth (m)

δ_r = residual loss angle (rad)

ϵ = volume fraction of specimen which is magnetic (numeric)

ϵ_0 = permittivity of free space (F/m)

ζ = anisotropy factor of a grain (numeric)

θ = angle between two directions (rad)

κ = magnetic susceptibility (numeric)

λ = wavelength of light (m)

μ = magnetic permeability (H/m)

μ_i = initial relative permeability (numeric)

μ_r = reversible relative permeability (numeric)

ν = viscosity (kg/m·s)

ξ = leakage factor (numeric)

ρ = resistivity (ohm·m)

ρ_0 = density of air (kg/m^3)

σ = density (kg/m^3)

σ_p = Poisson's ratio (numeric)

τ = torsional rigidity (N·m/rad)

ϕ = magnetic flux (Wb)

χ = intrinsic magnetic susceptibility (numeric)

Ψ = magnetic potential (A)

ω = angular frequency (rad/s)